Measurement of Charged Current and Neutral Current Cross Sections in Positron-Proton Collisions at $\sqrt{s} \simeq 300$ GeV

DISSERTATION

zur Erlangung des Doktorgrades
des Fachbereichs Physik
der Universität Hamburg

vorgelegt von

Beate Heinemann

aus Hamburg

Hamburg
1999

Abstract

An analysis is presented of data taken in positron-proton collisions at the ep-collider HERA with a centre of mass energy of $\sqrt{s} \simeq 300$ GeV. The data were taken in the H1 detector between 1994 and 1997 and correspond to an integrated luminosity of 35.7 pb^{-1}. The inclusive single and double-differential cross sections for charged and neutral current scattering are measured with four-momentum transfer squared Q^2 between 150 and 30000 GeV^2 and with Bjorken x between 0.0032 and 0.65. The entire analysis chain necessary for the determination of the cross sections is described where the emphasis is placed on the understanding of the performance of the H1 detector.

The cross section measurements are confronted with the predictions from the Standard Model and no significant deviation is found. The Q^2 evolution of the proton parton densities is tested by comparing the data to results from a phenomenological QCD analysis. At high Q^2 electroweak effects are observed which are consistent with the Standard Model expectation.

Zusammenfassung

Diese Arbeit stellt die Analyse von Wechselwirkungen zwischen Positronen und Protonen am HERA-Beschleuniger bei einer Schwerpunktsenergie von $\sqrt{s} \simeq 300$ GeV vor. Die Daten wurden zwischen 1994 und 1997 am H1 Detektor genommen und ensprechen einer integrierten Luminosität von 35.7 pb^{-1}. Die inklusiven Wirkungsquerschnitte wurden gemessen für Prozesse des geladenen und neutralen Stromes für Werte des Quadrates des Vierer-Impuls-Übertrages Q^2 zwischen 150 und 30000 GeV^2 und Bjorken-x-Werte zwischen 0.0032 und 0.65. Die gesamte Analyse-Kette, die hierfür notwendig war, wird beschrieben; insbesondere stellt das Verständnis des Ansprechverhaltens des Detektors einen Schwerpunkt der Arbeit dar.

Die Wirkungsquerschnitte werden den Vorhersagen des Standardmodells gegenübergestellt, wobei keine signifikante Abweichung gefunden wird. Die Vorhersagen der QCD über die Entwicklung der Partondichten mit Q^2 wird anhand der Daten in einem neuen kinematischen Bereich getestet. Bei hohen Q^2 werden Einflüsse der schwachen Wechselwirkung beobachtet, welche mit den Vorhersagen des Standardmodells übereinstimmen.

Contents

Introduction **I**

1 Theoretical Overview **3**

1.1 Deep Inelastic Scattering 3

1.2 Cross Sections and Structure Functions 4

1.3 Quantum Chromodynamics 8

1.4 Physics Beyond the Standard Model 10

2 HERA and the H1 Detector **12**

2.1 HERA 12

2.2 H1 13

2.3 Calorimeters 15

2.4 The Tracking System 18

2.5 The Luminosity System 19

2.6 The Time-of-Flight (ToF) system 20

2.7 The Trigger System and the Event Reconstruction 20

2.7.1 The First Trigger Level 20

2.7.2 The Second and Third Trigger Level 23

2.7.3 The Fourth Trigger Level and the Event Reconstruction . . . 23

3 Monte Carlo Simulation **24**

3.1 Backgrounds to Deep Inelastic Scattering 24

3.2 Monte Carlo Event Generators 25

3.3 Simulation of the H1 Detector 27

4 Kinematic Reconstruction **28**

5 Electron Angle Determination **31**

5.1 Track Fitting Procedure 31

5.2 Alignment of the LAr Calorimeter 32

5.3 Track Angle Measurement 35

5.4 Final Angle Determination 39

6 Electron and Hadronic Energy Measurement **40**

6.1 Electron Energy Measurement 40

6.2 Hadronic Energy Measurement 51

7 Selection of Neutral Current Events **57**

7.1 Run Selection 57

7.2 Trigger 58

7.3 Electron Identification 63

7.4 Vertex and Track link requirement 65

7.5 Background Rejection 72

7.6 The Final Neutral Current Data Sample 76

8 Selection of Charged Current Events **79**

8.1 Efficiency Evaluation using "Pseudo-CCs" 80

8.2 The Trigger 80

8.3 The Vertex Requirement 85

8.4 Rejection of non-ep-Background 85

8.5 Rejection of ep-induced Background 89

8.6 Scanning of the Data Sample 93

8.7 The Final Charged Current Data Sample 93

9 Cross Section Measurement Procedure **95**

9.1 Selection of Bins 95

9.2 Extraction of the Cross Section 98

9.3 Radiative Corrections 101
9.4 Systematic Uncertainties 106
9.5 QCD Analysis Procedure 110

10 Results and Interpretation **113**

10.1 The double differential NC cross section 113
10.2 Extraction of the Structure Function F_2 117
10.3 The double differential CC cross section 118
10.4 The x-dependence of the cross sections 121
10.5 The Q^2-dependence of the cross sections 123
10.6 The Total Charged Current Cross Section 125
10.7 Interpretation of the CC Cross Section 126
10.8 Constraints on Physics beyond the Standard Model 130
10.9 Comparison with e^-p Cross Sections 132

11 Summary and Outlook **135**

A Tables of Results **138**

Introduction

Experiments of deep inelastic scattering of leptons off nucleons have played a pivotal role in the understanding of the structure of matter and in the foundation of the Standard Model as the theory of the strong and electroweak interactions.

The first evidence for the presence of substructure in nucleons was found at the Stanford Linear Accelerator (SLAC) in which electrons were collided with nucleons [1]. The structure functions were found to be independent of the relevant scale Q^2 as it had been predicted by Bjorken [2]. Feynman [3] explained this behaviour by the presence of partons in the proton which were identified with the quarks postulated by Gell-Mann from the symmetry properties of the spectrum of hadrons [4]. Nowadays the interactions of partons within the nucleon are described by the theory of the strong interaction called Quantum Chromodynamics. However, the parton densities cannot be predicted by this theory yet.

The establishment of the weak interaction began in 1971 with the observation of neutral current neutrino scattering in the Gargamelle Bubble Chamber [5]. The electromagnetic and weak forces were unified in one theory developed by Glashow, Salam and Weinberg [6] which predicted the existence of two charged ($W^{\pm}$) and one neutral boson (Z) of large mass. The observation of these particles in collider experiments [7, 8] is one of the great successes of that theory. There are so far no results from high energy collider experiments which contradict this theory. However, the Higgs boson held responsible for the breaking of the $SU(2)_L \times U(1)$ gauge symmetry has not yet been observed.

In the past 30 years various DIS experiments [9, 10, 11, 12, 13, 14] have helped to constrain parameters of the electroweak theory and to understand the partonic structure of the proton. The results were obtained in both neutral and charged current scattering. These experiments were all made by colliding leptons with a stationary (fixed) target of protons or heavier nuclei. The energy in the centre of mass system was restricted to $\sqrt{s} \lesssim 40$ GeV. In 1992 the H1 and ZEUS experiments at the HERA accelerator, in which both the leptons and the protons are accelerated, began to take data. Since the centre of mass energy is almost an order of magnitude larger (about 300 GeV) than in the fixed-target experiments the structure of the proton can be studied in new kinematic regimes.

In the first years of data taking at HERA the physics program was largely concerned with measuring the proton structure function and QCD dynamics at low x where the partons carry only a very small fraction of the total momentum of the proton

[15, 16, 17, 18]. The strong rise of the structure function towards low x can be understood in terms of QCD as shown in [19]. Only now have the H1 and ZEUS experiments accumulated sufficient data to probe the high Q^2 region which is the topic of this thesis. The absolute value of the squared four-momentum transfer of the exchanged boson Q^2 is related to its wave-length via $\lambda = 1/\sqrt{Q^2}$ [1]. At the highest obtainable values of Q^2 the substructure of the proton is therefore resolved down to distances of $\lambda \approx 10^{-18}$ m which is about one thousandth of the proton radius. At these high values of Q^2 the weak sector of the Standard Model may also be tested. An earlier analysis of the Q^2 dependence of the charged current cross section revealed the mass of the exchanged boson to be consistent with the mass of the W boson measured elsewhere [20, 21, 22, 23].

In this thesis a measurement of charged current and neutral current cross sections is presented in the kinematic range $150 \leq Q^2 \leq 30000$ GeV^2 and $0.0032 \leq x \leq 0.65$. The analysis is based on a data set collected in the years 1994-97 in positron-proton collisions with an integrated luminosity of $\mathcal{L} = 35.7$ pb^{-1}. The data set is more than 10 times larger and the kinematic region is extended to higher Q^2 and higher x than previous measurements [19, 24, 21, 23]. The results obtained in this thesis are published in [25].

In the first chapter a theoretical overview of deep inelastic scattering is given. The influence of possible contributions from physics beyond the Standard Model is also briefly discussed. In the second chapter the HERA accelerator ring and the H1 experiment are described. The third and fourth chapters are devoted to the Monte Carlo simulation and the kinematic reconstruction respectively. The fifth chapter is devoted to the determination of the positron scattering angle. The subjects of the sixth chapter are the measurements of positron and hadronic energies and the estimation of their uncertainties. The seventh chapter describes the selection of neutral current events and the eighth that of charged current events. In the ninth chapter the correction procedure used to determine the cross section is given. The tenth chapter is devoted to the presentation and interpretation of the cross sections. It is shown that both the neutral and charged current cross sections can be understood in terms of Quantum Chromodynamics. The neutral current cross section shows clear evidence for the presence of the Z boson as predicted by the Standard Model. The charged current cross section is found to be consistent with the Standard Model expectation of one exchanged W boson. Constraints on physics beyond the Standard Model which can be deduced from the results are presented. Finally the results are summarised and an outlook is given.

[1] The units in this thesis are chosen such that $\hbar = c = 1$. Therefore energies, momenta and masses are all quoted in units of GeV.

Chapter 1

Theoretical Overview

This analysis is concerned with the measurement of the cross sections for deep inelastic positron proton scattering. The basics for the theoretical understanding of this process are introduced in this chapter. Firstly the deep inelastic scattering process is explained. Then the cross sections and their relation to the structure functions are discussed, followed by a brief outline of the theory of the strong interaction. Finally some ideas are presented on physics beyond the Standard Model.

1.1 Deep Inelastic Scattering

There are two contributions to deep inelastic scattering (DIS), both of which can be measured at HERA: neutral current (NC) interactions, $ep \to eX$ and charged current (CC) interactions, $ep \to \nu X$. In the Standard Model a photon (γ) or Z boson is exchanged in a NC interaction, and a W boson in a CC interaction. The diagrams for these processes are shown in figure 1.1.

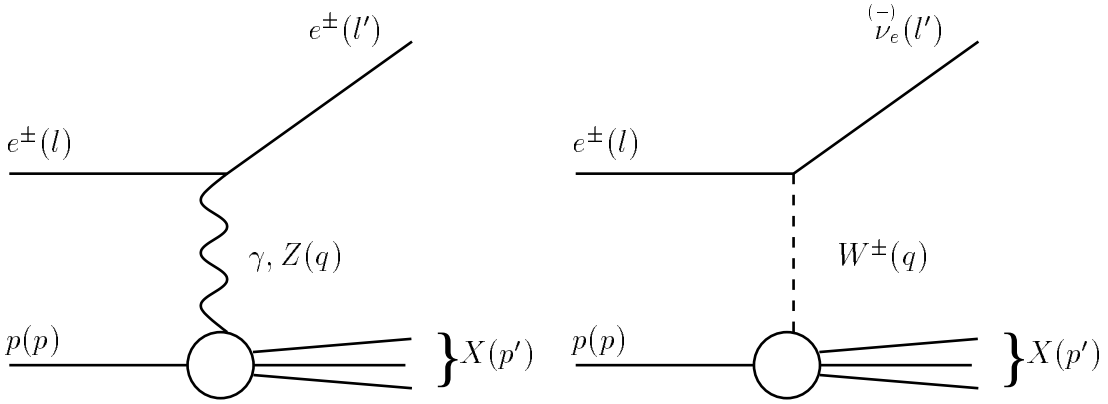

Figure 1.1: *Diagrams for deep inelastic NC (left) and CC (right) scattering. The particle types and their four-momenta are indicated.*

The 4-momenta of the particles involved in the scattering process are indicated, they are

- l for the incoming electron [1]
- l' for the outgoing lepton
- p for the incoming proton
- p' for the system of particles X in the outgoing hadronic final state
- $q = l - l'$ for the exchanged boson

The kinematics of the scattering process can be uniquely described by two variables for a fixed ep centre-of-mass energy $\sqrt{s}$. Variables which are commonly used are the virtuality Q^2, Bjorken-x and the inelasticity y, which are defined as

$$Q^2 = -q^2 = -(l - l')^2, \qquad x = \frac{Q^2}{2p \cdot q}, \qquad y = \frac{p \cdot q}{p \cdot l} \tag{1.1}$$

These variables are related to the centre-of-mass energy via $s = (p + l)^2 = Q^2/xy$.

In the Quark-Parton-Model (QPM) the DIS process is interpreted as the interaction of a lepton with a constituent of the proton, a so-called "parton". The remaining partons in the proton form the proton remnant system. The variable x is the fractional momentum of the proton carried by the struck parton if the proton and parton masses are neglected. In the QPM these partons are interpreted as quarks in the proton. The largest fraction of the proton momentum is assigned to the three "valence quarks".

1.2 Cross Sections and Structure Functions

The cross sections for deep inelastic ep scattering can be expressed by one propagator term and a structure function term. The Born cross section for the **NC process** is given by

$$\frac{\mathrm{d}^2\sigma_{\mathrm{NC}}^{e^\pm p}}{\mathrm{d}x\mathrm{d}Q^2} = \frac{2\pi\alpha^2}{x}\left[\frac{1}{Q^2}\right]^2 \phi_{\mathrm{NC}}^{\pm}(x, Q^2) \tag{1.2}$$

$$\text{with } \phi_{\mathrm{NC}} = Y_+ \tilde{F}_2^{\pm}(x, Q^2) + y^2 \tilde{F}_L^{\pm}(x, Q^2) \mp Y_- x\tilde{F}_3^{\pm}(x, Q^2) \tag{1.3}$$

in which $\alpha = e^2/4\pi$ is the fine structure constant. The NC "structure function term" ϕ_{NC} is a linear combination of the generalised structure functions $\tilde{F}_L$, $\tilde{F}_2$ and $x\tilde{F}_3$. $\tilde{F}_L$ is known as the longitudinal structure function. The dependence on the inelasticity is contained in the functions $Y_\pm = 1 + (1 \pm y^2)$.

The generalised structure functions are composed of five structure functions that discriminate between pure γ exchange, γZ interference and pure Z exchange and

[1] The expression "electron" is used as a generic word for electrons and positrons unless stated explicitly otherwise.

that are independent of the lepton charge. For scattering of unpolarised particles these are

$$\tilde{F_2}^{\pm} = F_2 - v_e \left[\frac{\kappa_w Q^2}{Q^2+M_Z^2}\right] F_2^{\gamma Z} + (v_e^2+a_e^2)\left[\frac{\kappa_w Q^2}{Q^2+M_Z^2}\right]^2 F_2^Z \quad (1.4)$$

$$x\tilde{F_3}^{\pm} = \pm a_e \left[\frac{\kappa_w Q^2}{Q^2+M_Z^2}\right] x F_3^{\gamma Z} \mp 2 a_e v_e \left[\frac{\kappa_w Q^2}{Q^2+M_Z^2}\right]^2 x F_3^Z \quad (1.5)$$

Here F_2 arises from the pure photon exchange, $F_2^{\gamma Z}$ and $xF_3^{\gamma Z}$ arise due to the γZ interference and F_2^Z and xF_3^Z due to the pure Z exchange. v_e and a_e are the vector and axial-vector couplings of the electron respectively which are related to its weak isospin $I_{3e} = -\frac{1}{2}$ via $v_e = I_{3e} + 2\sin^2\theta_W$ and $a_e = I_{3e}$. M_Z is the mass of the Z boson and κ_w is a function of the Weinberg angle

$$\kappa_w = \frac{1}{4\sin^2\theta_W \cos^2\theta_W}.$$

In the QPM the structure functions F_2, $F_2^{\gamma Z}$ and F_2^Z are related to the sum of the quark and anti-quark densities

$$[F_2, F_2^{\gamma Z}, F_2^Z] = x\sum_q [e_q^2, 2e_q v_q, v_q^2+a_q^2]\{q(x,Q^2)+\bar{q}(x,Q^2)\} \quad (1.6)$$

and the structure functions $xF_3^{\gamma Z}$ and xF_3^Z to the difference between quark and anti-quark densities:

$$[xF_3^{\gamma Z}, xF_3^Z] = x\sum_q [2e_q a_q, 2v_q a_q]\{q(x,Q^2)-\bar{q}(x,Q^2)\} \quad (1.7)$$

The sums are over all quark flavours q. The function $q(x,Q^2)dxdQ^2$ is the probability of finding a quark of flavour q in the proton with momentum fraction between x and $x+dx$ at a scale between Q^2 and Q^2+dQ^2. e_q is the charge of quark q in units of the electron charge. The vector and axial-vector couplings of the quarks are given by

$$v_q = I_{3q} - 2e_q \sin^2\theta_W, \qquad a_q = I_{3q} \quad (1.8)$$

where I_{3q} is the weak isospin of the quark.

The vector coupling of the electron $v_e = -\frac{1}{2} + 2\sin^2\theta_W \approx 0.04$ can, at large Q^2, be neglected and the structure functions become

$$\tilde{F_2}^{\pm} \simeq F_2 + a_e^2 \left[\frac{\kappa_w Q^2}{Q^2+M_Z^2}\right]^2 F_2^Z \quad (1.9)$$

$$x\tilde{F_3}^{\pm} \simeq \mp 2 a_e \left[\frac{\kappa_w Q^2}{Q^2+M_Z^2}\right] x F_3^{\gamma Z} \quad (1.10)$$

In this approximation $\tilde{F_2}$ is only sensitive to the contributions from pure γ and Z exchange and is therefore the same for electron-proton and positron-proton scattering. On the other hand, $x\tilde{F_3}$ depends only on the γZ interference term. The cross

section can then be written as

$$\frac{\mathrm{d}^2\sigma_{NC}^{e^\pm p}}{\mathrm{d}x\mathrm{d}Q^2} \simeq \frac{2\pi\alpha^2}{x}\left\{\frac{1}{Q^4}Y_+F_2 + a_e^2\kappa_w^2\left[\frac{1}{Q^2+M_Z^2}\right]^2 Y_+F_2^Z \mp 2a_e\kappa_w\left[\frac{1}{Q^2(Q^2+M_Z^2)}\right]Y_-xF_3^{\gamma Z}\right\} \quad (1.11)$$

Now the three contributions due to γ exchange, Z exchange and γZ interference are clearly seen from the propagator terms. Due to the destructive interference of the γ and Z boson in e^+p scattering the cross section is decreased at very high Q^2 compared to the cross section for e^-p scattering that is increased since in this case the interference is constructive.

The expected corrections to the cross section due to the presence of the Z are shown in figure 1.2 for e^+p scattering as a function of Q^2 at $x = 0.4$. Also indicated are the corresponding y values. For $Q^2 < 1000$ GeV^2 the influence of the Z is negligible. At $Q^2 = 20000$ GeV^2 the γZ interference reduces the cross section by about 45% whilst the Z exchange increases it by 25%. The net effect of the presence of the Z at this x value is a reduction of the cross section by about 30% at $Q^2 = 20000$ GeV^2.

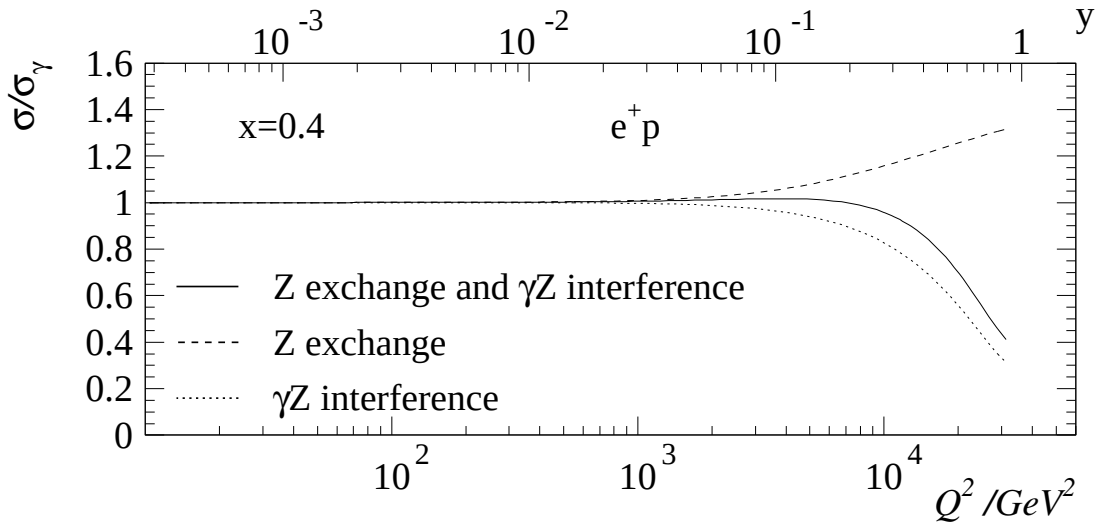

Figure 1.2: *The ratio of the NC cross section to the cross section when only γ exchange takes place (solid line). In addition the influences of the pure Z exchange (dashed line) and the γZ interference (dotted line) are shown separately.*

For **CC interactions** the expression for the cross section is similar to that for NC interactions (see eq. 1.2)

$$\frac{\mathrm{d}^2\sigma_{\mathrm{CC}}^{e^\pm p}}{\mathrm{d}x\mathrm{d}Q^2} = \frac{G_F^2 M_W^4}{2\pi x}\left[\frac{1}{Q^2+M_W^2}\right]^2 \phi_{\mathrm{CC}}^{\pm}(x,Q^2) \quad (1.12)$$

$$\text{with } \phi_{\mathrm{CC}}^{\pm} = Y_+\tilde{W_2}^{\pm}(x,Q^2) + y^2\tilde{W_L}^{\pm}(x,Q^2) \mp Y_-x\tilde{W_3}^{\pm}(x,Q^2) \quad (1.13)$$

where M_W is the mass of the W and G_F is the Fermi constant:

$$G_F = \frac{\pi\alpha}{\sqrt{2}\sin^2\theta_W M_W^2} = \frac{g^2}{4\sqrt{2}M_W^2} \tag{1.14}$$

with g being the electroweak coupling constant. The structure functions for CC interactions are defined in analogy to the NC case and are called $\tilde{W}_L$, $\tilde{W}_2$, $x\tilde{W}_3$.

The correspondence between the NC and CC cross sections can easily be seen when the cross sections are expressed in terms of the couplings e and g:

$$\frac{\mathrm{d}^2\sigma_{\mathrm{NC}}^{e^\pm p}}{\mathrm{d}x\mathrm{d}Q^2} = \frac{e^4}{8\pi x}\left[\frac{1}{Q^2}\right]^2 \phi_{\mathrm{NC}}^{\pm}(x,Q^2) \tag{1.15}$$

$$\frac{\mathrm{d}^2\sigma_{\mathrm{CC}}^{e^\pm p}}{\mathrm{d}x\mathrm{d}Q^2} = \frac{g^4}{64\pi x}\left[\frac{1}{Q^2+M_W^2}\right]^2 \phi_{\mathrm{CC}}^{\pm}(x,Q^2) \tag{1.16}$$

The Q^2 dependence of the cross sections principally arises from the propagator term which is $1/Q^4$ for the NC and $1/(Q^2+M_W^2)^2$ for the CC interaction. While the NC cross section decreases very rapidly with increasing Q^2, the CC cross section falls much less steeply until $Q^2 \approx M_W^2$. Since the coupling constants of the weak and electromagnetic interactions are related in the Standard Model by $g^2 = e^2/\sin^2\theta_W \approx 4e^2$ the NC and CC cross sections are expected to be of similar size at the electroweak unification scale $Q^2 \gtrsim M_W^2 \approx M_Z^2$ if $\phi_{\mathrm{CC}} \approx \phi_{\mathrm{NC}}$. This is seen in figure 1.3 where the Q^2 dependence of the CC and NC cross sections is shown for e^+p and e^-p scattering. At low Q^2 the NC cross section is about three orders of magnitude larger than the CC one. With increasing Q^2 they become more similar. In e^+p scattering the CC cross section remains even at the highest Q^2 smaller than the NC cross section. In e^-p scattering it is expected to be larger for $Q^2 > 10,000$ GeV^2. These differences arise from the coupling to different quark flavours depending on the lepton charge and will be discussed below. A complication to this picture also arises from the Z exchange so that not only the photon propagator but also the Z propagator $1/(Q^2+M_Z^2)^2$ is of importance (see eq. 1.11) at these high values of Q^2.

For unpolarised particles the generalised CC structure functions are

$$\tilde{W_2}^{\pm}(x,Q^2) = \frac{1}{2}W_2^{\pm}(x,Q^2) \tag{1.17}$$

$$x\tilde{W_3}^{\pm}(x,Q^2) = \mp\frac{1}{2}xW_3^{\pm}(x,Q^2). \tag{1.18}$$

They are related to the parton densities in the QPM via

$$W_2^+(x,Q^2) = 2x\left\{d(x,Q^2)+s(x,Q^2)+\bar{u}(x,Q^2)+\bar{c}(x,Q^2)\right\} \tag{1.19}$$

$$xW_3^+(x,Q^2) = 2x\left\{d(x,Q^2)+s(x,Q^2)-[\bar{u}(x,Q^2)+\bar{c}(x,Q^2)]\right\} \tag{1.20}$$

$$W_2^-(x,Q^2) = 2x\left\{u(x,Q^2)+c(x,Q^2)+\bar{d}(x,Q^2)+\bar{s}(x,Q^2)\right\} \tag{1.21}$$

$$xW_3^-(x,Q^2) = 2x\left\{u(x,Q^2)+c(x,Q^2)-[\bar{d}(x,Q^2)+\bar{s}(x,Q^2)]\right\} \tag{1.22}$$

Note that both the bottom and top quark don't contribute since the top quark is too massive to be produced in the kinematic range available at HERA.

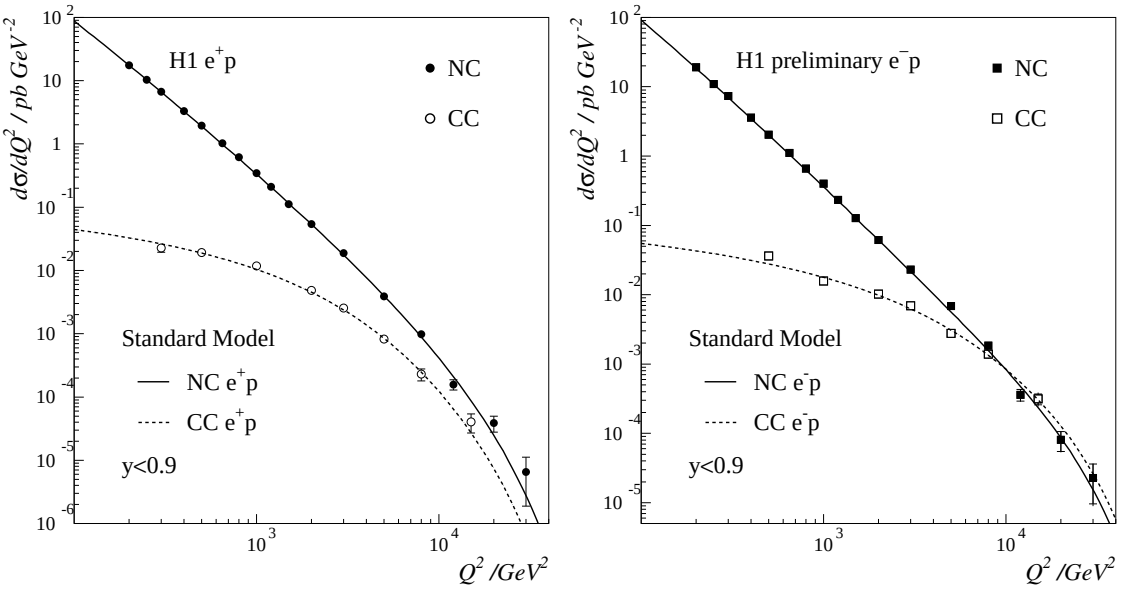

Figure 1.3: *The cross sections* $\mathrm{d}\sigma/\mathrm{d}Q^2$ *for CC and NC scattering (a) in positron-proton and (b) in electron-proton collisions. Shown are the H1 measurements (symbols) and the theoretical predictions (curves).*

When neglecting the contribution from Z exchange and F_L to the NC structure function term, the structure function terms of CC and NC interactions are related to the quark densities in the QPM via

$$\phi^{\pm}_{\mathrm{NC}} \simeq Y_+ F_2 = Y_+ x \left[\frac{4}{9}(u+\bar{u}+c+\bar{c}) + \frac{1}{9}(d+\bar{d}+s+\bar{s}+b+\bar{b})\right] \quad (1.23)$$

$$\phi^{+}_{\mathrm{CC}} = x\left[\bar{u}+\bar{c}\right] + (1-y)^2 x\left[d+s\right] \quad (1.24)$$

$$\phi^{-}_{\mathrm{CC}} = x\left[u+c\right] + (1-y)^2 x\left[\bar{d}+\bar{s}\right] \quad (1.25)$$

It can be seen that the NC cross section is, in this simple picture, mainly sensitive to the u-quark density, while the e^+p CC cross section is sensitive to the d-quark density at low y and to the $\bar{u}$- and $\bar{c}$-densities at high y. For e^-p scattering the CC cross section mainly probes the u-quark density.

1.3 Quantum Chromodynamics

The interactions of the partons within the QPM can be described by the theory of the strong interaction, Quantum Chromodynamics (QCD). QCD is a non-abelian gauge theory which is invariant under $SU(3)$ colour transformation. The gauge bosons are called gluons and couple to the colour-charge which is carried by all partons. Quarks appear in three colours; eight gluons carry different combinations of colour charges. The gluons are massless like the photons in the electromagnetic interaction but they interact, in contrast to the photon, with one another. This results in a strong dependence of the coupling strength α_s on the scale (e.g. Q^2). However, at small distances (high Q^2) the couplings between the quarks and gluons become small: this is known as "asymptotic freedom". At large distances the couplings increase which

leads to "confinement": quarks and gluons are not free but only appear in hadronic bound states. Therefore α_s is a function of the scale of the interaction which is in this analysis Q^2. In leading order the coupling strength is given by

$$\alpha_s(Q^2) = \frac{12\pi}{(33 - 2n_f)\ln(Q^2/\Lambda^2_{\rm QCD})}$$

At high Q^2 α_s is sufficiently small so that QCD can be treated as a perturbation theory like the electroweak theory. Within perturbative QCD it is not possible to calculate the parton densities, but at higher Q^2 it can be tested whether the predictions of perturbative QCD about the evolution of these parton densities with x and Q^2 are correct. The evolution as function of $\ln(Q^2)$ is given by the DGLAP [26] evolution equations. The parton densities also evolve as function of $\ln(1/x)$ as it is described by the BFKL [27] equations.

The DGLAP evolution equations are given by

$$\frac{\partial q(x,t)}{\partial t} = \frac{\alpha_s(t)}{2\pi}\int_x^1 \frac{\mathrm{d}}{y}\left[q(y,t)P_{qq}(\frac{x}{y}) + g(y,t)P_{qg}(\frac{x}{y})\right] \quad (1.26)$$

$$\frac{\partial g(x,t)}{\partial t} = \frac{\alpha_s(t)}{2\pi}\int_x^1 \frac{\mathrm{d}}{y}\left[q(y,t)P_{gq}(\frac{x}{y}) + g(y,t)P_{gg}(\frac{x}{y})\right] \quad (1.27)$$

where $t = \ln(Q^2)/\Lambda_{\rm QCD}$ and P_{ab} are the splitting functions. They give the probability of parton b with momentum fraction y producing parton a with momentum fraction x when Q^2 changes to $Q^2 + \ln Q^2$. The Feynman diagrams corresponding to the four splitting functions are shown in figure 1.4.

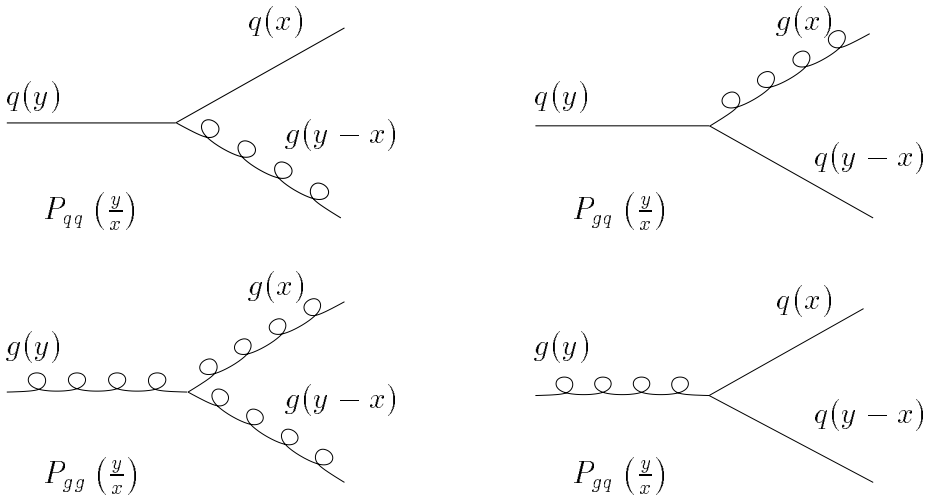

Figure 1.4: *The Feynman diagrams for the four splitting functions in the DGLAP evolution equation.*

The predictions of QCD are tested against data by making a fit to the data where the parton densities are parametrised by a functional form of typically five parameters (see e.g. [28], [29]).

1.4 Physics Beyond the Standard Model

In the kinematic region covered by this measurement there was a hint of possible physics beyond the Standard Model. In the analysis of the data taken in 1994-96 there was an excess of the observed number of events above the Standard Model expectation reported for $Q^2 > 15000$ GeV^2 by the H1 and ZEUS collaboration [30, 31]. In H1 this excess was found to be most pronounced at $M = \sqrt{sx} = 200$ GeV. A large number of theoretical explanations were given (see e.g. [32]) where possible new physics scenarios, which could lead to the observed excess, were discussed. The three most favoured scenarios are the interference of the Standard Model bosons with a new heavy boson (contact interaction), the production of a leptoquark (LQ) at $M_{LQ} \approx 200$ GeV and production of a super-symmetric squark $\tilde{q}$ at $M_{\tilde{q}} \approx 200$ GeV. These three scenarios are now briefly discussed.

Contact Interactions In the process $e^+p \to e^+X$ any new particles may produce indirect effects through the interference of a virtual particle exchange with the γ and Z bosons in the Standard Model. For particle masses above the centre of mass energy, such indirect signatures can be investigated by searching for a 4-fermion point-like $(\bar{e}e)(\bar{q}q)$ contact interaction. The Lagrangian for contact interactions [33] includes vector and axial couplings as well as couplings to left- and right- handed particles. The new particle may interfere destructively or constructively.

The coupling coefficients are given by $\eta_{if} \equiv \pm \left(g/\Lambda^{\pm}_{if}\right)^2$ where i and f denote the helicity of the lepton and quark, respectively. The coupling strength is conventionally chosen $g \equiv 4\pi$ and Λ denotes then the compositeness scale. Constraints on such new particles are expressed in terms of the compositeness scale Λ for different chiral models (LL,LR,...) and assuming constructive or destructive interference.

Presently the limits on the compositeness scale for $(\bar{e}e)(\bar{q}q)$ are $\Lambda \approx 1 - 5$ TeV as obtained at LEP, Tevatron and HERA.

Leptoquarks Leptoquarks are colour triplet bosons of spin 0 or 1, carrying lepton and baryon number. They appear naturally in many theories beyond the Standard Model, such as Grand Unified Theories [34] and Superstring inspired E_6 models [35], and in some Compositeness [36] and Technicolour [37] models. They can be produced at HERA in the s-channel if $M_{LQ} \lesssim \sqrt{s}$ or exchanged in the u-channel. The contact interaction analysis, described above, is mainly sensitive to the u-channel exchange, i.e. in this case $\eta_{if} = c_{if}(\lambda/M_{LQ})^2$ where λ is the coupling of the leptoquark.

Leptoquarks which are produced in the s-channel decay subsequentally. If they decay into eq, their existence cannot experimentally be distinguished on an event basis from DIS events, but can be inferred by analysing events in terms of the mass M_{LQ}- and the y-distribution. The mass of the leptoquark is related to the x-Bjorken value in DIS via $M_{LQ} = \sqrt{xs}$. The y-dependence of the cross section is sensitive to the spin of the leptoquark since y is related to the scattering angle θ^* in the centre of mass system via $1 - y = \cos^2(\theta^*/2)$. The cross section is independent of y

for leptoquarks of spin 0 and $\propto (1-y)^2$ for spin-1-leptoquarks. In both cases the y-dependence is different to DIS where at fixed x the cross section is $\propto 1/y^2$. The typical signature is an excess of events above the Standard Model expectation at a given mass M_{LQ} or x value and high y.

Squarks In Supersymmetry theories the super partner of the quark may be a squark which at HERA could be produced in the s-channel like a leptoquark. This is only possible under the condition that R-parity is not conserved. The observed excess discussed above has often been discussed (see e.g. [38]) in terms of the production of a stop quark $\tilde{t}$, the super-partner of the top quark. In this scenario it is also possible to explain an abnormally high rate of events observed by the H1 collaboration with a high momentum μ and a hadronic final state with high transverse momentum [39].

Chapter 2

HERA and the H1 Detector

In this chapter a brief overview of the HERA machine and the H1 detector are given. First the HERA machine is briefly introduced. Then the H1 detector is described with focus on the components which are important for the present measurement.

2.1 HERA

The HERA accelerator ring is situated at DESY in Hamburg and has a circumference of 6.4 km. It consists of two storage rings, one for electrons or positrons, and one for protons. In 1994-97 positrons were accelerated to an energy of $E_e = 27.6$ GeV and protons to an energy of $E_p = 820$ GeV leading to a centre-of-mass energy of $\sqrt{s} = 301$ GeV. In 1998 HERA accelerated electrons and the proton beam energy was increased to $E_p = 920$ GeV.

The positrons and protons are stored in up to 220 bunches in the two rings with a time interval of 96 ns between two consecutive bunches. The typical number of colliding bunches was ≈ 175. In addition there are so-called "pilot bunches" of positrons and protons which are not colliding with any bunch from the other beam. Every bunch consists of approximately 10^{11} particles. The particle density within a bunch follows in longitudinal direction a gaussian distribution with a width of $\sigma \approx 11$ cm. The proton bunch has a complicated longitudinal structure which leads to the presence of several "satellite bunches" near the "main bunch".

The positron and proton beam collide in two interaction regions where the detectors H1 and ZEUS have taken data since 1992. There are two more experiments, HERMES and HERA-B, which use only one of the beams. In the HERMES detector the longitudinally polarised positron beam is collided with a polarised hydrogen-, deuterium- or helium-gas target with the aim of measuring the spin structure of the nucleon. The HERA-B experiment is still under construction. It will start taking data in the beginning of 2000 to investigate CP violation in the $\bar{B}^0 B^0$ system by studying interactions of protons from the beam halo with a Wolfram wire target.

During the four years of positron-proton running the integrated luminosity delivered

by HERA per year was steadily increased. For the present analysis the luminosities are $\mathcal{L}_{94} = 2.74$ pb^{-1}, $\mathcal{L}_{95} = 3.76$ pb^{-1}, $\mathcal{L}_{96} = 7.88$ pb^{-1}and $\mathcal{L}_{97} = 21.30$ pb^{-1}amounting to a total integrated luminosity of $\mathcal{L} = 35.68$ pb^{-1}.

2.2 H1

The H1 detector (see 2.1) is situated in the North Hall of HERA. It is designed as a multi-purpose detector to study high-energy electron-proton collision events. It has almost hermetic coverage around the beam axis. The limitation comes from the space taken up by the beam pipe itself. Points within the H1 detector are described with a coordinate system (X, Y, Z) in which the nominal interaction point defines the origin, X is the direction to the centre of the HERA ring, Y is the upwards direction and Z is the direction of the proton beam. The polar and azimuthal angles are defined correspondingly, so that the polar angle is $\theta = 0^o$ in proton beam direction and $\theta = 180^o$ in electron beam direction. The azimuthal angle is $\phi = \arctan Y/X$ so that it is positive for positive values of Y.

Since the proton momentum is significantly larger than the electron momentum most particles produced in the interaction are scattered in the proton direction. Therefore the detector is asymmetric with more instrumentation in this region that is often referred to as "forward" region.

A schematic view of the 1994 setup of the H1 detector is shown in Fig. 2.1. The interaction region is surrounded by a tracking system which consists of a central [2] and forward [3] part. It is enclosed in the calorimeters. The central and forward regions are covered by the Liquid-Argon calorimeter (LAC) which consists of electromagnetic [4] and hadronic sections [5]. In the backward region it is supplemented by a backward calorimeter (BEMC) [12] and the backward proportional chamber (BPC). A super-conducting coil [6] surrounding the calorimeters provides a homogeneous magnetic field of 1.2 T. The Iron return yoke [10] contains layers of streamer tubes [9] to measure the tails from hadronic energy showers and to identify muons. In the forward direction the measurement of muons is made by six layers of drift chambers [9], three on either side of the toroid magnet [11]. In the forward region the PLUG calorimeter [13] is installed. In the negative Z direction the luminosity system is placed close to the beam-pipe [1]. In the forward direction Forward Proton Spectrometers (FPS) and a Forward Neutron Calorimeter (FNC) are installed to investigate interactions containing a leading baryon. In 1995 the BEMC and BPC were replaced by a Spaghetti Calorimeter (SPACAL) and a Backward Drift Chamber (BDC). In 1996 a Central Silicon Tracker (CST) was installed close to the beam-pipe around the interaction vertex for the precise measurement of charged particles. It was supplemented in 1997 in the backward region by the Backward Silicon Tracker (BST) which measures the angle of electrons scattered into the backward region.

A detailed description of the H1 detector can be found in [40]. In the following only the components important for the present analysis are described.

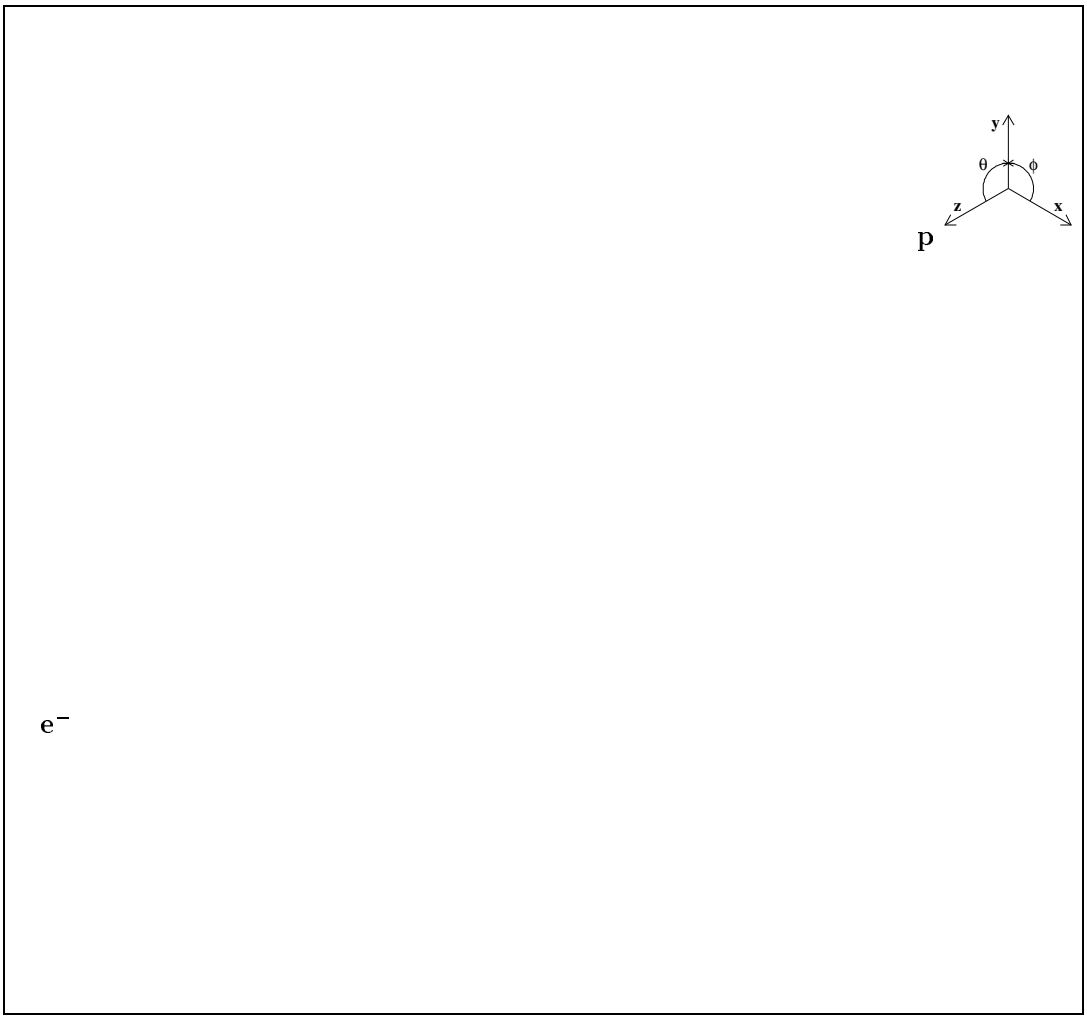

1	Beam pipe and beam magnets	9	Muon chambers
2	Central tracking device	10	Instrumented iron yoke
3	Forward tracking device	11	Forward muon toroid
4	Electromagnetic LAr calorimeter	12	Backw. electromagn. calorimeter (BEMC)
5	Hadronic LAr calorimeter	13	PLUG calorimeter
6	Superconducting coil (1.15 T)	14	Concrete shielding
7	Compensating magnet	15	Liquid argon cryostat
8	Helium supply for 7		

Figure 2.1: *Schematic 3D view of the H1 detector*

2.3 Calorimeters

There are four calorimeters in the central part of the H1 detector. The LAC is used in the present analysis for the identification of the scattered electron and the measurement of its energy and angle, as well as the energy measurement of the hadronic final state. It is also used for triggering CC and NC events as will be described in section 2.7. The other three calorimeters, the backward calorimeter, the PLUG and the Tail catcher, are of minor importance for the present analysis and are therefore only described briefly.

The Liquid-Argon Calorimeter

Energies of particles scattered into the central part ($4^o \lesssim \theta \lesssim 153^o$) of the H1 detector are measured by the Liquid-Argon calorimeter (LAC). It is a sandwich calorimeter consisting of an inner section (EM) for the measurement of electromagnetic showers and an outer section (HAD) to measure energies of hadronic showers . It is built out of different "wheels" as can be seen in the schematic $R-Z$-view of the LAC presented in figure 2.2(a).

- the Backward Barrel Electromagnetic calorimeter (BBE)
- the Central Barrel calorimeter modules (CB1,CB2,CB3)
- the Forward Barrel calorimeter modules (FB1,FB2)
- the Inner and Outer Forward calorimeters (IF,OF)

All wheels apart from the BBE and the OF consist of an EM and HAD section. The BBE consists of an electromagnetic section only, the OF only of two hadronic sections. The wheels are divided in azimuthal angle ϕ into 8 octants (see figure 2.2(b)). The shape of the BBE octants is made such that the BBE has a 16-fold symmetry (see figure 2.3). All other octants are plane, so that the other wheels have an 8-fold symmetry (see figure 2.2(b)). There are insensitive regions between the modules indicated by the vertical lines in figure 2.2 which are problematic for the measurement due to energy losses in these regions. These gaps between the wheels are called "z-cracks", between the octants "ϕ-cracks".

The LAC is segmented in to 44000 cells to ensure a good spatial resolution of deposited energies. Each cell consists of absorber plates supplemented by high voltage and readout electrodes. The sampling medium between the absorber plates is liquid Argon. The absorber material is lead in the electromagnetic and stainless steel in the hadronic section. The electromagnetic section consists of three cell layers in the BBE, CB and FB1 wheels, four in FB2 and seven in the IF. The cell sizes vary and are optimised to measure the longitudinal and transverse extension of electromagnetic showers which are used for the identification of the scattered electron. The depth of the electromagnetic section is $\approx 20-30$ radiation lengths, the total depth of the calorimeter $\approx 5-8$ interaction lengths.

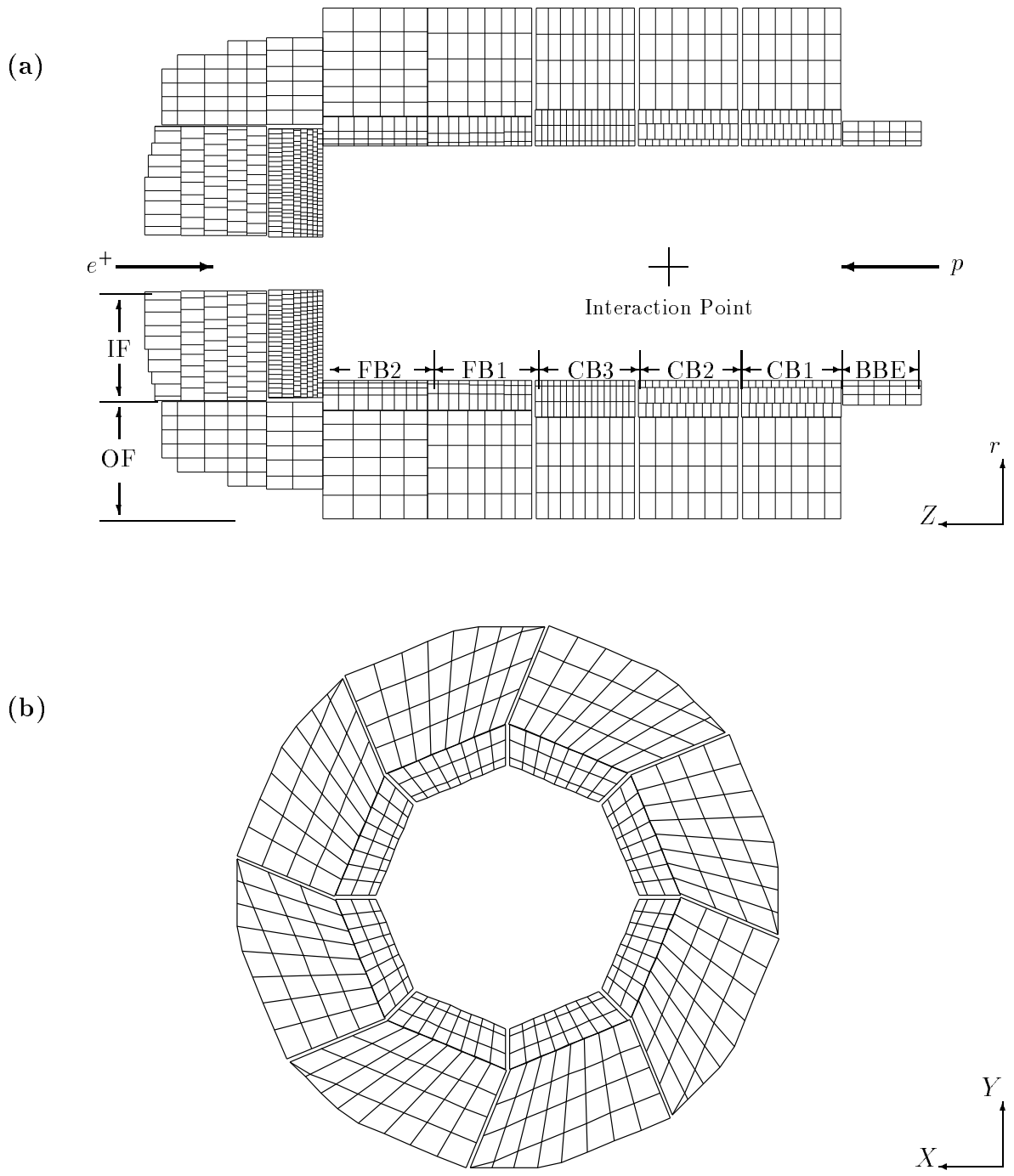

Figure 2.2: a) *Schematic view of the wheel and cell structure of the H1 liquid argon calorimeter with inner forward (IF) and outer forward (OF) wheels, the forward and central barrel wheels (FB and CB respectively) and the backward barrel electromagnetic wheel (BBE).* b) *Schematic view of the octant structure of the CB1 wheel.*

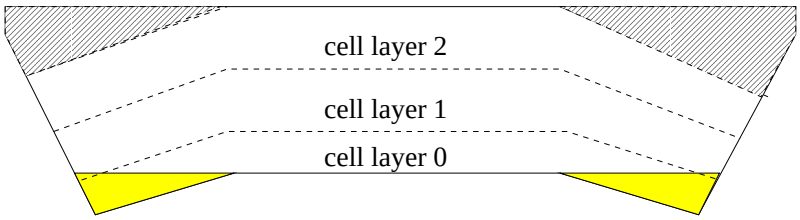

Figure 2.3: *Schematic view of a BBE octant. The grey areas indicate the regions where there is no overlap with the CB1 wheels.*

Test beam measurements [41, 42] of LAr calorimeter modules revealed an energy resolution of $\sigma_{em}(E)/E = 0.12/\sqrt{E/\mathrm{GeV}} \oplus 0.01$ for electrons and $\sigma_{had}(E)/E = 0.50/\sqrt{E/\mathrm{GeV}} \oplus 0.02$ for charged pions. The absolute energy scale uncertainty was established *in situ* in the present analysis (see section 6.1) to be in the range $0.7 - 3\%$ for the electromagnetic energy scale depending on the calorimeter wheel. The energy resolution for electrons was found to be slightly worse than expected by the test beam result $\approx 15\%/\sqrt{E/\mathrm{GeV}}$. The uncertainty of the hadronic scale was evaluated as 2% from studies based on the transverse momentum balance between the scattered electron and the hadronic final state in NC DIS events (see section 6.2).

The calorimeter is non-compensating, i.e. the energy response for hadronic showers is $\approx 30\%$ lower than for electromagnetic showers. Software algorithms are therefore used in the reconstruction software to correct for the different response [43]. The reconstruction of energies in the LAC is described in detail in [44]. More details on the performance of the LAC can also be found in [45].

The Backward Calorimeter

In 1995 the SPACAL was installed in the backward region of H1 replacing the former BEMC. The SPACAL covers a larger polar range of $153^o < \theta < 177.8^o$ compared to the BEMC ($151^o < \theta < 176^o$) and provides a better energy measurement. A further advantage is the existence of a hadronic section which leads to an improvement in depth from 1 to 2 interaction lengths. The electromagnetic energy resolution in the SPACAL was measured in test beam experiments [46] to $\sigma(E)/E = 7.5\%/\sqrt{E/\mathrm{GeV}} \oplus 2\%$. The hadronic energy resolution is $\sigma(E)/E \approx 30\%/\sqrt{E/\mathrm{GeV}}$.

The main purpose of the backward calorimeter is the measurement of the energy of the scattered electron in NC reactions with $Q^2 \lesssim 120$ GeV^2. For this measurement it is used for measurement of hadronic energies in the backward region.

The Iron System

The Iron return yoke is instrumented with a total of 16 layers of streamer chambers. From the digital information of wires so-called "Iron- tracks" are reconstructed which are used for the identification of muons. From ionisation energies of particles passing through the chambers the energy of tails of hadronic showers leaking out of the LAC are measured in the analog readout system. Therefore the system is also often called "Tail-catcher". The energy resolution is $\sigma(E)/E \approx 100\%/\sqrt{E/\mathrm{GeV}}$. This subdetector is mainly used for the identification of background in the CC analysis.

The PLUG Calorimeter

In the forward region the PLUG calorimeter covers the polar angle range $0.7^o < \theta < 3.2^o$, it consists of copper and silicon counters. It is not used in the present analysis.

2.4 The Tracking System

In figure 2.4 a radial view of the central tracking system is shown. It is designed to measure the momenta and angles of charged particles and to provide a fast trigger signal.

The Central Tracking Detector (CTD) consists of the central jet chambers (CJC1 and CJC2), two concentric Z-chambers: the Central Inner Z chamber (CIZ) and the Central Outer Z chamber (COZ) and the proportional chambers: the Central Inner Proportional chamber (CIP) and the Central Outer Proportional chamber (COP). The Forward Track Detector (FTD) consists of radial and planar segments and transition radiators and the Forward Proportional Chamber (FPC) . The angular acceptance of the CTD is $25^o < \theta < 155^o$. The FTD provides additional coverage down to 5^o.

- **The central proportional chambers** CIP and COP are Multi-wire Proportional Chambers (MWPC) which provide a fast timing signal with a time resolution of 21 ns which allows for a determination of the bunch crossing. A combination of pads hit in the CIP with pads hit in the COP and in the forward proportional chamber (FPC) is used to trigger on charged particles originating from the interaction vertex.
- **The central jet chambers** CJC1 and CJC2 are used for the track reconstruction in the central part of the detector. They have an active length of 2200 mm starting in the backward region at $z = -1125$ mm. The inner (outer) chamber CJC1 (CJC2) consists of 30 (60) cells with 24 (32) sense wires parallel to the z axis. They are drift chambers which provide a radial resolution of $\sigma_{r\phi} = 170$ μm and a resolution in z of $\sigma_Z = 22$ mm. From the drift times the event timing can be determined with a precision of 1 ns allowing the determination of the interaction time T_0.

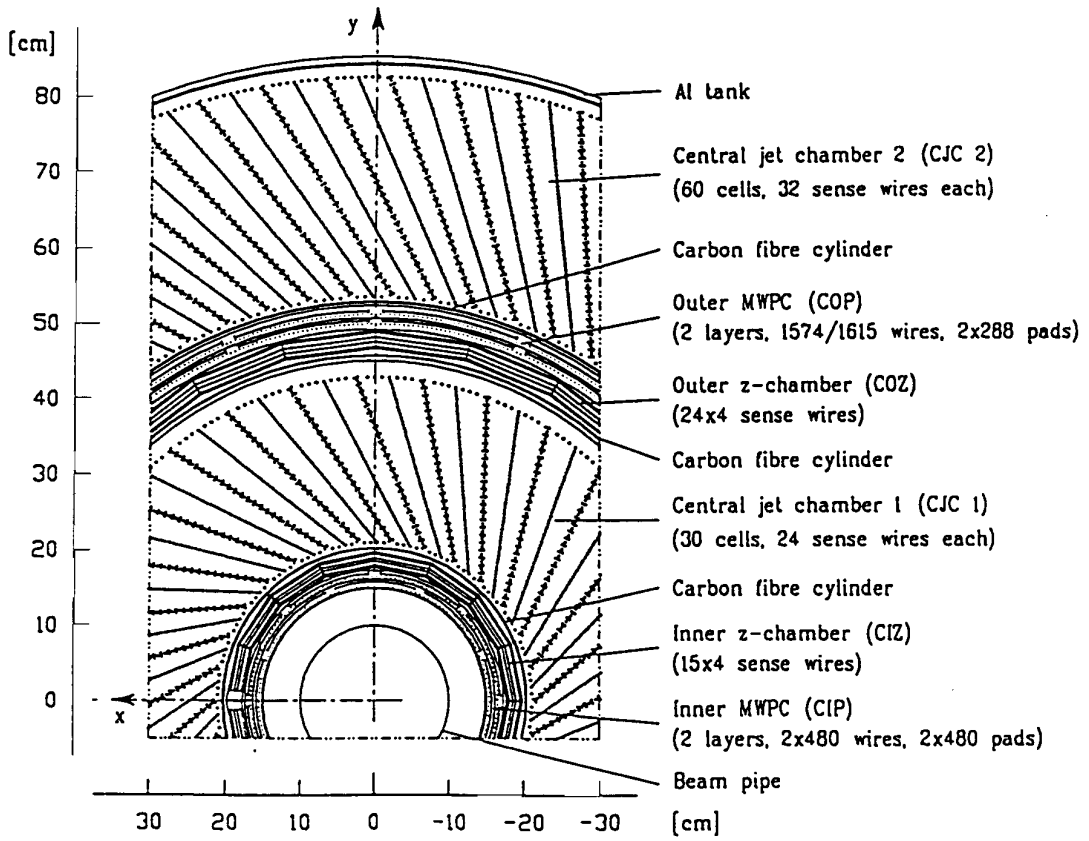

Figure 2.4: *Radial view of H1 central tracking system.*

- **The central Z-chambers** CIZ and COZ are drift-chambers with wires perpendicular to the beam axis. The purpose of the Z-chambers is the precise determination of the Z-position of particles allowing for a good polar angle measurement. The Z-measurement comes from the drift time with a resolution of $\sigma_Z = 0.26$ mm. The inner (outer) Z-chamber consists of 15 (24) concentric rings around the beam axis. Each ring has a length of 12 (9) cm and contains 4 layers of sense wires.

2.5 The Luminosity System

The luminosity system consists of two calorimeters, the "electron tagger" (ET) and the "photon detector" (PD). Their purpose is the measurement of the energies of the electron and photon in Bethe-Heitler events ($ep \to ep\gamma$). They are situated far away from the interaction region in the HERA tunnel at $Z = -33.4$ m (ET) and $Z = -102.9$ m (PD). The luminosity is determined from the rate of Bethe-Heitler events using the photon detector only. It is verified by using events with coincident signals in the ET and PD. An offline correction of the luminosity is made which

takes into account the fraction of luminosity in the satellite bunches [47].

The scattered electron in events at very low $Q^2 < 0.01$ GeV^2 ("photoproduction") is also measured in the electron tagger in the kinematic range $0.3 \lesssim y \lesssim 0.7$. The ET is therefore also used for the study of the background contamination from these events in this analysis. There are two additional electron taggers at $Z = -44$ m and $Z = -8$ m which are, however, not used in the present analysis.

2.6 The Time-of-Flight (ToF) system

The ToF system consists of three scintillators situated at different positions along the beam pipe, the backward ToF (BToF) at $z = -275$ cm, the forward ToF (FToF) at $z = 790$ cm and the Plug-ToF (PToF) at $z = 540$ cm. In addition there are two scintillator walls ("Veto Wall") installed at $z = -810$ cm and $z = -650$ cm. All these scintillators have a very good time resolution to a precision of one ns. They are used to reject beam induced background arriving out-of-time in the H1 detector.

2.7 The Trigger System and the Event Reconstruction

The purpose of the H1 trigger system is the fast separation of the interesting physics events from background events. The main background comes from interactions of the proton beam with gas particles or with the wall of the beam-pipe. They are called "beam-gas" and "beam-wall" interactions respectively. The rate of this background is $\approx 10^4$ times higher than the rate of events coming from electron-proton interactions. The trigger system is based on several levels in order to filter the interesting physics events.

2.7.1 The First Trigger Level

The first trigger level (L1) makes a decision within 2μs on whether to accept or to reject an event using information provided by the different subdetectors ("trigger elements"). The central trigger logic (CTL) combines these trigger elements into 128 "subtriggers". Not all subdetectors can provide this information fast enough to make a decision after each bunch crossing immediately. Therefore the information is sent into pipelines where it is kept until all subdetectors have provided their trigger elements. After 24 BC (2μs) the trigger elements are linked logically and the L1 decision is made whether an event is kept or rejected. If any of the subtrigger conditions is fulfilled by the event, the pipeline is stopped immediately and the signal is passed to the next trigger level [1].

[1]Some subtriggers are prescaled such that not every event fulfilling the subtrigger conditions is kept. None of the subtriggers used for the presented analysis was prescaled.

In the following paragraph the L1 trigger elements which are important in this analysis are briefly described.

The LAC Trigger Elements

The LAr calorimeter provides signals to the central trigger which are used for the triggering of CC and NC events. The analog signals of neighbouring "trigger towers" (TT) are summed and then digitised using FADC's (flash analog to digital converter). These FADC's are then summed into "Big-Towers" (BT). Several thresholds are introduced to suppress electronic noise and background, there are the so-called AGM-threshold for the sum of the analog signals and the BT-threshold for summing the digitised signals into big-towers. A detailed description of the LAr trigger and its performance can be found in [48].

For this analysis there are four important trigger elements (TE) provided by the LAr trigger

- **LAr-Etmiss:** The LAr-Etmiss TE is the transverse momentum measured in the calorimeter. It is calculated from the BT energies and angles:

$$\mathrm{LAr-Etmiss} = \sqrt{(\sum_i P_{x,i}^{BT})^2 + (\sum_i P_{y,i}^{BT})^2} \tag{2.1}$$

$$\text{with } P_{x,i}^{BT} = E_i^{BT} \sin\theta_i^{BT} \cos\phi_i^{BT} \tag{2.2}$$

$$\text{and } P_{y,i}^{BT} = E_i^{BT} \sin\theta_i^{BT} \sin\phi_i^{BT} \tag{2.3}$$

  where θ_i^{BT}, ϕ_i^{BT} and E_i^{BT} are the angles and the energy in big-tower i. The big-tower energies must exceed a threshold value in order to be used for the summation. These thresholds vary according to the polar angle. The two big-towers at the lowest angles (closest to the beam-pipe) are not included in the sum since they are very sensitive to background from beam-gas and beam-wall interactions. In the central barrel the threshold values are relatively high (6 GeV) due to high electronic noise. This trigger element is implemented with different thresholds: 4.5 (low), 6 (medium) , 7.5 (high) GeV. The medium and high threshold are used for triggering CC events.

- **LAr-el:** The LAr-el TE is set if the energy in one trigger tower exceeds a certain threshold value. In the backward region these thresholds are set to a minimum of 6 and 7.5 GeV for LAr-el1 and LAr-el2 respectively. They are increased in the forward region, because of the large beam-induced background. The LAr-el2 trigger element was changed in 1996 to trigger on two low energy electrons in the forward region.

- **LAr-T0:** The LAr-T0 provides a timing signal which is determined from the trigger tower signals. The signal of the trigger towers is copied with 500 ns delay. The crossing point of the delayed signal with the original signal determines the trigger tower T_0. These are combined into the big tower T_0 (BT-T_0). The LAr-T0 trigger is set when at least one BT-T_0 is set.

- **LAr-BigRay:** The LAr-BigRay TE combines the measurement in one LAr trigger tower and a "ray" from DCrϕ-trigger (see below). If the trigger tower energy exceeds 1 GeV and it is matched in azimuthal and polar angle with a ray from the DCrϕ-trigger this TE provides a signal.

The Track-based Trigger Elements

The tracking chambers CJC, CIP/COP, FPC and CIZ/COZ all provide information to the CTL.

- **zvtx-T0 and zvtx-sig1:** These trigger elements are based on signals from the multi-wire proportional chambers (MWPC). As every particle track in the central rapidity region passes through at least four layers of MWPC, track candidates ("rays") can be formed from the chamber signals and allow a fast determination of the event vertex. All rays corresponding to real tracks have a common vertex, whereas the origins of rays formed by random coincidences are equally distributed along the z-axis.

  The zvtx-T0 TE is set if at least one ray fired. The zvtx-sig1 TE is set when the ratio of number of rays from a common vertex to the total number of rays exceeds a certain value.

- **FwdRay-T0:** This trigger element is similar to the zvtx-t0, but the signal is formed in the FWPC. It is usually used in combination with the zvtx-t0: the logical OR of these two conditions is called Ray-T0.

- **DCrϕ-T0 and DCrϕ-Tc:** The $r\phi$-trigger makes use of the signals of the CJC. In parallel to the readout chain, the CJC signals are discriminated for triggering purposes [49]. Track candidates are formed from signals of seven layers of wires in CJC1 and three layers in CJC2. Since the drift times in the CJC extend up to 1 μs, the signals reach the input of the $r\phi$-trigger electronics at different times. Their combination is achieved by feeding them into shift-registers and applying masks which require coincidences between signals at different steps in the registers. As every track with a transverse momentum larger than 400 MeV crosses the sense wire plane at least once, every mask can be combined with a drift pad, where the drift time is smaller than the time between two consecutive bunch crossings. The signal of this particular drift pad is called a "prompt" bit [50].

  The DCrϕ-Tc TE is set when at least three track candidates with a transverse momentum larger than 420 MeV are reconstructed. The DCrϕ-T0 TE is set when at least one track candidate with a transverse momentum larger than 420 MeV exists and the prompt bit is set.

The Veto Conditions

Veto conditions are applied to a large number of subtriggers in H1. They mainly reject background from beam-gas and beam-wall interactions.

- **Veto Wall, BToF, PToF and FToF:** These scintillators have a very good time resolution and are therefore used to reject beam induced background arriving out-of-time in the H1 detector.

- **RZ-veto:** The RZ-trigger scans the hits in the Z chambers, CIZ and COZ, for possible track candidates. Only the RZ-veto is used by one of the CC subtriggers. Based on CIZ hits, track candidates originating from upstream vertices (proton-gas interactions) release a veto. The veto is however not set if, at the same time, the RZ-trigger logic detects a vertex candidate at the nominal place.

- **CIP backward veto and no SPACAL energy (CIPB-noSPCL):** This veto rejects events with high track multiplicities in the rear-most quarter of the inner proportional chamber. It helps to reduce upstream background, regardless of whether it originates from the main bunch or from the satellite bunches. This veto is set only if there is no energy in the SPACAL in the same time window.

2.7.2 The Second and Third Trigger Level

The 2nd trigger level (L2) is based on neural networks and topological requirements. The longer time available for a decision (20μs) allows a more sophisticated selection of events to be made on the basis of the subdetector information available at this stage. An example is the L2 TE LAr-BigT-miss which is used in this analysis for triggering CC events (see section 8.2).

The trigger level L3 allows further requirements to be placed on an event within a time of 2 ms but has not yet been used in H1.

2.7.3 The Fourth Trigger Level and the Event Reconstruction

On the next trigger level (L4) the full information on events is available and a partial reconstruction of the events can be done. This is realized on a processor farm with 32 RISC-processors working in parallel. For each event which is accepted by an L1 subtrigger a verification of the L1 decision is made with higher precision. The events accepted by L4 are written to tapes with a rate of approximately $10 - 20$ Hz

The last level (L5) makes the full reconstruction of the accepted raw data and assigns the events to certain physics event classes. When an event cannot be assigned to any physics class it is rejected. The data information after reconstruction is written in a compressed format to Data Summary Tapes (DSTs) which are the basis for physics analyses. The influence of the L4 and L5 selection can be studied on an event sample of $\approx 1\%$ of all the events which are rejected on L4 or L5 but which are retained for monitoring purposes.

Chapter 3

Monte Carlo Simulation

The cross section measurement requires corrections for acceptance, efficiencies and resolution effects of the detector system. Monte Carlo (MC) programs have been established as an important tool to determine these corrections. It is important to note that the cross section results are almost independent of the choice of Monte Carlo program used throughout the analysis. It should also be emphasised that the measurement is in particular independent of the cross section input to the MC program.

It is difficult to determine the corrections due to acceptance and smearing in the kinematic variables directly from the data, because several effects can have a correlated influence on them. The acceptance, for example, depends on the radiative corrections. Therefore the Monte Carlo is used to unfold from the measured number of events the cross section. If the Monte Carlo describes the data correctly in every respect the unfolding procedure can be simplified by using a simple bin-by-bin correction method as described in section 9.2. The main emphasis in this analysis is placed on ensuring that the detector response is modelled correctly. The efficiencies of all selection criteria, the detector calibration and resolution are directly derived from the data. Whenever a discrepancy between data and simulation is observed the MC is adjusted such that it models the behaviour of the data. As well as using the simulation of DIS events to determine the acceptance the background contribution is also estimated using a MC simulation.

The processes which can contribute as a background are introduced first. Then a description of the MC programs used to generate DIS and background events is given. Finally the simulation of the H1 detector response is briefly described.

3.1 Backgrounds to Deep Inelastic Scattering

For the measurement of the DIS NC and CC cross sections the background must be estimated. It can arise from both ep and non-ep interactions. The important sources for non-ep-background are

- interactions of the proton beam with gas particles or the beam-pipe wall ("beam-gas"- and "beam-wall"-background)
- muons originating from cosmic rays
- muons which are produced in beam-wall- and beam-gas-interactions, far away from the H1 interaction zone, travel parallel to the beam axis and are called "beam-halo muons".

The sources for ep background are

- **Photoproduction (γp) events** represent an important background source in the CC and NC analysis. They arise from ep interactions at very low $Q^2 \approx 0$ GeV^2. The electron is scattered through a very small angle such that it is not detected in the central part of the H1 detector.

  A special kind of background is the production of prompt photons ("prompt γ) which will sometimes be discussed separately. More details on photoproduction processes can be found in [51].

- **Low Q^2 DIS** events are events with $Q^2 \lesssim 100$ GeV^2 where the electron is scattered through a small angle such that it is observed in the SPACAL.

- **Elastic QED Compton events** ($ep \to ep\gamma$) are only important to consider in the NC analysis. They treated as a background since the exchanged photon has a very small virtuality $Q^2 \approx 0$. The final state electron and photons can, however, be scattered through a large angle into the LAC if the virtuality of the electron is large. These events are also used for the calibration of the electron energy (see section 6.1). The inelastic part of the cross section for QED Compton scattering must not be treated as a background, but is part of the signal as explained in section 9.3.

- **Photon-photon- ($\gamma\gamma$-) interactions** also constitute a background source: $ep \to epl^+l^-$ or $ep \to eXl^+l^-$. When the final state lepton pair is e^+e^- this background may contribute to the NC channel. When the final state lepton pair is $\mu^+\mu^-$ they can contribute to the CC sample. Events of the type $ep \to epe^+e^-$ are also used for the calibration of the electron energy (see section 6.1)

- **Real $W^\pm$- and Z- bosons** are produced at HERA with a small cross section $\sigma \approx 1(0.1)$ pb^{-1} via $ep \to eXW^\pm(Z)$. The scattered electron is usually not detected. However, if the boson decays leptonically it may be misidentified as an NC or CC event and the events are therefore treated as a background source.

3.2 Monte Carlo Event Generators

Monte Carlo events are generated assuming a specific physics production mechanism. The hard subprocess is generated according to the corresponding cross section at

leading order. Higher order QCD radiation is implemented using either the Colour Dipole Model as implemented in ARIADNE [52] or a DGLAP inspired parton showering parametrisation as implemented in LEPTO [53]. For the fragmentation of the outgoing parton into hadrons a phenomenological model called "string fragmentation model" (JETSET [54]) is used.

DIS events are generated using the programs DJANGO 6.2 [55] and DJANGOH 1.2 [56] [1]. The hard subprocess is generated according to the cross section obtained from the MRSH [57] parametrisations for the parton density functions [2]. The calculations include the Born processes and the leptonic part of the QED radiative corrections of $\mathcal{O}(\alpha)$ (see section 9.3). The parton shower evolution is generated according to the ARIADNE model since it gives the best description of most measurements of the hadronic final state at HERA. The influence of using the LEPTO program for modelling the parton showers was studied. The JETSET program is used for the fragmentation of the partons.

Several datasets were generated so that the statistical error on the MC prediction is smaller than statistical error of the data at all values of x and Q^2. For the NC DIS MC the integrated luminosity is $\mathcal{L} = 100$ pb^{-1} at low Q^2, in the CC analysis it is $\mathcal{L} = 2.8$ fb^{-1}. At high Q^2 and high x additional MC data sets are included, amounting to 10-1000 times the data luminosity.

Background Events The background processes discussed in the previous section are generated by different programs:

- Photoproduction events are generated by the PYTHIA 5.7 [59] event generator using the GRV LO [60] parton densities for the proton and the photon respectively. Direct and resolved processes (both $\mathcal{L} \approx 100$ pb$^-1$) are considered as well as the production of prompt photons ($\mathcal{L} \approx 5300$ pb^{-1}).

- Low Q^2 DIS events are generated by the DJANGO 6.2 program as described above. The corresponding integrated luminosity is 46.5 pb^{-1}.

- Elastic QED-Compton events are generated by the COMPTON 2.0 program [61].

- Elastic $\gamma\gamma$ processes are generated by LPAIR 2.0 [62].

- production of real $W^{\pm}$ and Z bosons is generated by EPVEC [64].

[1] For the NC measurement DJANGO 6.2 is used. It cannot be used for the CC measurement since an error was found in the calculation of the radiative corrections. This error was corrected for the version DJANGOH 1.2 which is therefore used.

[2] In DJANGO the cross section is calculated using the HERACLES 6.2.4 [58] program. This is done in DJANGOH within the program directly.

3.3 Simulation of the H1 Detector

The detector response to the particles generated in an event is simulated in detail using the H1SIM detector simulation which makes use of the GEANT [65] program. The parameters used by this program were determined in test beam measurements and optimised during *ep* data taking. For the simulation of the energy response of the calorimeters a fast parametrisation is used for the development of electromagnetic and hadronic showers as implemented in H1FAST [66] is used to save computing time. These simulated events are subject to the same reconstruction program as the data (H1REC) and the same analysis chain.

Chapter 4

Kinematic Reconstruction

The cross section determination relies on the precise reconstruction of the kinematic variables. Two kinematic variables are needed to describe the inclusive DIS process, e.g. x and Q^2. For the CC process these variables can only be reconstructed using the hadronic final state since the neutrino is not detected. For NC events there exist various methods to reconstruct the kinematics since there is redundant information with the reconstruction of both the lepton and of the hadronic final state. The choice of the reconstruction method determines the acceptance, the radiative corrections and the size of the systematic errors. The methods used in this analysis are introduced in this section.

In the **electron method** (e-method) the kinematic variables are determined from the energy $E_e^{'}$ and the polar angle θ_e of the scattered electron

$$Q_e^2 \equiv 4E_e E_e^{'} \cos^2 \frac{\theta_e}{2} \qquad y_e \equiv 1 - \frac{E_e^{'}}{E_e}(1 - \cos\theta_e) \quad \text{and} \quad x_e = \frac{Q_e^2}{y_e s}. \tag{4.1}$$

With decreasing y the x- and y resolution of the e-method degrade significantly due to the $1/y$ dependence of the partial derivative of y_e with respect to the energy $E_e^{'}$ and the angle θ_e:

$$\frac{\delta y_e}{y_e}|_{E_e^{'}} = \frac{y-1}{y}\frac{\delta E_e^{'}}{E_e^{'}} \qquad \frac{\delta y_e}{y_e}|_{\theta_e} = \frac{1-y}{y}\cot\frac{\theta_e}{2}\delta\theta_e \tag{4.2}$$

The Q^2 resolution of the e-method is, however, excellent over the full kinematic range.

For the hadronic final state it is convenient to introduce the quantity Σ, the transverse momentum $P_{T,h}$ and the inclusive hadronic angle γ_h defined by

$$\Sigma = \sum_i (E_i - p_{z,i}) \qquad P_{T,h} = \sqrt{(\sum_i p_{x,i})^2 + (\sum_i p_{y,i})^2} \qquad \tan\frac{\gamma_h}{2} = \frac{\Sigma}{P_{T,h}} \tag{4.3}$$

Here E_i and $p_{z,i}$ are the energy and longitudinal momentum components of particle i, and $p_{x,i}$, $p_{y,i}$ are its momentum components in the (transverse) plane orthogonal

to the z axis. The summation is over all particles apart from the scattered lepton. The particle masses are neglected.

For the **Jacquet-Blondel-method** [67] or **hadron-method** (h-method) [1] the kinematic variables are obtained from:

$$y_h = \frac{\Sigma}{2\ E_e} \qquad Q^2_h = \frac{P^2_{T,h}}{1-y_h} \qquad x_h = \frac{Q^2_h}{s\ y_h}. \tag{4.4}$$

The reconstruction of the kinematic variables using the h-method is only used for the CC measurement. For the NC measurement it is not used due to the degrading Q^2-resolution with increasing y:

$$\frac{\delta Q^2_h}{Q^2_h}|_{p_{t,h}} \propto \delta p_{t,h} p_{t,h} \qquad \frac{\delta Q^2_h}{Q^2_h}|_{\Sigma} \propto \frac{\delta \Sigma}{1-y} \tag{4.5}$$

With increasing y the term $1/(1-y)$ becomes increasingly important and severely affects the resolution in Q^2 and, consequently, also in x.

The **Σ-method** [68] makes use of both the electron and hadronic final state variables:

$$y_\Sigma = \frac{\Sigma}{E-p_z} \qquad Q^2_\Sigma = \frac{(E'_e \sin\theta_e)^2}{1-y_\Sigma} \qquad x_\Sigma = \frac{Q^2_\Sigma}{s\ y_\Sigma} \tag{4.6}$$

with $E-p_z \equiv \Sigma + E'_e(1-\cos\theta_e)$ which would be equal to twice the energy of the incoming electron in a perfect detector. The y- and Q^2-measurement are in this method independent of E_e and so there is less sensitivity on radiative corrections due to radiation of the incoming electron before the interaction (see also section 9.3). The y-resolution of the Σ method approaches the y resolution of the h-method at low y and that of the e-method at high y and is therefore reasonable in the full y range.

An alternative method which may be used to determine the kinematic variables in NC events is the **Double-Angle-method** (DA-method) [69] in which only the angles of the scattered electron and the hadronic final state are used:

$$y_{DA} = \frac{\sin\theta_e \cdot (1-\cos\gamma_h)}{\sin\gamma_h + \sin\theta_e - \sin(\theta_e+\gamma_h)} \qquad Q^2_{DA} = \frac{4\cdot E^2_e \cdot \sin\gamma_h(1+\cos\theta_e)}{\sin\gamma_h + \sin\theta_e - \sin(\theta_e+\gamma_h)} \tag{4.7}$$

and $x_{DA} = Q^2_{DA}/(s\cdot y_{DA})$. The resolution in x and Q^2 degrades as $\frac{\delta\theta_e}{\sin\theta_e} \oplus \frac{\delta\gamma_h}{\sin\gamma_h}$, that is at small and large scattering angles of both the electron and the hadronic final state. It is good at medium y where all particles are well contained in the central detector. This method is particularly useful for the calibration of the calorimeters

[1] There is a small difference between the h- and JB-method concerning the treatment of the proton remnant momentum. However, this does only play a minor role at HERA since the momentum of the proton remnant is not measured. Therefore the JB-method is usually referred to as the h-method at HERA.

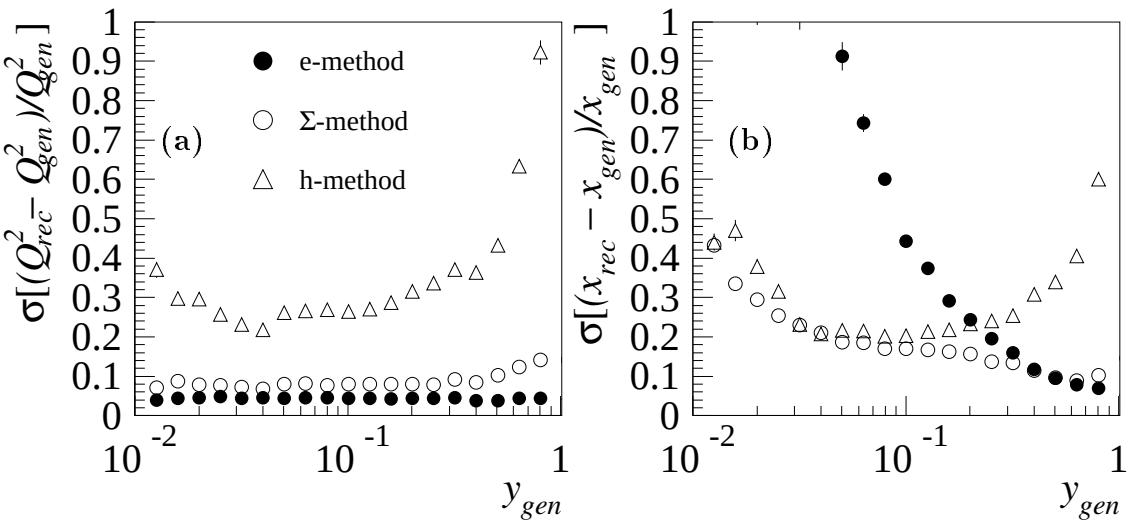

Figure 4.1: *Resolution in a) Q^2 versus y and b) x versus y for different reconstruction methods. Q^2_{rec} (Q^2_{gen}) and x_{rec} (x_{gen}) refer to the reconstructed (generated) values of Q^2 and x respectively.*

since it is to first order independent of the calorimetric energies. The energy of the scattered electron is given by

$$E_{DA} = \frac{2E_e \sin\gamma_h}{\sin\gamma_h + \sin\theta_e - \sin(\gamma_h + \theta_e)} \tag{4.8}$$

It is used for the calibration of the electron energy (see section 6.1).

The y-dependence of the x- and Q^2 resolutions are compared in figure 4.1 for the e, h and Σ methods. The best resolution in Q^2 is achieved when using the e-method, but a good resolution is also obtained when using the Σ-method. However, the hadron method is severely affected by the limited energy resolution of the calorimeter and particle losses in the beam pipe such that it is only used when unavoidable, namely in the CC analysis. In the e-method a very large increase of the resolution in x is seen towards low y due to the dependence on $1/y$ discussed above. The Σ-method provides a similarly good resolution at high y, but can also be used at low y where the increase in x-resolution is much less pronounced. The x-resolution of the h-method is similar to that of the Σ-method at low y. At high y it increases, however, to values of about 40%.

Thus the best reconstruction is achieved when using x_Σ and Q^2_e over the entire y range; this combination is called the **$e\Sigma$-method** [70]:

$$Q^2_{e\Sigma} = Q^2_e \qquad x_{e\Sigma} = x_\Sigma \qquad y_{e\Sigma} = \frac{Q^2_e}{x_\Sigma s} \tag{4.9}$$

This method is used to determine the kinematic variables for NC events in this analysis.

Chapter 5

Electron Angle Determination

The precise reconstruction of the electron angle is essential for the correct determination of the kinematic variables in NC events (see chapter 4). In this chapter the electron angle measurement is described. Since the angle is measured by different subdetectors simultaneously there is redundancy which can be used to study systematic effects in the angular measurement.

The scattered electron crosses three subdetector systems which measure the angle: the LAC, the CJC and the Z-chambers. The latter two are part of the central tracking system (CTD) which defines the H1 coordinate system. The polar and azimuthal angles of the electron with respect to the H1 coordinate system will be called θ_e^{H1} and ϕ_e^{H1} respectively.

The highest precision on the azimuthal angle is achieved by the CJC measurement due to its high resolution of $\sigma_{r\phi} = 170\ \mu$m (see section 2.4). The polar angle is determined most precisely by the Z-chamber measurement due to its high Z resolution. However, due to the limited efficiency of the Z-chambers occasionally there is no Z-chamber measurement available. It will be shown in this chapter that it is in these cases advantageous to use the LAC measurement instead of the track measurement.

Firstly the track fitting procedure which combines the CJC and Z-chamber measurements is described. Then the reliability of the LAC angle determination is ensured by aligning the LAC with respect to the H1 coordinate system. This alignment is done by comparing the measurement of the electron scattering angles of the CTD and LAC. Then the track determination is studied depending on whether there are hits in the Z-chambers linked to it. Finally the track and LAC measurement are combined and the angle is corrected for the beam direction.

5.1 Track Fitting Procedure

The tracking system was aligned internally using tracks from cosmic muons and high momentum tracks in ep interactions. It was also controlled on the SPACAL NC

sample using the redundancy of the BST, BDC and central tracker measurements [71].

Tracks of charged particles and the interaction vertex are reconstructed for each event during the standard vertex fit procedure on L5. Firstly, the hits in the CJC and FTD are analysed and track segments are constructed. Then these track segments are constrained to originate from the interaction vertex with coordinates $X_{vtx}, Y_{vtx}, Z_{vtx}$. Note, that only track segments which are consistent with originating from the vertex position within the error on the track angles are fitted to the interaction vertex. At this stage Z-chamber hits may be assigned to the track if these hits are close to the crossing point of the track segment in the Z-chamber. These tracks are called "DTRA" tracks. If there are Z-chamber hits assigned to the track the precision in Z is determined by the excellent Z resolution $\sigma_z \approx 0.26$ mm. When there are no Z hits linked, the θ_e resolution is inferior due to the Z resolution of the CJC $\sigma_z \approx 22$ mm (see section 2.4) which is 100 times worse than that of the Z-chambers.

The track closest to the electron candidate (see section 7.3) determines the polar angle $\theta_e^{\rm CTD}$ and azimuthal angle $\phi_e^{\rm CTD}$. This study is restricted to the central detector region $\theta_e \lesssim 40^o$ and therefore independent of the forward tracking detector FTD. Further details on the electron track selection can be found in section 7.4.

5.2 Alignment of the LAr Calorimeter

In this section the alignment of the LAr calorimeter with respect to the tracking system is studied.

Figure 5.1 shows a schematic view of an electron with angles $\theta_e^{\rm H1}$ and $\phi_e^{\rm H1}$ crossing the H1 detector. Only those detector components are shown which are important for the angle determination, i.e. the CJC, CIZ, COZ, FTD and LAC. In the central region of the detector the electron angles may be determined either by the combined information of the track chambers (CJC, CIZ and COZ) or the LAC. The alignment constants for the LAC are evaluated by comparing the angular measurements from the electron track and the calorimeter cluster for high Q^2 NC events. The selection of the NC events used for this study is the same as for the cross section measurement as described in chapter 7. Additionally, high precision on the Z-measurement is ensured by selecting only events where CIZ and COZ hits are assigned to the electron track.

The polar and azimuthal angle of the scattered electron in the LAC with respect to the H1 coordinate system are given by

$$\tan\theta_e^{\rm LAC} = \frac{\sqrt{(X_e^{COG}-X_{vtx})^2+(Y_e^{COG}-Y_{vtx})^2}}{Z_e^{COG}-Z_{vtx}} \tag{5.1}$$

$$\tan\phi_e^{\rm LAC} = \frac{Y_e^{COG}-Y_{vtx}}{X_e^{COG}-X_{vtx}} \tag{5.2}$$

with $X_e^{\rm COG}, Y_e^{\rm COG}, Z_e^{\rm COG}$ being the X-, Y- and Z-position of the centre of gravity (COG) of the electron cluster (see section 7.3) and $X_{vtx}, Y_{vtx}, Z_{vtx}$ being the X-, Y-

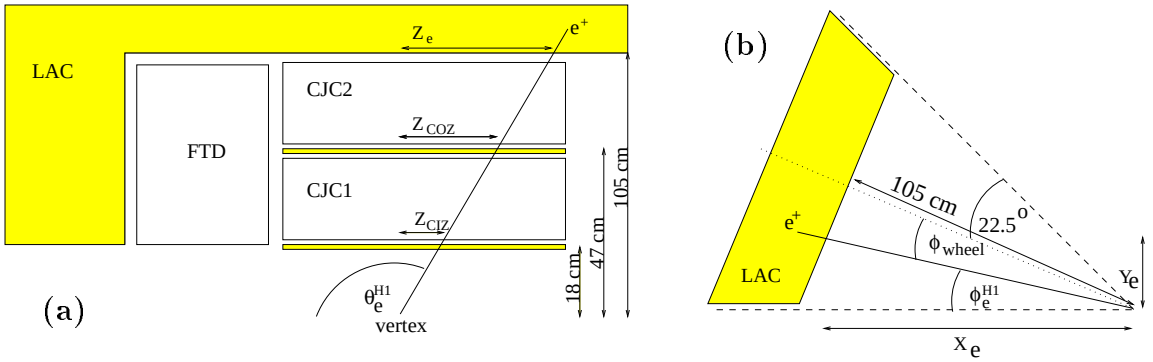

Figure 5.1: *Schematic view of an electron with angles θ_e^{H1} and ϕ_e^{H1} crossing the H1 detector (a) in the $R-Z$ plane and b) in the $X-Y$ plane. Shown is the electron trajectory, the tracking chambers (CIZ, COZ, CJC1, CJC2 and FTD) and the Liquid-Argon Calorimeter (LAC). In a) the Z positions of the electron at the CIZ, COZ and LAC surfaces (R_{CIZ} = 18, R_{COZ} = 47 and R_{LAC} = 105 cm) are indicated. In (b) the quantities ϕ_{wheel}, X_e and Y_e (see text) and R_{LAC} = 105 cm (see text) are indicated.*

and Z-position of the interaction vertex. The misalignment in X, Y and Z of the LAC with respect to the CTD is evaluated by comparing the impact position of the electron at the LAC surface as determined from the LAC and CTD angles.

The distance of the LAC surface to the Z axis is $R_z = 105.\ \mathrm{cm}/\cos(\phi_{\mathrm{wheel}})$ where ϕ_{wheel} denotes the azimuthal angle of the electron track with respect to the centre of the wheel (see figure 5.1(b)):

$$\phi_{\mathrm{wheel}} = \begin{cases} \mathrm{mod}(\phi_e^{\mathrm{CTD}}, 22.5^o) - 11.25^o & \text{in BBE} \\ \mathrm{mod}(\phi_e^{\mathrm{CTD}}, 45.0^o) - 22.5^o & \text{otherwise} \end{cases} \tag{5.3}$$

with $\phi^{\mathrm{CTD}} \in [0^o, 360^o]$. The BBE has a 16-fold symmetry due to the corresponding subdivision of the octants (see figure 2.3), the other wheels have an 8-fold symmetry in ϕ.

The impact point of the scattered electron at the LAC surface is calculated from the angles measured in the corresponding subdetector

$$X_e^{\mathrm{LAC(CTD)}} = R_z \cdot \cos\phi_e^{\mathrm{LAC(CTD)}} + X_{vtx} \tag{5.4}$$
$$Y_e^{\mathrm{LAC(CTD)}} = R_z \cdot \sin\phi_e^{\mathrm{LAC(CTD)}} + Y_{vtx} \tag{5.5}$$
$$Z_e^{\mathrm{LAC(CTD)}} = R_z / \tan\theta_e^{\mathrm{LAC(CTD)}} + Z_{vtx} \tag{5.6}$$

These quantities are also illustrated in figure 5.1.

The misalignment in the X coordinate is given by $\delta_X = \langle X_e^{\mathrm{CTD}} - X_e^{\mathrm{LAC}} \rangle$ and correspondingly for δ_Y and δ_Z in the Y and Z coordinate.

The misalignment δ_X and δ_Y is presented in figure 5.2 as a function of Z_e^{CTD}. The measured mean position of the LAr calorimeter is significantly shifted in Y and tilted

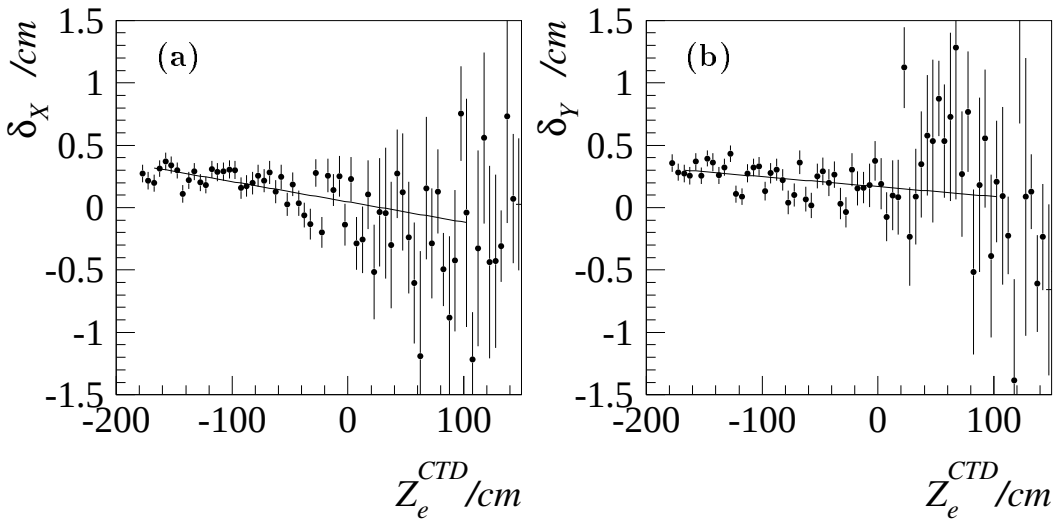

Figure 5.2: *The shifts* $\delta_X = \langle X_e^{\rm LAC} - X_e^{\rm CTD} \rangle$ *and* $\delta_Y = \langle Y_e^{\rm LAC} - Y_e^{\rm CTD} \rangle$ *in the measurement by the LAr calorimeter with respect to H1 coordinate system determined by the comparison of the impact point at the LAr surface as determined by the tracking system (CTD) and calorimeter cluster (LAC) for 1994-7 data. Also shown is a fit to the data of the functional form* $\delta_{X,Y} = a_{X,Y} + b_{X,Y} Z_e^{\rm CTD}$.

with respect to $Z_e^{\rm CTD}$ in X. The misalignments are parametrised by the functions $\delta_{X,Y} = a_{X,Y} + b_{X,Y} Z_e^{\rm CTD}$ where the shift and tilt relative to $Z_e^{\rm CTD}$ are $a_{X,Y}$ and $b_{X,Y}$ respectively. The values of the parameters, obtained by the fit shown in figure 5.2, are presented in table 5.1. It can be seen that there is a significant tilt in X and shift in Y, whereas the data are compatible with no shift in X and no tilt in Y. No significant tilts or shift are observed in the simulation.

	a_X (mm)	b_X (mrad)	a_Y (mm)	b_Y (mrad)
data	0.5 ± 0.3	1.6 ± 0.3	1.7 ± 0.3	0.8 ± 0.3
MC	-0.1 ± 0.2	0.1 ± 0.2	0.2 ± 0.2	0.1 ± 0.1

Table 5.1: *Table of alignment constants for the LAr calorimeter determined from* δX*- and* δY *for data and MC.*

Figure 5.3 shows δ_Z versus $Z_e^{\rm CTD}$ for data and simulation [1]. There are shifts between data and simulation observed for the CB1 ($-140 \lesssim Z \lesssim -60$ cm) and CB2 ($-60 \lesssim Z \lesssim 20$ cm) wheels of 0.4 and 0.6 cm, respectively, which are taken as alignment constants in Z for the CB1 and CB2 wheels for 1995-1997 data. In 1994 there is an additional shift of the whole calorimeter observed of -0.5 cm.

After applying the LAC alignment coefficients in X, Y and Z good agreement is observed between data and simulation as can be judged from figure 5.3. However,

[1] For this study the correction ZLARCOLD [72] was applied which is not part of the default H1 reconstruction

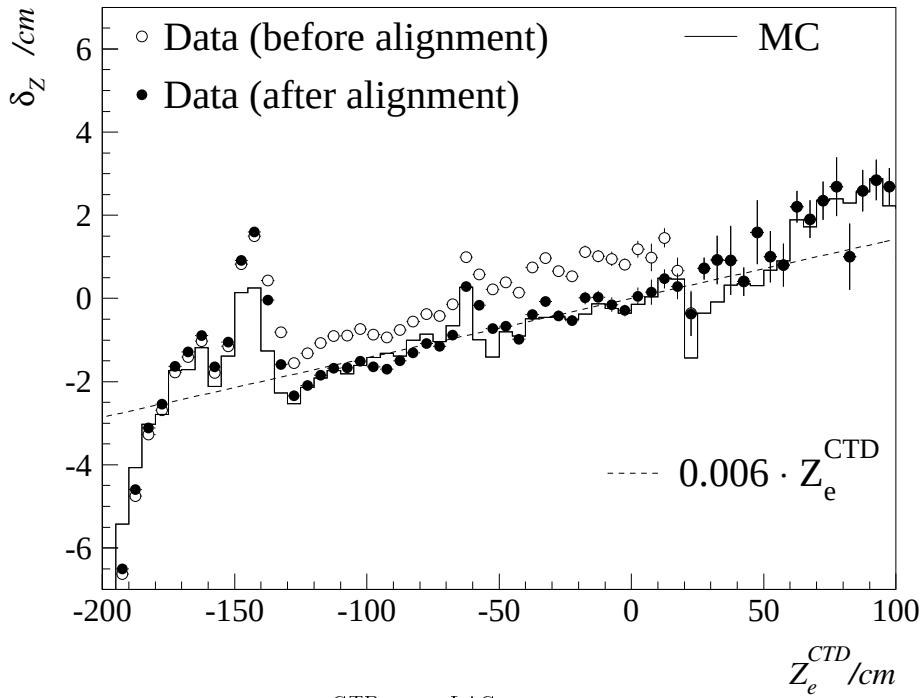

Figure 5.3: *Difference* $\delta_Z = Z_e^{\rm CTD} - Z_e^{\rm LAC}$ *between the Z impact position of the electron calculated from the track and from the cluster angles for data (symbols) and Monte Carlo (histogram). The data are shown before (open circles) and after alignment (filled circles). The dashed line shows the function* $\delta_Z = 0.006 \cdot Z_e^{CTD}$ *which is used for the correction to the true Z value.*

there is a systematic bias of $\langle Z_e^{\rm CTD} - Z_e^{\rm LAC} \rangle$ of up to -2 cm from 0 in both data and simulation. This translates into a shift in the polar angle $\theta_e^{\rm LAr}$ with respect to the true angle by up to 20 mrad. The cause of this the bias of the calorimetric measurement due to the shower evolution in the cells. The size of this effect depends on the $Z_e^{\rm CTD}$ position and can be parametrised by

$$(Z_e^{\rm LAC})_{fin} = [1 + 0.006] \cdot (Z_e^{\rm LAC})_{ini} \text{ cm}$$

This correction is shown in figure 5.3. It is applied to both data and simulation.

The measured polar angles of the cluster ($\theta_e^{\rm LAC}$) and track ($\theta_e^{\rm CTD}$) are compared after alignment and after all corrections for data and simulation in figure 5.4. They are in good agreement within a systematic uncertainty of $2 \oplus 1$ mrad. The deviations from 0 are due to local detector deficiencies, e.g. at $\theta_e^{\rm CTD} \approx 145^o$ because of the crack between the BBE and CB1 wheel. These differences are however smaller than the quoted systematic uncertainty and are reproduced by the simulation.

5.3 Track Angle Measurement

After the alignment of the LAC, described in the previous section, the calorimeter angle determination is in good agreement with the track measurement when Z-

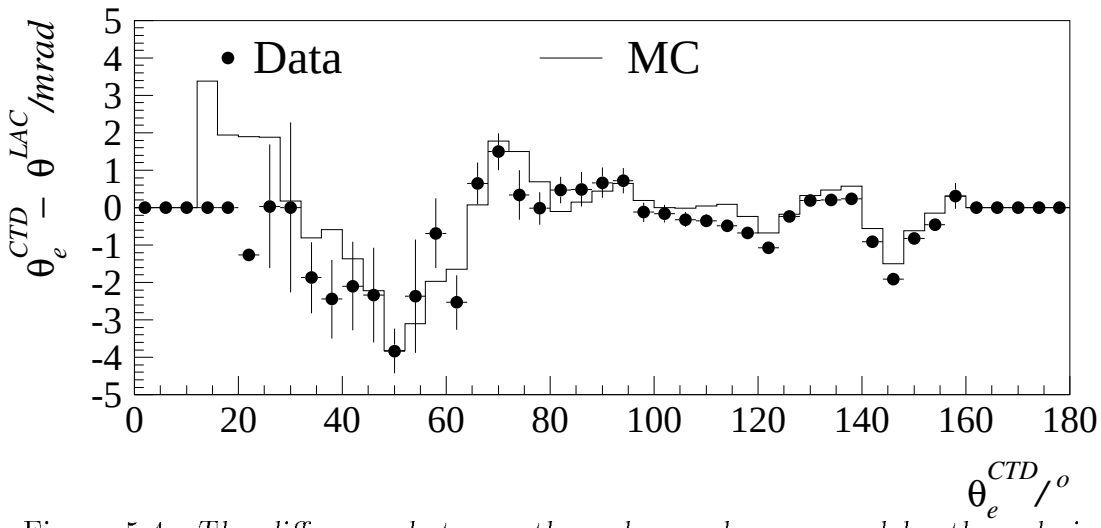

Figure 5.4: *The difference between the polar angle measured by the calorimeter cluster $\theta_e^{\rm LAC}$ and the track $\theta_e^{\rm CTD}$ versus $\theta_e^{\rm CTD}$ for the data (full points) and MC (histogram) event sample.*

chamber hits are assigned to the track. This section is mainly devoted to the study of the other tracks, i.e. when there are not hits from both the CIZ and COZ chambers linked.

The influence of the Z-chamber hits on the precision of the track angles is studied by comparing the CTD and LAC measurements for four classes of tracks. The track classification is made in terms of Z-chamber hits:

a) CIZ and COZ hits are linked to the electron track

b) only COZ hits are linked to the electron track

c) only CIZ hits are linked to the electron track

d) no Z-chamber hits are linked to the electron track

Sample a) was used in the previous section for the alignment of the LAC.

The difference between the LAC and CTD determination of the polar angle $\theta_e^{\rm LAC} - \theta_e^{\rm CTD}$ is shown in figure 5.5 for these four classes of tracks for the 1997 data. When there are hits in both Z-chambers (see figure 5.5(a)) this distribution is mainly sensitive to the resolution of the LAC measurement. The gaussian fit to the distribution, shown in figure 5.5(a), reveals the $\theta_e^{\rm LAC}$ resolution to be 3.4 mrad. When the track does not have hits assigned from either the CIZ or COZ chamber or both, the distributions are significantly broader and the mean values are shifted from 0 when there are no COZ hits. The degraded resolution is expected due to the limited precision of the CJC-Z-measurement (see section 2.4). The shifts are explained by a miscalibration of the CJC in Z by $\Delta Z/Z \approx 1.6\%$ which was also observed in a study of cosmic muons [73].

This study shows that the angle is determined more precisely from the LAC than the CTD in the cases where there are not hits from both Z-chambers assigned.

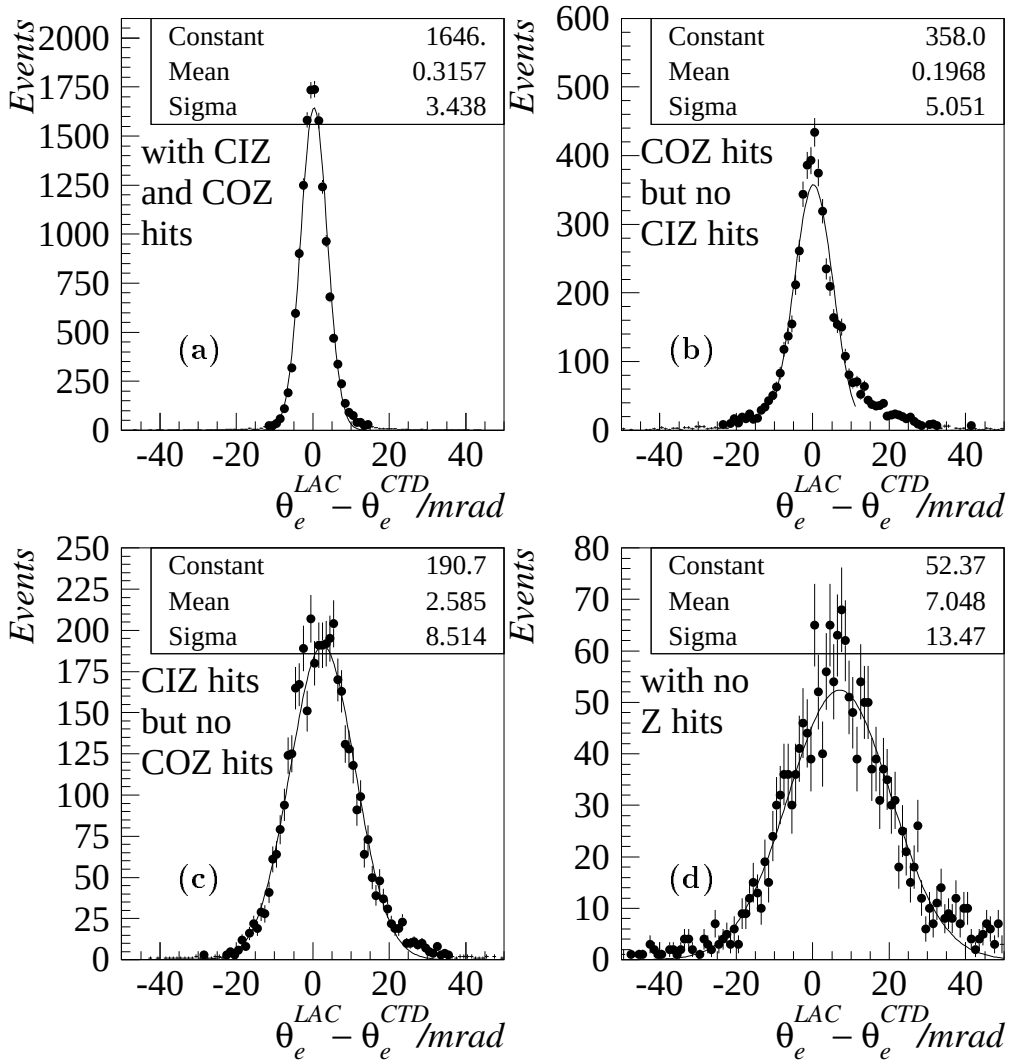

Figure 5.5: *Difference between the polar angle as measured by the LAC and CTD* $\theta_e^{\rm LAC} - \theta_e^{\rm CTD}$ *for electron tracks (a) with CIZ and COZ hits, (b) with only COZ hits, (c) with only CIZ hits and (d) with neither CIZ nor COZ hits. Shown are also gaussian fits to the distributions and the mean values and resolutions are given.*

Therefore a combination of the LAC and CTD measurement is chosen for the final angle determination as described in section 5.4. For this combination it is important to study the efficiency of the Z-chambers.

Efficiency of the Z-chambers The efficiency of the Z-chambers is examined as function of the Z position where the electron track crosses the corresponding chamber. The CIZ and COZ chambers are at radii of $R_{\rm CIZ} = 18$ cm and $R_{\rm COZ} = 47$ cm respectively. The impact position is then obtained from

$$Z_{\rm CIZ(COZ)} = \frac{R_{\rm CIZ(COZ)}}{\tan\theta_e^{LAC}} + Z_{vtx}.$$

These variables are shown in figure 5.1(a).

The efficiency of the CIZ and COZ is shown in figure 5.6 versus $Z_{\mathrm{CIZ(COZ)}}$ for all four years. It is defined as

$$\epsilon_{\mathrm{CIZ(COZ)}} = \frac{\text{number of electron tracks with linked hits from CIZ (COZ)}}{\text{number of electron tracks}}.$$

The bins in $Z_{\mathrm{CIZ(COZ)}}$, shown in figure 5.6, are chosen such that one bin corresponds to one ring in the corresponding chamber, i.e. 9 cm for the COZ and 12 cm for the CIZ (see section 2.4).

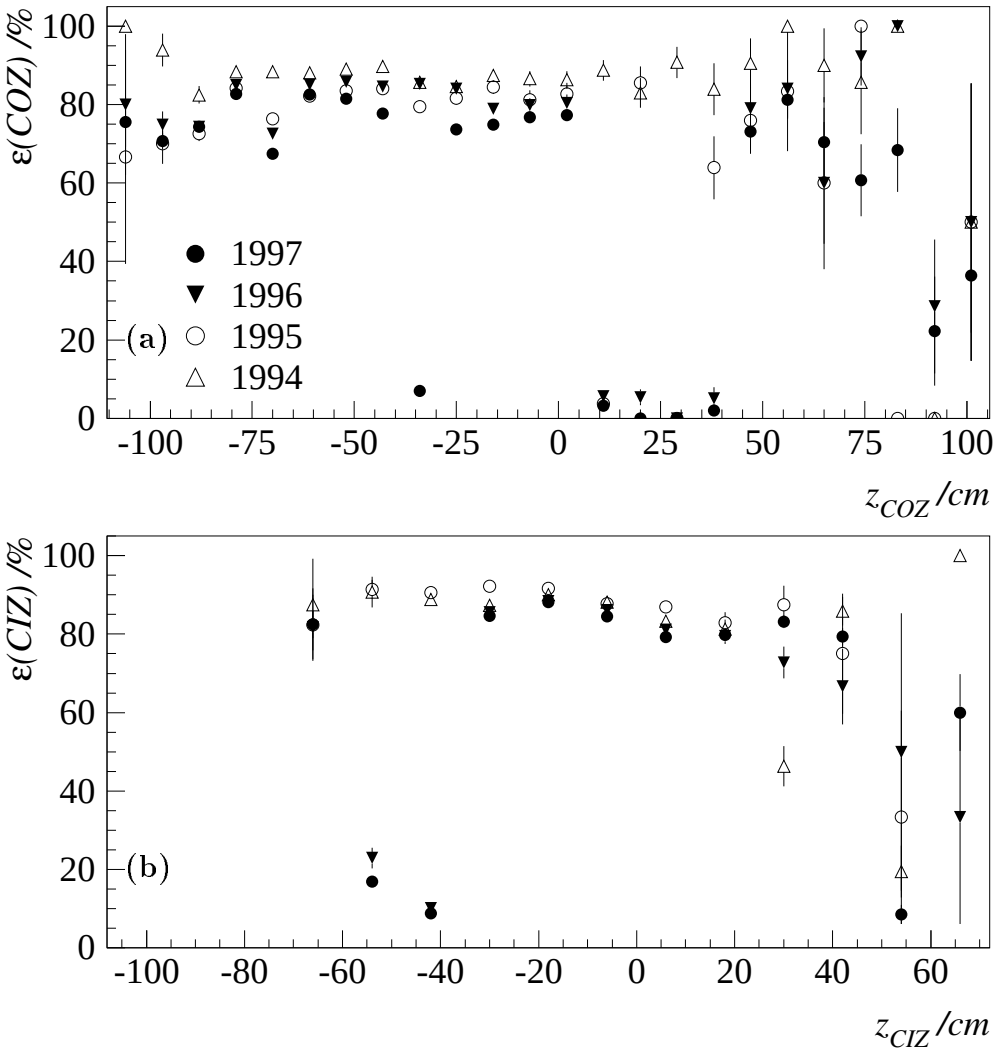

Figure 5.6: *Efficiencies of the (a) CIZ and (b) COZ chambers as function of the corresponding impact point of the electron (see text) for the data samples of the years 1994 to 1997.*

In most areas the efficiency of both chambers reaches $\approx 80 - 90\%$. There are, however, strong variations seen as function of $Z_{\mathrm{CIZ(COZ)}}$ throughout the years, in particular large inefficiencies are observed in 1997 at distinct values of Z_{CIZ} and Z_{COZ}. In 1994 and 1995 both chambers were fully operational, but in 1996 and 1997 some chamber rings were not active leading to the observed inefficiencies (see table

chamber	year	ring number	Z value
CIZ	96+97	4 and 5	-60 to -40 cm
COZ	96+97	13 to 16	$+10$ to $+40$ cm
	96+97	22	$+90$ cm
	97	8	-35 cm

Table 5.2: *Dead rings in the CIZ and COZ chambers and the corresponding Z values. There are further dead rings in the CIZ which are, however, out of the acceptance region of this analysis.*

5.2). These deficiencies of the Z-chambers are not implemented in the standard Monte Carlo simulation.

5.4 Final Angle Determination

The best estimate of the polar angle of the electron is obtained when using the track measurement, i.e. $\theta_e^{\rm H1} = \theta_e^{\rm CTD}$ and $Z_e = Z_e^{\rm CTD}$, when there are hits from both Z-chambers assigned to the electron track and the LAC measurement otherwise, i.e. $\theta_e^{\rm H1} = \theta_e^{\rm LAC}$ and $Z_e = Z_e^{\rm LAC}$. To ensure that the fraction of events in which the LAC measurement is used is modelled by the simulation, the simulation is degraded according to the CIZ and COZ efficiencies shown in figure 5.6. For each MC event θ_e^{H1} is determined from either the LAC or the CTD information on a random basis according to the fraction observed in the data. It is also verified that these fractions are the same between data and simulation in each cross section measurement bin in x and Q^2 (see section 9.1). The azimuthal angle $\phi_e^{\rm H1} = \phi_e^{\rm CTD}$ is best determined by the CJC measurement.

For events with $\theta_e^{\rm LAC} < 35^o$ the angle is always determined from the calorimeter, i.e. $\theta_e^{\rm H1} = \theta_e^{\rm LAC}$ and $\phi_e^{\rm H1} = \phi_e^{\rm LAC}$, since the track is then mostly measured by the FTD which could not be studied with high precision in this analysis due to low statistics of NC events.

This section described the determination of $\theta_e^{\rm H1}$, i.e. the polar angle with respect to the H1 coordinate system. For the final calculation of θ_e the difference between the beam axis and the H1 coordinate system ("beam tilt") must be taken into account. The X_{vtx} and Y_{vtx} positions are parametrised as function of Z_{vtx} for each run in the CJC fitting procedure [74]. From these parametrisations a correction of $\lesssim 2$ mrad in θ and $\lesssim 3$ mrad in ϕ is derived which is used for the final angle measurements θ_e and ϕ_e.

Chapter 6

Electron and Hadronic Energy Measurement

The determination of the kinematic variables in NC and CC processes at high Q^2 relies to a large extent on the energy measurement the Liquid-Argon calorimeter (LAC). In both interactions, the hadronic final state is mainly contained within the geometrical acceptance of the LAC. In NC events the electron is also measured by the LAC. The precise calibration, presented in this chapter, led to a considerable reduction of the systematic errors of both cross section measurements compared to previous publications and is published in [45].

Firstly the calibration of the electron energy is presented which is determined by comparing the calorimetric measurement to independent reference scales. Systematic studies verify the calibration by varying the assumptions, cuts and event samples. In the backward region, where there are high statistics, a precision of up to 0.7% is achieved. In this region also the resolution is examined and compared to the results from test beam measurements [41]. In the forward region (FB and IF) the calibration procedure is modified because of the small number of events. Finally the measurement of hadronic final state energies is discussed and a systematic uncertainty of 2% is estimated.

6.1 Electron Energy Measurement

In order to calibrate the energy of the scattered electron, events are used which are kinematically over-constrained so that the calorimetric energy can be compared to an independent prediction. The most precise calibration is achieved in the backward region (BBE and CB) using for NC events the double-angle reconstruction method. The systematic uncertainty on the calibration is determined by studying also QED-Compton events and by varying the assumptions which determine the reference scale. Finally the calibration of the forward region using low statistics event samples from DIS events, QED-Compton events and from elastic $\gamma\gamma$ interactions is described.

Calibration of BBE and CB

The kinematics for NC DIS events is over-constrained. The energy and angle of the scattered electron and the hadronic final state can be measured and the beam energies are known precisely. Thus the electron energy can be reconstructed from the double-angle method which is independent of the calorimetrically measured electron energy (see eq. 4.8).

In figure 6.1 the reconstruction of E_{DA} is studied. It is seen that the "true" energy, which is the generated electron energy E_{gen} in MC events [1], is well reconstructed and the resolution is $\lesssim 2\%$ for $y_\Sigma < 0.3$ (see eq. 4.6). The degradation of the resolution at high y_Σ is due to the less precise reconstruction of γ_h and due to the larger influence of radiative corrections.

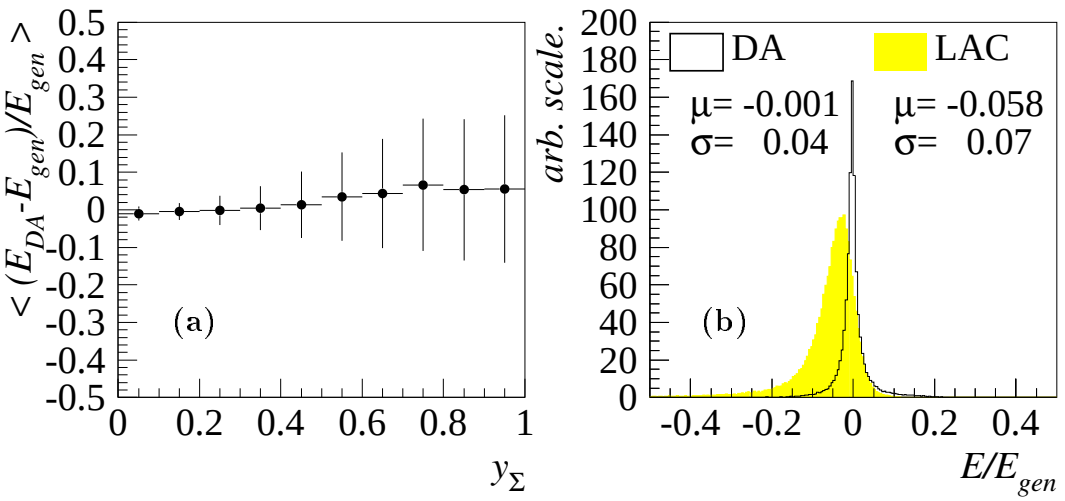

Figure 6.1: *(a) Reconstruction of the scattered electron energy using the DA method versus y_Σ for Monte Carlo events. The mean value (solid points) and the resolution (error bars) are shown. (b) The reconstructed energy using the DA method and the calorimetric measurement (LAC) compared to the generated energy. The mean μ and resolution σ are given for both methods.*

The selection criteria of events for the calibration are the same as given in section 7, but additional cuts are imposed:

- $44 < E - p_z < 66$ GeV: this cut reduces the effect of radiation on the DA energy (see section 9.3).
- $\gamma_h > 8^o$ ensures that the hadronic final state angle is well contained in the calorimeter and therefore well measured.

[1] For events with final state radiation the generated photon energy is added to the generated electron energy.

- $y_\Sigma < 0.3$ (< 0.5) for $Z_e < 20$ cm ($20 < Z_e < 100$ cm) is required to ensure a precise reconstruction and good resolution of the DA energy [2].

- No attempt is made to calibrate the ϕ-cracks which are excluded by $\phi_{\text{wheel}} \notin [-2^o, +2^o]$ (see eq. 5.3).

In figure 6.1(b) the energy reconstruction is compared between the DA and the calorimetric energy measurement E^{ini}_{LAC} after applying these cuts. The initial LAC energy E^{ini}_{LAC} is the energy as obtained from the primary H1 energy calibration, i.e. which is determined in the standard H1 reconstruction software. The calorimetric energy (LAC) is shifted by $\approx 6\%$ from the "true" energy and has a large tail towards low values. The shift is partially due to the measurement in Z crack regions: when excluding these cracks the shift is decreased to 3.6% and the resolution is improved to 5.5%. The DA energy agrees with the "true" energy and has better resolution than the LAC energy measurement with the above selection. Thus, the DA energy provides a good reference scale to test the absolute energy measurement as well as the energy resolution of the calorimeter.

The calibration is performed by comparing the calorimetric energy with the DA-prediction as a function of the impact position of the electron in the calorimeter. The main geometrical structures of the LAC are the Z-dependent separation into wheels and the ϕ- dependent octant structure (see figure 2.2). All calibration factors are determined for the data but also for the MC simulation to correct for any bias due to the reconstruction procedure. They are determined in two steps:

- Firstly, a year-by-year calibration is made for each stack independently. These stacks are 8 octants per wheel for the wheels BBE, CB1, CB2 and CB3. The stack number is given by $N_{stack} = 8 \cdot N_{wheel} + N_{octant}$ with $N_{wheel} = 0...3$ for the wheels BBE...CB3 and the octant number $N_{octant} = 0...7$ for $\phi = 0^o...360^o$. The calibration is restricted to regions where no large losses due to inactive material are present, i.e. the regions $Z_e < -180$ cm, $-160 < Z_e < -130$ cm, $-65 < Z_e < -55$ cm and $15 < Z_e < 25$ cm are removed. After applying the calibration coefficients obtained in this step the energy is called E^{oct}_{LAC}.

- Secondly, calibration constants are derived as a function of the calorimeter impact position Z_e of the electron in steps of 1 cm. After applying the calibration coefficients obtained in this step the energy is called E^{fin}_{LAC}.

In the first step the calibration factor δE^{oct}_{LAC} is determined by the average difference between the DA and LAC energy measurement:

$$\delta E^{oct}_{LAC} = \langle E^{ini}_{LAC} / E_{DA} - 1 \rangle \tag{6.1}$$

The calibration factors obtained in the first step are summarised in figure 6.2 where $\langle E^{ini}_{LAC} / E_{DA} \rangle$ is shown for the four backward wheels as a function of the stack number

[2] By restricting the calibration to the low y region, the calibration is limited to high values of the energy $E_{LAC} \gtrsim 25$ GeV.

N_{stack} for the 1994-97 data and the simulation. A shift of $3-5\%$ from unity and ϕ-dependent variations are seen clearly in the data that are not reproduced by the simulation. The ϕ-dependent variations are found to be within $\approx \pm 2\%$, except for 1995 where a single octant in the BBE region measured 8% less energy [3]. Good agreement throughout the years was also observed in CB3 within the statistical errors, where, due to limited statistics, only the full data sample is shown. For CB2 the calibration factors for all years agree also within their statistical precision. Therefore the calibration constants are determined from the average of the four years for CB2 and CB3, while for BBE and CB1 they are determined for each year individually.

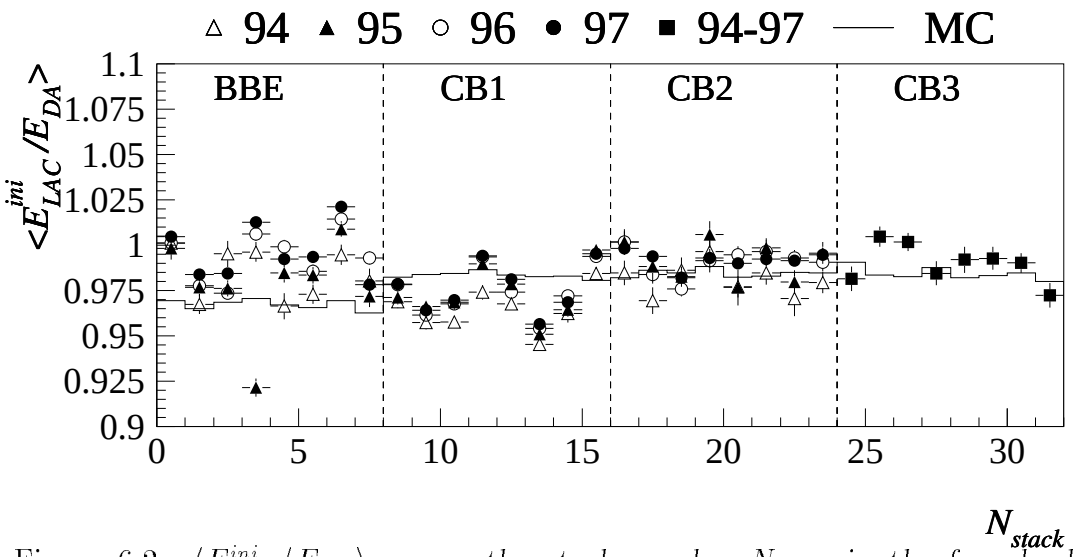

Figure 6.2: *$\langle E^{ini}_{LAC}/E_{DA}\rangle$ versus the stack number N_{stack} in the four backward calorimeter wheels. The line shows the MC values.*

After applying the calibration coefficients resulting from the first step, the ratio $\langle E^{oct}_{LAC}/E_{DA}\rangle$ is studied as function of Z_e in steps of one cm. For this second step the mean value is determined from a gaussian fit in order to reduce the sensitivity to tails in the distribution. The calibration constants δE^Z_{LAC} are determined by a smoothing procedure taking into account the values of $\langle E^{oct}_{LAC}/E_{DA}\rangle$ in the neighbouring bins:

$$\text{BBE+CB1: } \delta E^Z_{LAC} = \frac{\mu_z+(\mu_{z-1}+\mu_{z+1})/2+(\mu_{z-2}+\mu_{z+2})/4}{2.5}$$

$$\text{CB2+CB3: } \delta E^Z_{LAC} = \frac{\mu_z+0.8*(\mu_{z-1}+\mu_{z+1})+0.6*(\mu_{z-2}+\mu_{z+2})+0.4*(\mu_{z-3}+\mu_{z+3})}{4.6}$$

with $\mu_z = \langle (E^{oct}_{LAC} - E_{DA})/E_{DA}\rangle$ being the mean value at Z_e and μ_{z-i} the mean value at $Z_e - i$ cm, thereby reducing the dependence on statistical fluctuations. The calibration factors δE^Z_{LAC} are shown as a function of Z_e in figure 6.3 for the data and Monte Carlo sample. In the crack regions at $Z_e \approx -150$ cm and $Z_e \approx -60$ cm and $Z_e \approx +20$ cm the calibration factors reach up to 8% and are significantly different for data and simulation [4].

[3] This difference could not be traced back to a known source.

[4] The description of the energy measurement in cracks is better when using the detailed simu-

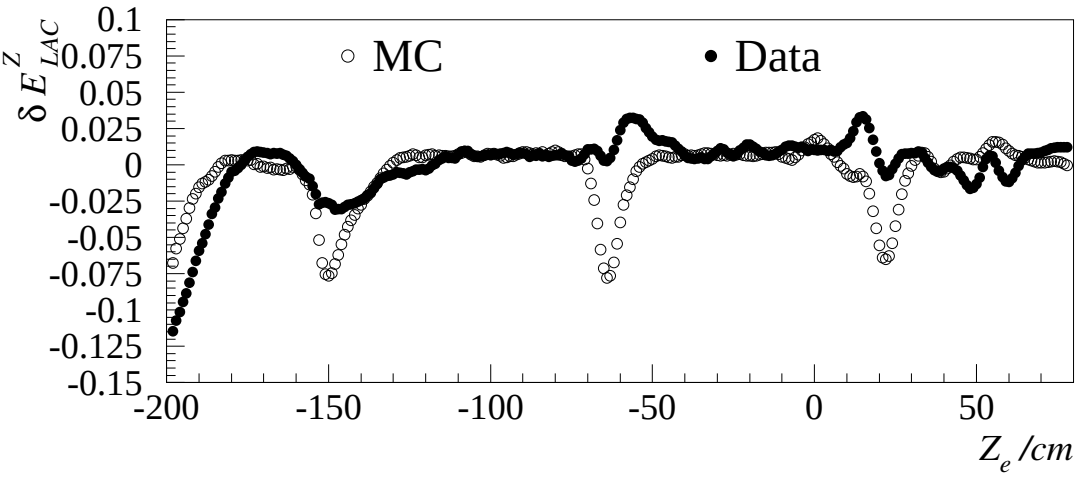

Figure 6.3: *Calibration factors δE^Z_{LAC} versus the impact position Z_e for data (full points) and MC (open points).*

The resulting calibration factors from step one and two are applied to events in data and simulation which are then compared in figure 6.4. The mean value $\langle E^{fin}_{LAC}/E_{DA}\rangle$ agrees well between data and simulation. It is also close to unity and independent of Z_e.

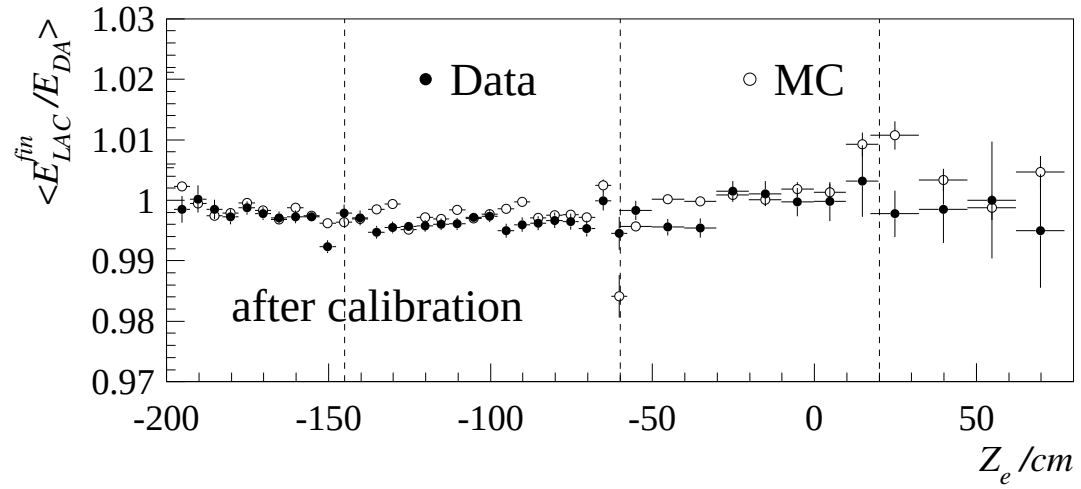

Figure 6.4: *$\langle E^{fin}_{LAC}/E_{DA}\rangle$ versus Z_e for data (full points) and simulation (open points) after calibration.*

Energy Resolution

Due to the superior resolution of the DA energy for the selected sample ($y_\Sigma < 0.3$) the energy resolution of the LAr calorimeter for electrons can also be determined. Test beam results revealed a resolution $\sigma(E)/\sqrt{E} = 12\%/\sqrt{E/\mathrm{GeV}} \oplus 1\%$ [41].

lation of the shower profiles instead of the fast parametrisation (see section 3.3).

LAr wheel	Z_e region of LAr calorimeter (cm)	$\sigma(E)/\sqrt{E/GeV}$ (%) data	MC	$< E^{fin}_{LAC} >$ (GeV)
BBE	$Z_e < -180$	32.4 ± 1.4	18.4	26.0
BBE	$-180 < Z_e < -160$	21.0 ± 0.5	15.8	25.9
BBE/CB1	$-160 < Z_e < -130$	20.9 ± 0.4	16.5	26.3
CB1	$-130 < Z_e < -70$	15.7 ± 0.2	13.0	28.4
CB1/CB2	$-70 < Z_e < -50$	21.0 ± 1.1	18.6	30.8
CB2	$-50 < Z_e < +15$	18.2 ± 0.6	13.1	36.3
CB2/CB3	$+15 < Z_e < +25$	41.3 ± 11.8	25.8	49.8
CB3	$Z_e > +25$	18.9 ± 1.3	14.7	59.3

Table 6.1: *Resolution of the electron energy measurement by the LAr calorimeter for data and simulation. The calorimeter region, the resolution for data and simulation and the mean electron energy of the used data sample are given.*

To determine the energy resolution of the calorimeter, $\sigma(E)/\sqrt{E}$, the quantity $(E^{fin}_{LAC} - E_{true})/\sqrt{E_{true}}$ must be measured. However, since E_{true} is unknown for data it is substituted by E_{DA}. An additional correction, estimated from the MC simulation, is applied to account for the finite resolution of the DA-energy:

$$\sigma(E)/\sqrt{E/GeV} = \sigma\left(\frac{E^{fin}_{LAC} - E_{DA}}{\sqrt{E_{DA}/GeV}}\right)\left[\frac{\sigma[(E^{fin}_{LAC} - E_{true})/\sqrt{E_{true}/GeV}]}{\sigma[(E^{fin}_{LAC} - E_{DA})/\sqrt{E_{DA}/GeV}]}\right]_{MC} \tag{6.2}$$

Table 6.1 gives the obtained values of $\sigma(E)/\sqrt{E/GeV}$ for data and simulation in different calorimeter regions. The best resolution of $\approx 16\%$ is observed in the three CB wheels outside the crack regions. The resolution is significantly worse in the BBE region and in crack regions where it reaches large values of $\gtrsim 20\%$. The experimental control becomes most difficult in the region $Z_e < -180$ cm where energy leakage becomes important and in the Z-crack between CB2 and CB3 at $15 < Z_e < 25$ cm. Therefore these regions are cut from the analysis.

The simulation predicts a better resolution by $\approx 3\%$ than observed in the data. This difference in resolution must be corrected, since otherwise the cross section cannot be measured reliably. When studying the resolution, $\sigma(E^{fin}_{LAC}/E_{\rm DA})$, with finer granularity in Z_e (see figure 6.5) there are, in addition to the overall difference, Z_e-dependent variations seen. The description of the energy resolution by the simulation is improved by applying an additional gaussian smearing for the energy in MC events. The width of the gaussian distribution used for this correction is given by the difference between the resolution in data and simulation. This difference is determined for every five cm in Z_e in BBE, CB1 and CB2 and taken to be 2% in CB3 and the more forward wheels. Figure 6.6 shows that the resolution observed in the data is well described by the simulation after applying this procedure. The final electron energy after calibration for data and MC and smearing of the MC energies is called E_{LAC}.

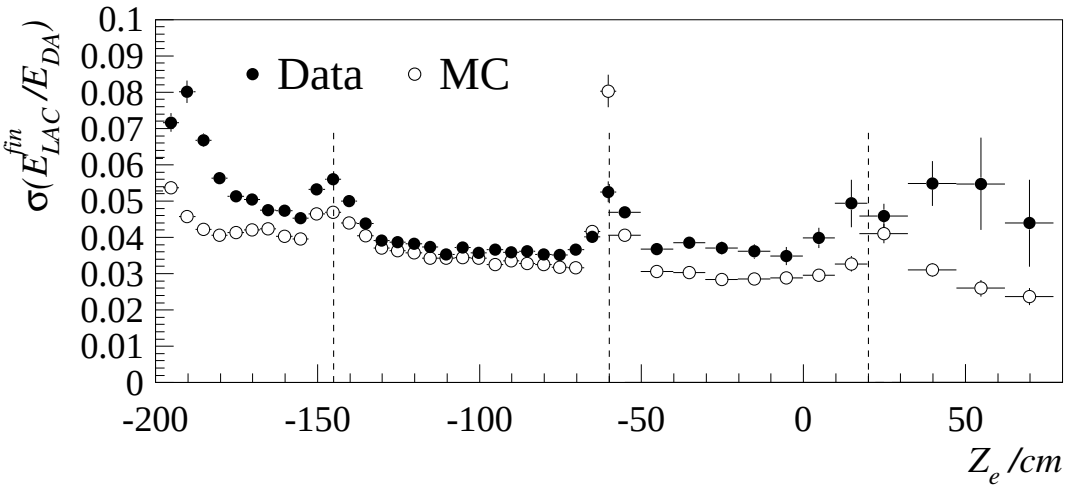

Figure 6.5: *Resolution $\sigma(E^{fin}_{LAC}/E_{DA})$ for data and simulation versus Z_e for data (full points) and simulation (open points) after calibration.*

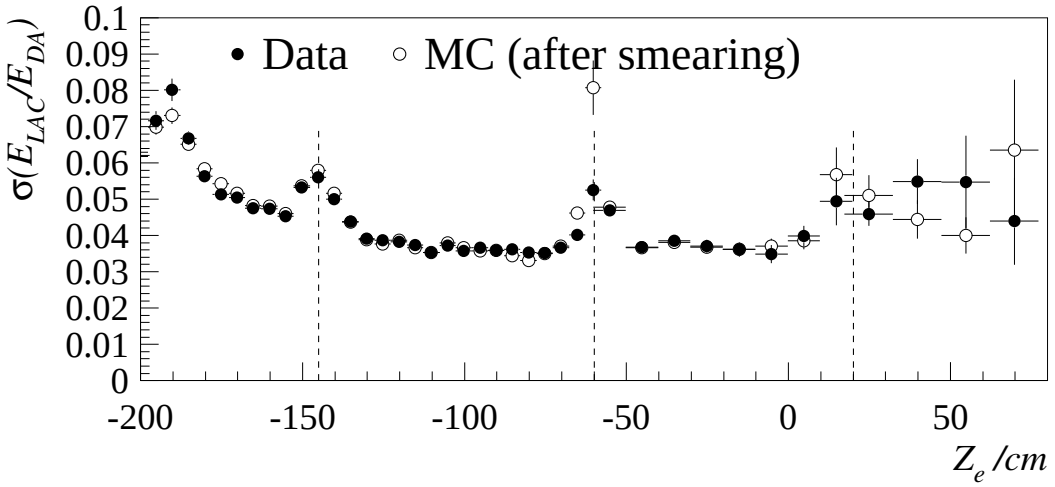

Figure 6.6: *Resolution $\sigma(E_{LAC}/E_{DA})$ for data and simulation versus Z_e for data (full points) and simulation (open points) after calibration and a gaussian smearing of the energy for the simulation.*

Systematic Studies of the Electron Energy Calibration

In this analysis the systematic uncertainties on the cross sections are split into correlated and uncorrelated sources. For the electron energy the correlated error is determined by estimating the uncertainty on the reference scale which would lead to correlated shifts of all measured cross section bins. The uncorrelated error represents the uncertainty assigned due to local deviations in particular detector regions, for example a Z-crack.

In order to estimate the correlated error on the electron energy measurement it is important to check the extent to which this calibration is independent of the method used to determine the reference scale. Here, the reference scale is E_{DA} which is sensitive to the measurement of the electron angle θ_e and the hadronic

angle γ_h which depends on Σ, $P_{T,h}$ and the noise subtraction. For this study Σ and $P_{T,h}$ are conservatively assumed to be uncorrelated, since a 100% correlation of Σ and $P_{T,h}$ would lead to no error, as can be seen from eq. 4.8. These quantities are varied within their uncertainty for eight bins in θ_e for the Monte Carlo data sample, i.e. θ_e is varied by ± 2 mrad, Σ and $P_{T,h}$ by $\pm 2\%$ and the noise by $\pm 25\%$ of the subtracted noise (see section 9.4). The total correlated systematic error is taken to be the quadratic sum of the individual differences w.r.t. the nominal DA energy and found to be $\approx 0.5\%$. The largest contribution to this error comes from the uncertainty on the hadronic energy scale, i. e. Σ and $P_{T,h}$.

The uncorrelated error is studied by comparing the calorimetric and DA energy for different event samples and by varying the method to determine the calibration coefficients:

- the event sample is divided into three subsamples depending on y_Σ: $y_\Sigma < 0.1$, $0.1 < y_\Sigma < 0.3$ and $y_\Sigma > 0.3$ corresponding also to different energy ranges
- the event sample is divided into three subsamples depending on the Z vertex position: $Z_{vtx} < -10$ cm, $10 < Z_{vtx} < 10$ cm and $Z_{vtx} > 10$ cm
- the sensitivity to tails in the E_{LAC}/E_{DA} distribution is studied using the mean value instead of the mean given by a gaussian fit to determine the calibration constants δE_{LAC}.

The first study showed no systematic trend which would indicate an energy dependence. However, the other two studies showed some systematic deviations in the BBE area. The calibration in the BBE crack region depends on the vertex position at a level of $\approx 0.5\%$. There is also a difference between the calibration coefficients determined from the mean of the distributions or a gaussian fit of 0.4% in the BBE, thereby indicating that there are non-gaussian tails in the distributions. In the other wheels no dependence on either of the two sources is seen. The uncorrelated error is estimated to be 0.87%/0.5%/1.4% in BBE/CB1-CB2/CB3. The uncertainty is larger in the BBE due to the dependences discussed above. In CB3 the larger uncertainty is quoted due to the limited statistical precision.

QED-Compton Calibration

To further check the universality of the calibration, the calibration is applied to a different physics sample, elastic QED-Compton events where the final state is formed by a photon and a electron. From the measured electron and photon angles their energies are predicted by the double-angle method. Events with the photon and the electron in the LAr calorimeter are selected as well as events having one of the 2 electromagnetic clusters in the SPACAL and one in the LAr calorimeter. The selection cuts are:

- both electromagnetic cluster have an energy > 11 GeV

- there is only one track in the event
- the event is balanced in longitudinal momentum $E - p_z > 45$ GeV
- there is no cluster with an energy > 400 MeV deposited in the forward region $\eta = \ln(\tan\frac{\theta}{2}) \geq 3$.

For events with the electron and the photon detected in the LAr calorimeter both calorimetrically measured energies are compared to their corresponding DA energies. For events with one cluster in the SPACAL only the calorimetric energy of the particle observed in the LAC is considered, irrespective of whether it is the photon or the electron. The mean values $\langle E_{LAC}/E_{DA}\rangle$ are shown in figure 6.7(a) versus E_{DA} for the QED Compton data and simulation. The data are well described by the simulation, but in the energy range of $15-25$ GeV there is a slight shift of $\approx 0.7\%$ observed between data and simulation. This shift is found to be independent of the calorimeter wheel. At low energies the mean value increases due to the bias from the selection cut on the LAC energy $E_{LAC} > 11$ GeV. This increase is therefore reproduced by the simulation.

The distribution E_{LAC}/E_{DA} are shown in figure 6.7 b) and c) for the electron and photon separately. There is no indication that the shift is more pronounced in either of the two samples. The small disagreement in this sample could be due to higher order photon radiation which is not fully included in the QED Compton MC. However, this study proves the linearity of the calibration to within the quoted total systematic uncertainty 0.7% which is the quadratic sum of the correlated and uncorrelated uncertainty.

Electron Energy Calibration of FB and IF

The calibration procedure has to be modified for the forward region, i.e. the wheels FB1, FB2 and IF. As the scattering angle decreases the number of events decreases rapidly so that, with the present event sample, it is impossible to calibrate the octants independently. The calibration is therefore only investigated wheel-wise, and two different event samples are used:

- DIS events were studied using the DA and ω method [75]. Under the assumption that the mismeasurement in Σ and $P_{T,h}$ are the same ($\delta\Sigma/\Sigma = \delta P_{T,h}/P_{T,h}$), the following equations are valid due to the conservation of the transverse and longitudinal momentum:

$$(y_e - 1)\frac{\delta E_{LAC}}{E_{LAC}} - y_h\frac{\delta\Sigma}{\Sigma} = y_e - y_h \tag{6.3}$$

$$P_{T,e}\frac{\delta E_{LAC}}{E_{LAC}} - P_{T,h}\frac{\delta\Sigma}{\Sigma} = P_{T,e} - P_{T,h} \tag{6.4}$$

  where δE_{LAC} and $\delta\Sigma$ denote the miscalibration of the electromagnetic and

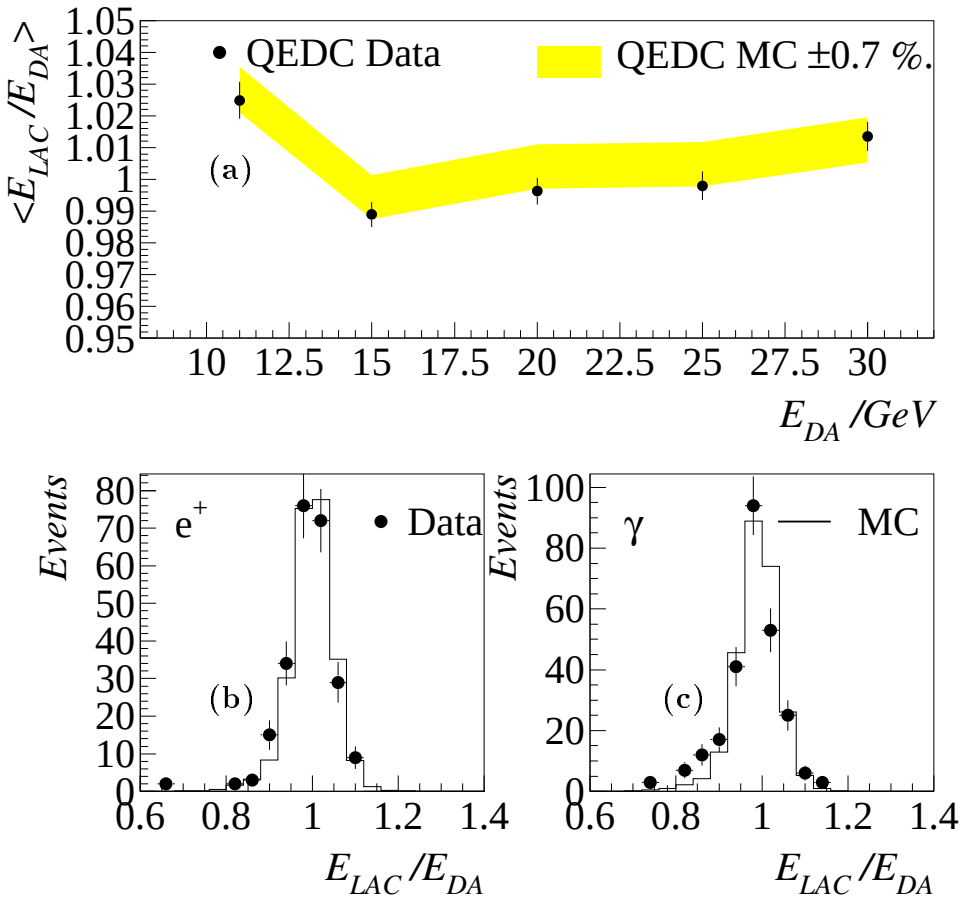

Figure 6.7: *(a) Mean of the ratio of calorimetric to DA-energy* $< E_{LAC}/E_{DA} >$ *for the photon and electron in elastic QED-Compton events for data (full points). The MC simulation is shown as an error band of* 0.7% *around the central value for the simulation. (b) and (c) show the ratio* E_{LAC}/E_{DA} *for electrons and photons respectively, for data (full points) and simulation (histogram).*

hadronic energy respectively. The solution of these equations yields:

$$\frac{\delta E_{LAC}}{E_{LAC}} = \frac{P_{T,h}y_e - P_{T,e}y_h}{[P_{T,h}(1-y_e) - P_{T,e}y_h]} \tag{6.5}$$

$$\frac{\delta\Sigma}{\Sigma} = \frac{P_{T,h} - P_{T,e}(1-\frac{\delta E_{LAC}}{E_{LAC}})}{P_{T,h}} \tag{6.6}$$

The advantage of the ω method compared to the DA method is that it allows events with ISR photons to be tagged. Events with

$$\frac{\delta E_{LAC}}{E_{LAC}} < 0.05 \quad \text{and} \quad \frac{\delta\Sigma}{\Sigma} < 0.05 \quad \text{and} \quad \frac{\delta\Sigma}{\Sigma} + \frac{\delta E_{LAC}}{E_{LAC}} < 0.15$$

are identified as those where the energy of the radiated photon is $> 5\%$ of the initial electron beam energy. This effect is corrected for by substituting the HERA electron beam energy of $E_e = 27.6$ GeV by the measured one $E_e^{corr} = (\Sigma + E_{LAC}(1-\cos\theta_e))/2$.

wheel	detector region	$e\gamma$ and e^+e^-	DIS
FB1	$100 < Z_e < 170$ cm	11	200
FB2	$170 < Z_e < 275$ cm	10	51
IF	$Z_e > 275$ cm	12	5

Table 6.2: *Table of numbers of events used for calibration*

The relative miscalibration between data and simulation is defined as

$$\langle\frac{\delta E_{LAC}}{E_{LAC}}\rangle_\omega = \langle\frac{\delta E_{LAC}}{E_{LAC}}\rangle_{\text{Data}} - \langle\frac{\delta E_{LAC}}{E_{LAC}}\rangle_{\text{MC}}$$

- Events with exactly two electromagnetic clusters and no other activity in the LAr calorimeter are selected. The reference scale is taken to be the transverse momentum of the backward cluster $P_{t,bwd}$. It is required to be in the region ($Z_e < 100$ cm) where the precise calibration was achieved with DIS events and verified with QED-Compton events (see previous subsection). The ratio of the transverse momenta $P_{t,fwd}/P_{t,bwd}$ is analysed.

  The selected events are elastic QED-Compton events ($e^+p \to e^+p\gamma$) and events from elastic photon-photon interactions ($e^+p \to e^+pe^+e^-$). In the first case an electron and a photon ($e^+\gamma$), in the latter a positron and an electron (e^+e^-) are measured in the LAC.

  The relative miscalibration between data and simulation is defined as

$$\langle\frac{\delta E_{LAC}}{E_{LAC}}\rangle_{QEDC/e^+e^-} = \frac{\langle P_{t,fwd}/P_{t,bwd}\rangle_{\text{Data}} - \langle P_{t,fwd}/P_{t,bwd}\rangle_{\text{MC}}}{\langle P_{t,fwd}/P_{t,bwd}\rangle_{\text{MC}}} \qquad (6.7)$$

The calorimeter is divided into three regions corresponding to FB1, FB2 and IF. The exact definitions of the regions and the number of events used for the calibration from the two processes per region are given in table 6.2. In the FB wheels the number of DIS events is larger than the number of QED-Compton and e^+e^- events, but in the IF wheel ($Z_e > 275$ cm) the statistical precision of the calibration is improved by including the extra physics processes.

The calibration methods agree well and yield a realtive miscalibration of all forward wheels by -4.2% on average. This study also constitutes a cross check of the linearity of the LAC since the average energy is different for the two samples. In DIS events it varies between $100-300$ GeV, in the other sample between $20-100$ GeV depending on the wheel. Due to the limited precision a single calibration constant of $+4.2\%$ is applied to data and no attempt is made to calibrate the wheels independently. An additional correction of $\approx 1\%$ is made to correct the measured energy to the "true" energy which is determined from the comparison of measured to the generated energy in the simulation. This correction is applied to both, data and simulation.

The mean fractional energy shift $\delta E_e'/E_e'$ from the absolute energy scale is presented for various methods in figure 6.8 after applying the final calibration. Within the statistical uncertainties there is good agreement between the different event samples.

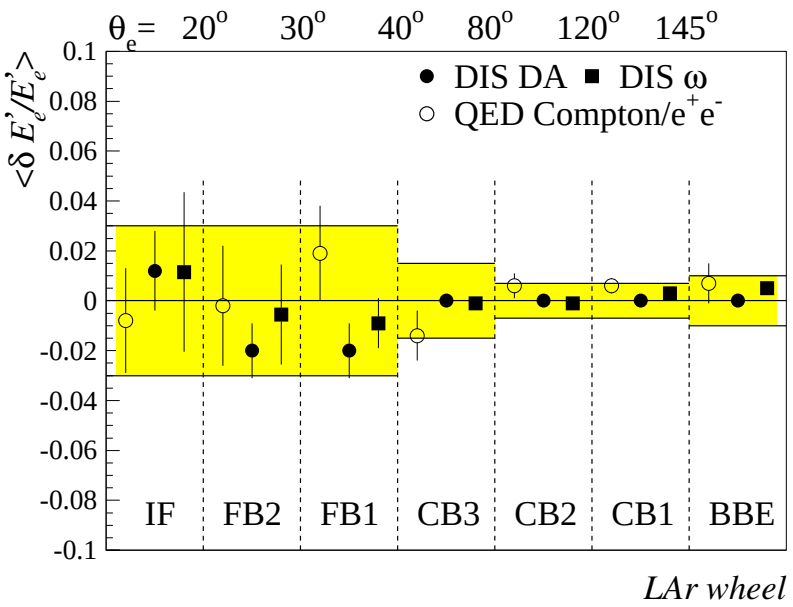

Figure 6.8: *Comparison of the electromagnetic energy scale as determined by different calibration methods. Shown is* $\delta E_e'/E_e'$*, the mean fractional energy shift from the absolute energy scale. The grey error bands shows the systematic uncertainty on the energy quoted on this measurement, which varies from* 0.7% *to* 3%*.*

They are consistent with no miscalibration within the quoted energy scale uncertainties. In addition the calibration using the DA method in the forward region is shown and found to be in good agreement with the ω-method. However, it should be noted that the same events are used in the two methods and it therefore cannot be seen as an independent cross check.

6.2 Hadronic Energy Measurement

The hadronic final state four-vector is measured in H1 as a sum of four components:

$$p = (E_h, p_{x,h}, p_{y,h}, p_{z,h}) = p_{LAr} + p_{track} + p_{spacal} - p_{noise}$$

where p_{LAr}, p_{track}, p_{spacal} and p_{noise} correspond to the four-momenta measured in the LAC, by central tracks, the SPACAL calorimeter and the contribution assigned to noise and backscattering.

Most of the hadronic energy is measured in the Liquid-Argon calorimeter, but the energy measurement can be improved significantly by algorithms developed to include track momentum measurement, the SPACAL energy measurement and by reducing effects from electronic noise and backscattering in the LAC. First the algorithms for the inclusion of track momenta and the tagging of noise and their impact

on the quality of the reconstruction of the kinematic variables are discussed, then the calibration of the hadronic energy scale of the LAC is described.

The momentum measurement of the tracking system is superior to the calorimetric measurement for low momentum particles. This is exploited by an algorithm (FSCOMB) which was developed to include track momenta in the hadronic final state reconstruction [76]. "Good" central tracks [5] with small transverse momenta < 2 GeV are selected and extrapolated to the calorimeter surface. Energy in a cylinder with $r = 25(50)$ cm in the electromagnetic (hadronic) section around the track impact point is assigned to the track. If the calorimetric energy in this cylinder exceeds the track momentum the calorimetric energy is used. Otherwise the track momentum is taken and the calorimetric energy is neglected henceforth. If a track does not reach the calorimeter the track momentum is also used. Therefore in this algorithm there is no double counting of energies.

The quality of the measurement is further improved by tagging noise in the LAC. During the L5 reconstruction cells which have an energy consistent with noise are excluded in order to suppress electronic noise [44]. This suppression is, however, not sufficient for this measurement. Studies of random trigger events [78] revealed the presence of noise clusters which degrade the reconstruction of y_h when there is very little genuine energy in the calorimeters. In addition backscattering of forward particles (e.g. off the collimators) into the calorimeter under large angles can distort the y_h measurement. Both effects can be reduced by a simple tagging of isolated low energetic clusters [76]. Clusters of low energy < 400 MeV (< 800 MeV) are rejected if they are isolated by at least 40 cm (80 cm) at polar angles $> 15^o$ ($< 15^o$). The cuts are tightened in the forward region since backscattering becomes more important.

The improvement of the y_h reconstruction by including the track momenta and SPACAL energies and suppressing additional noise can be judged from figure 6.9, where the reconstructed y_h is compared to the generated y_{gen} for MC events. At low y_{gen} the measured y_h is overestimated by $\approx 30 - 40\%$ when the noise suppression algorithm is not applied. After noise suppression the mean and the resolution on y_h/y_{gen} are significantly improved. At high y_{gen} the addition of track momenta and SPACAL energies improves the resolution and the absolute value of y_h.

Figure 6.10 shows the effect on the $P_{T,h}$ reconstruction. The transverse momentum $P_{T,h}$ is underestimated at low y mainly due to particles at very low angles $\theta < 4^o$ escaping the detection in the LAC and energy loss in the material in front of the calorimeter. The inclusion of track momenta and SPACAL energy deposits in the central region of the detector improves the $P_{T,h}$ measurement at high y.

The conclusion from these studies is that the usage of tracks and the SPACAL improves the reconstruction of $P_{T,h}$ and y_h at high y_h, the noise subtraction algorithm improves the resolution and absolute value of y_h (and therefore x) at low y_h, but does not affect the $P_{T,h}$ reconstruction. Therefore this method can be used for the CC and NC measurement consistently, because neither $P_{T,h}$ nor y_h is distorted.

[5] The track selection is based on a package in H1PHAN [77]. The main requirements are a minimum track length and a starting point close to the interaction vertex.

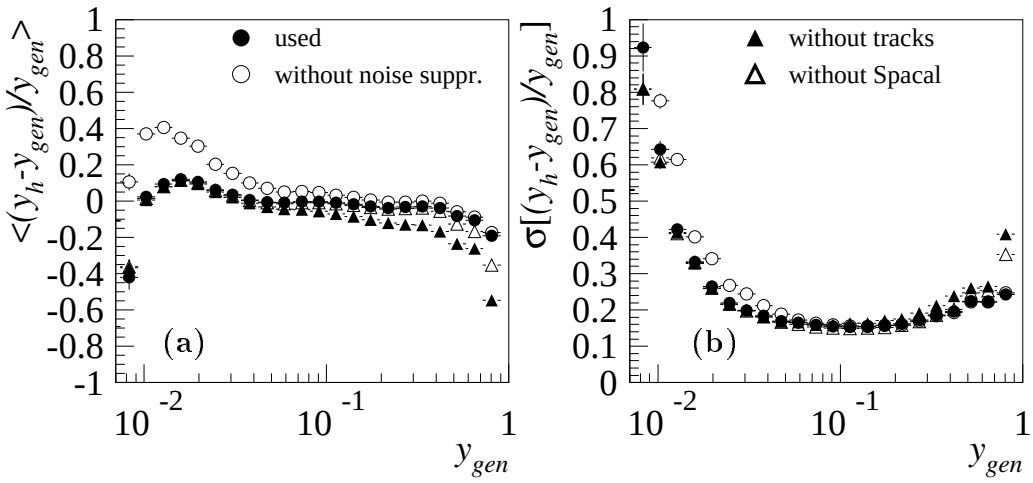

Figure 6.9: *Comparison of the measured y_h with the "true" y_{gen} for the simulation using the LAr, the tracks, the SPACAL and the noise suppression (used: full circles) and when excluding any one of the components: without noise suppression (open circles), not using track momenta (full triangles) and without including SPACAL energy deposits (open circles). Shown are the (a) mean value and the (b) resolution of $(y_h - y_{gen})/y_{gen}$.*

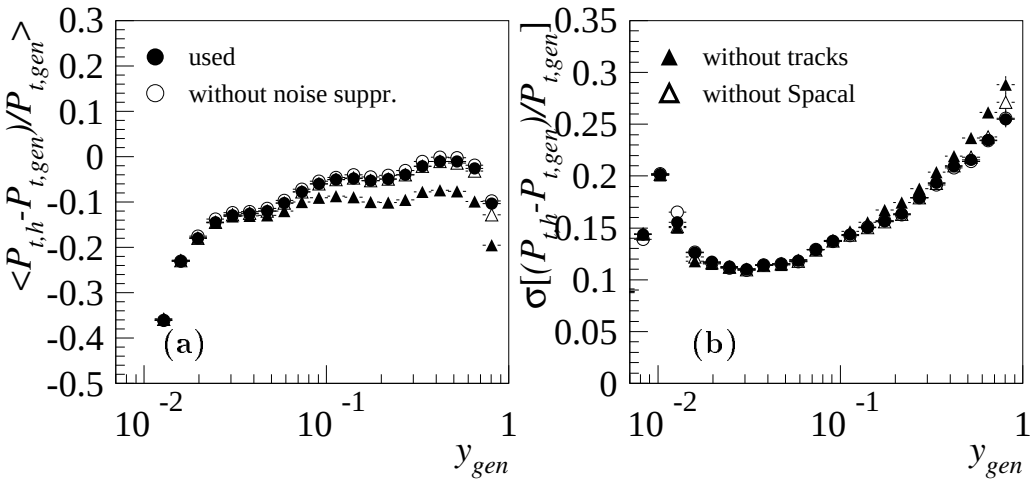

Figure 6.10: *Comparison of the measured $P_{T,h}$ with the "true" $P_{T,gen}$ for the simulation using the LAr, the tracks, the SPACAL and the noise suppression (used: full circles) and when excluding any one of the components: without noise suppression (open circles), not using track momenta (full triangles) and without including SPACAL energy deposits (open circles). Shown are (a) the mean value and (b) the resolution of $P_{T,h}/P_{T,gen}$.*

Fig. 6.11 a shows the fraction of y_h and $P_{T,h}$ carried by each of the four components

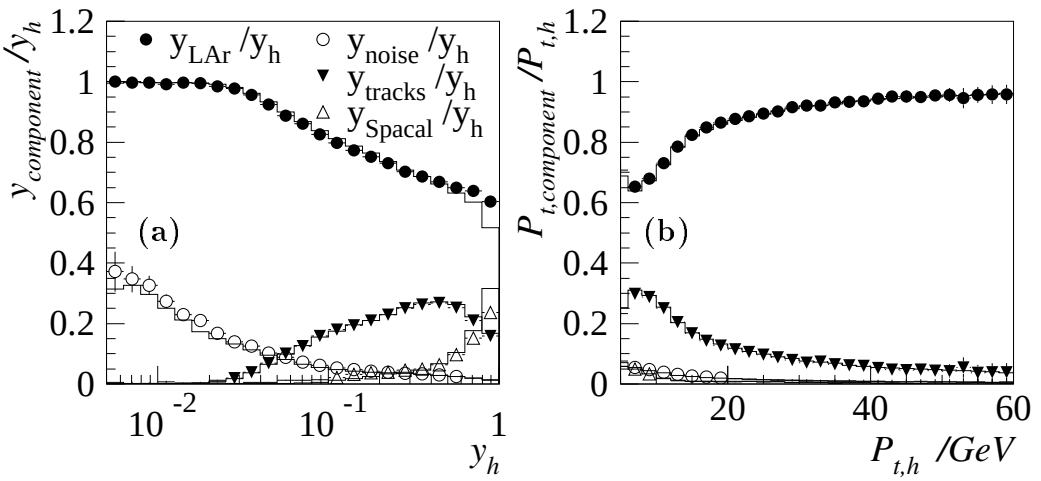

Figure 6.11: *(a) Distribution of the fraction of y_h contributed by the tracks, the LAr and the SPACAL calorimeters, and the fractional contribution of noise which is subtracted. (b) Distribution of the fraction of $P_{T,h}$ contributed by the tracks, the LAr and the SPACAL calorimeters, and the fractional contribution of noise which is subtracted. In both figures the data (points) are compared to the simulation (histograms).*

for data and simulation. At low y_h a large fraction $\approx 30\%$ of the LAr energies is identified as noise in both data and simulation. At high y_h the track momenta contribute about 20%. The SPACAL contribution is negligible over a large range, apart from at the highest $y \gtrsim 0.7$. Since most of the energy is measured in the LAC the understanding of the hadronic energy scale of the LAC is of major importance. The following section will focus on the understanding of the hadronic energy scale of the LAC.

Hadronic Energy Scale of the LAr Calorimeter

The approach for the calibration of the LAr hadronic energy scale is different to that for the the electron energy calibration. While the electron is calibrated to the absolute scale, the "true" energy, the hadronic calibration is performed relative to the Monte Carlo simulation. The reason is the different behaviour of the y_h- and $P_{T,h}$-measurement: y_h is on average slightly overestimated, $P_{T,h}$ is underestimated as shown in figure 6.9(a) and 6.10(a). Therefore any simple energy calibration will only improve the measurement of one variable, but degrade the other.

The LAC calibration for hadronic objects is complicated since the hadronic final state is generally spread over more than one wheel and octant of the calorimeter. Therefore, a method developed to calibrate the SPACAL calorimeter [71] was adapted for this analysis. It is based on the comparison of the transverse momentum of the hadronic system $P_{T,h}$ and that of the electron $P_{T,e}$ after calibration (see section

6.1). Calibration constants are determined for the data for each electromagnetic and hadronic calorimeter wheel separately.

An event pull is defined $\delta^{ev} = P_{\perp,LAr}/P_{T,e}$ where $P_{\perp,LAr}$ is the projection of $P_{T,LAr}$ onto the electron direction $P_{\perp,LAr} \equiv -P_{T,LAr} \cdot cos(\phi_e - \phi_h)$. The relative contribution of the wheel i to the event pull is given by the fractional transverse momentum deposited in the wheel $W_i^{ev} = P_{t,i}/P_{T,LAr}$. Finally the weighted pull average is determined for each wheel by averaging over all events

$$\Delta_i = 1 - \sum_{events} \delta^{ev} W_i^{ev}.$$

The ratio of the means of these distributions in data and simulation is taken as the calibration factor for data. The procedure requires iteration. This means that after applying the calibration factors there is still a miscalibration observed which is then applied again. After about 3 iterations for the electromagnetic and about 8 for the hadronic wheels the calibration factors converged to a stable result.

The events used for the calibration described above are predominantly at low values of P_t. To check the linearity of the calibration of the hadronic final state the P_t-balance was studied in different calorimeter wheels as function of $P_{t,e}$. The wheel is determined by the z-impact position determined from the inclusive hadronic angle γ at the average shower maximum $R_h = 125$ cm:

$$Z_h = R_h / \tan\gamma_h + Z_{vtx}$$

The ratio of the P_t balance $\langle P_{t,LAr}/P_{t,e}\rangle^{Data}/\langle P_{t,LAr}/P_{t,e}\rangle^{MC}$ in data to the one in the simulation versus $P_{t,e}$ is shown in figure 6.12. At low transverse momenta this ratio is smaller than unity, i.e. the hadronic $P_{T,LAr}$ in data is smaller than predicted by the simulation, the opposite is true at high $P_{T,e}$ [6]. Therefore a $P_{T,LAr}$-dependent correction of the hadronic energies was performed

$$P_{LAr}^{fin} = P_{LAr}^{ini} \cdot \frac{1.04}{e^{(-20.61 - P_{t,LAr}^{ini})/10.65} + 1.}$$

for events with $Z_h < 100$ cm. This correction function is shown in fig. 6.12.

After this correction the hadronic energy measurement for data and Monte Carlo events agree to within 2% as can be seen from figure 6.13 where the P_T balance $\langle P_{T,h}/P_{T,e}\rangle$ is compared between data and simulation versus the hadronic angle γ for events with low and high $P_{T,e}$. In both kinematic regions good agreement is observed over the entire angular range. The comparison of the y balance between data and simulation is also shown for $y_e > 0.1$ and found to be described by the simulation to within 2%.

[6] The observed difference between data and simulation difference is not yet understood, it is likely to be due to small differences in the hadronic final state which affect the energy measurement at low energies.

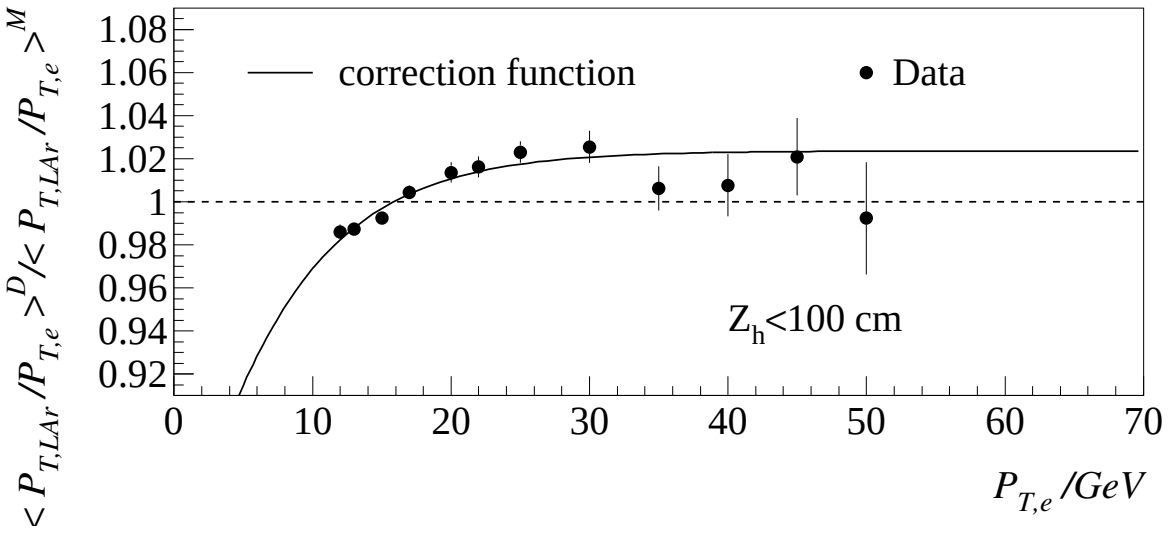

Figure 6.12: *The ratio of the P_t balance $\langle P_{T,LAr}/P_{T,e}\rangle^D$ for data to that for the MC simulation $\langle P_{T,LAr}/P_{T,e}\rangle^M$ for the central barrel ($Z_h < 100$ cm) as function of $P_{t,e}$. Shown is also the correction function used to calibrate the data.*

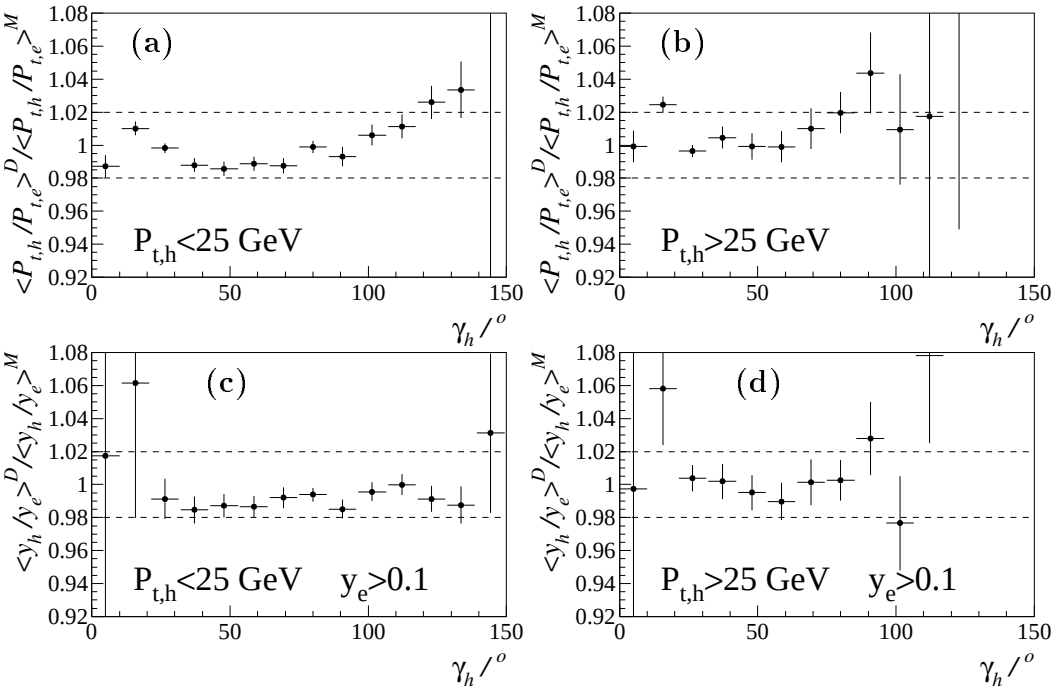

Figure 6.13: *The ratio of the P_t balance $\langle P_{T,h}/P_{T,e}\rangle^D$ for data to that for the MC simulation $\langle P_{T,h}/P_{T,e}\rangle^M$ for (a) $P_{T,e} < 25$ GeV and (b) $P_{T,e} > 25$ GeV. The ratio of the y balance $\langle y_h/y_e\rangle^D$ for data to that for the MC simulation $\langle y_h/y_e\rangle^M$ for $y_e > 0.1$ and for (c) $P_{T,e} < 25$ GeV and (d) $P_{T,e} > 25$ GeV.*

Chapter 7

Selection of Neutral Current Events

Neutral current events with $Q^2 \gtrsim 100$ GeV^2 are selected by requiring a high energy electron candidate in the LAr calorimeter. Additional kinematic and fiducial cuts are applied to suppress background and to reduce uncertainties in the measurement. These criteria and their efficiencies will be described in the following.

Firstly the run and trigger selection are described which ensure that the sample is well defined and the luminosity is determined correctly. Then the algorithm used for identification of the scattered electron is studied. Thereafter the requirements of a primary interaction vertex and a track linked to the electron candidate are investigated. Finally further studies are presented which reduce the background contamination in the final data sample to a very small amount.

7.1 Run Selection

The times in which data are taken at HERA are divided into "luminosity fills" which are defined by one filling of proton and electron bunches in the HERA ring. These luminosity fills are divided into "runs" which last at maximum two hours for each of which the luminosity is measured individually. The detector conditions within a run are rather stable, but they may differ for different runs and luminosity fills.

The run selection is common to both the NC and CC analysis (see chapter 8). It ensures that the subdetectors which are essential for the analysis are operational. These are the luminosity system, the ToF system, the LAr and SPACAL calorimeters, the central jet chambers (CJC1 and CJC2) and the central proportional chambers (CIP and COP). Additionally, runs are excluded if coherent noise in the LAr calorimeter is detected and if the subtriggers that are used in this analysis are disabled. The neutral current event yield, the number of observed events per unit of integrated luminosity (nb^{-1}), is checked for each luminosity fill after application of the final data selection. Luminosity fills for which the event yield is more than

6σ smaller than the average yield are excluded[1]. Figure 7.1 shows the event yield for each of the four years after applying this run selection. The event yields are constant throughout the years, and are about 5% higher in 94 and 95 due different fiducial cuts which are described in section 7.2. The integrated luminosity used for the analysis is $\mathcal{L} = 35.68$ pb^{-1}.

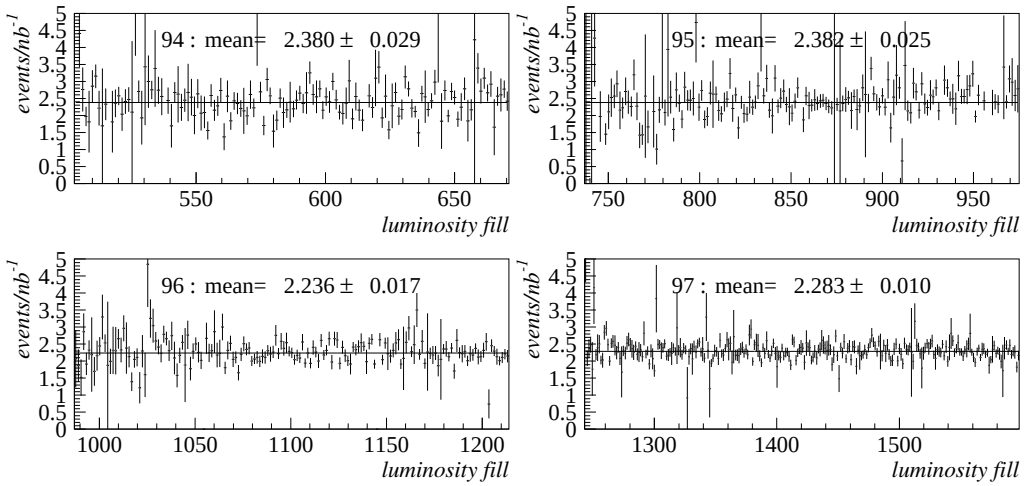

Figure 7.1: *Event yields for the different years versus the luminosity fill number. Given are also the average values for each year.*

7.2 Trigger

The triggering of NC events is based on the detection of a high energy deposit in a trigger tower of the LAr calorimeter (see section 2.7.1). The two trigger elements (TE) LAr-el1 and LAr-el2 are based on this condition. These trigger elements are combined on trigger level L1 with timing information from the LAr calorimeter (LAr-T0) or the central and forward proportional chambers (Ray-T0) to form the physics subtriggers (ST) ST67 and ST75. A more detailed explanation of the trigger elements is given in section 2.7. The physics trigger conditions are:

- **1994-95**
  - **ST67:** LAr-el2 && (Ray-T0 || LAr-T0)[2]
  - **ST75:** LAr-el1 && (Ray-T0)

[1] For most of these fills the reason for the low event yield could be traced back to a problem during data taking

[2] A || B is the logical OR of A and B, i.e. it means that either condition A or B or both are fulfilled. A && B is the logical AND of A and B, i.e. A and B must be fulfilled.

- **1996-97**

  - **ST67:** LAr-el1 && (Ray-T0 || LAr-T0)

In 1996 the LAr-el1 TE had a sufficiently low rate to allow the timing requirements on ST67 to be relaxed such that events, where only the LAr-T0 triggered, were taken as well. Since there was then redundancy between ST75 and ST67, the LAr-el2 TE was changed such that it is not useful for the present analysis of 1996-97 data. In addition to the above conditions there are veto conditions which will be discussed separately at the end of this section.

The efficiency of each trigger element described above is studied separately using a monitor trigger (MT) condition that is independent of the trigger element:

- **LAr-el1 and LAr-el2** are monitored by ST71 in 1996+97 and ST64 in 1994+95
- **LAr-T0** is monitored by ST67 && (Ray-T0)
- **Ray-T0** is monitored by ST67 && (LAr-T0)

The efficiency of the TE is therefore given by

$$\epsilon_{TE} = \frac{\text{number of events triggered by MT and TE}}{\text{number of events triggered by MT}}$$

Energy Condition

In order to identify regions of limited triggering efficiency within the detector, the efficiency of LAr-el1 is evaluated as a function of the electron impact position Z_e (see eq. 5.6) and scattering azimuth ϕ_e as shown in figure 7.2 for $E_e' > 11$ GeV. It can be seen that there are regions in CB1 and CB2 where the trigger efficiency is significantly smaller than 100%. These inefficiencies were correlated with trigger cells in the central barrel (CB) which had been deactivated due to a high noise level. The inefficiency is less pronounced in the 1995 data and not seen in the 1994 data, since most of these cells were only deactivated in 1996.

The areas with low efficiencies (see figure 7.2) are cut for the analysis:

- **1996/97:**

$$\begin{aligned} -60 < Z_e < +20 \text{ cm} \quad &\text{and} \quad -135^o < \phi_e < -112.5^o \\ -120 < Z_e < -30 \text{ cm} \quad &\text{and} \quad +90^o < \phi_e < +112.5^o \\ -10 < Z_e < +20 \text{ cm} \quad &\text{and} \quad +90^o < \phi_e < +112.5^o \\ -90 < Z_e < -60 \text{ cm} \quad &\text{and} \quad +135^o < \phi_e < +157.5^o \end{aligned}$$

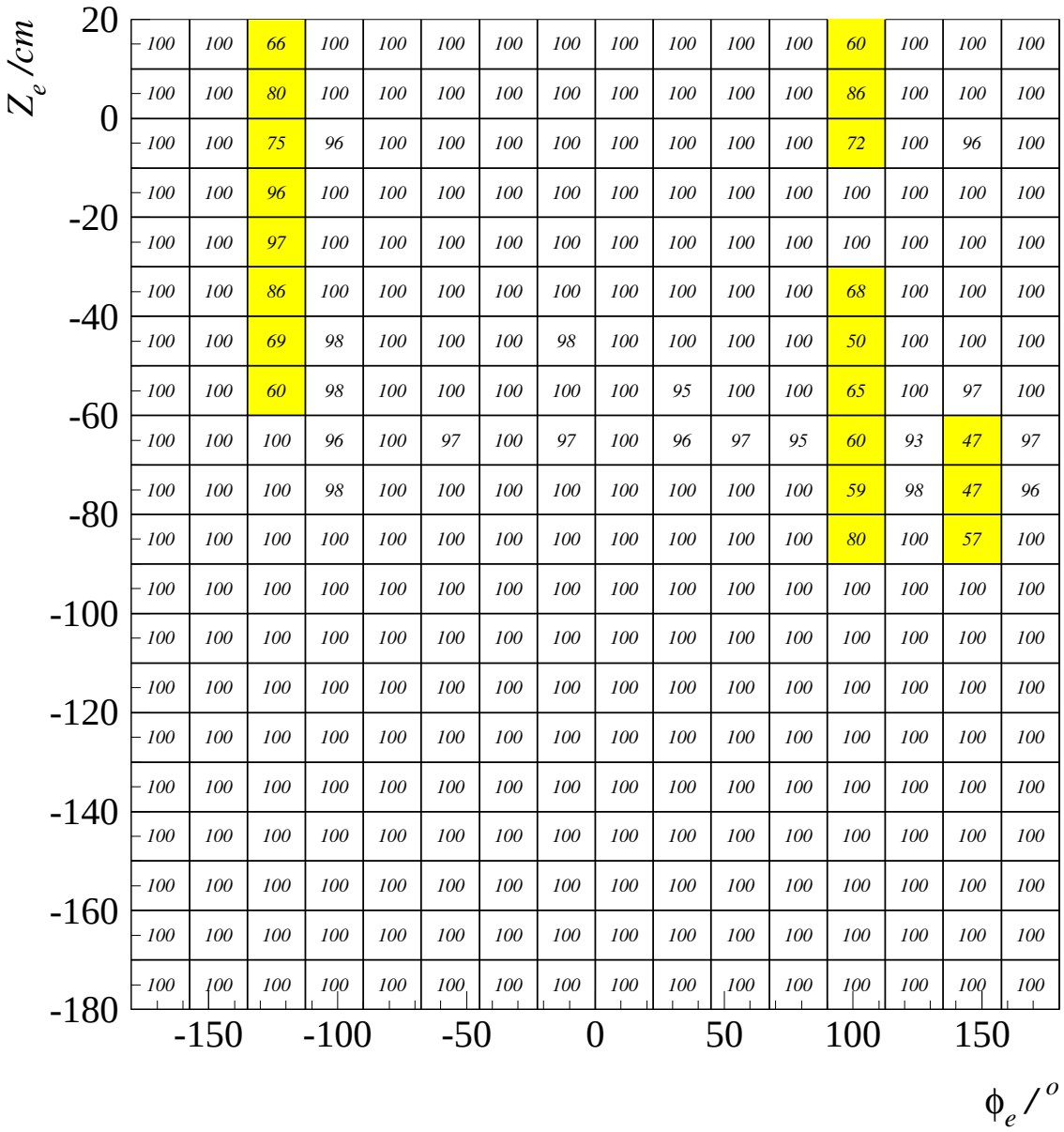

Figure 7.2: *The efficiency of the trigger element LAr-el-1 in % for electrons with* $E_e' > 11$ *GeV as function of* Z_e *and* ϕ_e *for 1994-97 data. The grey regions indicate the fiducial cuts applied in the analysis.*

- **1995:**

$$-80 < Z_e < -60 \text{ cm} \quad \text{and} \quad +90^o < \phi_e < 112.5^o$$
$$-90 < Z_e < -60 \text{ cm} \quad \text{and} \quad +135^o < \phi_e < 157.5^o$$

No fiducial cuts are necessary in the BBE, CB3 and more forward wheels, since there the efficiency is consistent with 100% for the measured kinematic range.

After applying these fiducial cuts the trigger efficiency is shown in figure 7.3 as function of the energy of the scattered electron for the LAr-el1 TE in different

calorimeter wheels. It is parametrised by

$$f(x) = C \cdot \int_{-\infty}^{x} e^{-t^2/2} dt \text{ with } x = \frac{E_e' - A}{B} \tag{7.1}$$

where A denotes the value where the efficiency is 50%, B the width [3] of the trigger threshold and C the plateau value. The threshold is consistent with the nominal value of 6 GeV in all wheels. The width is about 2 GeV but varies by about 0.5 GeV between the individual wheels. In all wheels the efficiency reaches a plateau value consistent with 100% for energies $E_e' > 11$ GeV which is therefore chosen as the analysis cut. In CB3 and the more forward wheels the threshold can not be analysed with NC events, because energies lower than $E_e' < 11$ GeV are kinematically excluded due to the cut $y_e < 0.9$ (see section 7.5).

Timing Condition

The T0 trigger elements allow the bunch crossing of the interaction to be determined. There are three different trigger T0 requirements combined with the electron requirement to form the subtriggers: the LAr-T0, the Zvtx-T0 and the FwdRay-T0. The efficiency of the LAr-T0 TE depends on the electron energy as can be seen in figure 7.4(a), it reaches a value of 90% at high energies $E_e' \gtrsim 30$ GeV. The efficiency of the Ray-T0 TE varies with the track multiplicity in the acceptance region of the proportional chambers and is therefore shown as function of y_h in figure 7.4(b), it is $\approx 98\%$ decreasing to $\approx 95\%$ at low y_h where the hadronic final state is not measured in the central region of the detector. The efficiency of the LAr-T0 TE decreases at high y_h since this corresponds to low E_e'. The combined efficiency of the two timing requirements is obtained from the individual efficiencies via

$$\epsilon(\text{LAr} - \text{T0}||\text{Ray} - \text{T0}) = \epsilon(\text{LAr} - \text{T0}) + [1 - \epsilon(\text{LAr} - \text{T0})] \cdot \epsilon(\text{Ray} - \text{T0})$$

under the assumption that the LAr-T0 and Ray-T0 are independent of each other. It is $99.74 \pm 0.06\%$ in most of the measured kinematic range as is shown in figure 7.4. The small inefficiencies ($\lesssim 1\%$) at low y_h and low E_e' is corrected in the simulation by reweighting the Monte Carlo events according to this difference.

The efficiency of the physics trigger can for example for 1996-97 be determined via

$$\epsilon(\text{ST67}) = \epsilon(\text{LAr} - \text{el1}) \cdot \epsilon(\text{LAr} - \text{T0}||\text{Ray} - \text{T0})$$

Since the LAr-el1 efficiency is consistent with 100 % for $E_e' > 11$ GeV, the efficiency of ST67 is identical to the efficiency of the timing requirements discussed above.

Veto Condition

There are so-called "global veto conditions" used in the H1 trigger system which are described in section 2.7.1. Since these vetoes are independent of the underlying

[3] The width is the value that corresponds to an increase of the trigger efficiency by 1σ starting from the 50% value, i.e. where $\epsilon(A + B/2) = 68.3\%$.

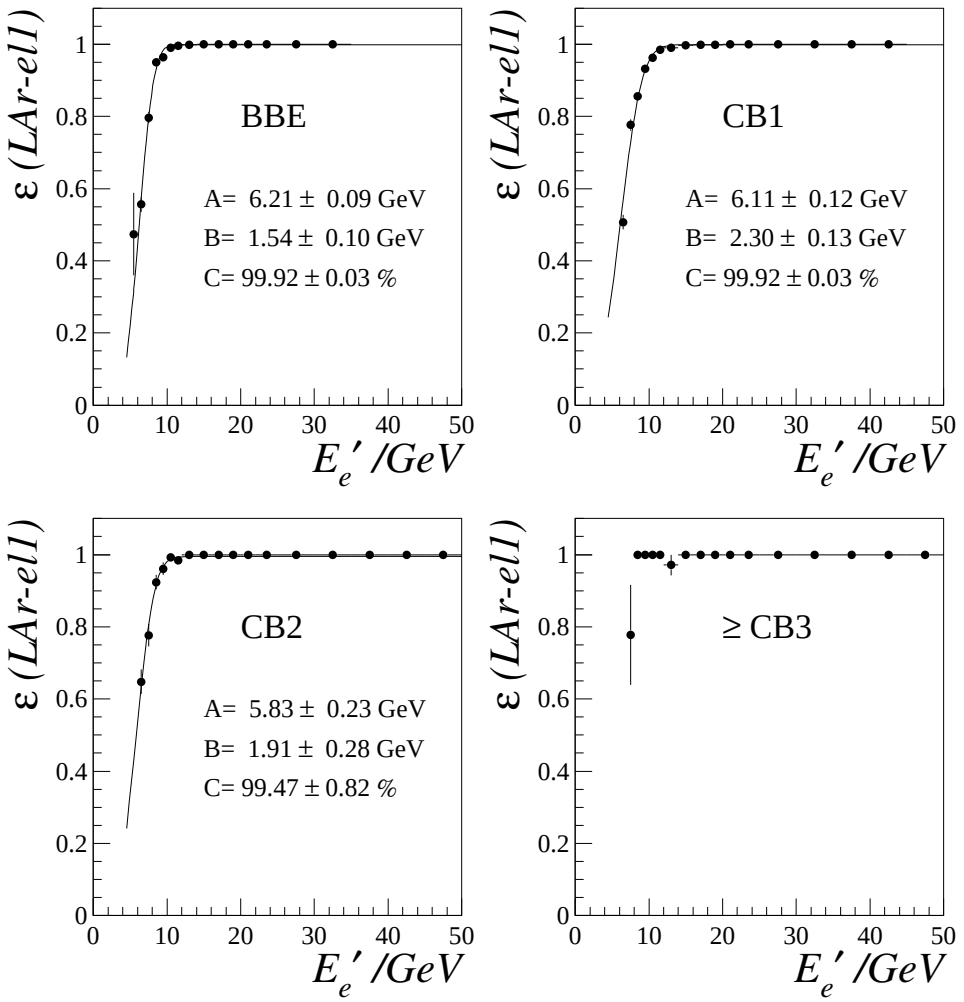

Figure 7.3: *The efficiency of the trigger element LAr-el1 versus the energy of the scattered electron for different calorimeter wheels BBE, CB1, CB2 and more forward ($\geq$ CB3). Shown is also a parametrisation of the trigger efficiency (see equation 7.1) and the values of the fitted parameters are given.*

physics process the present section applies to the NC selection as well as to the CC selection (see chapter 8). There are common veto conditions to all CC and NC subtriggers which are the BToF (in 1994 ToF) and the FToF vetoes. These were studied in dedicated runs taken without these conditions applied. The BToF veto introduces an inefficiency of $0.100 \pm 0.003\%$ [79]. Only one event was observed which was rejected due to the FToF veto, leading to an inefficiency of $0.4 \pm 0.4\%$. The other veto conditions could be studied with higher precision because they are only applied to some of the subtriggers. They are given in table 7.1.

The inefficiency due to the RZ-veto, the PToF and the CiPB-noSPCL veto are significant. However, the subtriggers which make use of them are always supported by ST67 (see also chapter 8) which does not have this veto condition. Due to the variations of the efficiencies throughout the years and the large number of subtriggers involved, each having different conditions, it is very difficult to determine a global correction factor. Since the inefficiency of the conditions is either very small or only

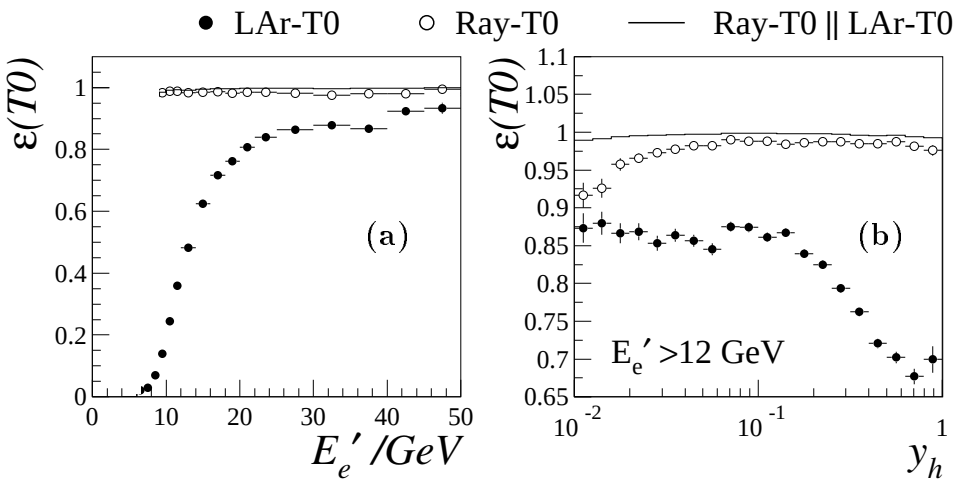

Figure 7.4: *The trigger efficiency for the LAr-T0 TE (closed circles), the Ray-T0 (open circles) and the combination of the two trigger elements (histogram) are shown versus E_e' and y_h.*

		inefficiency (%)			
veto	ST	1994	1995	1996	1997
veto-wall	ST67, ST66, ST71	0.10 ± 0.04	0.04 ± 0.03	0.07 ± 0.02	0.07 ± 0.01
RZ-veto	ST75, ST77	-	0.61 ± 0.10	2.03 ± 0.11	3.41 ± 0.08
PToF	ST71	-	-	-	2.00 ± 0.06
CiPB-noSPCL	ST71	-	-	-	1.10 ± 0.05
SPACAL-AToF	ST71, ST66	-	-	-	0.03 ± 0.01

Table 7.1: *Table of inefficiencies due to the global veto conditions for 1994-1997. Given are the conditions for the CC subtriggers ST77, ST66 and ST71 and the NC subtriggers ST67 and ST75.*

applied to some of the subtriggers, it is justified to neglect the inefficiency at the present stage of precision. However, a systematic uncertainty of 0.5% is assigned to the trigger efficiency in the NC analysis to cover these effects. In the CC analysis they are taken into account by the method used to determine the efficiency (see section 8.2).

7.3 Electron Identification

The electron identification is based on the expected behaviour of a high energy electron in the H1 detector, namely an isolated and compact electromagnetic shower in the LAr calorimeter with high transverse momentum. For this analysis the electron finder QECFWD [80] is used. Electron candidates are identified using information

estimator	description	cut value
ETOT	total cluster energy	> 5 GeV
EAEM	energy fraction in first 2 (3 in IF) layers of em section	$> 0.94 + 0.05\cos(2\theta)$
EAHN	(ETOT-EAEM)/EAEM	$> 0.4(0.8)$ in fwd (bwd) region
EATR	transverse dispersion	$< 3(7.5)$ in fwd (bwd) region
NCEL	number of cells assigned to electron candidate	> 3
EAIF	energy fraction in isolation cone (R=0.25) carried by electron candidate	ETOT/EAIF > 0.98
EAHD	had. energy in isolation cone	EAHD ≤ 300 MeV and ETOT/EAIF > 0.95

Table 7.2: *Table of the cluster estimators, the description of the parameters and the cut values which are used by QECFWD.*

provided by estimators which are related to the shape and size of the electromagnetic shower profile.

The electron shower envelope is defined by a cone of 7.5^o around the centre of gravity of any calorimeter cluster having the tip at the position of the interaction vertex. A new cluster is defined from all cells in the electromagnetic and first layer of the hadronic section in this cone. The parameters NCEL, EAEM, EAHN and EATR (see table 7.2) are used to ensure that the cluster is compact. Energies in all cells within a cone of $R = \sqrt{(\eta_{clus} - \eta_{cell}) + (\phi_{clus} - \phi_{cell})} = 0.25$ around the candidate cluster are summed up to define the variables EAHD and EAIF which are used for testing the isolation of the candidate. The cut details are given in table 7.2. If more than one electron candidate exists in an event the scattered electron is taken to be the cluster with the highest transverse momentum. In less than 0.2% of the simulated NC events a hadronic final state particle is misidentified as the scattered electron.

It is important to check whether the efficiency for finding electrons in the data is well modelled by the simulation. Since the electron finding algorithm is mainly based on the shower shape, its efficiency must be examined by an electron finder which is independent of the shower profile. For this purpose the electron finding algorithm ELJET was developed. It finds electrons by selecting jets using a cone jet finder (QJCONE [77]) with a cone size $R = 0.5$. A jet is identified as the electron if there is exactly one track in the event fulfilling

$$|\phi_e^{jet} - \phi_e^{track}| < 90^o \text{ and } |\eta_e^{jet} - \eta_e^{track}| < 1$$

where ϕ_e^{jet} (ϕ_e^{track}) and η_e^{jet} (η_e^{track}) are the azimuthal angle and the pseudo-rapidity of the jet (track closest to the jet). Events where two or more jets satisfy this requirement are rejected. Further selection criteria are applied to suppress background: $E_e^{jet} > 10$ GeV, $P_{t,e}^{track} > 5$ GeV, $E - p_z > 40$ GeV and $P_{t,e}^{track}/P_{t,e}^{jet} > 0.4$

for $\theta_e^{jet} < 40^o$ [4] The background contamination after these cuts is $\lesssim 0.5\%$. The ELJET electron observables which are used henceforth are: $E_{EJ} = E_e^{jet}$, $\theta_{EJ} = \theta_e^{track}$ and $\phi_{EJ} = \phi_e^{track}$. All other observables, e.g. y_{EJ} or Z_{EJ}, are calculated as for the QECFWD electron. The efficiency of the QECFWD electron finder is then defined as

$$\epsilon_{\mathrm{QECFWD}} = \frac{\text{Number of events found by QECFWD and ELJET}}{\text{Number of events found by ELJET}}.$$

The QESCAT electron finding efficiency for data and Monte Carlo simulation is shown in figure 7.5 as a function of the the impact position Z_{EJ}, ϕ_{wheel}^{EJ} (see section 5.2) and the inelasticity y_{EJ} of the electron. It is generally very high $> 99\%$ but shows some less efficient regions in the very backward region $Z_{EJ} < -190$ cm, in the crack between CB2 and CB3 ($Z_{EJ} \approx 20$ cm) and in the phi cracks $\phi_{wheel}^{EJ} = 0 \pm 2^o$.

These inefficiencies occur since in these regions the electron can pass the electromagnetic section without interacting and directly enter the hadronic section. It is therefore not recognised as an electromagnetic shower by QECFWD. The inefficiencies are reproduced by the simulation in most of the range to better than 2% but deviations of up to 5% are seen. According to the simulation the inefficiency in these crack areas depends also on the energy of the electron but the statistics of the data sample are not sufficient to study the energy dependence in these areas. Due to the large inefficiencies and the rather imprecise $E_e^{'}$ measurement (see section 6.1) the regions indicated by the dotted lines in figure 7.5 are removed from the analysis.

The electron finding efficiency is also shown in figure 7.5(c) as function of y_{EJ}, corresponding to y_e for NC events, after cutting the cracks as described above. At high values of y_{EJ}, corresponding to low electron energies, an apparent decrease is observed due to the contribution of photoproduction background in the ELJET selected monitoring events (see section 7.5) as indicated by the difference between the dashed and full lines. There is also a slight disagreement between data and simulation. This difference is taken into account in the systematic error, indicated in figure 7.5(c), which is conservatively quoted to be 2% (4%) at $y < 0.5$ ($y > 0.5$). Further studies of the estimators used by the algorithm show no indication of significant discrepancies between data and simulation. In addition the same analysis was performed using a further electron finder [81] and the cross sections of these two analysis are found to be in good agreement (see chapter 10).

7.4 Vertex and Track link requirement

A primary interaction vertex is required for NC events. This requirement reduces non-ep-collision background substantially and enables a more precise measurement of the event kinematics. At large polar angles $\theta_e > 35^o$ a track linked to the electromagnetic cluster is required to reduce the contamination to the NC sample due to misidentified photons and hadrons from background processes. At small polar

[4] E_e^{jet}, θ_e^{jet} and $P_{t,e}^{jet} = E_e^{jet}\sin(\theta_e^{jet})$ are the energy, the polar angle and the transverse momentum of the jet. $P_{t,e}^{track}$ is the transverse momentum of the track closest to the jet.

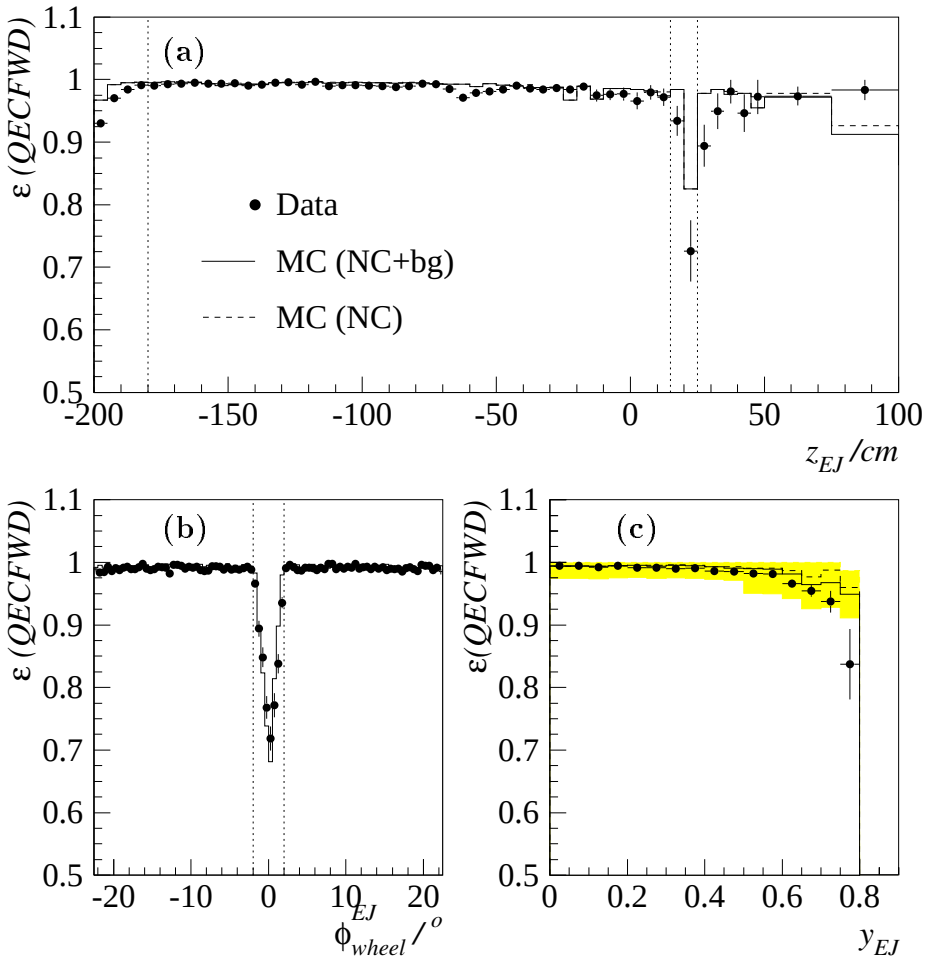

Figure 7.5: *The efficiency of the electron finder QECFWD (a) versus the Z_{EJ} position, (b) versus the ϕ_{wheel}^{EJ} position within the calorimeter octants and (c) versus y_{EJ} for data (full points) and MC (solid histogram). Shown is also the expectation from NC MC alone (dashed histogram). In figure a) the cut $\phi_{wheel}^{EJ} = 0 \pm 2^o$, in figure b) the cuts $Z_{EJ} > -180$ cm and $15 < Z_{EJ} < 25$ cm, and in figure c) all these cuts are applied. These cuts are indicated in a) and b) by dotted lines. The grey band in figure (c) indicates the quoted systematic uncertainty on the electron finding efficiency (see text).*

angles $\theta_e > 35^o$ where the acceptance of the central tracker is limited no track link is not required.

The track and vertex requirements are closely related since the track segments ("DTNV tracks") are constrained to originate from a vertex ("DTRA tracks") during the vertex fitting procedure (see section 5.1). For this analysis the following efficiencies are important:

- the efficiency of finding an interaction vertex in the acceptance region of the central jet chamber $\epsilon_{\rm CVX}$,

- the efficiency of finding an interaction vertex in the acceptance region of the central or forward jet chamber ϵ_{VX} ,
- the efficiency of finding a track linked to the vertex (DTRA-track) and linked to the electromagnetic cluster ϵ_{DTRA},
- the efficiency of finding any track segment linked (DTRA or DTNV) to the electromagnetic cluster $\epsilon_{\mathrm{track}}$.

These efficiencies are determined using a clean NC event sample which is selected applying all selection cuts apart from the vertex and track requirements. Instead the events are required to be well balanced in longitudinal ($45 < E - p_z < 65$ GeV) and transverse momentum ($0.6 < P_{T,h}/P_{T,e} < 1.2$) to suppress non-ep-collision and γp background [5]. Background from QED-Compton events is rejected by removing events with two electron candidates. Additional cosmic finders, which are otherwise only used in the charged current analysis (see section 8.4), are applied to further suppress non-ep-background. The same cuts are applied to the Monte Carlo event sample. This sample will be referred to as "clean NC sample".

Vertex Reconstruction

The vertex finding efficiency is presented in figure 7.6. It can be seen that a central vertex is reconstructed for all events except at low $y \lesssim 0.1$ where the efficiency falls slightly. In this region the hadronic final state is scattered forward and the only charged track leading to a central reconstructed vertex is that of the scattered electron. This inefficiency at low y is recovered when vertices reconstructed using the FTD are also included as can be seen in figure 7.6 b.

Figure 7.7 shows an example of an NC event at low $y_h = 0.024$ where no central vertex is reconstructed. In this event the hadronic final state is scattered forward so that all tracks originating from the hadronic final state are detected in the FTD. These track segments are fitted to the interaction vertex thereby providing a "forward vertex". In this event it also happens that a track segment which points to the electron cluster in the central tracking detector is not fitted to the vertex; therefore no central vertex exists.

The Z_{vtx} distribution is shown for data and Monte Carlo events in figure 7.8. A shift in the mean value is seen between data and simulation, the distribution is also broader for the data than the simulation. A good agreement between data and simulation is achieved by reweighting the MC event vertex distribution to the distribution observed in the data for each year individually. After this reweight the distributions agree between the data and the simulation in mean value, width and in the tails of the vertex distribution as can be seen from figure 7.8. A cut of ± 35 cm around the nominal position of $Z_{vtx}^{nom} = -1$ cm is applied. Outside this range the control of this distribution becomes difficult, due to the contribution of

[5] For events without a primary vertex the vertex position is set to the nominal position $Z_{vtx} = 0$ for the calculation of the angles of the electron and the hadronic final state particles

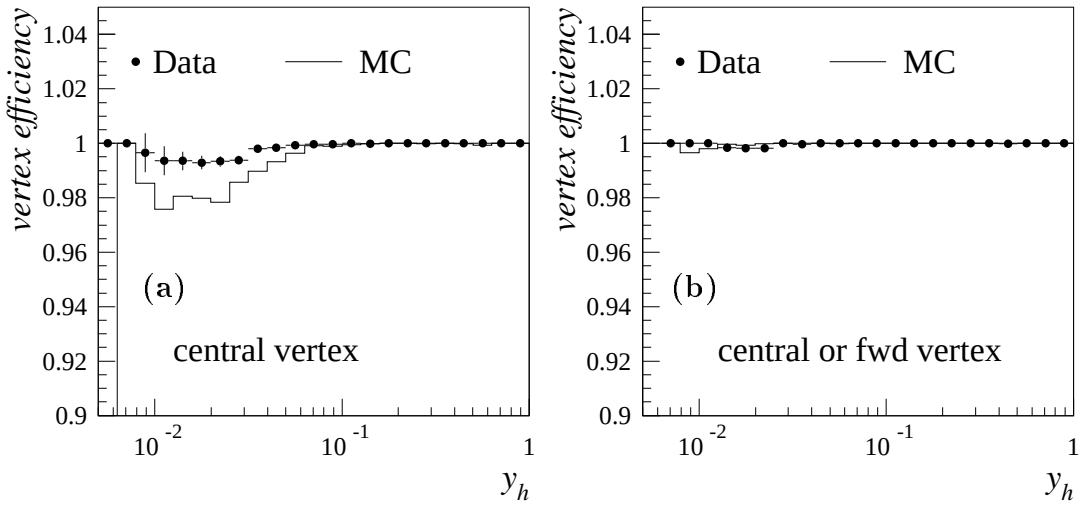

Figure 7.6: *Vertex finding efficiency versus y_h for neutral current events in data (closed circles) and MC (histogram) for (a) the central tracker alone and (b) the forward or central tracker.*

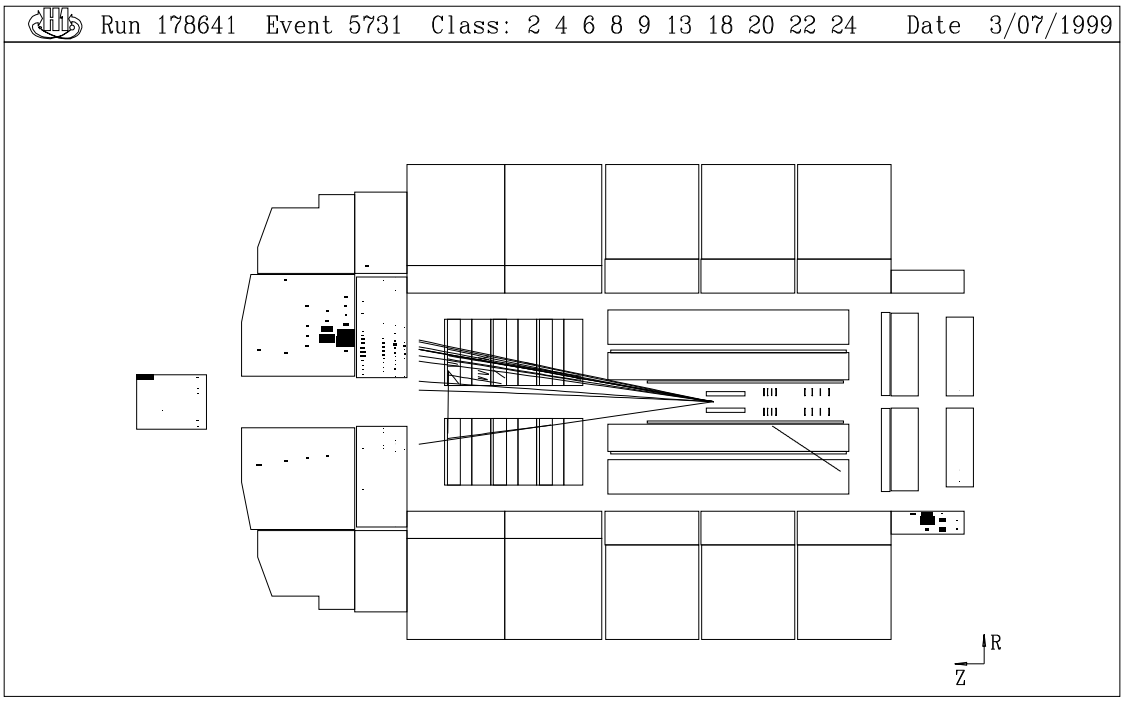

Figure 7.7: *Display of a NC DIS event at low $y_h = 0.024$ where no central vertex but a forward vertex was reconstructed. Shown are the vertex fitted tracks and the non-vertex fitted tracks. The vertex position is determined by tracks in the FTD, the electron track is not fitted to the event vertex.*

satellite bunches (see section 2.1) which cause large tails that are not modelled by the simulation.

A good description of the tails of the vertex distribution is particularly important because of the fiducial cut $Z_e > -180$ cm, since the value of Z_e depends on the vertex position (see eq. 5.6). If there are too few MC events at high values of Z_{vtx} for fixed θ_e that satisfy the Z_e cut, this reflects in a undershoot of the simulation at large polar angles θ_e (see figure 7.8(c)) and, correspondingly, at low Q^2.

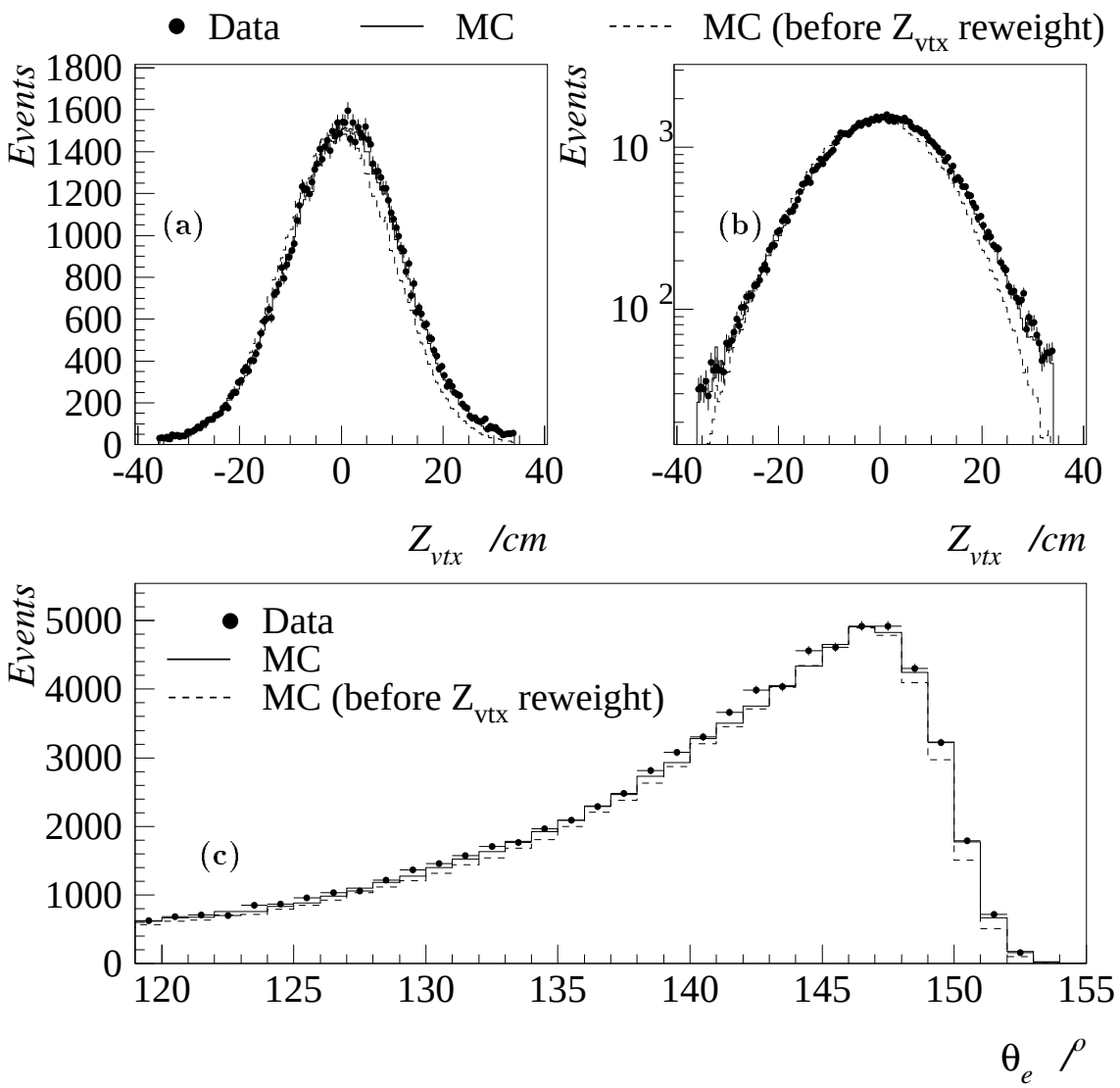

Figure 7.8: *The z-vertex distribution for data (filled circles) and MC (dashed line) and MC after reweighting the events according to the vertex distribution observed in data (solid line). It is shown on a linear (a) and logarithmic (b) scale. Figure (c) shows the polar angle distribution of the electron θ_e. The simulation is normalised to the data luminosity.*

Electron Track Reconstruction

Background from photoproduction and non-ep collision processes is reduced by the requirement of a track linked to the electron cluster. The variable DCA (distance of closest approach) quantifies the proximity of a track to the electron cluster. The

DCA of the nearest vertex-fitted (DTRA) track to the electron cluster is shown in figure 7.9(a) for the DIS and photoproduction background simulation. The distribution is peaked at low values for DIS events and flat for the background MC, thereby showing that a cut on this variable reduces the background efficiently. Figure 7.9(b) shows the same distribution for data and simulation. Two different data samples are shown: events where CIZ and COZ hits are assigned to the electron track and events where no Z-chamber hits are assigned. The distribution is well described by the simulation for events with Z-chamber hits, but there is a significant tail for events without Z-chamber hits assigned to the track due to the inferior θ-resolution of the CJC (see section 5.3).

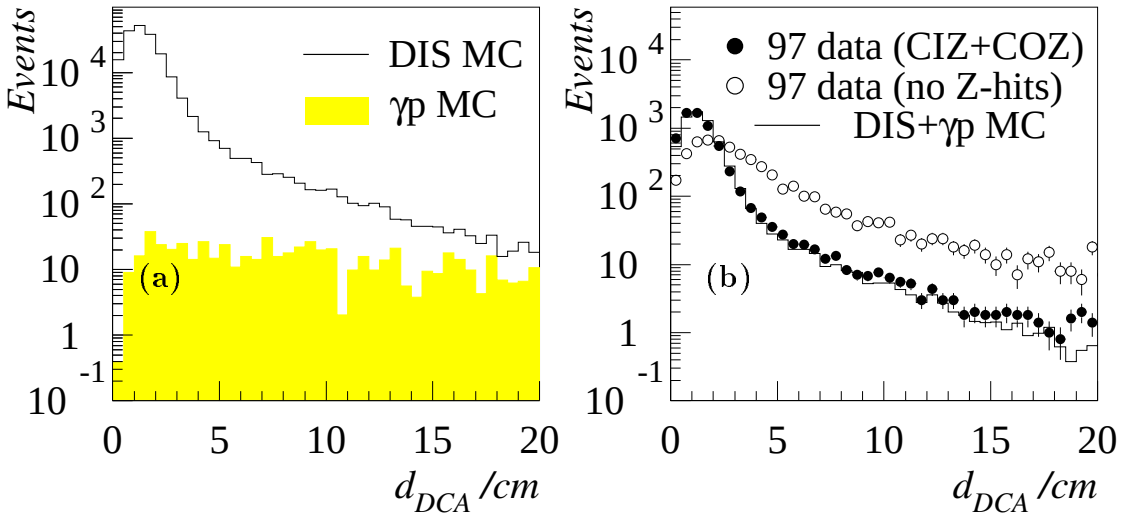

Figure 7.9: *(a) The distance of closest approach between the electron track and LAr cluster for DIS MC events with (histogram) and photoproduction MC events (grey histogram). (b) The distance of closest approach between the electron track and LAr cluster for 1997 data with (full points) and without Z-chamber hits (open points) and for MC events. The simulation (histogram) is normalised to the number of data events with hits in both Z-chambers (full points).*

To maintain a high selection efficiency a rather loose cut value of $DCA < 12$ cm was chosen. The efficiency of this cut is examined in the following. This study is based on the "clean NC sample" that was also used for the determination of the vertex efficiency with the additional requirement of the existence a central or forward vertex.

The efficiency of the requirement of a DTRA-track linked to the electron cluster is shown versus the polar angle in figure 7.10(a) for data and simulation. The average efficiency is $95.96 \pm 0.08\%$ for data and 98.12% for the simulation. Figure 7.10(b) shows the fraction of events where only a DTNV-track is linked to the cluster, it is significantly higher in the data than the simulation. An example of an event leading to the larger fraction of events with DTNV track links is shown in figure 7.7. The simulation is corrected for this difference by ignoring the DTRA track information for $\delta_{DTRA} = 2.16\%$ of the events. The comparison of the data and the

simulation after this correction shows that there is then good agreement between the two samples independent of the polar and azimuthal angles.

The efficiency of the track requirement is increased by also allowing for DTNV tracks: the efficiency of either a DTRA or a DTNV track linked to the electron cluster is $99.67 \pm 0.02\%$ for data and 99.93% for the simulation. The remaining small difference of $\delta_{DTNV} = 0.26\%$ is applied as a correction to the simulation. The efficiency in data and simulation are then also found to be in good agreement as function of the electron energy (see figure 7.11(a)). Figure 7.11(b) shows the electron energy spectrum for the 0.33% of all events without any track linked within 12 cm. It is well described by the DIS Monte Carlo simulation. Therefore the remaining inefficiency originates from DIS events and is not introduced by background events.

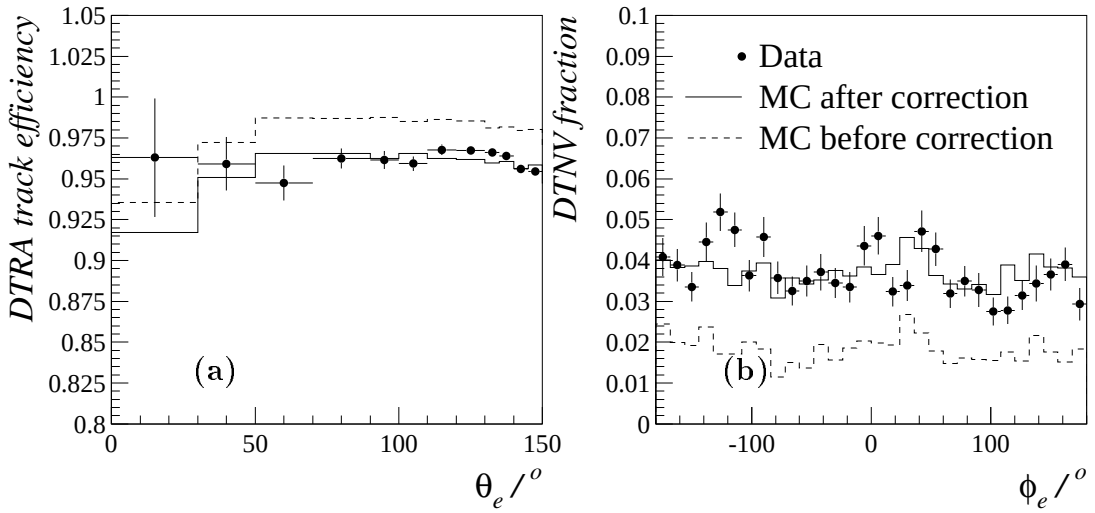

Figure 7.10: *(a) Efficiency of the requirement of a link of a DTRA track to the electron cluster versus the polar angle for data (full circles) and MC before (dashed line) and after (full line) the corrections δ_{DTRA} and δ_{DTNV}. (b) Fraction of events with DTNV track link for data (full circles) and MC before (dashed line) and after (full line) the corrections δ_{DTRA} and δ_{DTNV}.*

In case there is only a DTNV track, the polar angle is determined from the electron cluster ($\theta_e = \theta_{e,LAr}$) measurement which has a better precision than the CJC θ measurement (see 5.3). In figure 7.10 it is seen that the efficiency of the track link requirement is $\approx 6\%$ lower than the average efficiency for $\theta < 30^o$ according to the simulation. To maintain the highest possible efficiency for events at very high Q^2 the track link requirement is not enforced for electrons in the very forward region: $\theta_e < 35^o$. At these low angles the electron passes through the end-wall of the CJC into the FTD. This large amount of inactive material may cause a showering of the electron which can distort the track angle measurements. Therefore for $\theta_e < 35^o$ the LAC angular measurements are used for the cross section measurement even if there is a track linked to the electron cluster.

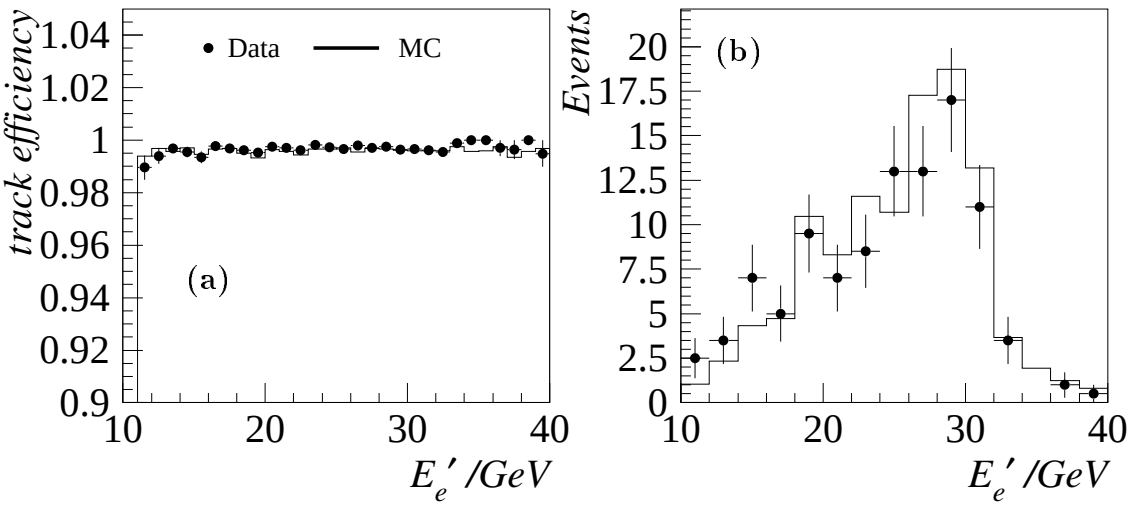

Figure 7.11: *(a) Efficiency of the track link requirement versus the electron energy for the data (full points) and MC (histogram) event sample. (b) Electron energy spectrum for events where no track is linked to the calorimeter cluster for data (full points) and MC (histogram) events.*

7.5 Background Rejection

Two distinct kinds of background can contribute to the NC event sample. Non-ep-collision background originating from cosmic rays or beam-halo muons and ep-collision background.

Non-ep-induced background:

Muons from cosmic rays or the beam-halo can interact in the calorimeter and cause electromagnetic showers which may be misidentified as a electron. This background is already reduced to a small level by the interaction vertex and track link requirements. It can further be separated from ep events on the basis of the timing information given by the central jet chamber. The event timing is determined from the drift times in the CJC. Events which are not within ± 20 ns of a bunch crossing are rejected. The inefficiency of this cut is studied using the "clean NC sample", as defined in section 7.4, it amounts to $0.26 \pm 0.02\%$ independent of the kinematics of the event. In addition a subset of the background finders used in the CC analysis (see section 8.4) is applied when the event is either not well balanced in transverse momentum ($P_{T,h}/P_{T,e} < 0.1$) or has only a DTNV track linked and a small value of $\eta_{max} < 3$ [6]. Events which are tagged by one of the finders and fulfil one of these requirements are rejected. The inefficiency of these cuts is negligible.

To estimate the remaining non-ep background contribution, the number of events

[6] η_{max} is the maximum value of the pseudo-rapidity $\eta = \ln(\tan(\theta/2))$ of any cluster with an energy > 400 MeV.

which fail the timing cut, but pass the NC selection otherwise, is scanned visually. These are in total 182 events, 143 of which are NC events. The other 39 events are background events: 28 cosmic ray, 9 halo muon and 2 beam-gas events. 34 out of these 39 events are rejected by the background "finders", the remaining 5 events are only rejected by the CJC-T_0 cut. When assuming that this background is uncorrelated with the bunch crossing time, the expected number of non-ep-background events is $5 \cdot \frac{20 \text{ ns}}{96 \text{ ns}} = 1.04 \pm 0.47$ events. This is negligible compared to the size of the data sample of 85,000 events. However, all events with $Q^2 > 5000$ GeV^2 were scanned and no non-ep-background event was found.

ep-induced background:

The sources of ep-background which can contribute to the NC sample are photoproduction, low Q^2 DIS, QED-Compton scattering (QEDC), $\gamma\gamma$ events and the production of heavy bosons $W^{\pm}, Z$. These processes are explained in section 3.1.

Photoproduction and low Q^2 DIS Background: The main background arises from photoproduction events where the scattered electron is not detected in the main detector and a final state particle is misidentified as an electron. It is efficiently reduced by the track link requirement (see figure 7.9(a)). A further reduction is achieved by restricting the measurement to $y_e < 0.9$ as can be seen in figure 7.12 in which the y_e distribution is shown for NC and γp simulation for $Q^2 > 1000$ GeV^2. For $y_e > 0.9$ the contamination from γp background is large and is therefore cut in this analysis. At lower Q^2 values $y_e > 0.9$ is kinematically forbidden due to the cut $E_e' > 11$ GeV.

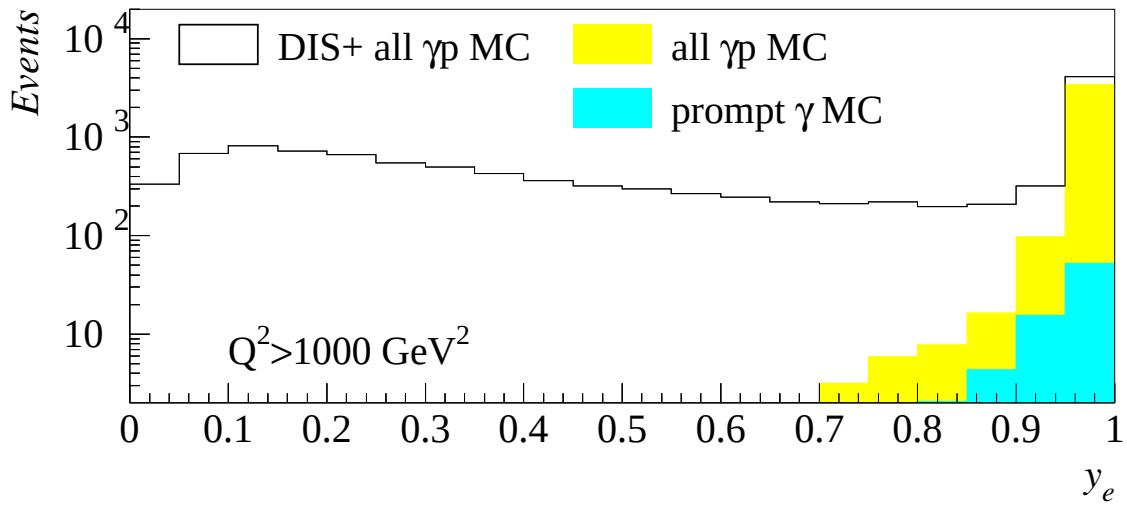

Figure 7.12: *simulated y-distribution for DIS and background MC (line), and only the photoproduction background processes. The contribution of prompt γ events is shown separately.*

The contamination of background to the NC sample is studied with events where the scattered electron is detected in the electron tagger of the luminosity system. The acceptance of the electron tagger is restricted to $0.3 \lesssim y \lesssim 0.7$; a subset of about 10% of all photoproduction events is measured in the electron tagger. To suppress accidental overlap of DIS events with Bethe-Heitler events the energy in the photon tagger is required to be < 2 GeV. The energy in the electron tagger must be $E_{tag} > 5$ GeV. Figure 7.13(a) shows the $(E-p_z)_{all} = E-p_z+2\cdot E_{tag}$ distribution of the selected events. The peak at 55 GeV corresponds to photoproduction events while the events at high values of $(E-p_z)_{all}$ are overlap events of DIS and Bethe-Heitler-events. The data are compared to the γp Monte Carlo simulation which is corrected for the y acceptance of the electron tagger by averaging over different beam positions on a run dependent basis. The data are well described by the simulation for $(E-p_z)_{all} \lesssim 60$ GeV. After selecting events with $(E-p_z)_{all} < 60$ GeV, the energy spectrum of the electron candidate in the LAr calorimeter is shown in figure 7.13(b). The contamination from γp-background is well modelled by the simulation of photoproduction events even at lower energies than the analysis cut of 11 GeV. It is also seen that the total number of γp events is very small in this sample.

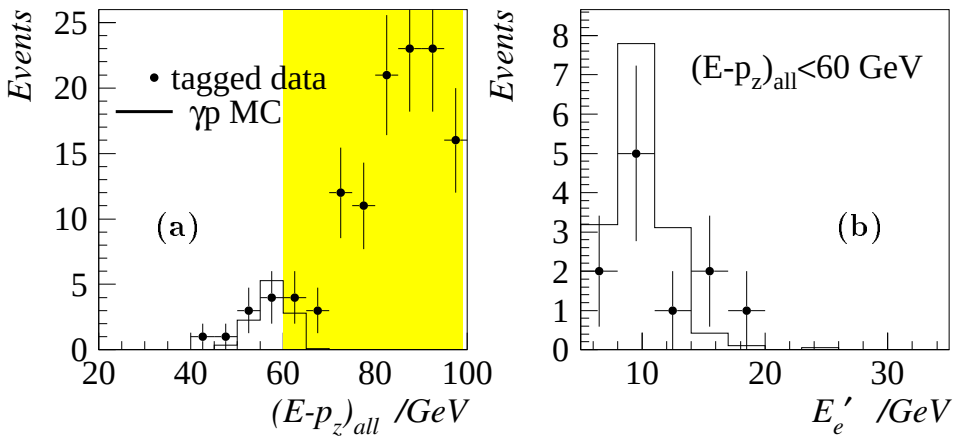

Figure 7.13: *(a) $(E-p_z)_{all}$ distribution (including the energy measured in the electron tagger) for events with energy measured in the electron tagger for data (full points) and γp simulation (histogram). (b) Electron energy spectrum for events with energy measured in the electron tagger and $(E-p_z)_{all} < 65$ GeV for data (full points) and simulation (histogram).*

The background from low Q^2 DIS events in which the electron is scattered into the SPACAL is expected to be much smaller than that from γp events due to the $1/Q^4$ dependence of the cross section. However, it can not be suppressed as efficient by the cut on $E-p_z$ such that the contribution is as large as from photoproduction events according to the simulation.

An additional cross check was performed by exploiting the fact that γp and low Q^2 DIS background events are expected to be induced by pions which can have posi-

tive or negative charge while in the high Q^2 NC events the charge is expected to be positive for positrons. At low energies $E_e^{'} < 20$ GeV there are 549 events with tracks of negative charge observed in data while 540.6 are expected from the simulation. The majority of the expectation is due to photoproduction (403.3 events); the remaining events are arise from DIS NC where the charge is wrongly determined. This good agreement between the data and the simulation gives confidence that the normalisation of the background is correct. An uncertainty of 30% is quoted for its normalisation.

Elastic QED-Compton and $\gamma\gamma$ Events: Elastic QED-Compton and $\gamma\gamma$ events can have an electron in the LAr calorimeter and may therefore pass the selection criteria described above. They are removed on the basis of their characteristic signature: they have one or two reconstructed tracks, no activity in the hadronic section of the LAC ($E_{had}/E_{tot} < 10\%$) and no energy deposits in the remnant fragmentation region ($\eta_{max} < 3$) The distributions E_{had}/E_{tot} is shown in figure 7.14(a) for these two background processes and DIS events for events with only one or two tracks. For elastic processes the energy in the hadronic section is very small, while in DIS most events have a large amount of energy in the hadronic section. For events with $E_{had}/E_{tot} < 10\%$ the η_{max} distribution is shown in figure 7.14(b). While in DIS events there is usually an energy deposit close to the beam-pipe hole ($\eta_{max} > 3$), the QEDC and $\gamma\gamma$ have a large tail towards low values. The background contamination is reduced significantly when applying the cuts indicated in figure 7.14.

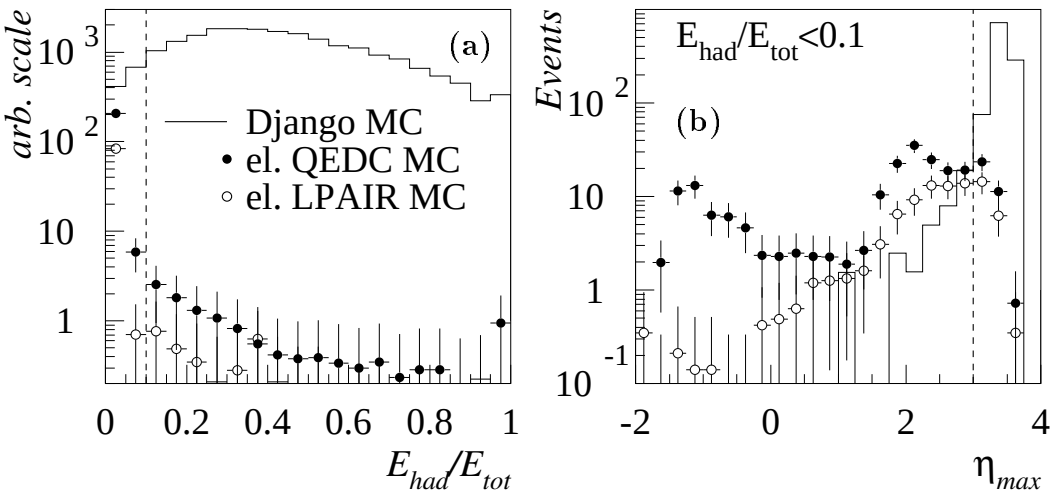

Figure 7.14: *(a) Fraction of energy in the hadronic section over total energy E_{had}/E_{tot} for DIS (histogram) events and elastic QED Compton (full points) and $\gamma\gamma$ events (open points) with only one or two tracks. (b) the η_{max} distribution for the same event samples with the additional cut $E_{had}/E_{tot} < 10\%$. The cuts are indicated by the dashed lines.*

The decay lepton in events, where a heavy gauge boson is produced, can be misidenti-

fied as the scattered electron and are therefore also considered as background source. Since this contribution is very small no additional cuts are applied to reject these events.

The overall background contribution, expected from the simulation, is subtracted bin by bin from the observed number of data events. It is overall $\approx 1\%$ and smaller than 5% in any x-Q^2 bin.

7.6 The Final Neutral Current Data Sample

In summary 85,000 neutral current events are selected using the following selection criteria:

- run selection;
- triggered by subtrigger ST67 or ST75;
- CJC-T0 timing;
- $E_e^{'} > 11$ GeV;
- $E - p_z > 35$ GeV;
- $y_e < 0.9$;
- interaction vertex with $-36 < Z_{vtx} < 34$ cm;
- $Z_e > -180$ cm and $Z_e \notin [15, 25]$ cm;
- $\phi_{wheel} \notin [-2^o, 2^o]$;
- $DCA < 12$ cm for DTRA or DTNV track;
- cuts against elastic QEDC and $\gamma\gamma$ events.

The NC sample is presented in figure 7.15. Shown is the angular distribution of the scattered electron which falls rapidly towards small angles. Also shown are the electron energy spectra at low and high Q^2. All distributions are well described by the simulation in both shape and normalisation. As a result of the precise calibration procedure the electron energy spectrum at low Q^2 is particularly well described in the kinematic peak region ($E_e^{'} \approx E_e$).

In figure 7.16 control distributions for the measurement of the hadronic final state energies are presented. The fractional contributions to y_h shown in 7.16 (a) and the y_h/y_e distribution shown in 7.16 (b) are well described by the simulation. The $P_{T,h}/P_{T,e}$ distribution is also well reproduced by the simulation at low and high values of $P_{T,e}$.

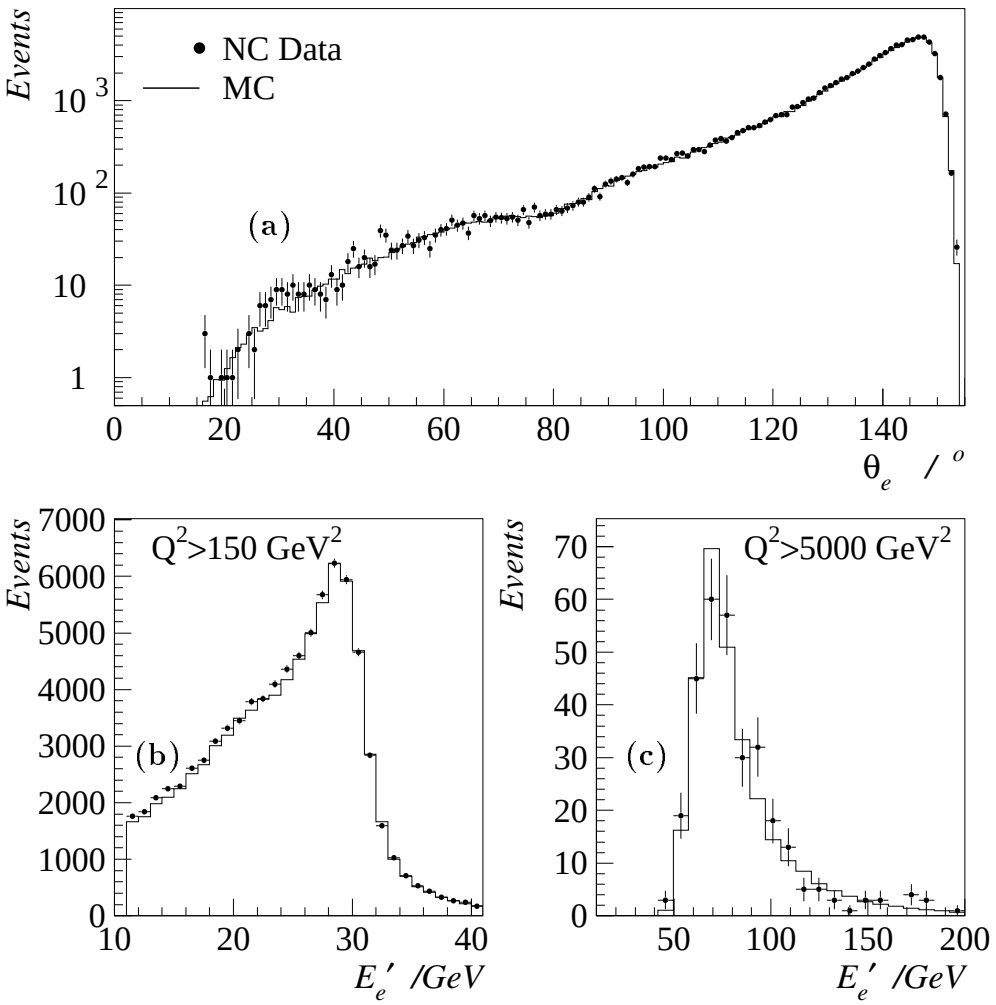

Figure 7.15: *(a) Distribution of the polar angle of the scattered electron for data (full points) and simulation (histogram). The distribution of E_e' for the NC sample is shown in (b) for $Q^2 > 150\ GeV^2$ and (c) for $Q^2 > 5000\ GeV^2$.*

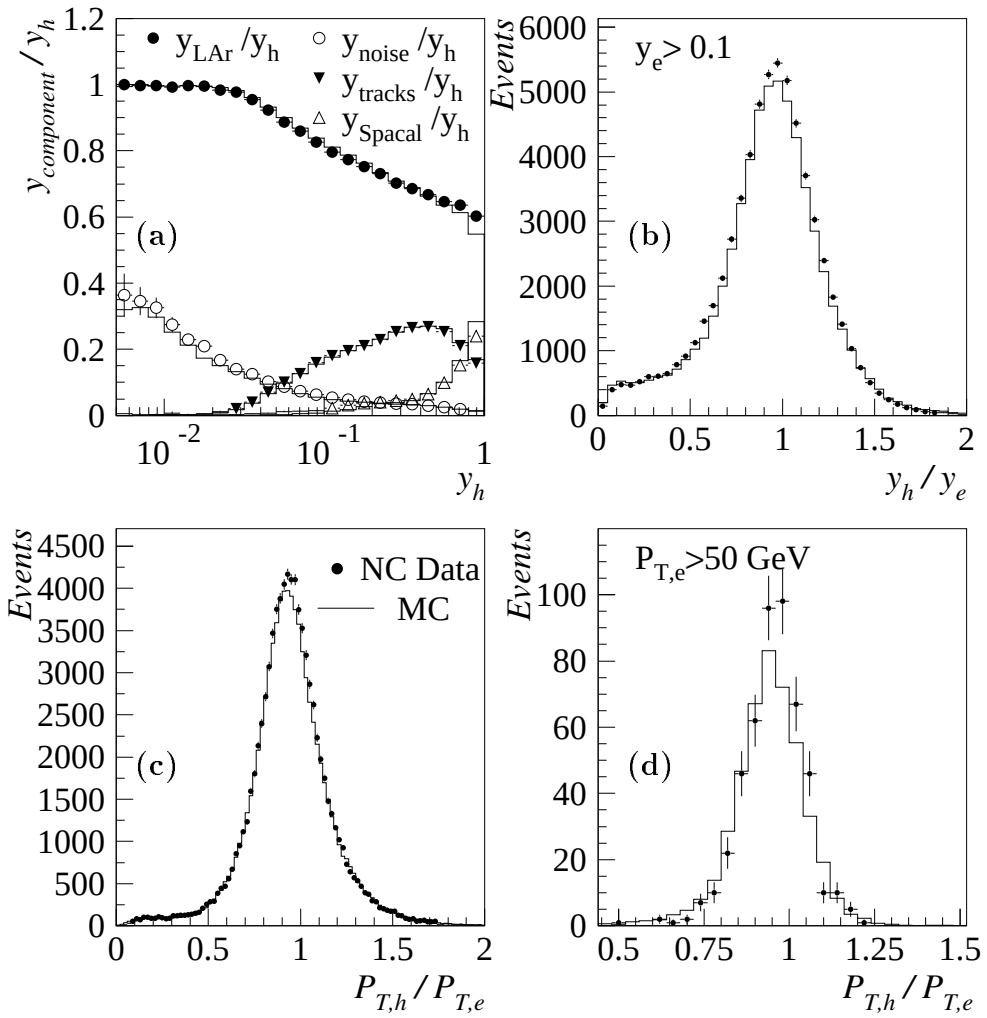

Figure 7.16: *(a) Distribution of the fraction of y_h contributed by the tracks (y_{tracks}), the LAr (y_{LAr}), and the SPACAL calormimeters (y_{Spacal}), and the fractional contribution of the subtracted noise (y_{noise}). (b) Distributuion of y_h/y_e for $y_e > 0.1$. (c) Distributuion of $P_{T,h}/P_{T,e}$ for the complete NC sample, (d) for the subsample at $P_{T,e} > 50$ GeV. The data (points) are compared to the simulation (histogram) which is normalised to the integrated data luminosity.*

Chapter 8

Selection of Charged Current Events

The characteristic signature of charged current events is an imbalance in transverse momentum measured in the detector due to the outgoing neutrino which escapes undetected. The selection is therefore based on this imbalance in transverse momentum, called P_T^{miss}. Note that P_T^{miss} and $P_{T,h}$ are identical in CC events.

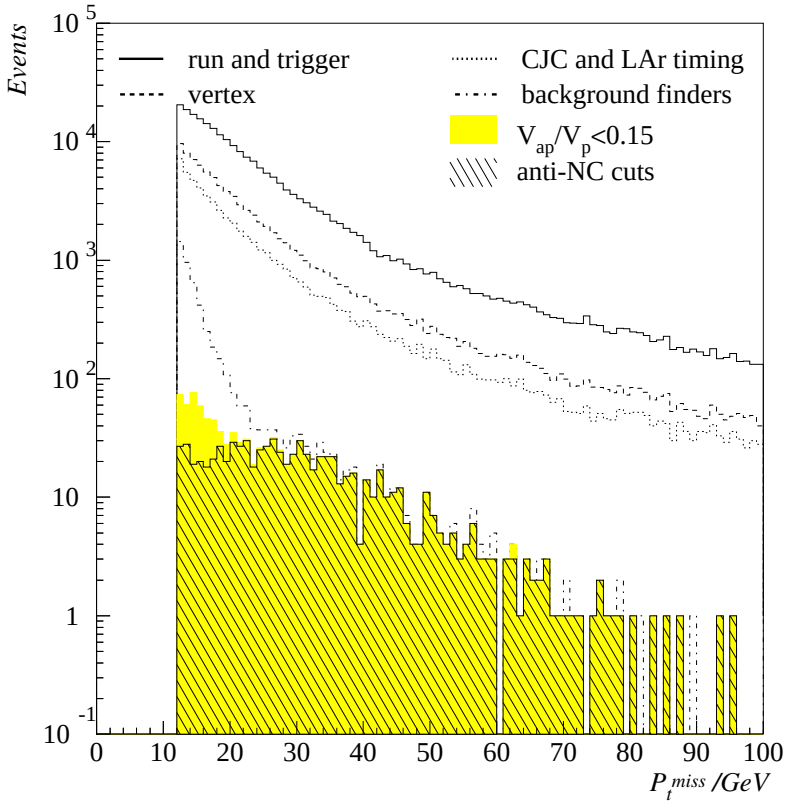

Figure 8.1: *The P_T^{miss} distribution at different stages of the selection: the trigger selection (solid line), the vertex requirement (dashed line), the event timing requirements (dotted line), background "finders" (dashed-dotted line), the photoproduction cut (grey histogram) and after cuts against NC background.*

The run selection for the CC analysis is equivalent to the NC analysis described in section 7.1. Figure 8.1 shows the P_T^{miss} distribution at different stages of the selection. The sample is decreased by more than two orders of magnitude by the selection described in this chapter, namely the trigger selection, the vertex requirement and the background rejection. All efficiencies of the selection cuts are studied using so-called "Pseudo-CC's".

8.1 Efficiency Evaluation using "Pseudo-CCs"

As in the NC analysis it is important that all efficiencies are correctly described by the Monte Carlo simulation. Due to the low number of CC events, these efficiencies cannot be checked with high precision using the CC data sample alone. Therefore the so-called "Pseudo-CC"-technique was developed [83] which makes use of the high statistics NC sample. Pseudo-CC events are constructed from NC events by removing the identified positron from all subdetectors: they are then indistinguishable from CC events. These events are reweighted to the CC cross section, such that the distributions in the kinematic variables for CC scattering are correctly reproduced. The kinematic variables x and Q^2 are obtained from the $e\Sigma$ method. The weight is given by

$$w(x, Q^2) = \frac{\mathrm{d}^2\sigma_{CC}/\mathrm{d}x\mathrm{d}Q^2}{\mathrm{d}^2\sigma_{NC}/\mathrm{d}x\mathrm{d}Q^2}$$

where the NC and CC cross sections $\mathrm{d}^2\sigma_{NC}/\mathrm{d}x\mathrm{d}Q^2$ and $\mathrm{d}^2\sigma_{CC}/\mathrm{d}x\mathrm{d}Q^2$ are calculated using the the parametrisation from the NLO QCD fit described in section 9.5.

The efficiency ϵ of a selection requirement for CC events is determined by

$$\epsilon = \frac{\text{Sum of all weights of Pseudo-CC events fulfilling requirement}}{\text{Sum of all weights of Pseudo-CC events}}$$

It can be compared to the efficiency determined in the CC simulation.

This method relies on the assumption that the hadronic final state in CC and NC interactions is very similar. This is verified by studies of the hadronic final state in NC and CC interactions [84].

8.2 The Trigger

The triggering of CC events is based on the LAr-Etmiss trigger element (TE) (see section 2.7.1) in coincidence with timing information from either the proportional chambers (Ray-T0) or the LAr calorimeter (LAr-T0). These trigger elements are combined into the subtriggers ST66 and ST77 for all years 1994-97. At the end of 1996 a new subtrigger ST71 was developed to increase the CC trigger efficiency at low P_T^{miss} and high y. The trigger elements of these three subtriggers are given in table 8.1. In addition to the conditions given in that table there are global vetoes set which are discussed in section 7.2.

subtrigger	trigger elements
ST66	LAr-Etmiss (high) && LAr-IF && (Ray-T0 || LAR-T0)
ST77	LAr-Etmiss (medium) && Ray-T0
ST71	DCrϕ-Tc && LAr-BR (low) && Zvtx-sig1 && DCrϕ-T0 && Ray-T0 && L2:LAr-BigT-miss

Table 8.1: *Table of CC subtriggers and the corresponding trigger elements on L1 and L2. The ST71 conditions are only valid for 1997.*

The trigger efficiency of the LAr-Etmiss TE is shown versus P_T^{miss} and y_h for Pseudo-CC events for 1994-97 data and the simulation in figure 8.2(a). No difference is observed between the four years. The efficiency increases steeply from $\approx 30\%$ at $P_T^{\text{miss}} = 12$ GeV to $> 90\%$ for $P_T^{\text{miss}} \gtrsim 30$ GeV. The data are not described by the simulation where the rise with increasing P_T^{miss} is significantly steeper. Since this crucial trigger element is not described sufficiently well by the simulation, all efficiencies are determined from the Pseudo-CC data and the MC events are weighted accordingly, i.e. the trigger simulation is ignored for this analysis.

The low efficiency at values of $P_T^{\text{miss}} < 25$ GeV is most prominent at low and high values of y_h as can be seen from figure 8.2(b). At low y_h the hadronic final state is scattered forward. The inefficiency occurs therefore mainly because the two Big-Towers at lowest polar angles are not considered for the sum to form the LAr-Etmiss TE (see section 2.7.1). For this reason an analysis cut of $y_h > 0.03$ is made. At high values of y_h and low P_T^{miss} the energy of the hadronic final state is mainly measured by the central barrel of the LAr calorimeter. In this region the noise level is relatively high so that the energy thresholds are correspondingly high (see 2.7.1). This leads to the observed inefficiency at high y_h.

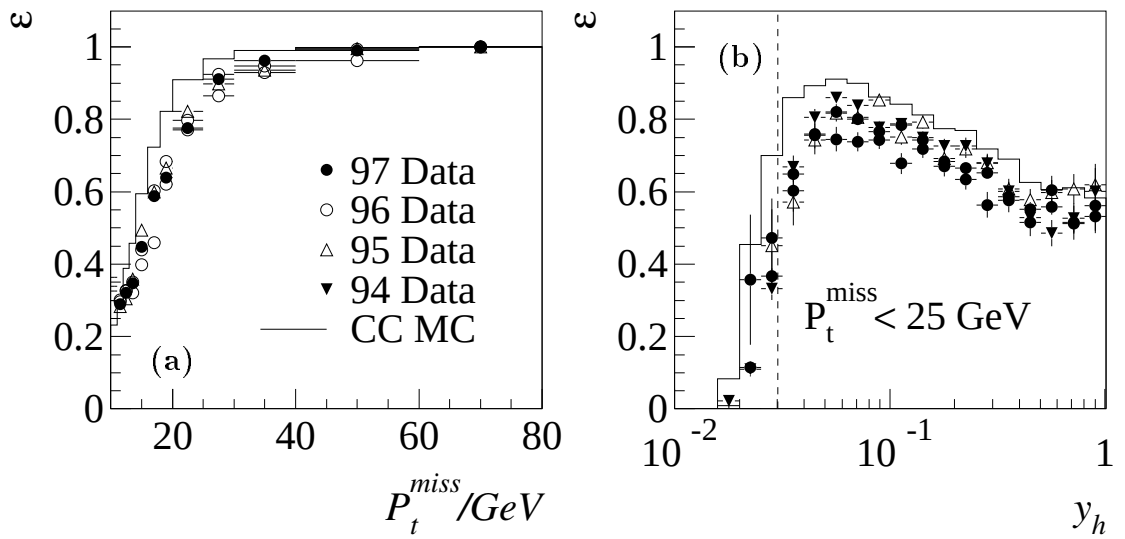

Figure 8.2: *The efficiency of the LAr-Etmiss trigger element versus (a) P_T^{miss} and (b) y_h for CC events determined from Pseudo-CC events. The dashed line in (b) indicates the analysis cut $y > 0.03$.*

The steep fall of the efficiency towards low P_T^{miss} to values of only $\approx 30\%$ introduces a large systematic uncertainty in the cross section measurement and reduces the statistical precision. Therefore a new trigger ST71 was developed at the end of 1996 designed to increase the efficiency at low P_T^{miss} and high y.

trigger element	efficiency (%)
LAr-BigRay	89.95 ± 0.71
DCrϕ-Tc	94.07 ± 0.62
DCrϕ-T0	98.42 ± 0.40
zvtx-sig1	85.41 ± 0.85
Ray-T0	97.27 ± 0.62
L2:LAr-BigT-miss	83.12 ± 0.72

Table 8.2: *Table of trigger elements and their efficiencies for events with $\gamma_h > 25^o$ which compose the subtrigger ST71. The trigger elements are explained in section 2.7.*

The TE conditions of ST71 are given in table 8.2. The L1 conditions are mainly based on the track activity in the CJC and the central proportional chambers. Therefore triggering is only possible in the acceptance region of the central tracking detectors ($\gamma_h \gtrsim 25^o$). These tracking conditions are chosen to suppress the high contribution of noise in the central barrel. Additionally a loose energy requirement of 1 GeV is made by imposing the LAr-BigRay TE. The inefficiency introduced on L1 is mainly due to the LAr-BigRay and zvtx-sig1 conditions. The background triggered on L1 (mainly from beam-gas- and beam-wall-interactions) is reduced by the 2nd trigger level condition. The L2 trigger element is set up to trigger only events with a non-isotropic energy flow in the barrel. An energy of at least 2.5 GeV must be concentrated in one Big-Tower or in two adjacent ones [85] and these Big-Towers must be at polar angles $> 20^o$.

The L1 and L2 trigger rates of ST71 are shown in figure 8.3 versus the luminosity fill number in 1997. The rate of the L1 conditions is stable during the data taking period and is $\approx 20 - 30$ Hz. Due to the L2 condition a rate reduction by about a factor 40 to ≈ 0.5 Hz is achieved. This is at the limit of what is tolerated in H1 for a single subtrigger. A further rate reduction could not be achieved without reducing the efficiency of the subtrigger significantly.

The efficiency of ST71 is shown in figure 8.4 versus the angle γ_h and P_T^{miss}. Also shown is the efficiency of the L1 and L2 conditions alone. In the central region $\gamma_h > 50^o$ the efficiency is $\approx 60\%$, since both the L1 and L2 conditions introduce an inefficiency of $\approx 25\%$. At low P_T^{miss} the remaining efficiency loss is mainly due to the L2 condition.

The improvement due to this new trigger can be judged from figure 8.5 where the efficiency is shown in the cross section measurement bins. At low x and Q^2 the efficiency is increased by 20% due to the looser energy requirements. For $Q^2 \geq 3000$ GeV^2 the trigger efficiency is already very high and it is not improved by the

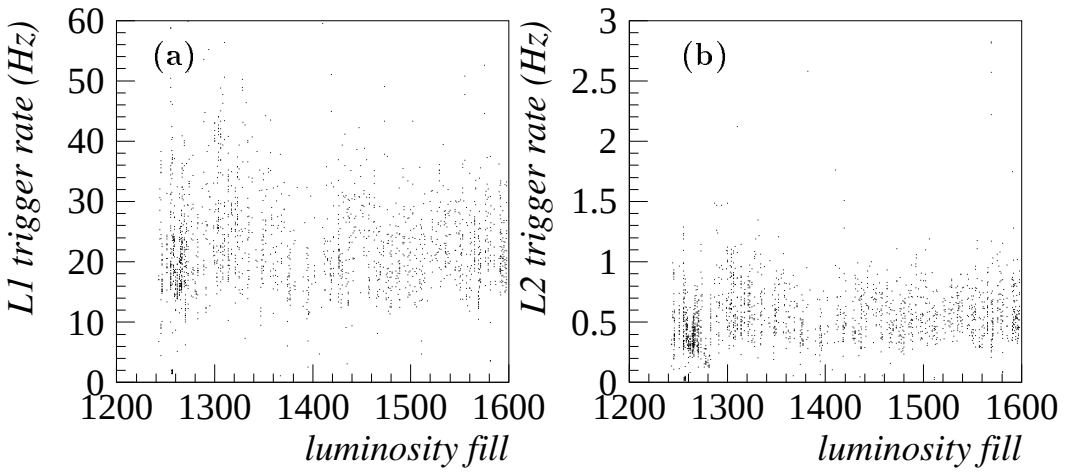

Figure 8.3: *The trigger rate of subtrigger ST71 (a) on the first (L1) and (b) after verification on the second (L2) trigger level versus the luminosity fill number in 1997.*

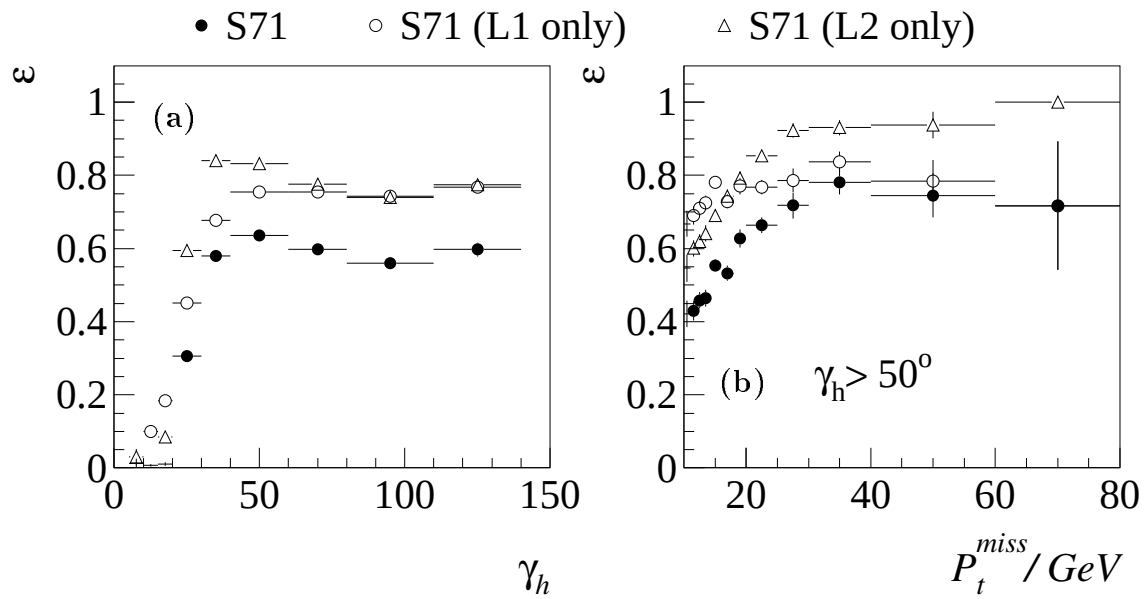

Figure 8.4: *The efficiency of subtrigger ST71 (closed circles) and its L1 (open circles) and L2 (open triangles) condition versus (a) γ_h and (b) $P_T^{\rm miss}$ for $\gamma_h > 50^o$.*

newly developed subtrigger.

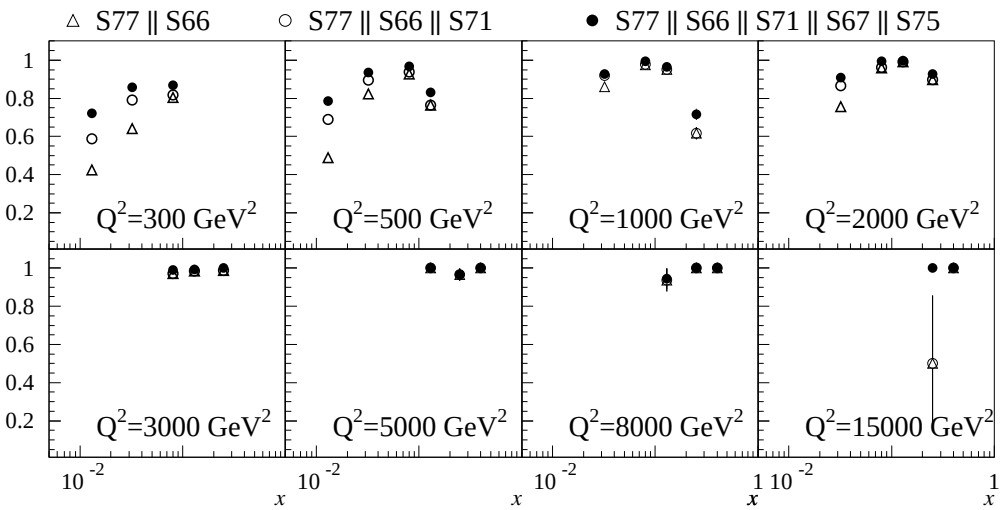

Figure 8.5: *The efficiency of the Subtriggers used for the CC analysis versus x in bins of Q^2. The efficiency is shown for different combination of subtriggers: ST77 OR ST66 (open triangles), ST77 OR ST66 OR ST71 (open triangles), and ST77 OR ST66 OR ST71 OR ST67 OR ST75.*

A further improvement of the CC trigger efficiency is achieved by also selecting events triggered by the NC triggers ST67 and ST75. It increases by $\approx 10\%$ at the lowest x as can also be seen in figure 8.5. An improvement of $\approx 5\%$ is also seen at high x.

This is the optimum which could be achieved with the 1994-97 trigger setup. Since the measurement error is still dominated by the statistical precision it is desirable to improve the trigger further at low and high x where the largest inefficiencies are seen. This may be achieved with the LAr trigger upgrades in the 1997/98 HERA shutdown [86] and the upgrade planned for the year 2000 [87]. In winter 1997/98 new preamplifiers were installed which should reduce the noise in the central barrel. In addition the settings of the LAr trigger thresholds now allow higher flexibility. Presently there are studies ongoing of how to explore the new features of the LAr trigger for triggering CC events in the optimum way. After the luminosity upgrade the granularity of the trigger will be increased so that at the first trigger level jet finding can be performed. This allows simple topological requirements to be made which will in particular improve the trigger efficiency at low y and correspondingly high x as shown in [87].

The efficiency is determined in all measured cross section bins for the full data sample. Due to the availability of ST71 in 1997 it is higher by $\approx 20\%$ for this part of the data sample. The Monte Carlo events are then weighted by this efficiency depending on the cross section bin. A systematic uncertainty on the trigger efficiency is quoted depending on the efficiency in that bin: $\delta_{trig} = (1-\epsilon) \cdot 15\% \oplus 2\%$. This results in an uncertainty of $\approx 8\%$ at the lowest x and Q^2 and 2% at high Q^2.

8.3 The Vertex Requirement

An interaction vertex is required to be found within 35 cm of the nominal position. The efficiency of this requirement is also determined using Pseudo-CC events. A new vertex fit is performed ignoring the hits in the chamber from original positron track in these events. The efficiency is shown in figure 8.6 versus y_h for data and simulation. The efficiency of the central tracker decreases rapidly at $y_h \approx 0.1$ and is not well described by the simulation. By allowing for vertices from the forward tracking system it is increased to $\gtrsim 80\%$ in the measured kinematic range.

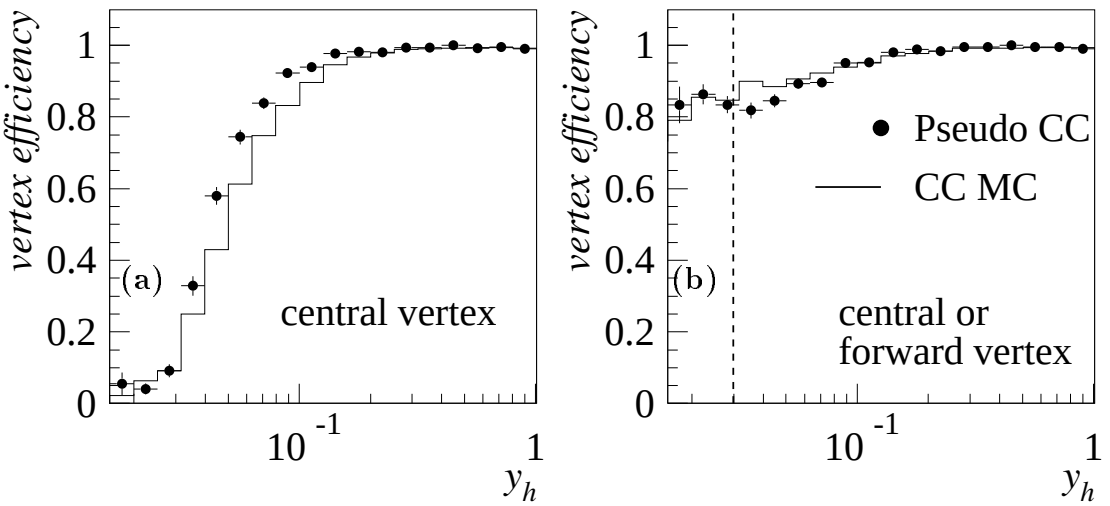

Figure 8.6: *Vertex finding efficiency for a vertex from a) the central tracker and from b) either the central or forward tracker for Pseudo-CC events (closed circles) and MC events (histogram). Indicated by a dashed line is the $y = 0.03$ cut value.*

The uncertainty on the vertex efficiency is included as a systematic error of 2% (5%) for $y > 0.1$ ($y < 0.1$). The efficiency as determined from Pseudo-CCs and CC MC agrees well within this uncertainty.

8.4 Rejection of non-*ep*-Background

The selection cuts for CC events can be satisfied by proton beam halo events and cosmic rays showering in the LAr calorimeter. With a basic selection $P_T^{\text{miss}} > 12$ GeV and a vertex requirement the fraction of *ep* collision events is $< 10\%$ in this sample (see figure 8.1). This background can partially be rejected by the event timing information in a way similar to the NC analysis. However, a further reduction of the background is necessary which exploits the topological difference between CC and background events.

Timing Requirements: As in the NC case a rejection of this background is achieved by requiring the T_0 determined from the drift time to the wires of the central jet chamber (CJC) to coincide with the bunch crossing time. Further timing information is given by the T_0 determined by the LAr calorimeter [88]. The timing information is shown in figure 8.7 for events rejected by the background finders, described in the next paragraph, and for events which pass the background finder selection. A large fraction of events which are rejected by topological background finders are also identified as background on the basis of the timing information. The cut values are also shown, i.e. ± 9 ns (corresponding to 0.1 bunch crossings) around the average value for the CJC-T_0 and ± 0.5 bunch crossings for the LAr-T_0. The resolution of the CJC-T_0 is ≈ 2 ns and the resolution of the LAr-T_0 ≈ 0.1 BC but in both of the T_0-distributions there are significant non-gaussian tails. Note, that the cut values correspond to $\approx 5\sigma$. The requirements are chosen loose in order to retain the events in the non-gaussian tails, thereby maintaining a high selection efficiency. The inefficiency for the CC selection is determined from Pseudo-CC events, it is $0.43 \pm 0.01\%$ for the CJC-T_0 and $1.98 \pm 0.06\%$ for the LAr-T_0.

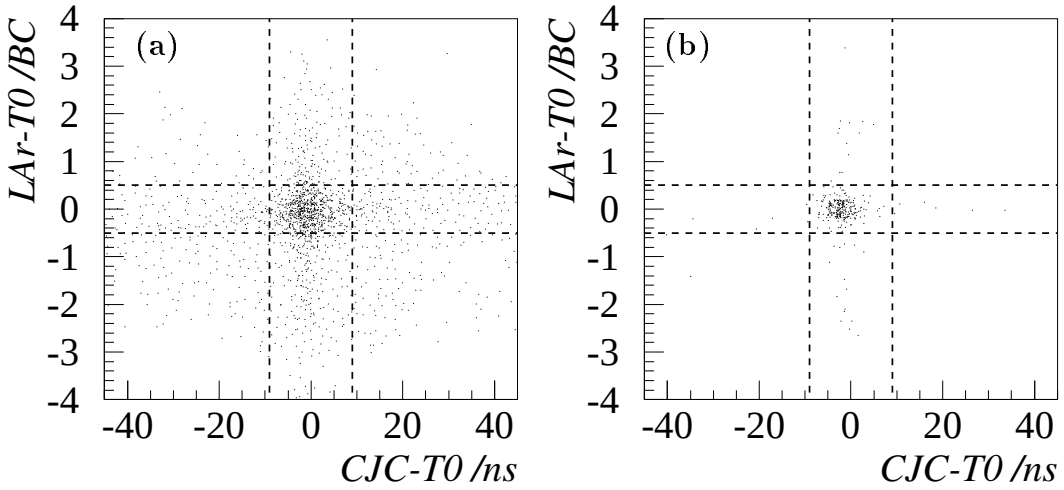

Figure 8.7: *(a) LAr-T_0 versus CJC-T_0 for events after applying all CC selection criteria but the topological background finders. (b) LAr-T_0 versus CJC-T_0 for events after applying all CC selection criteria (including the topological background finders). The dashed line indicate the cut values of ± 9 ns (± 0.5 bunch crossings) for the CJC-T_0 (LAr-T_0).*

Background "Finders": The remaining background originates mainly from accidental overlap of halo-muons or cosmic rays with photoproduction events. It is crucial for the measurement to reject this background very efficiently while still maintaining a high selection efficiency for CC events. This is achieved by using a large set of cuts that are sufficiently sensitive to discriminate between CC events and non-ep background. These are the so-called background "finders".

A rather elaborate set of topological finders QBGFMAR [89] is used for the back-

ground rejection which is based on the characteristic signature of cosmic and halo muon events. Only a brief outline of this package is given here. The details can be found in [90, 91]. Using different subdetector components, three kinds of signatures are tagged:

- **halo muons** are recognised by energy deposits which line up in parallel to the beam axis. A typical event is shown in figure 8.8(a). This signature is tagged using the subdetectors LAC, Instrumented Iron and SPACAL. A cylinder around the cosmic direction is defined. For finders which use the LAr calorimeter a cylinder around the cosmic direction is defined and the energy outside this cylinder is required to be small.

- **cosmic rays** are tagged by reconstructing its track using information from the LAr calorimeter, the central tracking and the Iron system. A cylinder around the cosmic direction is defined. For finders which use the LAr calorimeter a cylinder around the cosmic direction is defined and the energy outside this cylinder is required to be small. An example event is shown in 8.8(b).

- **overlap events** of cosmic rays or beam halo events with soft photoproduction events, which are not rejected by the two sets discussed above, are rejected by requiring $P_{t,tracks}/P_{t,LAr} > 0.015$ for events where the cluster with highest transverse momentum is at large polar angle $\theta_{cluster} > 20^o$. Additional cuts are made which reject events where there is no track near the highest P_t LAC cluster and the LAC energy is concentrated in a cylinder.

The application of these finders reduces the signal/background ratio significantly, from 2% to about 87%, whilst introducing an inefficiency in the CC selection of $\approx 2.5\%$.

In addition the following cuts were developed to reject non-ep background

A) **Hadronic Energy (FHK):** Events with an energy in the hadronic section larger than 80% of the total energy are rejected. Showers caused by cosmic muons often start in the hadronic section of the calorimeter, thereby giving rise to large values of FHK. In CC events the shower development always starts in the electromagnetic section, such that typically only $10 - 20\%$ of the energy is measured in the hadronic section.

B) **Cluster-Track link (CL-TRACK):** Events are rejected in which the highest energy cluster is in the central region ($\theta_{cl} > 30^o$) and there is no track within a cone of radius $R = \sqrt{(\eta_{cl} - \eta_{tr})^2 + (\phi_{cl} - \phi_{tr})^2} < 1$ around this cluster.

C) **Forward Vertex (FWVX):** There is a larger fraction of background events when no vertex is reconstructed from the hits in the central tracking detector, but only from those in the forward tracking detector. These events are therefore only accepted if the inclusive angle of the hadronic final state $\gamma_h < 20^o$ or the highest energy cluster $\theta_{cl} < 20^o$ and $y_h < 0.1$.

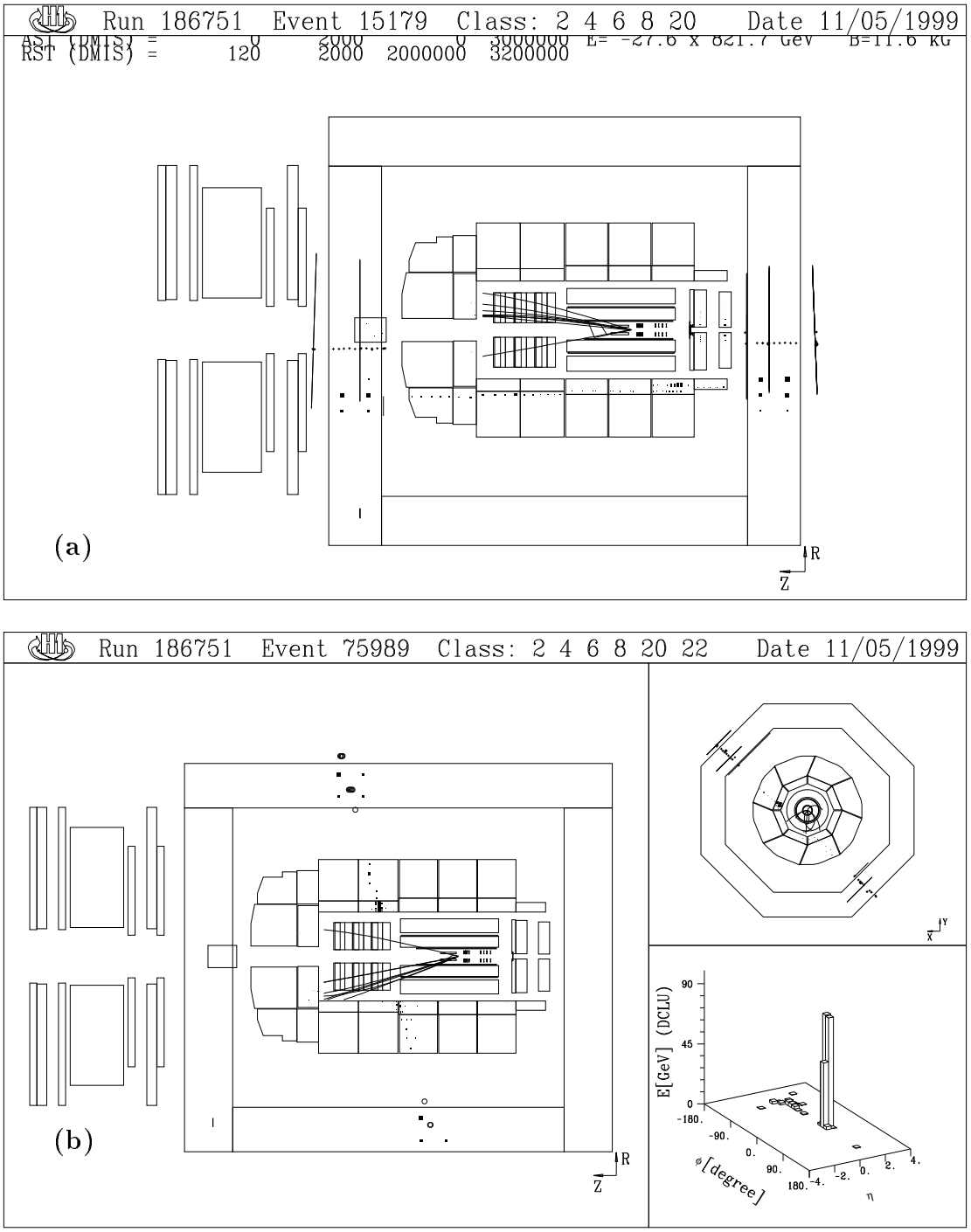

Figure 8.8: *Displays of a) a beam halo and b) a cosmic ray event which pass the selection and are rejected by topological background finders*

D) **Noise (NOISE):** Large values of P_T^{miss} can also be induced by calorimeter noise. In particular, coherent noise of a number of neighbouring cells can lead to the measurement of high energies in the calorimeter. If such coherent noise occurs very often within a run it is tagged by the Liquid-Argon Monitoring

software (ARMON [82]) and the events are rejected. If the noise is only present for a short time the events are accepted by ARMON and enter the analysis sample. Algorithms are developed to remove these events by recognising the characteristic noise pattern. If there is noise tagged for a large part of a run that run is rejected (see section 7.1). Also events with one hot cell are removed by cutting events where more than 90% of the $P_T^{\rm miss}$ are measured in one calorimeter cell.

Table 8.3 lists the applied finders. It gives the total number of events rejected and the number of events only rejected by this finder. In addition it gives the inefficiency as determined from CC MC and Pseudo-CC events. The inefficiencies of the individual sets are well described, overall it is $\approx 4.8\%$. There is a large fraction of events which are identified as background by several of the estimators. However, each finder also rejects events exclusively. The large impact on the CC analysis is seen in figure 8.1, the number of events is reduced by more than a factor 10.

Name	rejected events		inefficiency (%)	
	exclusively	total	MC	PSCC
QBGFMAR	8046	56581	2.60	2.08
FHK	53	14529	0.70	1.31
CL-TRACK	393	44424	1.05	1.00
FWVX	207	19800	0.09	0.37
NOISE	313	1025	0.03	0.08
all		59700	4.47	4.84

Table 8.3: *Table of background "finders" used for non-ep background rejection. The finder name (see text), the total number of rejected events, the fraction of events exclusively rejected and the inefficiency as determined from the MC simulation and the Pseudo-CC event sample are given.*

The efficiency of the background finders for selecting CC events is shown in figure 8.9 versus $P_T^{\rm miss}$ and y_h as determined from Pseudo-CC events and the CC Monte Carlo simulation. The efficiency is $\gtrsim 95\%$ and well described by the simulation in the full kinematic range.

8.5 Rejection of *ep*-induced Background

The main background for CC events originates from γp and NC events. Mismeasurements of energies and limited geometrical acceptance can in both cases lead to events which are not balanced in transverse momentum. This is illustrated in figure 8.10 where the $P_T^{\rm miss}$ distribution is shown for CC, NC and γp MC events. At low $P_T^{\rm miss}$ the background (NC+γp) expectation is larger than the signal (CC), at higher values of $P_T^{\rm miss} \gtrsim 30$ GeV the background becomes negligible. In order to reject this

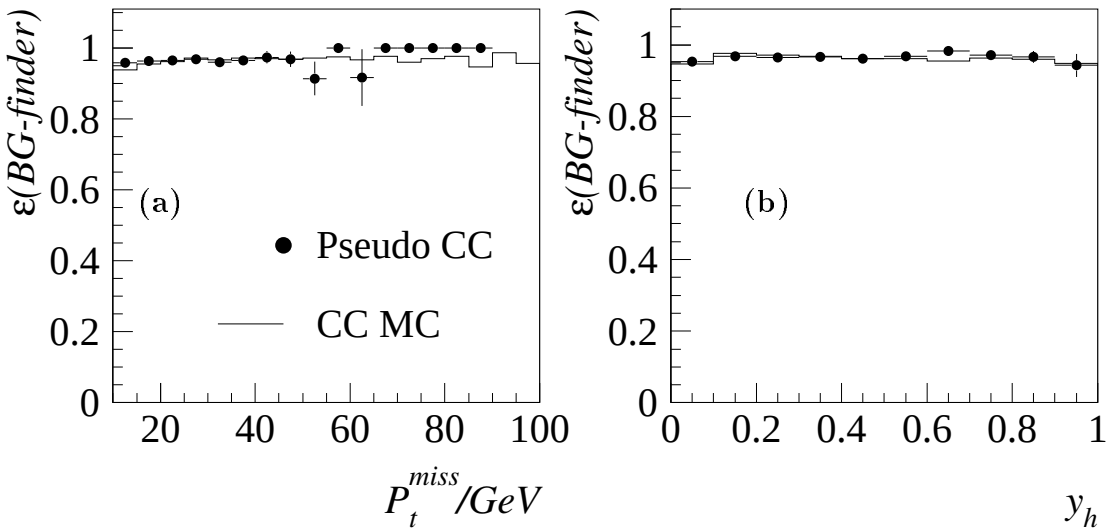

Figure 8.9: *Efficiency of the background selection for Pseudo-CC events (full circles) and CC MC events (histogram) versus* a) P_T^{miss} *and* b) y_h

background two variables V_{ap} and V_p are defined [92]:

$$V_p \equiv \sum_i \frac{\vec{P}_{T,h} \cdot \vec{P}_{T,i}}{P_{T,h}} \qquad \text{for} \qquad \vec{P}_{T,h} \cdot \vec{P}_{T,i} > 0 \tag{8.1}$$

$$V_{ap} \equiv -\sum_i \frac{\vec{P}_{T,h} \cdot \vec{P}_{T,i}}{P_{T,h}} \qquad \text{for} \qquad \vec{P}_{T,h} \cdot \vec{P}_{T,i} < 0 \tag{8.2}$$

with $\vec{P}_{T,h} = \sum \vec{P}_{T,i}$, where the summation is over all particles in the detector. For well measured CC events with only one jet transverse momentum component opposite to the jet (V_{ap}) is expected to be much smaller than that in the direction of the outgoing jet (V_p) thereby leading to $V_{ap}/V_p \approx 0$. For γp and NC events the energy is expected to be distributed isotropically, resulting in $V_{ap}/V_p \approx 1$. By selecting events with an imbalance in transverse momentum $P_T^{\text{miss}} > 12$ GeV the ratio decreases for these events to $V_{ap}/V_p \approx 0.5$. The distribution V_{ap}/V_p is shown in figure 8.10.b) for CC, NC and γp MC events. At low values of $V_{ap}/V_p \lesssim 0.2$ the expectation from the CC Monte Carlo exceeds the NC and γp expectation. To suppress the background a cut value of $V_{ap}/V_p < 0.15$ is chosen. The impact is seen in figure 8.1, at low P_T^{miss} the data sample is reduced significantly while at high $P_T^{\text{miss}} > 25$ GeV there are only few events rejected due to this cut.

The efficiency of this cut for the CC selection is shown in figure 8.11 versus x_h for the simulation and the Pseudo-CC event sample. At low $x_h \approx 0.01$ the efficiency is only $\approx 50\%$, but increases with increasing x_h such that it is nearly 100% efficient for $x_h > 0.1$. The reason for the low efficiency at low x is that the hadronic final state in CC events in this kinematic region is less collimated, so that higher values of V_{ap}/V_p occur. The efficiency obtained from the Pseudo-CC sample is well reproduced by

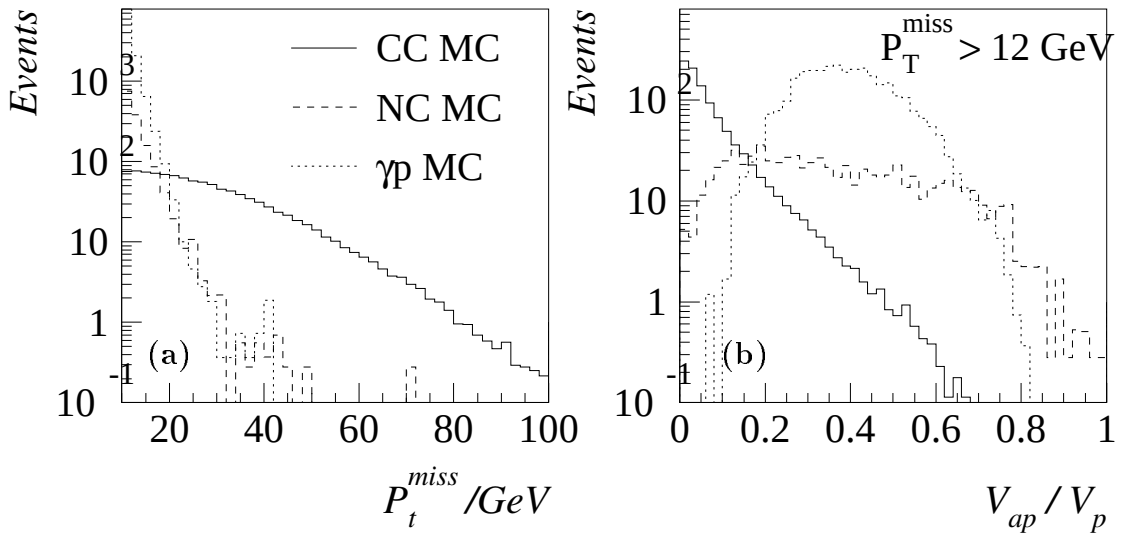

Figure 8.10: *a) $P_T^{\rm miss}$ and b) V_{ap}/V_p distribution for CC (full line), NC (dashed line) and γp (dotted line) Monte Carlo events. The number of events corresponds to the data luminosity of 35.6 pb^{-1}.*

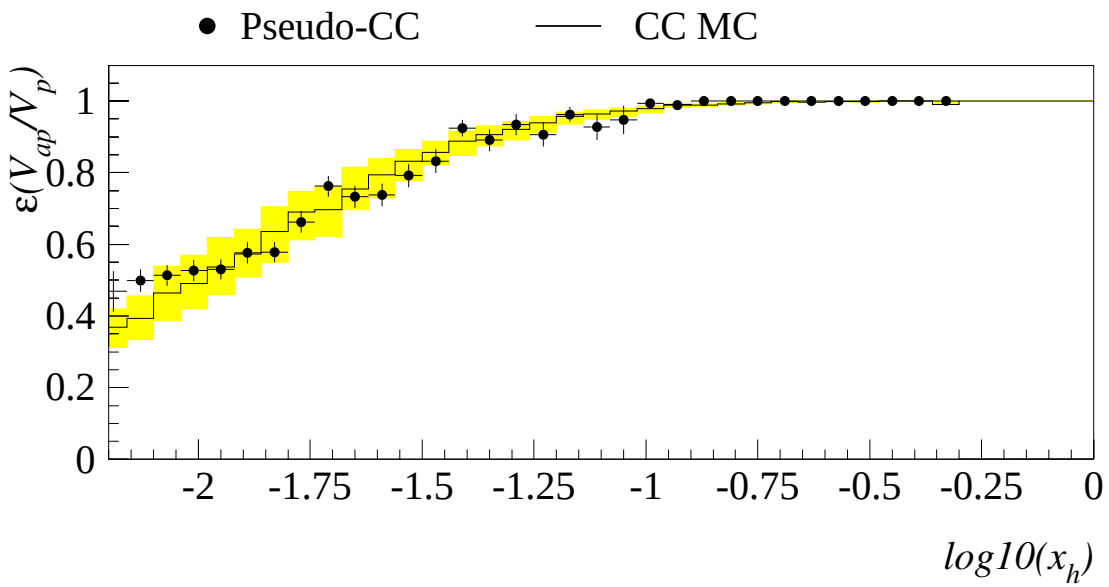

Figure 8.11: *Efficiency of the requirement $V_{ap}/V_p < 0.15$ for the Pseudo-CC event sample (closed circles) and the CC simulation (histogram). Shown is also the effect of a variation of the cut value by ± 0.02 as the grey band.*

the simulation. A systematic uncertainty is assigned by varying the cut by 0.02 around the nominal value. The systematic error due to this variation is shown in figure 8.11: it is about 10% at low x and negligible at high x.

The modelling of photoproduction background by the simulation is studied by comparing the V_{ap}/V_p distribution between data and simulation for γp events. The full CC selection is applied to these events apart from the cut on V_{ap}/V_p. As in the NC analysis the luminosity system is used to identify γp events in the data and the sim-

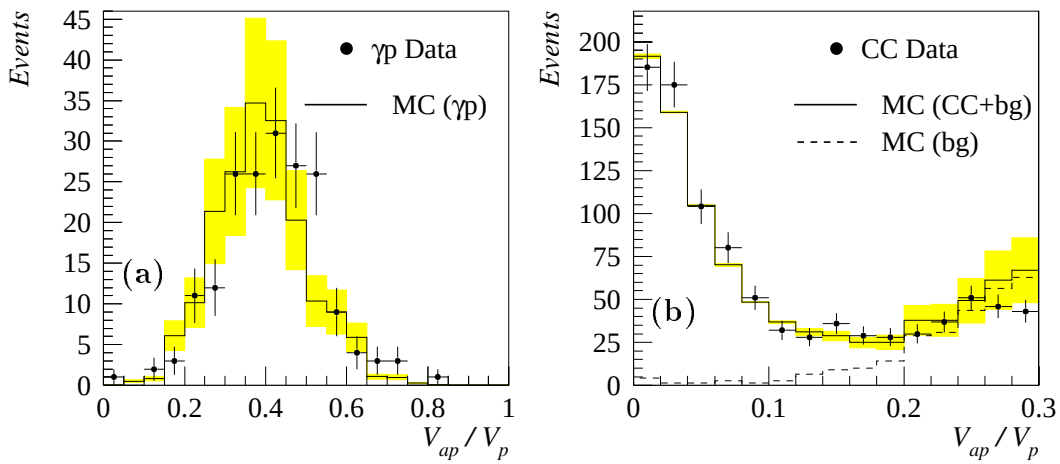

Figure 8.12: *Distribution of V_{ap}/V_p (a) for tagged photoproduction events passing the CC selection except for the V_{ap}/V_p cut. The simulation (histogram) of the photoproduction background normalised to the experimental luminosity is compared to the data. (b) The same distribution is shown for all events which pass the CC selection except for the V_{ap}/V_p cut. The simulation (histogram), which includes the CC and the background (bg ≡ photoproduction + NC) events, is normalised to the experimental luminosity and compared to the data. A cut at $V_{ap}/V_p < 0.15$ is applied in the CC selection. The grey error bands represent the systematic uncertainty of the background simulation.*

ulation is corrected for the acceptance of the electron tagger (see section 7.5). The V_{ap}/V_p-distribution is shown in figure 8.12(a) for the tagged γp events and compared to the simulation: it is well described in both shape and normalisation by the MC simulation. Figure 8.12(b) shows that the V_{ap}/V_p-distribution is well described up to values $V_{ap}/V_p = 0.3$ for CC candidates. A rather conservative error of 30% on the normalisation of the background is quoted because the acceptance of the electron tagger is limited to $0.3 \lesssim y \lesssim 0.7$. Photoproduction events can only be identified in this y-range, and the background from events at higher and lower values of y can not be controlled experimentally. The influence of this systematic error on the control distributions is shown in figure 8.12.

Neutral current events may have large P_T^{miss} and low values of V_{ap}/V_p when the scattered positron goes into a region where the energy measurement is poor, e.g. in a ϕ-crack. Such NC events are identified on the basis of a track which is isolated from all other tracks by $R = \sqrt{(\Delta\phi^2 + \Delta\eta^2)} > 0.5$ with $\Delta\phi$ and $\Delta\eta$ being the distance in azimuthal angle and pseudorapidity of one track to another. Events are rejected if such an isolated track is opposite to the hadronic final state, $|\phi_h - \phi_{itr}| > 160^o$, where ϕ_{itr} denotes the angle of the isolated track. Additionally events with an identified electron candidate and $E - p_z > 45$ GeV are rejected. Finally also events which satisfy the NC selection described in chapter 7 are removed from the CC analysis.

Another background source is the production of W bosons on mass-shell which

decay semi-leptonically. These events have large values of $P_T^{\rm miss}$ due to the outgoing neutrino from the decay of the W which is not detected. The contamination of this background is reduced by rejecting events with a high momentum track ($P_t^{track} > 10$ GeV) which is isolated from the jet with highest transverse momentum [1] by $R = \sqrt{(\phi^{jet} - \phi^{track})^2 + (\eta^{jet} - \eta^{track})^2} > 1.5$ where ϕ^{jet} and η^{jet} (ϕ^{track} and η^{track}) are the azimuthal angle and pseudo-rapidity of the jet (track) respectively. In the 1994-97 data 6 events were observed with high $P_T^{\rm miss}$ and a lepton with high transverse momentum isolated from the hadronic final state [39]. These events were studied in detail and found to be inconsistent with CC events. None of these events passes the CC selection. They are all rejected by the cut against W-background.

The inefficiency introduced by the cuts to reject background from NC DIS events and events from real W production is $< 1\%$, as determined from the CC MC. At low $P_T^{\rm miss}$ the sample is reduced by a factor of about three (see figure 8.1).

8.6 Scanning of the Data Sample

After applying these cuts the remaining 789 data events are scanned visually. 49 events are identified as background and rejected: 29 cosmic ray events, 17 halo muon events, 2 noise events and one overlap of a cosmic ray with a CC event.

8.7 The Final Charged Current Data Sample

After applying the following CC selection criteria 740 events are selected

- run selection;
- Subtriggers ST66,ST67,ST75, ST77 and ST71 (only in 1997);
- CJC- and LAC-T_0 timing;
- $P_T^{\rm miss} > 12$ GeV;
- $y_h > 0.03$;
- interaction vertex with $-36 < Z_{vtx} < 34$ cm;
- Non-ep-background rejection cuts;
- $V_{ap}/V_p < 0.15$;
- cuts against NC background and W production;
- visual scanning.

[1] The jet is defined by the longitudinal invariant k_t jet finding algorithm [93].

The $P_T^{\rm miss}$ and y distributions are shown for the CC candidates in figure 8.13. It is seen that they are well modelled at all $P_T^{\rm miss}$ and y.

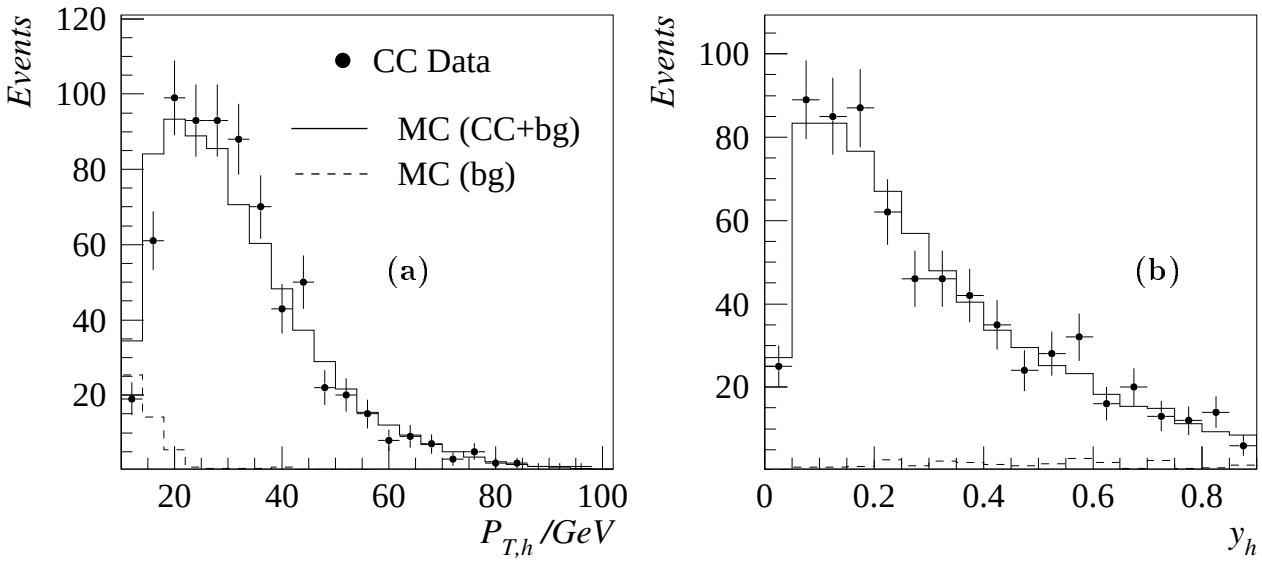

Figure 8.13: *Distribution of $P_{T,h}$ and y_h for the CC sample. The complete simulation (histogram) normalised to the experimental luminosity is compared to the data (points). The simulated background is also shown (dashed histogram).*

Chapter 9

Cross Section Measurement Procedure

In this chapter the procedure used to determine the cross section is described. The kinematic plane is divided into bins of x and Q^2 according to the statistical precision and the resolution. The observed number of events is then converted into a cross section. Also explained are the radiative corrections which are applied in this procedure. Then the systematic errors on the cross sections are discussed. Finally the QCD analysis used for the interpretation of the data is briefly described.

9.1 Selection of Bins

The cross sections measured in this analysis are performed in bins of x and Q^2. The binning for the NC measurement is illustrated in figure 9.1. There are ten bins per decade in Q^2 and five bins per decade in x. At $Q^2 \geq 3000$ GeV^2 the bin size is doubled due to limited statistics. At $Q^2 \leq 500$ GeV^2 and $x > 0.1$ the binning is also modified to accommodate the limited x resolution. The resolution is always better than the width of the bin. The bin boundaries for the NC measurement are:

bin boundaries in $\log_{10}(Q^2/GeV^2)$									
2.15	2.25	2.35	2.45	2.55	2.65	2.75	2.85	2.95	3.05
3.15	3.25	3.35	3.55	3.7782	4.0	4.2222	4.4437	4.6659	

bin boundaries in $\log_{10}(x)$									
-2.8	-2.6	-2.4	-2.2	-2.0	-1.8	-1.6	-1.4	-1.2	-1.0
-0.84	-0.68	-0.5	-0.3	0.0					

The binning for the CC measurement is coarser due to poorer resolution and lower statistics (see figure 9.2). Three bins per order of magnitude are chosen in both x and Q^2. The bin boundaries for the CC measurement are:

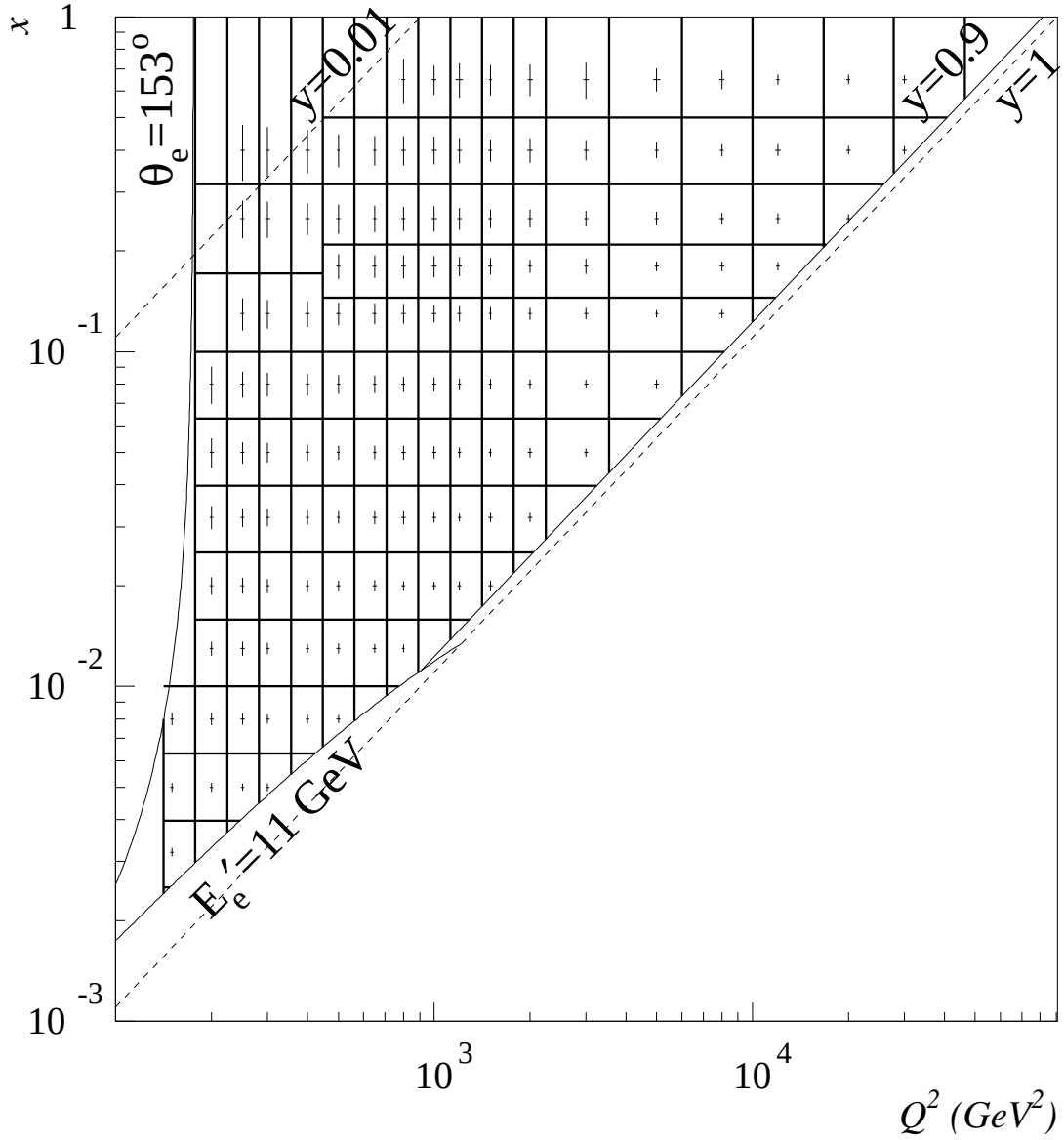

Figure 9.1: *The vertical and horizontal lines show the Q^2 and x bin boundaries respectively for the NC measurement. Also shown are the upper $y = 0.9$-cut, the $E_e' = 11$ GeV cut and the line of constant $\theta = 153^o$. The bin centres of the measurement are marked by crosses. The length of horizontal and vertical cross bar indicates the Q^2 and x resolution, respectively.*

bin boundaries in $\log_{10}(Q^2/GeV^2)$								
2.35	2.6	2.85	3.1	3.35	3.6	3.85	4.1	4.4

bin boundaries in $\log_{10}(x)$							
-2.0	-1.67	-1.33	-1.0	-0.75	-0.5	-0.25	0.0

The bins are chosen according to the purity ($\mathcal{P}$), the stability ($\mathcal{S}$) and the acceptance

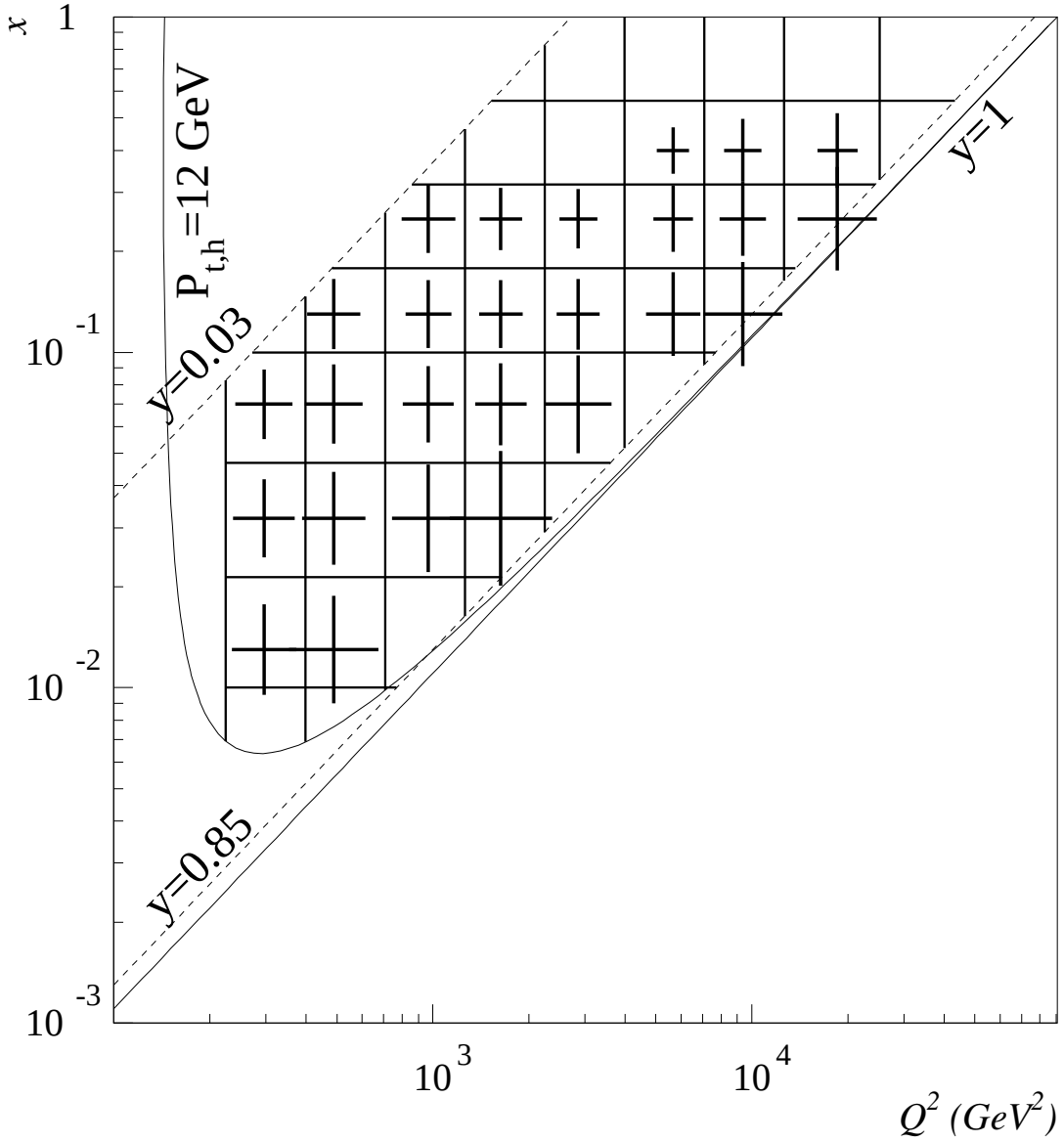

Figure 9.2: *The vertical and horizontal lines show the Q^2 and x bin boundaries respectively for the CC measurement. Also shown are the upper (0.85) and lower (0.03) cuts on y and the cut on $P_{T,h}$. The bin centres of the measurement are marked by crosses. The length of horizontal and vertical cross bar indicates the Q^2 and x resolution, respectively.*

($\mathcal{A}$) which are determined from the MC simulation. They are defined

$$\mathcal{P}(i) = N^{MC}_{rec+gen}(i)/N^{MC}_{rec}(i) \quad (9.1)$$

$$\mathcal{S}(i) = N^{MC}_{rec+gen}(i)/N^{MC}_{gen+sel}(i) \quad (9.2)$$

$$\mathcal{A}(i) = N^{MC}_{rec}(i)/N^{MC}_{gen}(i) \quad (9.3)$$

where

- $N^{MC}_{rec+gen}(i)$ is the number of events generated and reconstructed in bin i;

- $N_{gen}^{MC}(i)$ is the number of events generated in bin i;
- $N_{gen+sel}^{MC}(i)$ is the number of events generated in bin i and passing all selection criteria (i.e. reconstructed in any bin);
- $N_{rec}^{MC}(i)$ is the number of events reconstructed in bin i.

The purity and stability are required to be larger than 30% and the acceptance larger than 20%.

These quantities are shown in figure 9.3(a) for the NC measurement as determined using the $e\Sigma$-method. The purity and stability are highest at low x. With increasing x and correspondingly decreasing y both of them decrease. This is the reason for the increased bin size at high x and low Q^2. With increasing Q^2 the purity and stability become higher and approach values of $\approx 70\%$. The acceptance for the NC measurement is limited at low Q^2 and high x due to the limited acceptance of the Liquid-Argon calorimeter. Here the cut $Z_e > -180$ cm, corresponding to $\theta \approx 153^o$, means that only a small fraction of the events in a bin are experimentally accessible in the LAC (see also figure 9.1). The other events are measured in the SPACAL.

The purity, stability and acceptance for the CC measurement are displayed in figure 9.3(b) as determined using the hadron-method. The purities and stabilities are in general lower for the CC measurement than the NC measurement, due to the inferior resolution of the hadron-method relative to the $e\Sigma$-method. At low x and correspondingly high y, the resolution of the h-method is rather poor (see also figure 4.1) causing the purity to decrease. At high x, the hadronic final state goes forward so that a significant fraction of the transverse momentum is not measured in the detector, resulting on average in an underestimation of $P_{T,h}$ (see also figure 6.10). This causes the observed decrease in stability.

9.2 Extraction of the Cross Section

The cross section measured in a single bin in x and Q^2 is given by

$$\frac{\mathrm{d}^2\sigma}{\mathrm{d}x\mathrm{d}Q^2} = \frac{N^{data} - N^{bg}}{\mathcal{L} \cdot \mathcal{A}} \cdot \delta^{bc} \cdot \frac{1}{1+\delta^{RC}} \tag{9.4}$$

where

- N^{data} is the number of selected events in a bin;
- N^{bg} is the number of background events estimated by MC;
- $\mathcal{L}$ is the total integrated luminosity (see section 2.5);
- $\mathcal{A}$ is the detector acceptance. It is determined from MC as defined in eq. 9.3;

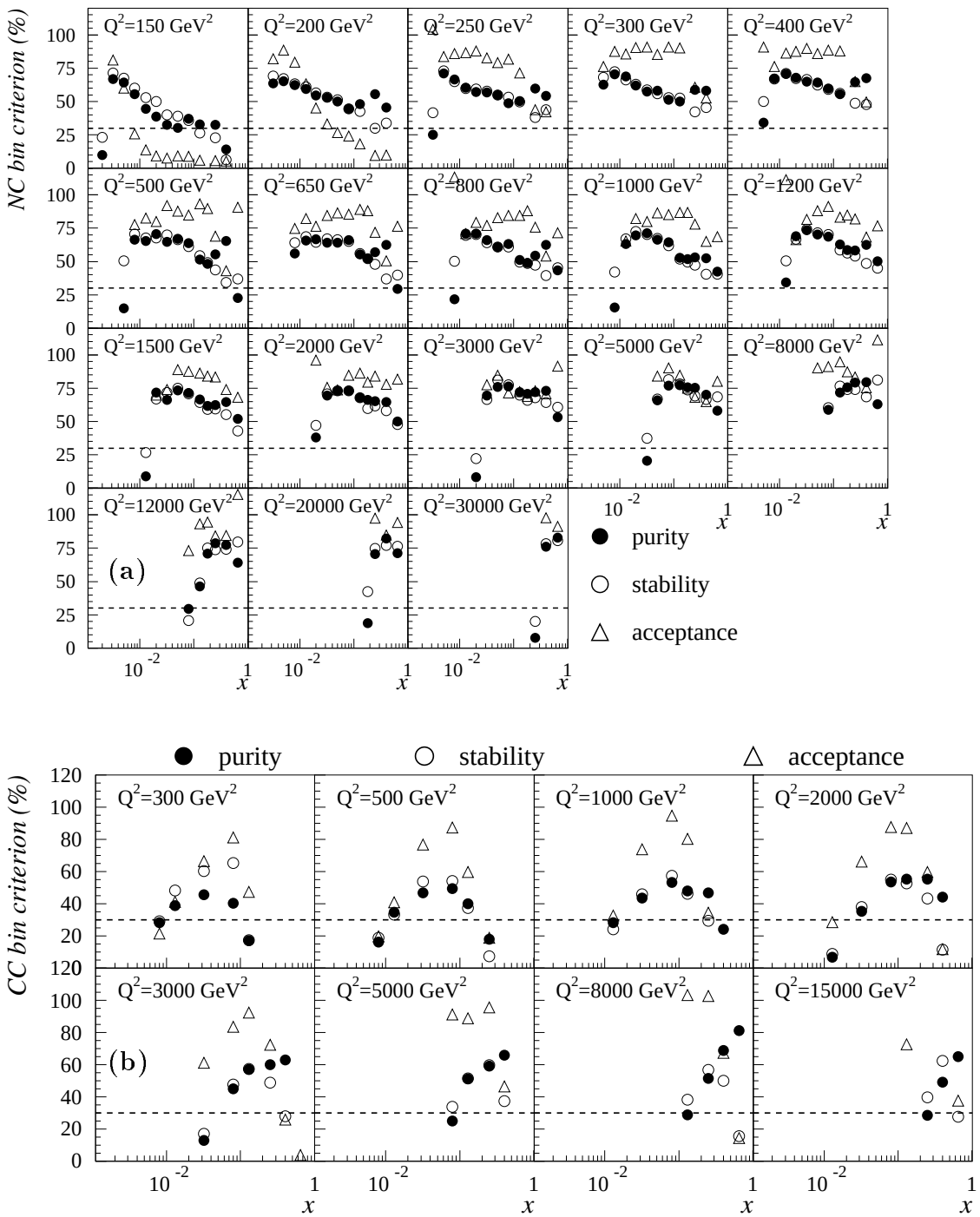

Figure 9.3: *Purity, stability and acceptance for the (a) NC and (b) CC measurement. The dashed lines indicate the cut values for the purity and stability.*

- δ^{bc} is the correction from the cross section in a bin of finite size $\Delta x_i = x_{i,max} - x_{i,min}$ and $\Delta Q_i^2 = Q_{i,max}^2 - Q_{i,min}^2$ to the bin centre position $(x_{i,c}, Q_{i,c}^2)$.

$$\delta_i^{bc} = \frac{\frac{\mathrm{d}^2\sigma}{\mathrm{d}x\mathrm{d}Q^2}|_{x=x_{i,c},Q^2=Q_{i,c}^2}}{\int_{x_{i,min}}^{x_{i,max}} \int_{Q_{i,min}^2}^{Q_{i,max}^2} \frac{\mathrm{d}^2\sigma}{\mathrm{d}x\mathrm{d}Q^2} dx dQ^2};$$

- $\delta^{RC} = \sigma_{rad}/\sigma - 1$ is the radiative correction estimated by the MC or an analytical program. In this measurement only parts of the radiative corrections $\delta^{RC} = \delta^{QED} + \delta^{weak}$ are applied. The δ^{QED} includes the leptonic corrections of $\mathcal{O}(\alpha)$, as discussed in 9.3. The weak corrections (δ^{weak}) are only performed when the structure function F_2 is extracted.

The acceptance, the radiative corrections and the bin centre correction depend on the assumption for the cross section of the underlying process. If this assumption deviates significantly from the measurement the derived corrections may be wrong. Therefore an iteration is needed where the theoretical model is adjusted to fit the measurement. In this case, the NC and CC cross sections in the Monte Carlo are generated using the cross section predicted by the MRSH parametrisation which is found to undershoot the NC data at low x by $\approx 10\%$. The MC events are then re-weighted to the cross section determined by a fit to this measurement. However, the difference between the measured cross section when using the original MRSH cross section and the re-weighted cross section is $< 1\%$ for all bins. Therefore the result of this measurement is independent of the cross section input to the MC simulation.

The acceptance, the radiative corrections and the bin centre correction were all obtained with the MC program DJANGO. In this case, formula 9.4 can be simplified to

$$\frac{\mathrm{d}^2\sigma}{\mathrm{d}x\mathrm{d}Q^2} = \frac{N^{data} - N^{bg}}{N_{rec}^{MC}} \cdot \frac{\mathcal{L}_{MC}}{\mathcal{L}} \frac{\mathrm{d}^2\sigma^{MC}}{\mathrm{d}x\mathrm{d}Q^2} \tag{9.5}$$

with the acceptance substituted by $\mathcal{A} = N_{rec}^{MC}/N_{gen}^{MC} = N_{rec}^{MC}/(\mathcal{L}\sigma_{rad})$.

The double differential cross sections are presented in the form of "reduced cross sections"

$$\tilde{\sigma}_{\mathrm{NC}} = \frac{xQ^4}{2\pi\alpha^2}\frac{1}{Y_+}\frac{\mathrm{d}^2\sigma_{NC}}{\mathrm{d}x\mathrm{d}Q^2} = \frac{1}{Y_+}\phi_{NC}^+(1+\delta_{NC}^{weak}) \tag{9.6}$$

$$\tilde{\sigma}_{\mathrm{CC}} = \frac{2\pi}{G_F}\left[\frac{Q^2+M_W^2}{M_W^2}\right]^2 \frac{\mathrm{d}^2\sigma_{CC}}{\mathrm{d}x\mathrm{d}Q^2} = \phi_{CC}^+(1+\delta_{CC}^{weak}) \tag{9.7}$$

which are closely related to the structure function terms. The NC cross section can be converted into the reduced cross section without assuming any electroweak parameters apart from the well measured fine structure constant α. In the CC case the value of the W-mass must be assumed. It is set to $M_W = 80.4$ GeV for this analysis. The measurement of $\mathrm{d}^2\sigma_{CC}/\mathrm{d}x\mathrm{d}Q^2$, which is independent of this assumption, is also quoted in table A.1. Note that the reduced NC cross section is still dependent on the ratio of the photon to the Z propagator while the reduced CC cross section is independent of the propagator term.

Extraction of the Structure Function: The structure function F_2 is extracted from the NC cross section measurement by correcting for the contributions from Z exchange and the purely weak radiative corrections and due to F_L:

$$\tilde{\sigma}_{\rm NC} = F_2(1 + \Delta_{F_2} + \Delta_{F_3} + \Delta_{F_L}) \;/\; (1 + \delta_{NC}^{weak}) \;= F_2\,(1 + \Delta_{all}) \qquad (9.8)$$

with the Δ_{F_2} and Δ_{F_3} terms originating from the $F_2^{\gamma Z}, F_2^Z$ and $xF_3^{\gamma Z}, xF_3^Z$ terms defined in eq. 1.6 and 1.7, and the Δ_{F_L} term from the longitudinal structure function. These terms are obtained from the NLO QCD Fit described in chapter 10 and the corrections applied are given in table A.2.

In the kinematic range investigated the effect of Z° exchange $(\Delta_{F_2} + \Delta_{F_3})$ on $\tilde{\sigma}_{NC}$ is expected to be $\leq 5\%$ for $Q^2 < 5000$ GeV^2. It is thus possible to extract F_2 with little uncertainty from the measured cross-section for values of Q^2 below 5000 GeV^2. At higher Q^2 values, the contribution of the xF_3 term significantly reduces the e^+p cross-section. The determination of F_2 then relies strongly on the calculation of Δ_{F_2} and Δ_{F_3}. In QCD calculations the Δ_{F_L} term is small and decreases at constant y with increasing Q^2. It reaches 6% for $y \geq 0.65$ and $Q^2 \leq 1500$ GeV^2 but is negligible for $y \lesssim 0.4$.

Single Differential and Total Cross Sections: The single differential cross sections are defined as

$$\frac{{\rm d}\sigma}{{\rm d}Q^2} = \int_{x_{min}}^{x_{max}} \frac{{\rm d}^2\sigma}{{\rm d}x{\rm d}Q^2}{\rm d}x \qquad\qquad \frac{{\rm d}\sigma}{{\rm d}x} = \int_{Q^2_{min}}^{Q^2_{max}} \frac{{\rm d}^2\sigma}{{\rm d}x{\rm d}Q^2}{\rm d}Q^2$$

and equation 9.5 is modified correspondingly. The x and Q^2 limits are chosen according to the experimental cuts. For the NC measurement, they are determined by the energy cut $E_e^{'} > 11$ GeV and the $y_e < 0.9$ cut. For the CC cross section, the cuts $P_t^\nu > 12$ GeV and $0.03 < y < 0.85$ are used. Comparisons of the two processes are made using corrections for the cuts on $E_e^{'}$ and P_t^ν, with a modified y range for the CC measurement. The corrections are obtained from the QCD fit to the data (see chapter 10) and are given in tables A.3 and A.4.

9.3 Radiative Corrections

Radiative corrections in deep inelastic scattering arise from the exchange or emission of additional bosons and from the self-energies of the particles involved. These processes are suppressed by the coupling strength, e.g. α for photon radiation. The cross sections need to be corrected for the real photon emissions, since their effect is dependent on the acceptance of the detector and the experimental cuts applied in the analysis.

It is convenient to separate the radiative corrections into two contributions: those from electromagnetic processes and those involving weak ones

$$1 + \delta^{RC} = (1 + \delta^{QED})(1 + \delta^{weak}) \qquad (9.9)$$

The δ^{QED} term depends on the detector acceptance while the δ^{weak} term is independent of the experimental procedure. The exact definition of this separation can be found in [94].

In order to compare with analytical calculations for the theoretical prediction of the Standard Model cross section only those corrections which depend on the acceptance have to be applied to the cross section. Whether the acceptance independent corrections are performed or not is a matter of judgement. The approach taken in this analysis is to correct only for the parts which are known to be insensitive to the masses or couplings of any new particles which could interfere with the Standard Model bosons at very high Q^2 at HERA. Such particles could only give rise to radiative corrections assigned to the δ^{weak} term which is therefore not applied. For the extraction of the structure function, however, it is necessary to correct to the Born cross section. This is done in this analysis assuming the Standard Model.

Unlike for the NC cross section, the separation of radiative corrections into weak and electromagnetic parts is not unique for the CC cross section. Here, the separation was made using the procedure described in [95].

Charged Current

The radiative corrections to the CC cross section are studied in [96] which incorporates studies made for the presented analysis. From these studies an uncertainty of 3% on the radiative corrections is deduced.

Neutral Current

The radiative correction term to the NC cross section contains the Bremsstrahlung process and vertex corrections as well as the self-energies of the lepton, quark and the bosons (see [94]).

The corrections due to the Bremsstrahlung process have the largest sensitivity to the detector acceptance. The Feynman diagrams with external fermions for eq scattering are shown in figure 9.4. The diagrams of $\mathcal{O}(\alpha)$ which contain internal fermion or boson lines may be found in [94]. In 9.4(a) and 9.4(b) a photon is radiated from the lepton line. Figure 9.4(c) and 9.4(d) show the Feynman diagrams where a photon is radiated from the quark line.

The effects of radiative corrections on the cross section can be divided into five contributions

- Leptonic contributions are described by diagrams containing an additional photon attached to the lepton line. They are proportional to α. They contain terms which are enhanced by the large $\log(Q^2/m_e^2)$. This contribution has a dependence on the kinematic variables as will be explained later. The approximation of considering only terms depending on $\log(Q^2/m_e^2)$ is called "Leading Logarithmic Approximation" (LLA).

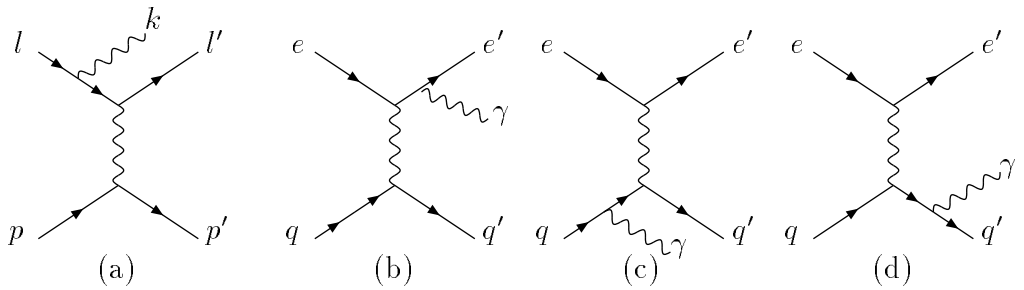

Figure 9.4: Feynman diagrams for radiative neutral current scattering. In figure (a) the four-momenta of the particles are denoted, in the others the particle types.

- Quarkonic contributions are described by diagrams containing an additional photon attached to the quark line. They contain $\log(Q^2/m_{q_f}^2)$ terms. These are absorbed into the Q^2 evolution of parton densities, i.e. the DGLAP evolution equations receive an additional QED term. Numerical estimates [97] show that the effect is very small such that only at very high x and Q^2 the corrections may reach about 1%.

- Interference contributions are described by diagrams containing an additional photon attached to both the lepton and the the quark line and from the interference of the diagrams shown in figure 9.4.

- The self-energy of the exchanged photon in NC interactions which can be taken into account by the use of the running fine structure constant α [98].

- The purely weak corrections describe all other diagrams (see [94]).

Since only the leptonic contributions from photon radiation depend on the detector acceptance and the kinematic variables, the following discussion will mainly focus on this correction.

The radiation of a photon from the lepton line influences the reconstruction of the kinematic variables. With the notation of the four-momenta of the particles, as shown in figure 9.4(a), the kinematic variables at the leptonic vertex are

$$Q_l^2 = -(l - l')^2, \qquad x_l = \frac{Q_l^2}{2p \cdot (l - l')}, \qquad y_l = \frac{p \cdot (l - l')}{p \cdot l} \tag{9.10}$$

while at the hadronic vertex the kinematic variables are given by

$$Q_h^2 = -(p' - p)^2, \qquad x_h = \frac{Q_h^2}{2p \cdot (p' - p)}, \qquad y_h = \frac{p \cdot (p' - p)}{p \cdot l} \tag{9.11}$$

Under the assumption that only one photon is radiated the virtuality at the hadronic and leptonic vertex are related via

$$Q_h^2 = -(p' - p)^2 = -(l - l' - k)^2 = Q_l^2 + 2k(l - l') \tag{9.12}$$

such that $Q_h^2 \leq Q_l^2$ for all events.

In the LLA the leptonic corrections can be subdivided into three components

- Initial State Radiation (ISR) denotes the emission of a photon from the incoming electron. Since the ISR terms are of the form $1/(kl)$, the photon is predominantly collinear with the incoming electron.
- Final State Radiation (FSR) is the emission of a photon from the outgoing electron. This contribution has a pole $1/(k'l)$ such that the photon is mainly emitted collinear to the outgoing electron.
- The QED-Compton term arises from events where $Q_h^2 \approx 0$ GeV^2 and the photon is usually well separated from both the incoming and outgoing electron.

Since, in FSR, the photon is predominantly emitted in the direction of the outgoing electron, these events are usually experimentally detected as one calorimeter cluster. Therefore they only give rise to a small correction. ISR, however, leads to an effective reduction of the centre-of-mass energy such that

$$Q_h^2 = zQ_l^2 \qquad x_h = \frac{x_l y_l z}{y_l + z - 1} \qquad y_h = \frac{y_l + z - 1}{z}$$

with $z = (E_e - E_\gamma)/E_e$ being the remaining fraction of the incident electron energy after a photon of energy E_γ is radiated.

In the NC analysis, this correction due to ISR can be reduced by requiring balance in longitudinal momentum

$$(E - p_z)_{all} = E - p_z + (E - p_z)_\gamma = E - p_z + 2E_\gamma \equiv 2E_e$$

where $E - p_z$ is reconstructed from the momenta of the scattered lepton and the hadrons. Since these particles are predominantly scattered into the central region of H1, within the kinematic range considered in this analysis, it can be experimentally accessed from the measurement in the central part of the H1 detector. In this analysis a cut of $E - p_z > 35$ GeV was chosen (see chapter 7) thereby rejecting NC events with a photon of energy $E_\gamma > 10$ GeV radiated from the incoming electron. Furthermore, for the NC analysis the $e\Sigma$ method is chosen for the reconstruction of the kinematic variables. This method is less sensitive to ISR effects since y is reconstructed by making use of the measured $E - p_z$ instead of assuming a fixed electron beam energy.

In figure 9.5, the radiative corrections in the LLA are shown for different kinematic reconstruction methods for the NC cross section at $Q^2 = 500$ GeV^2. In leptonic variables, the corrections are large at high y. This is explained by the strong Q^2 dependence of the NC cross section which leads to large kinematic migrations due to photon radiation. The $e\Sigma$ method is also shown, which requires corrections of about 15% at all values of y. These corrections are reduced to about 8% by applying the analysis cut of $E - p_z > 35$ GeV.

The previous study was made using the `HELIOS` [99] program which allows the corrections in LLA for several kinematic reconstruction methods to be calculated. It is part of the program package `HECTOR`[100], which also includes the `DISEPW` package. This program provides the possibility to calculate the full radiative corrections of

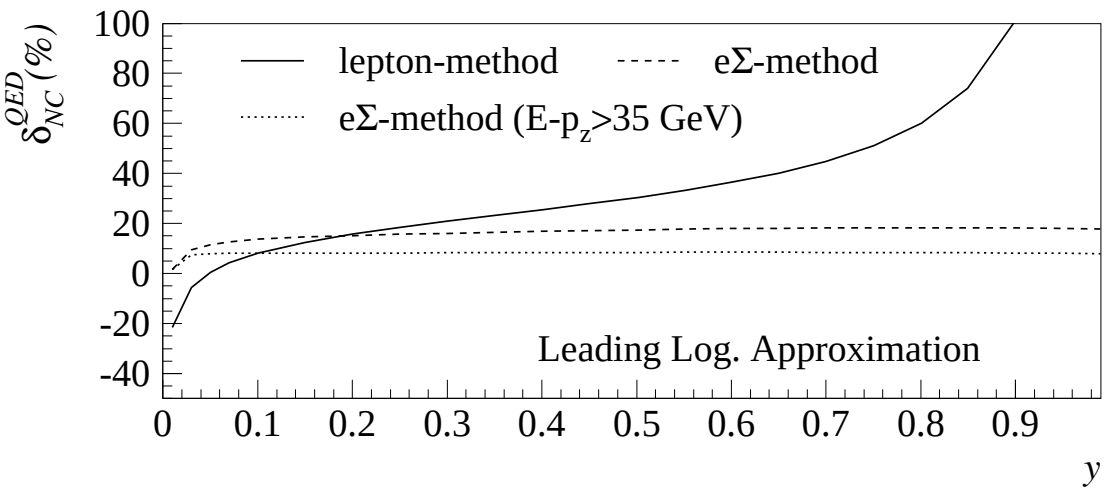

Figure 9.5: *Radiative corrections in the LLA for NC scattering versus y for $Q^2 = 500$ GeV^2. The correction is shown for the lepton method (solid line), the $e\Sigma$-method without an $E - p_z$-cut (dashed line) and with the analysis cut $E - p_z > 35$ GeV (dotted line). The corrections are obtained from the* `HELIOS` *program.*

$\mathcal{O}(\alpha)$, but can only be used in leptonic variables. The `TERAD` program can also be used for the estimation of higher orders. The effects of different approximations and the intrinsic uncertainty is estimated by comparing these different programs.

The most important correction to the NC cross section, apart from those considered in LLA, is the self-energy of the photon, also known as the "running of α". This is implemented in `DJANGO` by the parametrisation proposed in [98].

Since `DJANGO` is used to determine the radiative corrections, it is important to study the effects of higher order contributions $\mathcal{O}(\alpha^2)$, soft photon exponentiation (SPE) as well as the quarkonic and lepton-quark interference contributions. This can only be studied in leptonic variables with the available programs. The study is presented in figure 9.6 where the difference of each of the calculations to the leptonic term of $\mathcal{O}(\alpha)$ is shown. Also shown is the LLA. It can be seen that the differences are in general smaller than 5% and, in most of the y range, smaller than 1%. Note, that these differences are small compared to the large correction required in the e-method shown in figure 9.5. Since the $e\Sigma$-method requires much smaller corrections of only $\approx 8\%$, no differences larger than 1% are expected due to the effects studied in figure 9.6.

Within the kinematic range of the measurement, the `DJANGO` and `HELIOS` predictions are in agreement within 1%, using the $e\Sigma$ method, which is therefore quoted as systematic uncertainty.

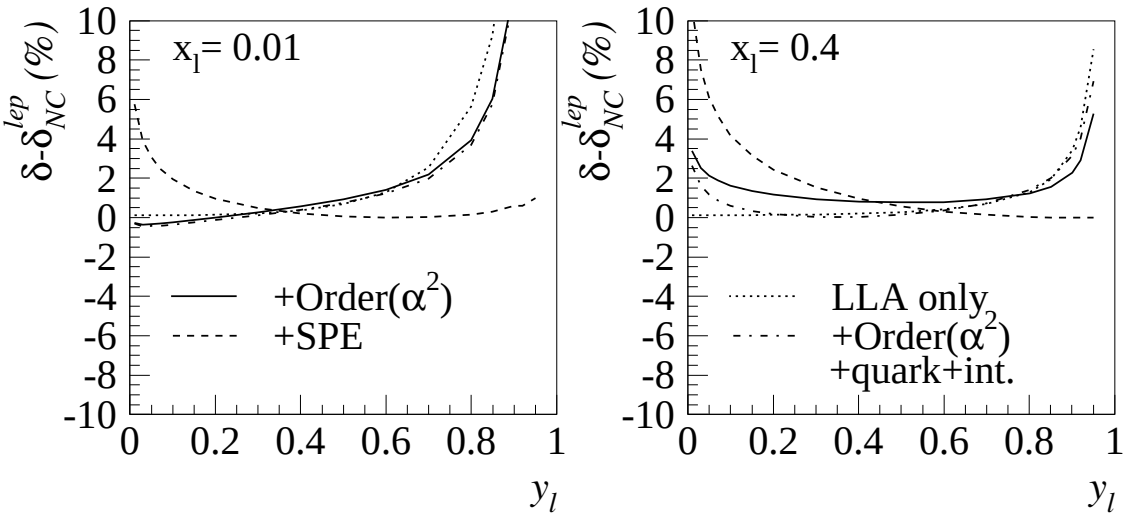

Figure 9.6: *Comparison of radiative corrections for the NC cross section as function of y_l for fixed values of x_l. Shown is the difference to the purely leptonic corrections of $\mathcal{O}(\alpha)$ for four different approximations of the radiative corrections: the inclusion of terms of $\mathcal{O}(\alpha^2)$ (solid line), soft photon exponentiation (dashed line), the Leading Logarithmic Approximation (dotted line) and of terms of $\mathcal{O}(\alpha^2)$ with quarkonic and quark/lepton-interference terms. (see text)*

9.4 Systematic Uncertainties

The systematic uncertainties for the cross section measurements are determined from the data. The studies which lead to the quoted systematic uncertainties are described in chapters 5 - 8. All selection criteria are monitored using and independent reference sample (see chapters 7 and 8). The redundancy of the detector is used for the studies the angle and energy measurements (see chapters 5 and 6) which are important for the reconstruction of the kinematic variables. The systematic uncertainties are estimated from the statistical precision of the data and from possible biases in the method used for the corresponding study. A distinction is made between errors which are correlated between all cross section bins and errors which are uncorrelated from bin to bin. A correlated error on the hadronic energy of 1% means for example that it is possible for the hadronic energy scale to differ from the "true" hadronic energy scale by 1%. This can cause a shift of all cross section points by the amount given in the corresponding tables A.2 and A.1. The uncorrelated errors are assumed to be due to local fluctuations or deficiencies. The trigger efficiency may for example be different by 0.5% at low Q^2 in a certain calorimeter region, but this has no impact on the efficiency at high Q^2. Some errors are treated as being partially correlated and partially uncorrelated. All errors are assumed to be gaussian and correspond to 1σ of a gaussian distribution.

The uncorrelated error sources are

- A 2% (4% at $y > 0.5$ and $Q^2 < 400$ GeV^2) error on the NC cross section due

to the uncertainty of the positron identification efficiency in the NC analysis (section 7.3);

- A 1% error on the NC cross section due to the cluster-track link requirement (section 7.4);
- A 0.5% error on the cross section due to the NC trigger efficiency (section 7.2);
- A $15\% \cdot \epsilon_{CC} \oplus 2\%$ uncertainty due to the CC trigger efficiency ϵ_{CC} (section 8.2) leading to an error of $8-2\%$ on the CC cross section;
- A 1% (3%) error on the cross section due to the radiative correction for NC (CC) (section 9.3);
- A 3% error on the CC cross section due to the background finder cuts (section 8.4);
- A 2% (5% at $y < 0.1$) error on the CC cross section due to the efficiency of the vertex reconstruction (section 8.3).

The following fully correlated errors are considered:

- An uncertainty of 25% on the energy identified as noise in the LAr calorimeter (section 6.2). The error on the NC cross section due to this uncertainty is largest at high x and low Q^2 where it is about 10%.
- A $4-6\%$ uncertainty on the efficiency of the V_{ap}/V_p cut, determined by varying the cut by ± 0.02 around the standard value of 0.15 for the simulation while keeping it fixed in data (section 8.5). This uncertainty has the largest influence at low Q^2 and low x where the error on the CC cross section due to it is about 10%.
- A 30% uncertainty on the subtracted background contribution (sections 7.5 and 8.5). This gives an maximum error of about 5% at high y (low x) for the NC cross section. The error on the CC cross section is largest at low x and low Q^2 where it is at maximum 8%.
- A 1.5% uncertainty on the cross section due to the luminosity uncertainty which is not included in the tables.

Some errors are determined to be only partially correlated. These are the uncertainties on the positron and hadronic energy scale and on the positron angle. Due to the imperfect knowledge of the reference scale, a correlated shift of a given amount is possible. In addition there can be larger local fluctuations due to areas where there is e.g. a large amount of dead material (e.g. calorimeter cracks) or insufficient statistical precision. The following uncertainties are considered:

- A correlated uncertainty of 0.5% on the positron energy as estimated from the uncertainty of the reference scale (DA-energy) used for calibration. The total

uncertainty is determined to be 1% in the BBE, 0.7% in CB1 and CB2, 1.5% in CB2 and 3% in FB and IF (section 6.1). The error on the cross section due to the 0.5% uncertainty is largest at high x where values of about 8% are typical.

- An uncertainty of 1 mrad on the positron angle as estimated from the uncertainty on the angle determined by the tracking chambers when Z-chamber hits are present. In addition an uncorrelated error of 2 mrad is assigned to take the discrepancies of the cluster θ determination between data and simulation into account (chapter 5). The NC cross section error due to the 1 mrad correlated uncertainty is always smaller than 2%.

- An uncertainty of 1% on the hadronic energy scale as estimated from the uncertainty of the reference scale (positron energy) used for calibration. The total uncertainty is 2%.(section 6.2). The influence of the 1% correlated uncertainty on the NC cross section is largest at high x where the maximum values are about 5%. The CC cross section error due to this uncertainty is largest at high Q^2 where it is up to about 10%.

The total uncertainty is the quadratic sum of the correlated and uncorrelated error.

The errors on the NC cross section due to the correlated systematic uncertainties are given in table A.2. The correlated errors are largest at high x, where there is an influence of the positron energy, the hadronic energy and the noise treatment. The error due to the photoproduction uncertainty is negligible except at low x (high y).

Figure 9.7 shows the statistical, correlated and uncorrelated errors for the NC measurement. For $Q^2 < 500$ GeV^2, the systematic errors dominate. They are typically $4-5\%$ while the statistical precision is $\approx 2-2.5\%$. The systematic error is predominantly coming from the uncorrelated error sources. At high $x \geq 0.4$, the correlated error becomes important, mainly due to the noise contribution at low y. In the region $Q^2 > 1000$ GeV^2 the statistical error dominates in all bins.

The errors on the CC cross section due to the correlated systematic uncertainties are given in table A.1. At $Q^2 \lesssim 1000$ GeV^2 the errors due to the V_{ap}/V_p cut and the uncertainty on the photoproduction background dominate. At high Q^2, they are negligible and the uncertainty on the hadronic energy scale gives the largest contribution.

The precision of the CC cross section is limited by statistics, as can be seen in figure 9.8. The systematic uncertainty is typically 8% while the statistical precision is $\approx 20\%$ for $Q^2 \leq 5000$ GeV^2. The dominant systematic error source at low Q^2 are the trigger efficiency and the efficiency of the V_{ap}/V_p cut. At high Q^2, the uncertainty on the hadronic energy scale is most important.

The measured cross section should be independent of the kinematic reconstruction method with which it was determined. Therefore the reliability of the cross section measurement is checked by determining the NC cross section using different methods for the reconstruction of the kinematic variables. Different kinematic reconstruction methods are sensitive to different observables. A wrong positron energy calibration

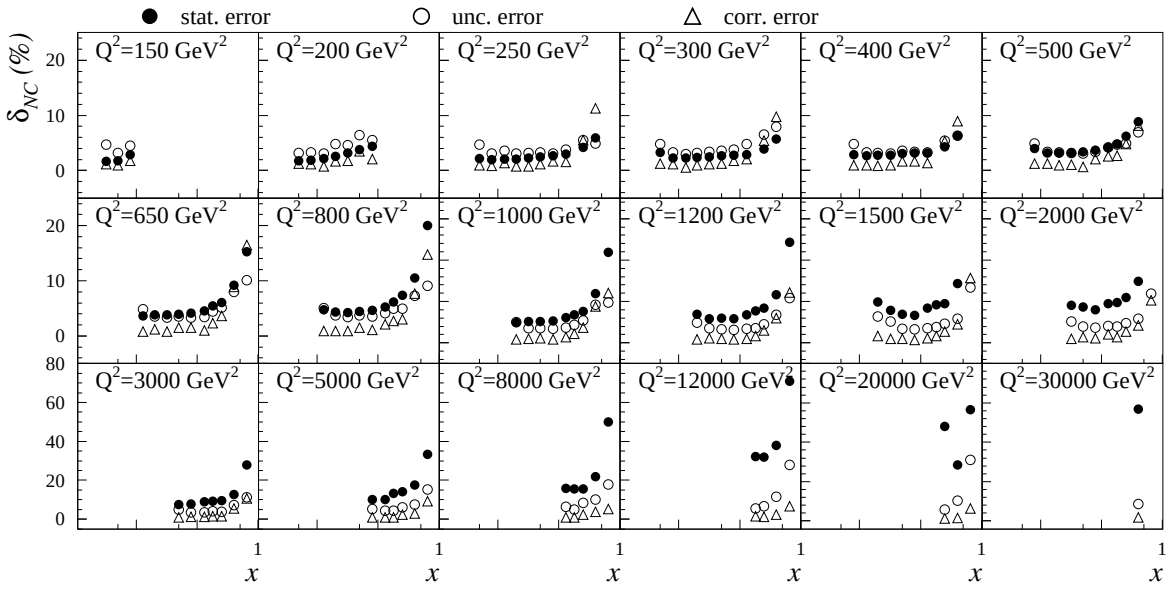

Figure 9.7: *Statistical (full points), correlated systematic (open points) and uncorrelated systematic (open triangles) errors on the NC cross section measurement.*

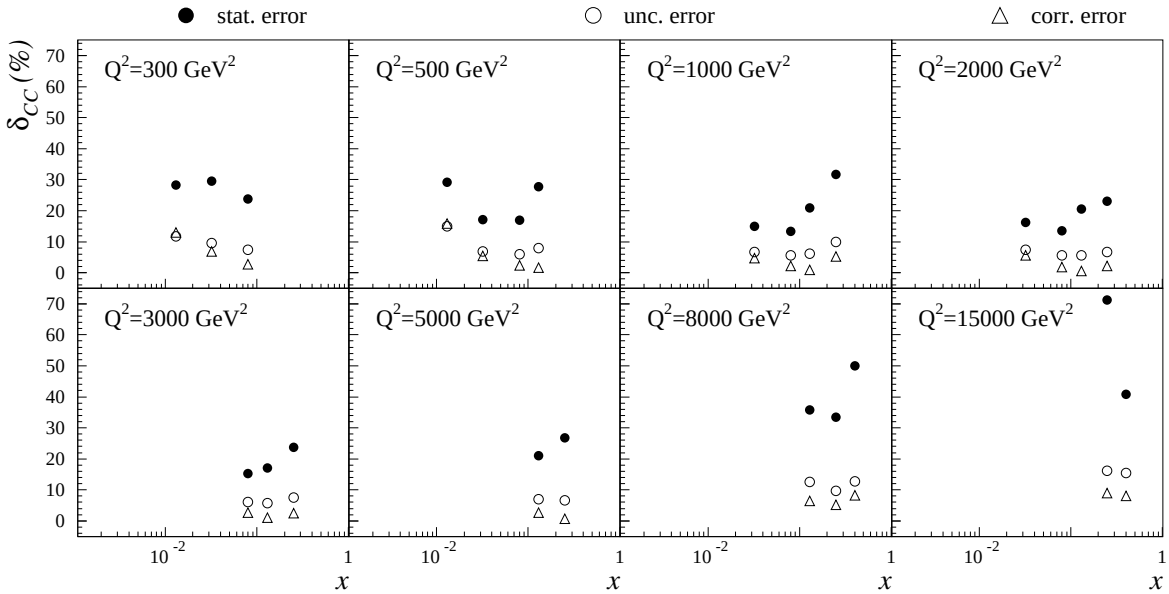

Figure 9.8: *Statistical (full points), correlated systematic (open points) and uncorrelated systematic (open triangles) errors on the CC cross section measurement.*

would e.g. lead to a disagreement between the Σ and e method. Such a disagreement could also point to inconsistencies in the radiative corrections or a wrong hadronic calibration. A comparison of the e and Σ method, in the NC binning, is shown in figure 9.9, in the bins where the corresponding methods are reliable, i.e. the purities and stabilities are $> 30\%$. The two methods give a consistent picture; no systematic deviations are observed.

Figure 9.10(a) shows the comparison of the results obtained with the $e\Sigma$ and DA

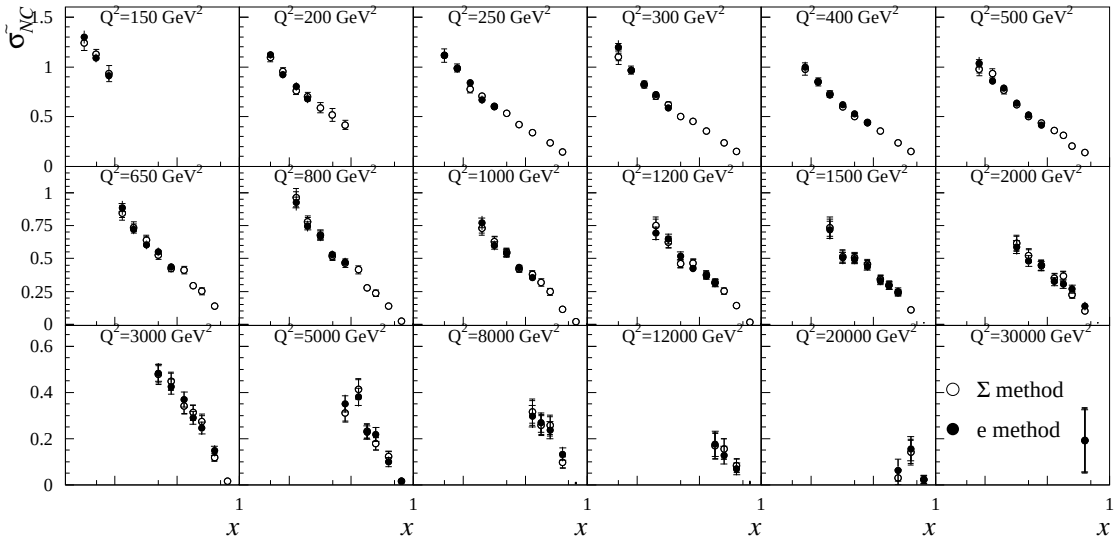

Figure 9.9: *Comparison between the reduced NC cross sections $\tilde{\sigma}_{\rm NC}$ as determined using the electron(e)- and Σ method.*

methods in eight selected Q^2 bins. Note, that these two methods are rather independent: the DA method is to first order independent of the energy scales of the calorimeter while the $e\Sigma$ method largely relies on those. The comparison between these two methods shows again no systematic deviations, thereby giving confidence to the final result which is obtained using the $e\Sigma$ method.

For the CC analysis there is only the h method available. The reliability of the h method is investigated in figure 9.10(b) by comparing the NC cross section in the CC binning, as measured using the h and e method. Both cross section determinations are in agreement within the quoted systematic uncertainties; no systematic deviations are seen.

In summary, the comparison of five different methods to reconstruct the event kinematics, all of which have a different sensitivity to different observables, shows no indication that the final results are biased due to any undetermined effects.

9.5 QCD Analysis Procedure

In order to test how well the cross sections can be described by QCD two fits were made both of which are based on the DGLAP evolution equations in next-to-leading-order (NLO):

- The first fit is made to the proton and deuteron structure function results of the fixed-target experiments BCDMS [10] and NMC [11] and the H1 low $Q^2 < 150$ GeV^2 data [19]. This fit is labelled "Low Q^2 Fit".

- The second fit includes the same data but additionally the NC and CC data

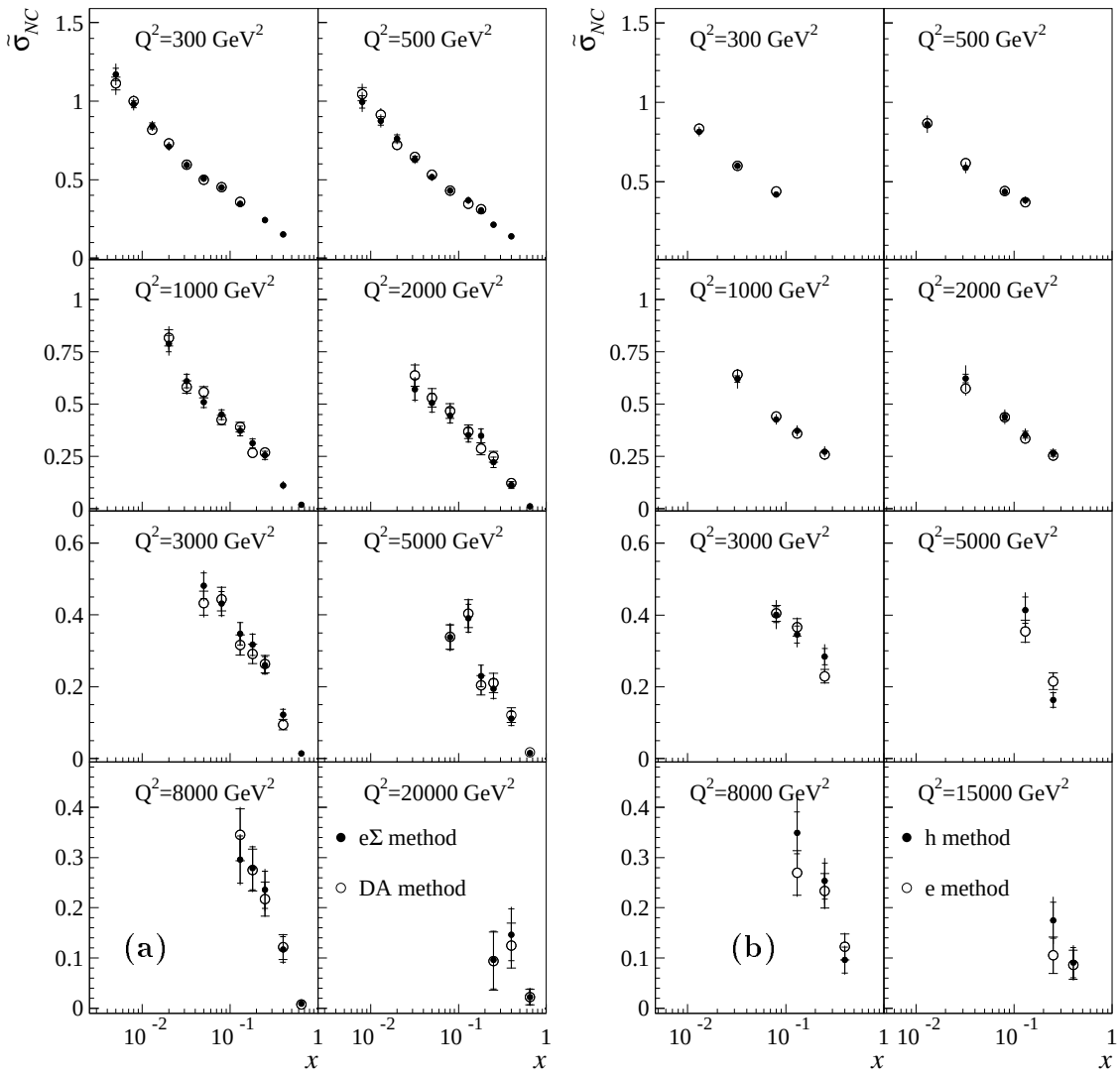

Figure 9.10: *Comparison of the NC reduced cross-section $\tilde{\sigma}_{NC}$ measured (a) in the NC binning at eight different Q^2 values, with the DA (open points) and the $e\Sigma$ method (solid points), and (b) in the CC binning with the e (open points) and the h method (solid points).*

at high Q^2[25]. This fit is labelled "NLO QCD Fit" and is also used to define the "Standard Model expectation".

Only data with $Q^2 > 10$ GeV^2 are included in the fit. Additional cuts on the data sets were made to reduce non-perturbative effects and to ensure a suitable treatment of the heavy quarks for this kinematic regime. The details of the fits can be found in [25]. They turn out to give a very similar result: when including the high Q^2 data the fitted NC cross section is about 2% higher at low x and at most 3% lower at high x. The theoretical uncertainty on the Standard Model prediction for the cross section due to the uncertainty on the parton densities is also assessed by making a large number of QCD fits with varying assumptions. Firstly there is an experimental uncertainty due to the correlated systematic uncertainties of the data sets. This is

taken account of by repeating the fits after shifting the data coherently under the influence of any of these errors. Secondly an uncertainty arises due to the theoretical assumptions entering the fits, e.g. the value of $\alpha_s(M_Z^2)$ or the Q^2 cut on the data. The total theoretical uncertainty is given by the quadratic sum of all individual contributions. The uncertainty on the NC cross section is found to be about 3% at low Q^2 and up to 7% at high Q^2. For the CC cross section it is larger: about 5% at low Q^2 and 15% at high Q^2. The two fits discussed above agree within this uncertainty.

Chapter 10

Results and Interpretation

In this section the results of the analysis are presented. The NC and CC cross sections are measured double differentially in x and Q^2 and single differentially in both of these variables. The data are confronted with the Standard Model prediction. The strong interaction sector of the Standard Model is tested by comparing the data to QCD fits based on the DGLAP evolution equations. The sensitivity of the data to weak effects is also studied: it is shown that there is a noticeable influence of Z exchange in the high Q^2 NC data and the CC cross section is interpreted in the context of parameters of the electroweak sector of the Standard Model. The impact of the data on constraints on physics beyond the Standard Model in e^+p scattering is shown. Finally the differences between the e^+p and recent e^-p cross section measurements are discussed.

The cross section measurements presented in this analysis are partially published by the H1 collaboration in [25] and are labelled "H1 e^+p 94-97". In the case where the presented analysis differs from the published result this measurement is labelled "H1 (this analysis)".

10.1 The double differential NC cross section

The NC reduced cross section is shown in figure 10.1 as a function of x at fixed Q^2. It covers the range of $150 \leq Q^2 \leq 30000$ GeV^2 and $0.0032 \leq x \leq 0.65$ which is a substantial extension of the kinematic range compared to previous H1 measurements ($Q^2 \leq 5000$ GeV^2, $x \leq 0.32$). In total the measurement comprises 130 measurement points. The precision of the data is about $4-5\%$ at low Q^2. At high Q^2 the errors become increasingly larger due to the limited statistical precision. The measurement presented in this thesis is compared to the result published by H1 on the same data set (see above). Both analyses are very consistent in the entire kinematic range.

In figure 10.2 the NC data are compared to the "Low Q^2 Fit" and the "NLO QCD Fit" (see section 9.5). Both fits are very similar and give a good description of the data. The steep rise of the measured cross section towards low x is well reproduced

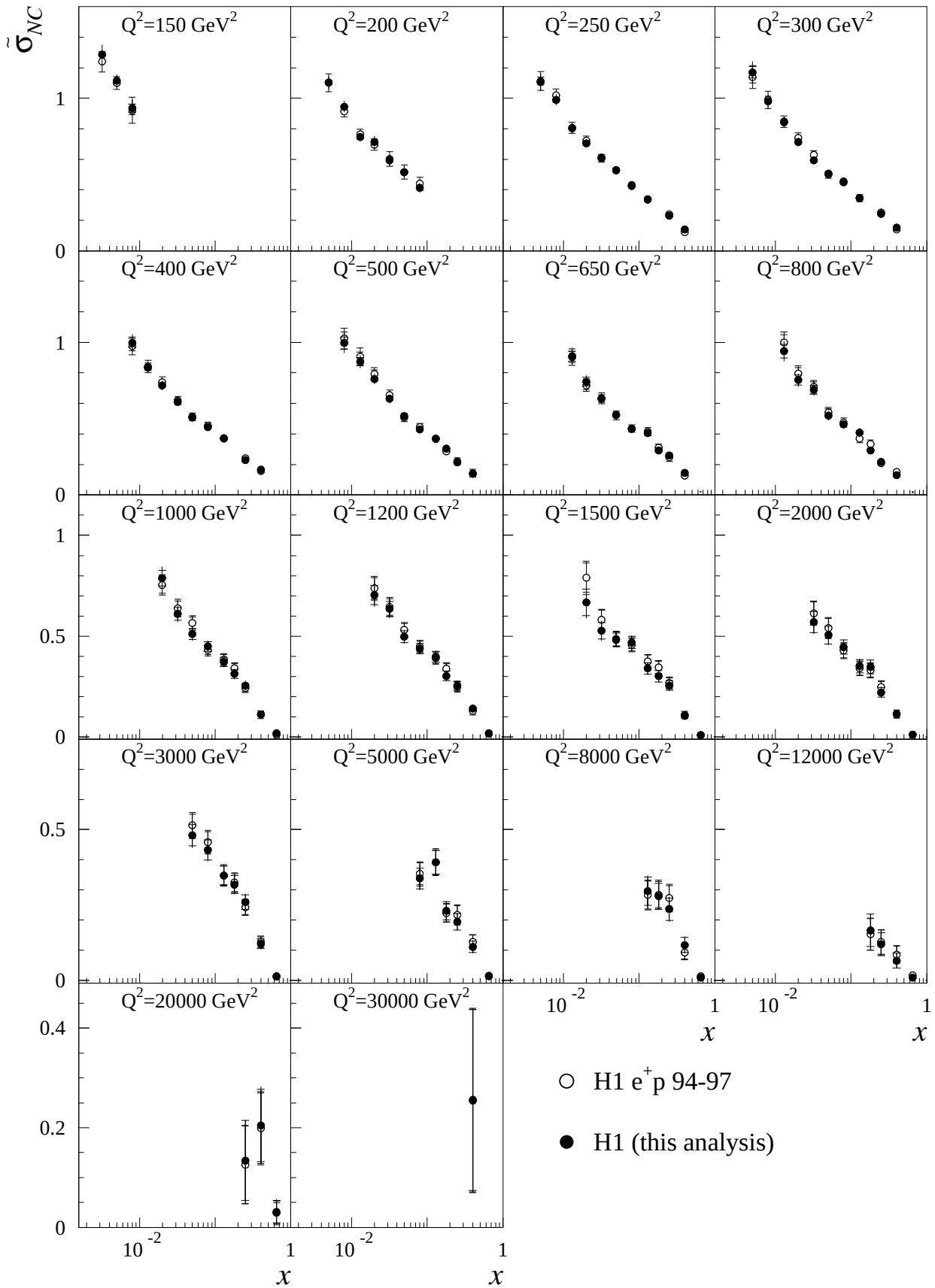

Figure 10.1: *The reduced NC cross section (as defined in eq. 9.6) as a function of x for different values of Q^2. Shown is the result from this analysis (closed circles) and the published H1 result (open circles). The inner error bars represent the statistical errors, the outer ones correspond to the total error.*

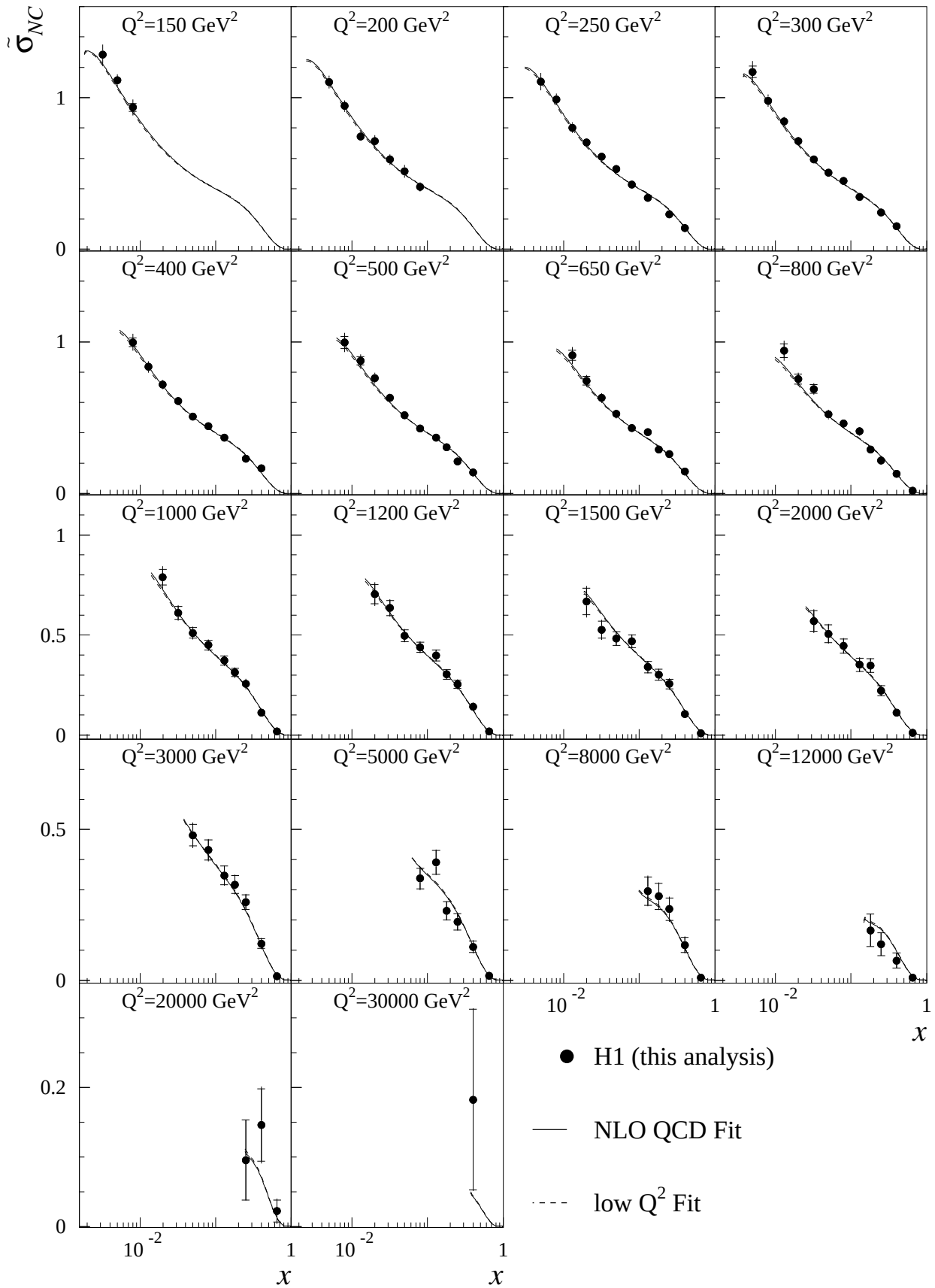

Figure 10.2: *The reduced neutral current cross-section (as defined in eq. 9.6) as a function of x for different values of Q^2 compared with the NLO QCD fit described in [25]. Also shown is the low Q^2 QCD fit. The inner error bars represent the statistical errors, the outer ones correspond to the total error.*

by the QCD predictions.

The Q^2 evolution can better be tested when studying the cross section at fixed x as function of Q^2 as it is done in figure 10.3. All data are well described by the QCD fit, thereby showing that the DGLAP evolution equations of the parton densities are applicable over four orders of magnitude in Q^2 in the region of high x where the valence quarks carry most of the proton momentum.

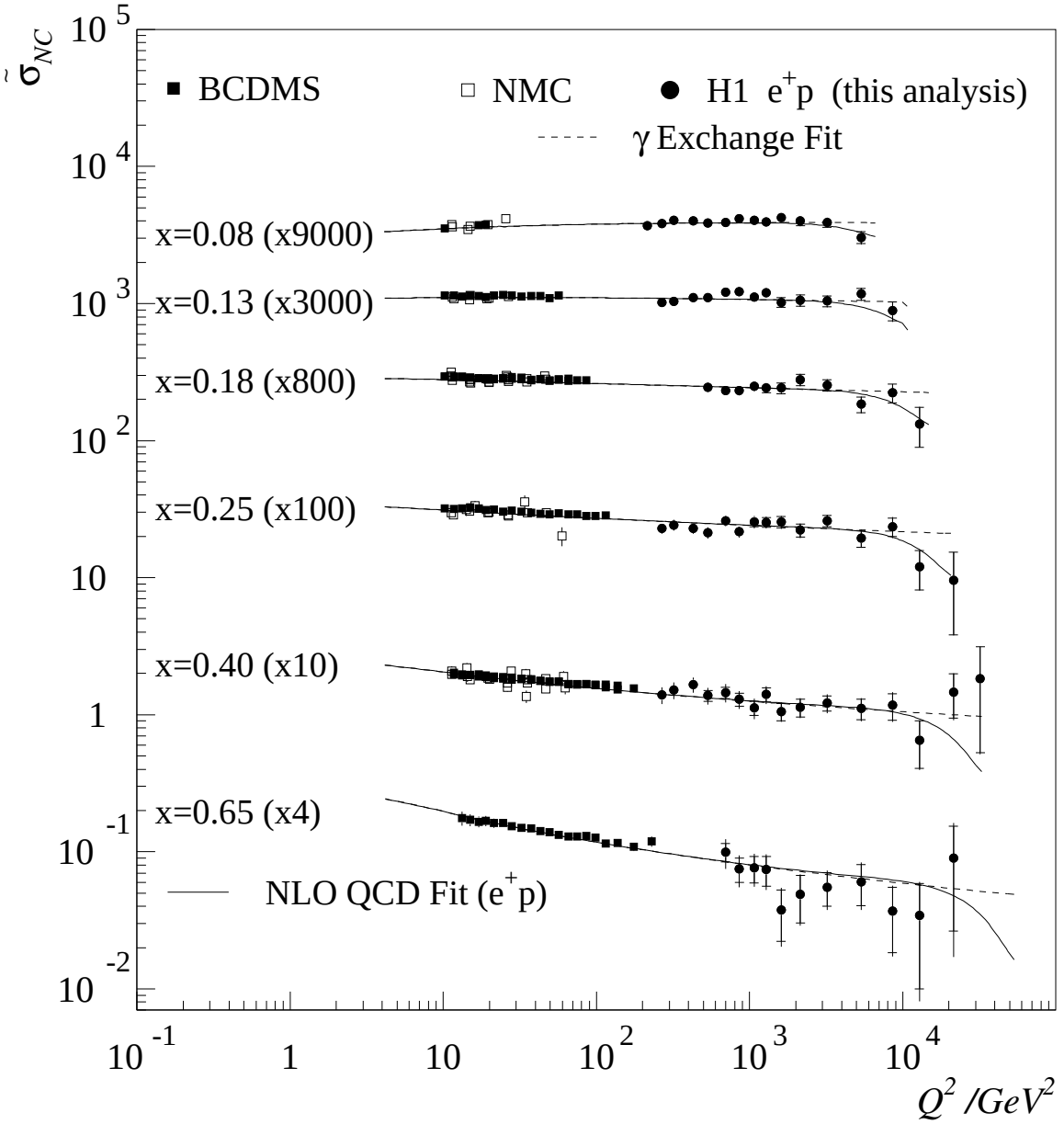

Figure 10.3: *NC reduced cross-section (as defined in eq. 9.6, solid points) at high x compared with Standard Model expectations as given by the NLO QCD fit (solid line) and with the γ-exchange fit (dashed line). The inner error bars represent the statistical errors, the outer ones correspond to the total error. Also shown are the NMC data (open squares), and the BCDMS data (solid squares)*

At the largest Q^2 a decrease of the cross section is observed in the data for $x < 0.4$. This decrease is explained by the negative interference of the photon with the Z boson. The extent to which the data are sensitive to Z exchange is assessed by the comparison with a QCD fit where no Z exchange is considered, i.e. setting $x\tilde{F}_3 = 0$, $\tilde{F}_2 = F_2$ and $\tilde{F}_L = F_L$. This fit is also shown in the figure and labelled "γ Exchange Fit". The data agree better with the Standard Model prediction (NLO QCD Fit) than with the γ Exchange Fit: the χ^2 of the H1 NC data increases by 14 units from 114 to 128. 11 units come from the H1 NC data with $Q^2 > 5000$ GeV^2 while the description of all other data is nearly unchanged. The Standard Model prediction was evaluated using $M_Z = 91.187$ GeV [107].

The $x = 0.4$ bin is of particular interest since this x-value corresponds to an invariant mass of the positron-quark system of ≈ 200 GeV where an excess of events above the Standard Model was observed by the H1 collaboration based on 1994-96 data [30]. This excess is seen in the present analysis in the two highest Q^2 bins with a significance of about 2.3σ. Note, that at lower Q^2 the data are in good agreement with the QCD expectation and there is no systematic trend to exceed the theoretical prediction. The ability to measure at these high x values down to $Q^2 = 250$ GeV^2 is one of the most important achievements in the present analysis. It was only possible due to the improvement in the calibration, the suppression of noise and backscattering contributions and the usage of the $e\Sigma$ method. Note, that in this kinematic region there were no cross section measurements before this result.

The cross section is shown in figure 10.4 for the two highest x bins on a linear vertical scale. The data are compared to the NLO QCD fit and to a second fit which was made in the same way apart from that the BCDMS data were not used. It is seen that both fits are very similar at $x = 0.4$ and give a good description of the data. At $x = 0.65$ the two expectations differ by about 20%. The fit that excluded the BCDMS data is significantly lower and gives a better description of the H1 data. However, it fails to describe the BCDMS data. At the lowest Q^2 the SLAC data are not described by either of the two fits. The reason for this is the contribution of so-called "Higher Twist" terms which are not taken into account in these QCD analyses and expected to be large at high x and low Q^2 (see e.g. [102]).

This study shows that there may be an inconsistency between the BCDMS and H1 NC cross section measurements at very high x. However, both the statistical and systematic uncertainties of the H1 data are large at this x value: the points share a correlated systematic error of $\approx 15\%$ mainly due to the noise subtraction (see table A.2). So within the present uncertainties the BCDMS and H1 measurement are consistent, but it will be interesting to investigate this further with future data.

10.2 Extraction of the Structure Function F_2

The reduced cross section can be converted into the structure function F_2 assuming F_L and xF_3 and applying the weak corrections (see eq. 9.8). The values of F_2 and the corrections are given in table A.2.

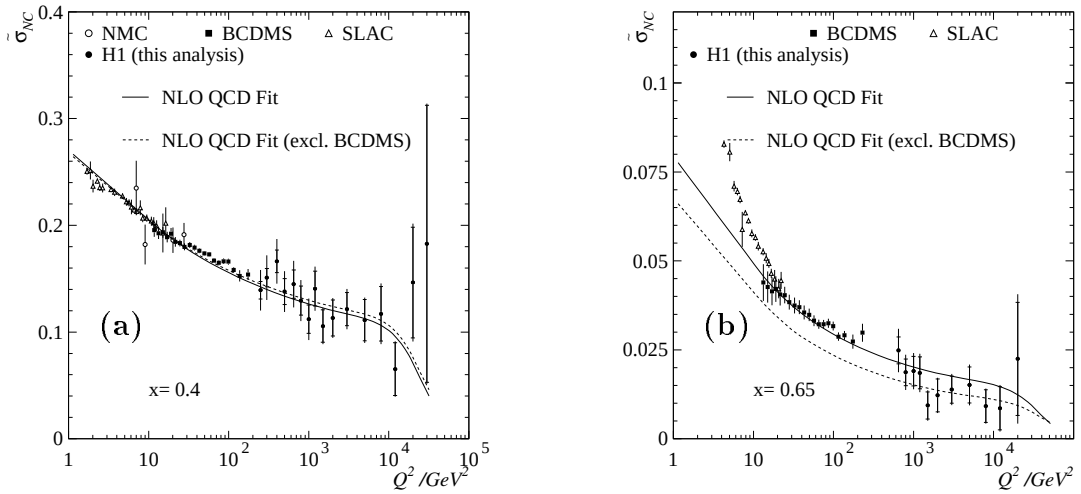

Figure 10.4: *The reduced NC cross section versus Q^2 a) for $x = 0.4$ and b) for $x = 0.65$. Shown are the data from this analysis (closed circles), the NMC (open circles), BCDMS (closed squares) and the SLAC (open triangles) data. The inner error bars represent the statistical errors, the outer ones correspond to the total error. Additionally two QCD fits are shown: the full line is the standard QCD fit where the BCDMS data were used in the fit, the dashed line shows a fit where this data set was not included.*

The proton structure function F_2 is shown in figure 10.5 as function of Q^2 in bins of x. The data presented here are shown together with the preliminary H1 low Q^2 results and the fixed-target measurements. It is seen that the kinematic range where the proton structure function is measured is extended significantly towards low x and high Q^2 by the HERA experiments. At high x the structure function decreases with increasing Q^2, and at low x it increases with increasing Q^2. This violation of the Bjorken scaling behaviour is well reproduced by the QCD fit shown in the figure [1].

10.3 The double differential CC cross section

The double differential charged current cross section $\mathrm{d}^2\sigma_{CC}/\mathrm{d}x\mathrm{d}Q^2$ is measured for $300 \leq Q^2 \leq 15000$ GeV^2 and $0.013 \leq x < 0.4$. The results are given in table A.1. It is displayed in figure 10.6 as a reduced cross section as defined in eq. 9.7.

The double-differential measurement was possible for the first time in H1 due to the increased statistics in the years 1994-97 compared to the 1994 data alone. The errors on the measurements are, however, relatively large ($\approx 30\%$). The data agree well with the theoretical expectation given by the NLO QCD fit shown in the figure.

[1] Since in this figure F_2 is plotted with an artificial offset (c) for display purpose the uncertainties of the measurement are no longer visible at high x.

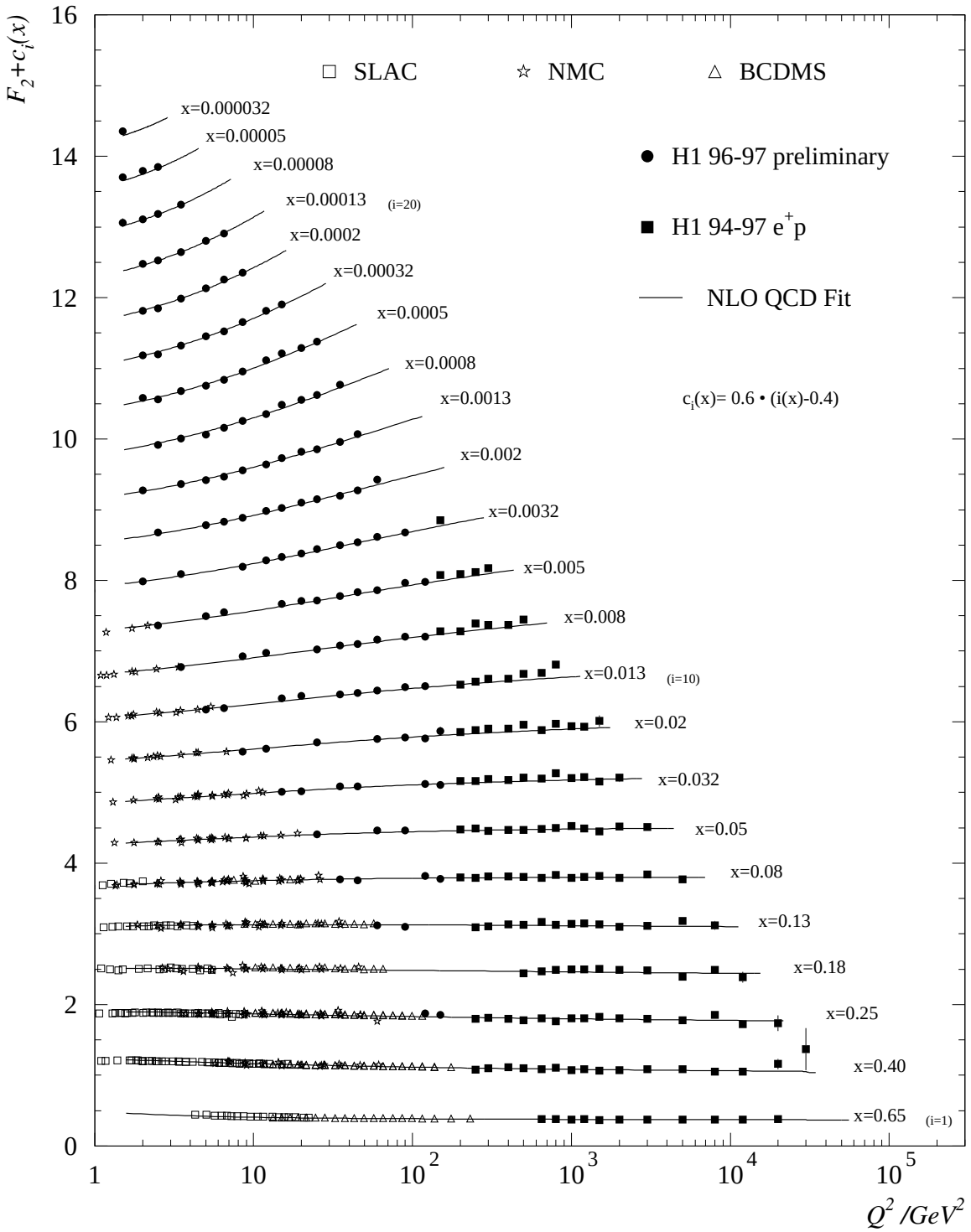

Figure 10.5: *The structure function $F_2(x, Q^2)$ as a function of Q^2 for different values of x. Shown are the data presented in this analysis (solid squares), the preliminary H1 results at $Q^2 < 150$ GeV^2 [103] (solid circles), the SLAC (open squares), NMC (open stars) and BCDMS (open triangles) data. The error bars represent the total error. Also shown is an NLO QCD Fit.*

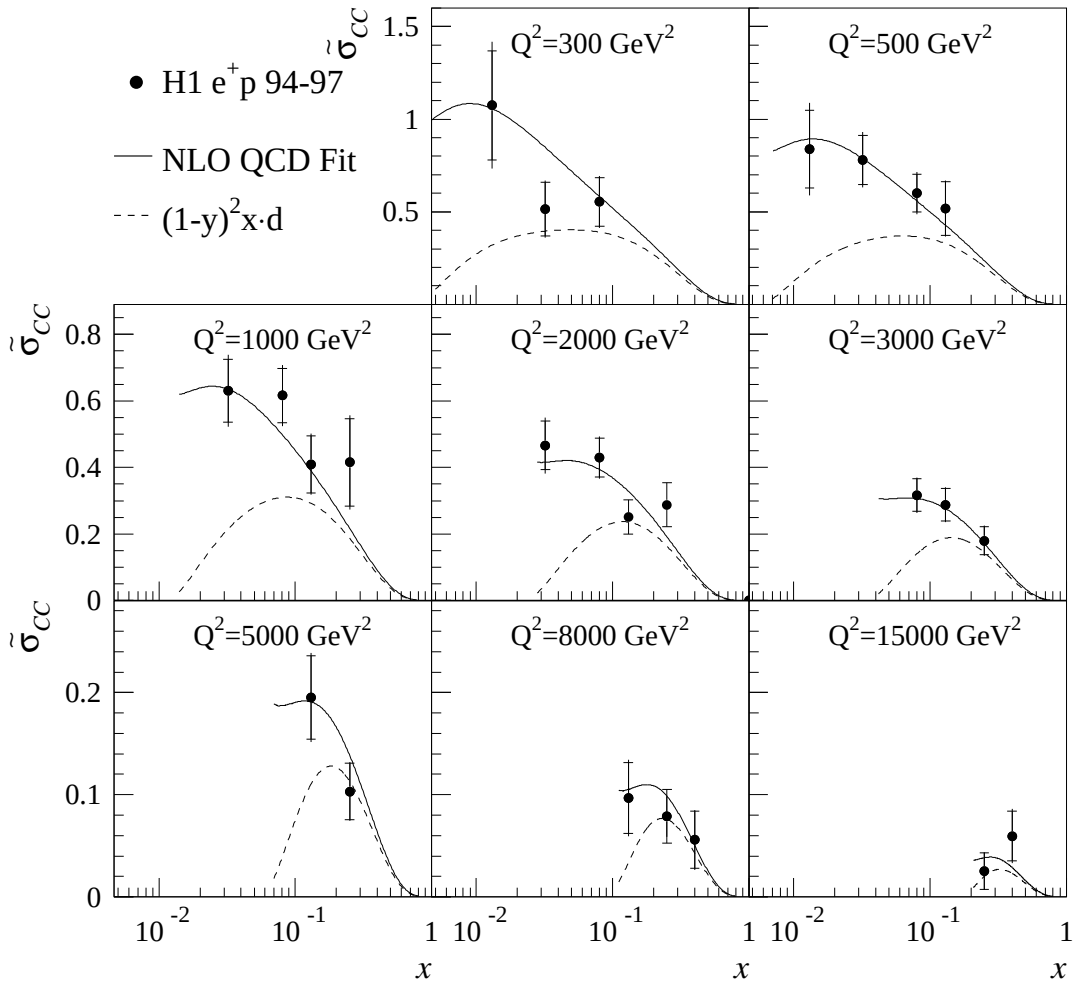

Figure 10.6: *The reduced charged current cross-section (as defined in eq. 9.7) is shown as a function of x for different Q^2 values and compared with the Standard Model expectation (using the NLO QCD Fit parton distributions). Also shown is the d quark contribution to the Standard Model expectation. The inner error bars represent the statistical errors, the outer ones correspond to the total error.*

Also indicated is the contribution from the d quark only. At high x, in the valence quark region, the cross section is dominated by this contribution. The observed rise of the CC cross section towards low x is explained by the contributions of anti-quarks, namely the $\bar{u}$ and $\bar{c}$, since the d quark density is suppressed in this region by the $(1-y)^2$ term (see equation 1.24).

The sensitivity to the quark and anti-quark densities can better be analysed by studying the CC structure function term ϕ_{CC} as function of $(1-y)^2$ at fixed values of x as shown in figure 10.7. The structure function term ϕ_{CC} is determined from the reduced cross section $\tilde{\sigma}_{CC}$ by applying the weak corrections (see eq. 9.7). The data are compared to the prediction from the NLO QCD Fit. Shown are also the contributions to ϕ_{CC} from the anti-quarks, $x(\bar{u}+\bar{c})$, and the quarks, $(1-y)^2 x(d+s)$.

At high x the scaling violations are small (see figure 10.5) so that the Q^2 dependence of the parton densities can to a good approximation be neglected. Therefore in this region the y-dependence of the cross section arises only from the substructure of the proton. For $(1-y)^2 = 0$ the cross section is a direct measure of the density of $\bar{u}$ and $\bar{c}$ quarks and at $(1-y)^2 = 1$ it is a measure of the sum of all negatively charged quarks : $\bar{u}+\bar{c}+d+s$. Therefore the y-dependence of the structure function terms allows the quark and anti-quark content of the proton to be separated. For example at $x = 0.13$ one finds $x(\bar{u}+\bar{c}+d+s) \approx 0.45$ and $x(\bar{u}+\bar{c}) \approx 0.1$ so that $x(d+s) \approx 0.35$ (see figure 10.7).

In the two lowest x bins this simple picture is not valid any more since the parton densities also depend on Q^2 due to the scaling violations. Therefore in this region the theoretical expectation has not the shape of a straight line as at $x \geq 0.08$.

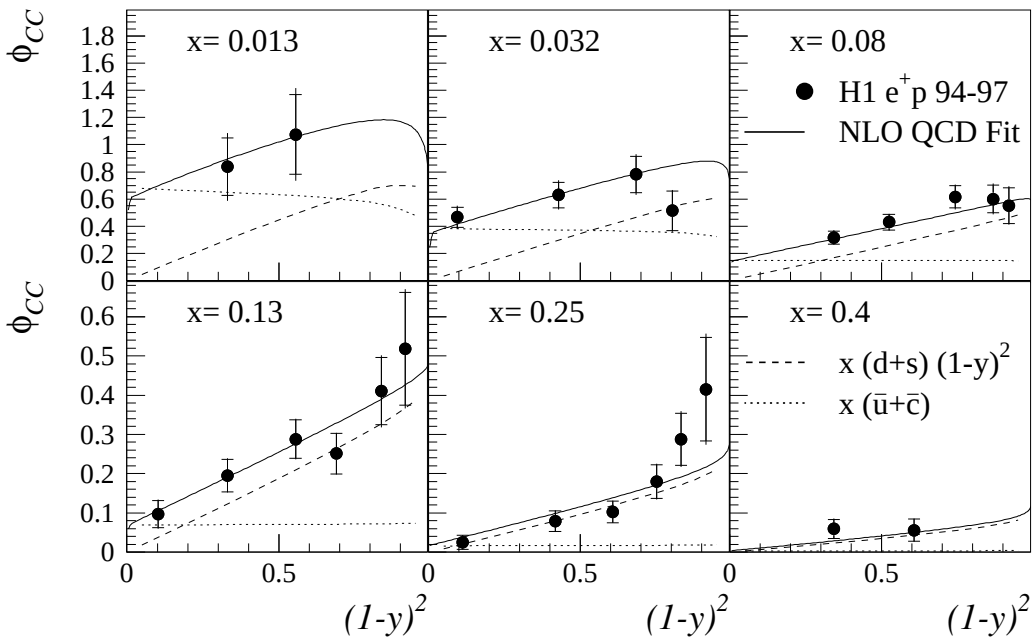

Figure 10.7: *The charged current structure function term ϕ_{CC} (as defined in eq. 9.7) is shown as a function of y for different x values and compared with the Standard Model expectation (solid line) using the NLO QCD Fit parton distributions. Also shown is the $d+s$ quark (dashed line) and $\bar{u}+\bar{c}$ anti-quark contribution (dotted line) to the Standard Model expectation. The inner error bars represent the statistical errors, the outer ones correspond to the total error.*

10.4 The x-dependence of the cross sections

The measurements of the single differential cross sections have smaller systematic uncertainties compared to double differential cross section. The purities and stabilities are in general larger in the individual bins, because events can only migrate in one variable instead of in two.

The NC and CC cross sections $d\sigma_{NC}/dx$ and $d\sigma_{CC}/dx$ are shown in figure 10.8 for $Q^2 > 1000$ GeV^2. The results are given in tables A.5 and A.7. Both cross sections rise towards low x. The Standard Model expectation shown in the figure decreases at low x due to the kinematic cuts $y < 0.9$ and $Q^2 > 1000$ GeV^2.

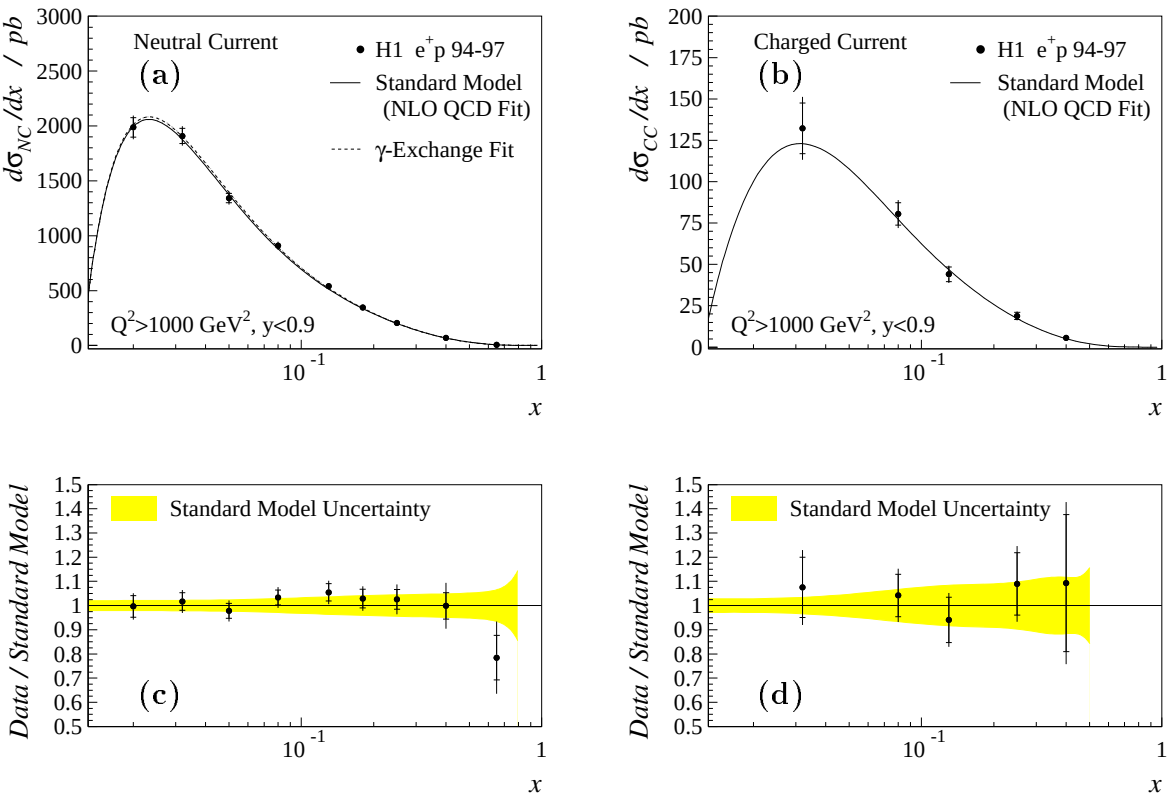

Figure 10.8: *(a) NC and (b) CC cross sections versus x for $Q^2 > 1000$ GeV^2 and $y < 0.9$ compared with the Standard Model expectation as obtained from the NLO QCD Fit (solid line). (c,d) NC,CC cross sections divided by the Standard Model expectations. The grey band in (c,d) represent the uncertainty on the Standard Model (see text). The inner error bars represent the statistical errors, the outer ones correspond to the total error.*

In figures 10.8(c) and (d) the ratios of the measured cross sections to the Standard Model expectations is shown. The grey error band shows the uncertainty on this expectation as determined in the phenomenological QCD analysis (see section 9.5).

The NC and CC data are found to agree well with the Standard Model prediction. The uncertainty on the Standard Model prediction is $\approx 3\%$ for the NC cross section in this region and increases slightly towards high x. The uncertainty on the CC cross section is significantly larger, in particular at high x where it is about 10%. This large uncertainty comes predominantly from the lack of direct constraints on the d-quark density which is only constrained indirectly by the deuteron structure function measurements of BCDMS. The inclusion of these data in the QCD fits requires nuclear binding effects to be modelled which are only known to about 4% [104]. Note that the experimental precision of both measured cross sections is

competitive with the theoretical uncertainties of the corresponding cross section.

The NC cross section is shown in figure 10.9 for $Q^2 > 10000$ GeV^2 where γZ interference and Z exchange are expected to play a role. The result is given in table A.6. The data are compared to the expectation when including weak effects (NLO QCD fit) and when neglecting them (γ-Exchange Fit). The two theoretical predictions are significantly different in contrast to what is observed in figure 10.8 at lower Q^2. The Standard Model prediction is lower that that from the γ-Exchange Fit due to the destructive γZ interference. As already discussed in section 10.1 the data agree better with the Standard Model prediction thereby again illustrating the emerging sensitivity of the data to weak effects at high Q^2.

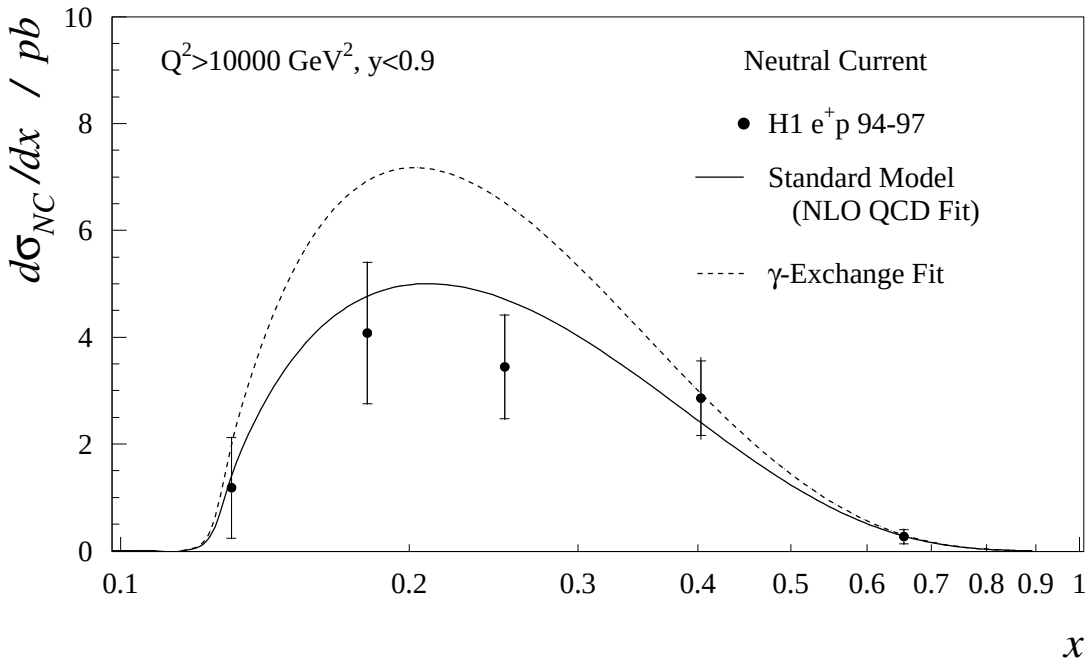

Figure 10.9: *The neutral current cross-section* $\mathrm{d}\sigma_{NC}/\mathrm{d}x$ *for* $Q^2 > 10000$ *GeV*^{2} *and* $y < 0.9$ *compared with the Standard Model expectation (solid line) and with the expectation when the coupling to the Z boson is not taken into account (dashed line). The inner error bars represent the statistical errors, the outer ones correspond to the total error.*

10.5 The Q^2-dependence of the cross sections

The NC and CC cross sections $\mathrm{d}\sigma_{NC}/dQ^2$ and $\mathrm{d}\sigma_{CC}/dQ^2$ are shown in figure 10.10 for $y < 0.9$. The cross sections are corrected for the cuts on $E_e^{'}$ and $P_{T,\nu}$ such that they can be compared in the same kinematic range (see section 9.2). The CC cross section is also corrected for the range $0.85 < y < 0.9$. The values of these corrections are obtained from the NLO QCD Fit and are given in tables A.3 and A.4.

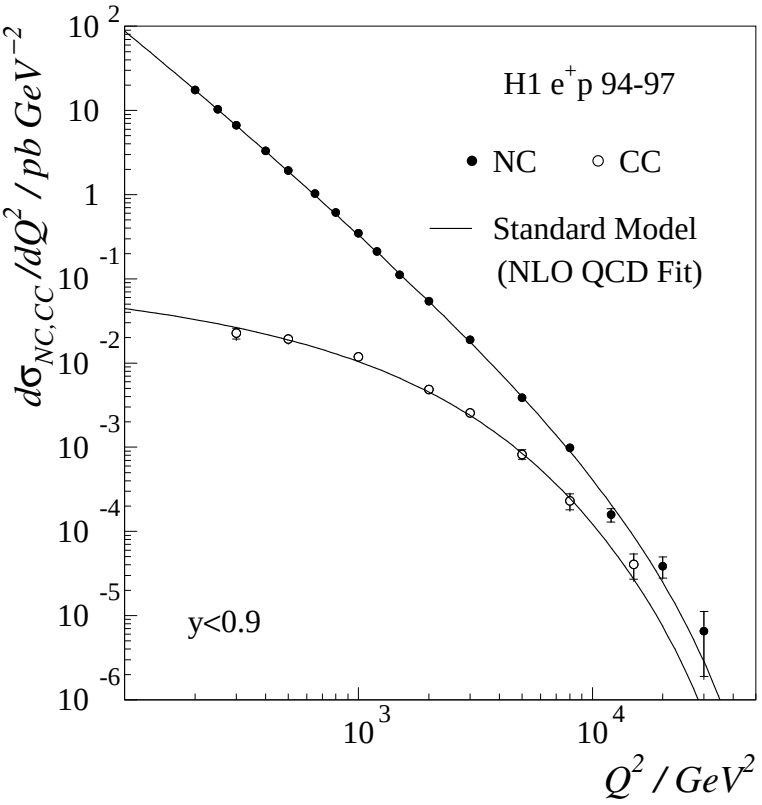

Figure 10.10: *Measurement of the NC (solid points) and CC (open points) cross sections $d\sigma_{NC}/dQ^2$ and $d\sigma_{CC}/dQ^2$ compared with the Standard Model expectation (solid curves). The cross-sections are given for $y < 0.9$. The inner error bars represent the statistical errors, the outer ones correspond to the total error.*

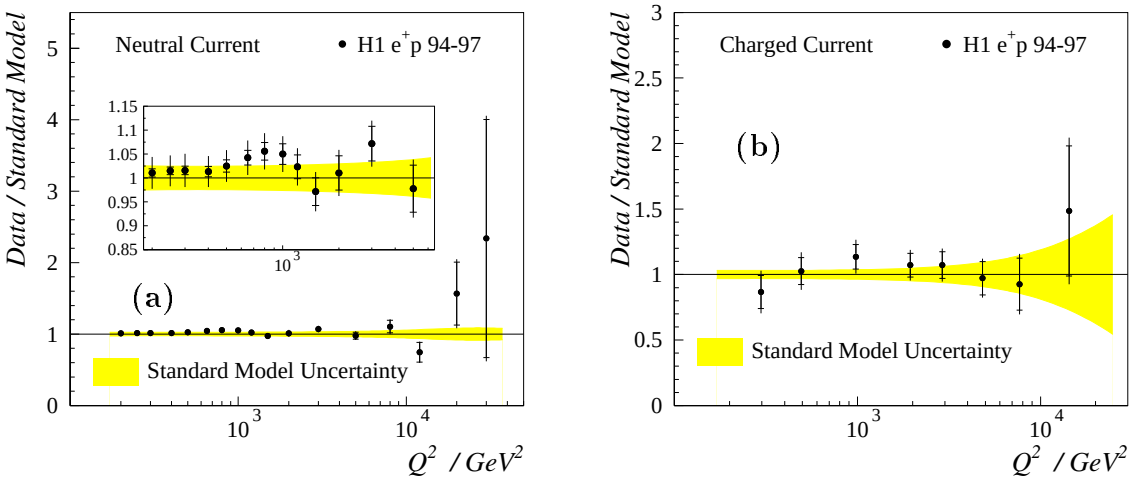

Figure 10.11: *NC (a) and CC (b) cross-sections divided by the Standard Model expectation. The inner error bars represent the statistical errors, the outer ones correspond to the total error. The grey bands represent the Standard Model uncertainty.*

In the measured kinematic range, spanning two orders of magnitude in Q^2, the NC cross section falls by seven orders of magnitude while the CC cross section falls, in a similar kinematic, range by only three orders of magnitude. Both cross section become steeper when approaching higher Q^2. At low Q^2 the observed NC cross section is about 1000 times larger than the CC cross section since the CC cross section is suppressed by the mass of the W-boson $(1/(Q^2 + M_W^2)^2)$ while the NC cross section is dominated by the photon propagator $1/Q^4$. When Q^2 becomes comparable to the squared masses of the heavy gauge bosons ($Q^2 \approx M_W^2 \approx M_Z^2$) the two cross sections are of similar size. This is explained in the Standard Model by the similarity of the couplings and the propagator terms at these high values of Q^2 and reflects the unification of the electromagnetic and weak forces at the electroweak unification scale (see section 1.2). The remaining difference in e^+p scattering is explained by the coupling to different quark flavours and the y dependence of the contributions [2].

Both cross sections are well described by the theoretical expectations as can be seen in 10.11 (c) and (d) where the ratios to the Standard Model predictions is shown. The central value for the Standard Model is again taken to be the NLO QCD fit. The Standard Model uncertainty shown in the figure is due to uncertainties in the parton density functions as discussed in section 9.5. The NC cross section is slightly higher than the central value of the Standard Model, but agrees within the uncertainty on the expectation. In the two highest Q^2 bins the data slightly exceed the expectation. This excess is directly related to the excess at $x = 0.4$, and will be further investigated in section 10.8 in terms of contributions from processes due to physics beyond the Standard Model.

10.6 The Total Charged Current Cross Section

The kinematic range where the total CC cross section is measured is optimised such that the uncertainty on the measurement is minimised. The optimum cuts are found to be $Q^2 > 500$ GeV^2 and $0.03 < y < 0.85$. The statistical error increases when increasing the lower Q^2 cut. When decreasing the lower Q^2 cut or increasing the y range to higher y the uncertainties from the γp background and the V_{ap}/V_p cut become larger so that the total systematic error increases.

The result for the total CC cross section is

$$\sigma_{CC}^{tot}(Q^2 > 500 \text{ GeV}^2, 0.03 < y < 0.85) = 21.5 \pm 0.9(\text{stat.}) \pm 1.4(\text{syst.}) \text{ pb}.$$

This is in agreement with the theoretical expectation of 21.1 ± 1.2(theo.) pb. The theoretical error (theo.) is evaluated in the QCD analysis as described in section 9.5.

[2] In e^-p scattering the CC cross section even exceeds the NC one at very high Q^2 (see figure 1.3(b) and [105]).

10.7 Interpretation of the CC Cross Section

DIS charged current interactions are understood in the Standard Model as the t-channel exchange of a W boson. In this section the consistency of the measurement with the Standard Model is tested and values for the Fermi coupling constant G_F and the mass of the W boson M_W are determined.

The **normalisation** of the CC cross section is given by the Fermi coupling constant G_F. It is determined most precisely from the measurement of the μ life time and yields $G_\mu = 1.16637(1) \times 10^{-5}$ GeV^{-2} [107]. Other measurements of electroweak parameters can be translated into a measurement of G_F as shown in [108]. Although the precision of these other measurements is more than 100 times worse than that of G_μ, the comparison of these measurements with the measurement from the μ-decay can be used to set constraints on new physics [108].

The $\boldsymbol{Q^2}$ **dependence** of the cross section is mainly determined by the term $M_W^4/(Q^2 + M_W^2)^2$. For $Q^2 \ll M_W^2$ this term is negligible and the cross section is only proportional to G_F and the structure function term. In this kinematic region measurements were made in fixed-target experiments which demonstrated the validity of the Standard Model at low Q^2 [12, 13, 14]. When $Q^2 \approx M_W^2$ the term $M_W^4/(Q^2 + M_W^2)^2$ can not any longer be neglected so that the cross section falls more steeply with increasing Q^2. This kinematic region can only be accessed at HERA. The highest precision on the mass of M_W is achieved at LEP II [109] and the Tevatron [110]: the world average is presently $M_W = 80.394 \pm 0.042$ [111].

In the Standard Model M_W and G_F cannot be chosen freely but are related to each other and to the other Standard Model parameters

$$G_F = \frac{\pi \alpha M_Z^2}{\sqrt{2}(M_Z^2 - M_W^2)M_W^2} \frac{1}{1 - \Delta r(\alpha, M_W, M_Z, M_{Higgs}, m_{top})} \tag{10.1}$$

with $\sin^2 \theta_W = 1 - M_W^2/M_Z^2$. This relation is also known as the 'G_F constraint'. In lowest order there are only three independent parameters of the Standard Model, e.g. α, M_Z and M_W. Due to loop corrections an additional dependence on m_{top} and M_{Higgs} arises which is included in the term Δr. Since α and M_Z are known precisely [107] the relation between the parameters G_F and M_W, which appear in the CC cross section formula (eq. 1.12), is uniquely predicted in the Standard Model if the masses of the Higgs boson and the top quark are known.

In the first part of this section the G_F constraint is ignored. The focus of this part will be make a measurement of these two parameters independent of the Standard Model theory. The values determined in this section will be called G_{CC} and M_{prop} corresponding in the Standard Model to G_F and M_W respectively. In the last part of this section the relation between M_W and G_F is used to test the sensitivity of the CC cross section to the mass of the Higgs boson.

In order to determine G_{CC} and M_{prop} from the CC cross section a fit of the following functional form was made to the data

$$\left[\frac{\mathrm{d}^2\sigma_{CC}}{\mathrm{d}x\mathrm{d}Q^2}\right]_{theo} = \frac{(G_{CC})^2}{2\pi x}\left[\frac{M_{prop}^2}{M_{prop}^2+Q^2}\right]^2 \cdot \phi_{\mathrm{CC}}(x,Q^2)$$

The result of the fit taking only the statistical errors into account is

$$\begin{aligned} G_{CC} &= 1.176 \pm 0.043 \times 10^{-5}\ \mathrm{GeV}^{-2} \\ M_{prop} &= 79.8 \pm 5.6\ \mathrm{GeV}. \end{aligned}$$

The two parameters are largely correlated: the correlation parameter is $\rho = -81.7\%$. The deviation from a correlation of 100% arises from the term $1/(M_W^2 + Q^2)^2$. The result is illustrated in figure 10.12, where the 39% confidence level contour, corresponding to an increase in χ^2 by 1 point, is shown. It is seen that the parameters G_{CC} and M_{prop} agree with the most precise values of G_μ and M_W respectively which are also indicated in figure 10.12. Also shown is the result obtained by the ZEUS collaboration [112] and the combination of the H1 and ZEUS result. The smaller errors in the ZEUS measurement are mainly due to higher statistics at low P_T^{miss} for charged current events.

The agreement of G_{CC} with G_μ implies the universality of the CC interaction over a wide range from $Q^2 \approx 0$ to $Q^2 \approx 10000$ GeV^2. Before the start of the HERA experiments this was tested in CC reactions in fixed target neutrino experiments only up to $Q^2 \approx 100$ GeV^2 [13]. The comparison of the propagator mass with the measurement of the W-boson mass in time-like processes therefore constitutes an important consistency check of the Standard Model. For this purpose another fit is made where G_{CC} is fixed to the experimental value of G_μ and only the propagator mass M_{prop} is left free. Deviations of M_{prop} from M_W, as measured in time-like processes, could be caused by a second heavier W-boson which couples to the fermions in the same way as the Standard Model W-boson, but is too heavy to be produced on mass-shell at LEP or Tevatron. This fit yields

$$M_{prop} = 80.9 \pm 3.3(\mathrm{stat.}) \pm 1.7(\mathrm{syst.}) \pm 3.7(\mathrm{theo.})\ \mathrm{GeV}$$

with a χ^2/ndf of $19.9/(25-1) = 0.83$. The theoretical error (theo.) is determined by evaluating the uncertainties on the QCD fit parameters as discussed in section 9.5. The largest uncertainty comes from the variation of the $\bar{u}/\bar{d}$ parametrisation and the deuteron binding correction [25]. This determination can be seen as a direct measurement of M_W since it is independent of assumptions on other electroweak parameters like e.g. M_{Higgs} or M_{top}. When combining the H1 and ZEUS result the statistical error decreases to 2.0 GeV.

The result is illustrated in figure 10.13 in which are shown the ratio of the measured CC cross section $\mathrm{d}\sigma_{CC}/\mathrm{d}Q^2$ and of the Standard Model prediction from the Low Q^2 Fit, to the result of the propagator mass fit. Note, that the theoretical error is as large as the experimental one. Therefore the precision of this measurement in e^+p scattering with future data will only be improved significantly, if the uncertainty

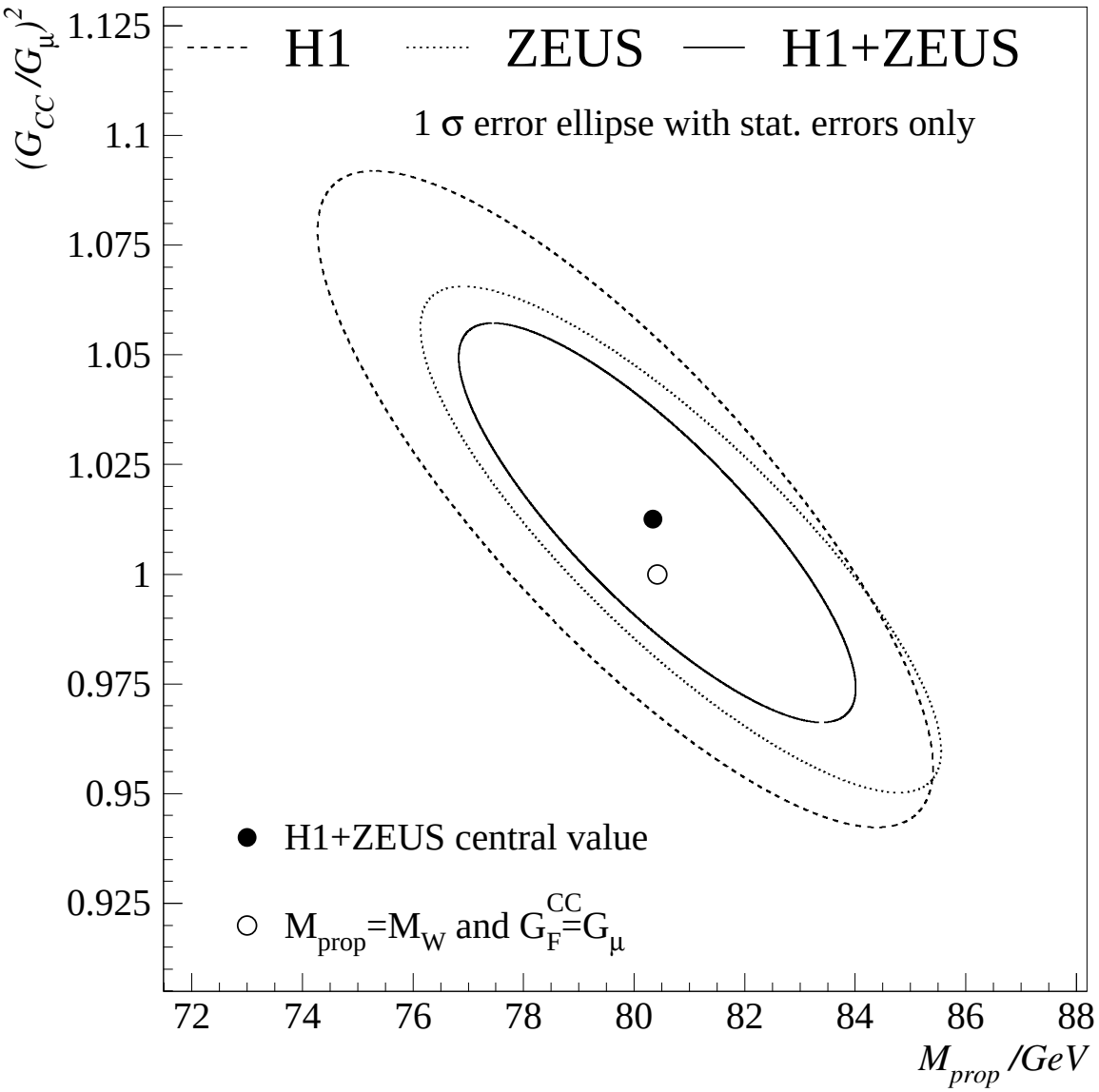

Figure 10.12: *The H1 (dashed line) and ZEUS (dotted line) result for the fit to G_{CC} and M_{prop} as free parameters. Shown is the ellipse corresponding to an increase of χ^2 by 1 based on the statistical error. The contour and the central value (closed circle) of the combination of the H1 and ZEUS result (solid line) is also shown. The Standard Model expectation where $G_{CC} = G_\mu$ and $M_{prop} = M_W$ is indicated (open circle).*

on the parton density functions is reduced by a similar amount as the statistical and systematic uncertainties. Further tests of the propagator will be possible in $e^- p$ scattering where the e^- mainly couples to the u quark of which the density in the proton is better known than that of the d quark. An additional sensitivity is expected from the comparison of the cross sections for different polarisations of the lepton beam. This will be possible after the HERA luminosity upgrade "HERA

2000".

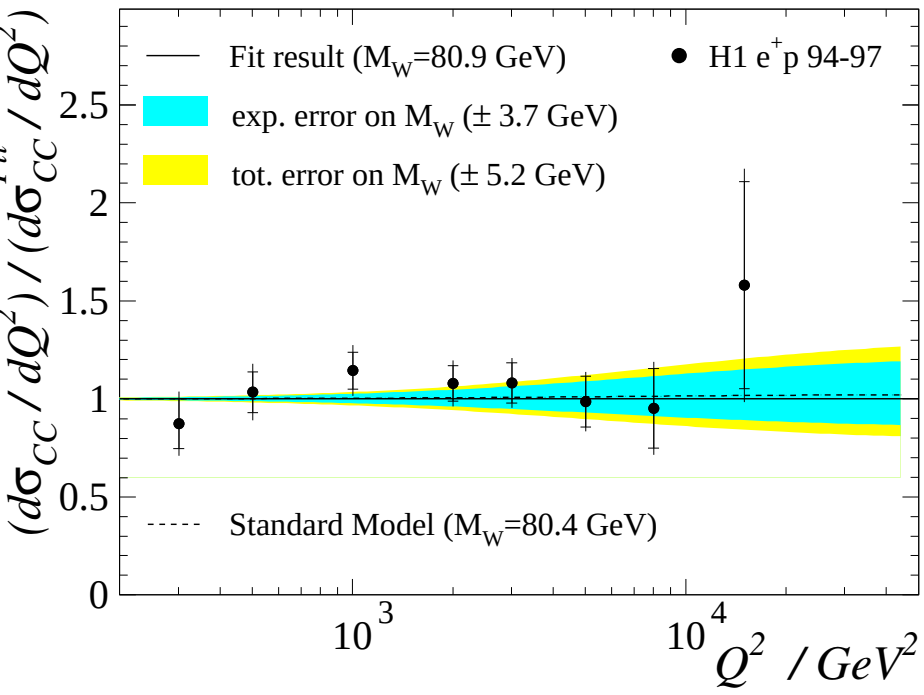

Figure 10.13: *CC* $\mathrm{d}\sigma/\mathrm{d}Q^2$ *cross section divided by the result of the fit of the propagator dependence of the CC cross-section. The bands indicate the effect of a variation of* M_{prop} *by the experimental* (± 3.7 *GeV) and the total* (± 5.0 *GeV) error.*

The sensitivity of the CC cross section to the only unknown Standard Model parameter M_{Higgs} can be illustrated using the measurement of the total CC cross section. The total CC cross section is mainly sensitive to G_F which is related to α, the masses of the W, Z and Higgs bosons and the top quark as shown in eq. 10.1. The parameters α and M_Z are precisely measured and are fixed to the experimental values for this analysis. The uncertainty on the total cross section can easily be translated into an uncertainty on M_W using the G_F constraint:

$$\Delta M_W = \left(\frac{\mathrm{d}\sigma}{\mathrm{d}M_W}\right)^{-1} \Delta\sigma \simeq 60 \text{ MeV} \cdot 100 \cdot \frac{\Delta\sigma}{\sigma} \qquad (10.2)$$

The precision on the total cross section is 7.7% as shown in section 10.6. This translates into a precision on M_W of $\delta M_W = 460$ MeV when assuming $M_{Higgs} = 100$ GeV and $m_{top} = 174$ GeV. Note that this precision on M_W can only be seen as a consistency check of the Standard Model and not as a direct measurement of the mass of the W boson.

The term Δr also depends on $\ln M_{Higgs}$: a variation of the Higgs boson mass from 100 GeV to 300 GeV changes the expectation by about 1% from 21.1 pb to 21.3 pb. Due to the dependence of Δr on m^2_{top} a change of the top quark mass by ± 5 GeV results in a change for the cross section expectation by ∓ 0.1 pb, i.e. 0.3%.

The measured cross section is in agreement with the theoretical expectation and with the present experimental uncertainty there is no sensitivity to the mass of the Higgs boson. Only if the experimental error was decreased by a factor of ten could a distinction be made between $M_{Higgs} = 100$ GeV and $M_{Higgs} = 300$ GeV. However, this is only true if the uncertainty on the parton densities, presently 5.7%, is also decreased significantly as stated before.

10.8 Constraints on Physics beyond the Standard Model

Since the NC and CC cross sections are well described by the Standard Model, i.e. no significant deviation was found, they can be used to set constraints on extensions of the physics of the Standard Model.

One possibility of setting constraints on new physics in a model independent way is to analyse the data in terms of contact interactions as described in section 1.4. Such an analysis was performed on the preliminary results of the NC cross section $\mathrm{d}\sigma/\mathrm{d}Q^2$ [115]. A large number of different fits were made assuming different kinds of couplings, e.g. vector or axial couplings to left- or right-handed particles. Since all fits are consistent with no contact term, limits on lepton-quark compositeness scales, virtual leptoquark exchange and form factors were obtained. The best fit yields a compositeness scale of $\Lambda^-_{LR} = 1.8$ GeV for a particle which interferes in a destructive way with the Standard Model bosons (Λ^-) and the lepton is left-handed and the quark right-handed. This fit is, however, consistent with $\Lambda^-_{LR} = \infty$. The best fit and the corresponding lower limit with 95% confidence level are shown in figure 10.14. In addition the 95% C. L. limit is shown for the compositeness scale parameter Λ^+_{LR}. This is a similar scenario with the only difference that the particle interferes constructively instead of destructively with the Standard Model bosons.

In general a destructive interference term is favoured since the ratio of the measured cross section to Standard Model expectation decreases at $Q^2 \approx 8000$ GeV^2 and rises at the highest Q^2. The 95% C.L. limits on the compositeness scale Λ vary between 1.2 and 5.0 GeV.

If such a particle is a leptoquark the limits on the compositeness scale parameter can be translated into limits depending on the mass M_{LQ} and coupling strength λ of the leptoquark. The limits are in the range $M_{LQ}/\lambda \approx 200 - 1000$ GeV.

The NC cross section can also be analysed in order to obtain limits on the presence of fermion substructure. A convenient way is to introduce form factors [113] which depend on Q^2:

$$f(Q^2) = 1 - \frac{1}{6} R^2 Q^2$$

where R denotes the "fermion radius". The expression for the cross section is then

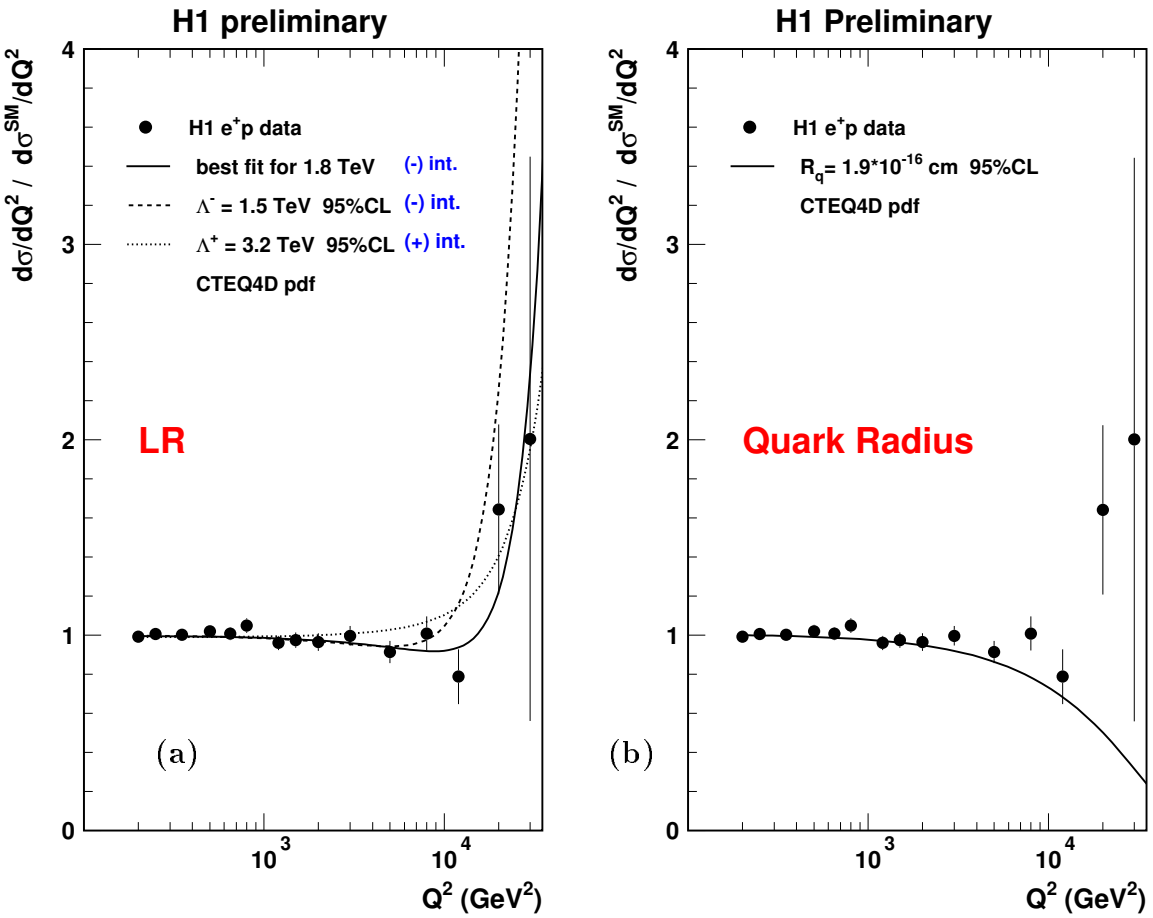

Figure 10.14: *NC cross section divided by the Standard Model expectation using CTEQ4D parton distributions. a) The data (solid points) are compared to the best contact interaction fit (solid line) and the limits at 95% C.L. for Λ^-_{LR} (dashed) and Λ^+_{LR} dotted line) (see text). b) The data are compared to the theoretical expectation of the NC cross section when assuming a finite quark radius of $R_q = 1.9 \cdot 10^{-19}$ cm (see text). The errors represent the quadratic sum of statistical and uncorrelated systematic uncertainties.*

modified

$$\frac{\mathrm{d}\sigma_{NC}}{\mathrm{d}Q^2} = \frac{\mathrm{d}\sigma^{SM}_{NC}}{\mathrm{d}Q^2} f_e(Q^2) f_q(Q^2)$$

where $\mathrm{d}\sigma^{SM}_{NC}/\mathrm{d}Q^2$ denotes the Standard Model expression. The fit of this function to the NC cross section with R as the only free parameters yields

$$R < 1.9 \times 10^{-16} \text{ cm}$$

as an upper limit with 95% confidence level. This result can be interpreted as a limit on the "quark radius" since the point-like nature of the electron is already established down to much lower distances [114]. The effect of a form factor corresponding to a quark radius of $R = -1.9 \times 10^{-16}$ cm is shown in figure 10.14b. More details on the

contact interaction analysis and the form factor determination also can be found in [116].

The slight excess at $x = 0.4$ at high Q^2 (see figure 10.3) could be caused by the resonant production of a positron-quark bound state called leptoquark. A dedicated analysis was carried out on the same data as used for this measurement and limits on the mass and coupling of leptoquark bosons were obtained. The results of this analysis can be found in [117].

10.9 Comparison with e^-p Cross Sections

The analysis of the H1 data taken in 1998/99 when electrons were collided with protons followed very closely the analysis presented here. Together with the change of charge the proton energy was also increased from $E_p = 820$ GeV to $E_p = 920$ GeV corresponding to an increase in centre of mass energy to ≈ 320 GeV. The integrated luminosity of the e^-p data sample is $\mathcal{L} = 15.3$ pb^{-1}.

A comparison of the NC e^-p and e^+p cross sections is shown in figure 10.15 (a). It is seen that the magnitude of the e^-p cross section is similar to that in e^+p scattering at low $Q^2 \lesssim 3000$ GeV^2. As Q^2 becomes larger the e^- and e^+p cross sections become increasingly different This is expected from the Standard Model as can be seen from the theoretical predictions indicated in the figure which agree with the corresponding cross sections. The reason for this behaviour is the interference of the photon with the Z boson which is destructive in e^+p scattering and constructive in e^-p scattering. Note that the e^-p data agree with the Standard Model prediction which is determined from the NLO QCD Fit discussed in 9.5 including only high Q^2 e^+p data.

The CC cross section is larger in e^-p scattering at all values of Q^2 due to the coupling to different quark flavours. While the e^+ is predominantly scattered off the d-quark and is suppressed by the kinematic factor $(1-y)^2$, the e^- is mainly scattered off the u-quark and there is no y-dependent factor (see eq. 1.24). Since the u-density is about two times larger than the d-density and the coupling to the u-quark is not suppressed by $(1-y)^2$ the e^-p cross section is larger than the e^+p cross section. At low Q^2 the difference is a factor of about $2-3$ while at high Q^2 it is about a factor of 10. This is seen in accordance with the Standard Model expectation when comparing the H1 e^-p and e^+p measurements in figure 10.15 (b).

Also shown are the Standard Model predictions for e^+p scattering for $\sqrt{s} = 320$ GeV. The differences due to the increased beam energy are much smaller than the differences due to the lepton charge in both NC and CC scattering.

In figure 10.16 the NC reduced cross sections for e^-p and e^+p scattering are shown versus Q^2 at different values of x. The reduced cross section in e^+p scattering decreases with increasing Q^2 (and correspondingly y) for a fixed value of x due to the negative interference of the photon and the Z. The opposite is true for the reduced cross section in e^-p scattering which increases due to the constructive

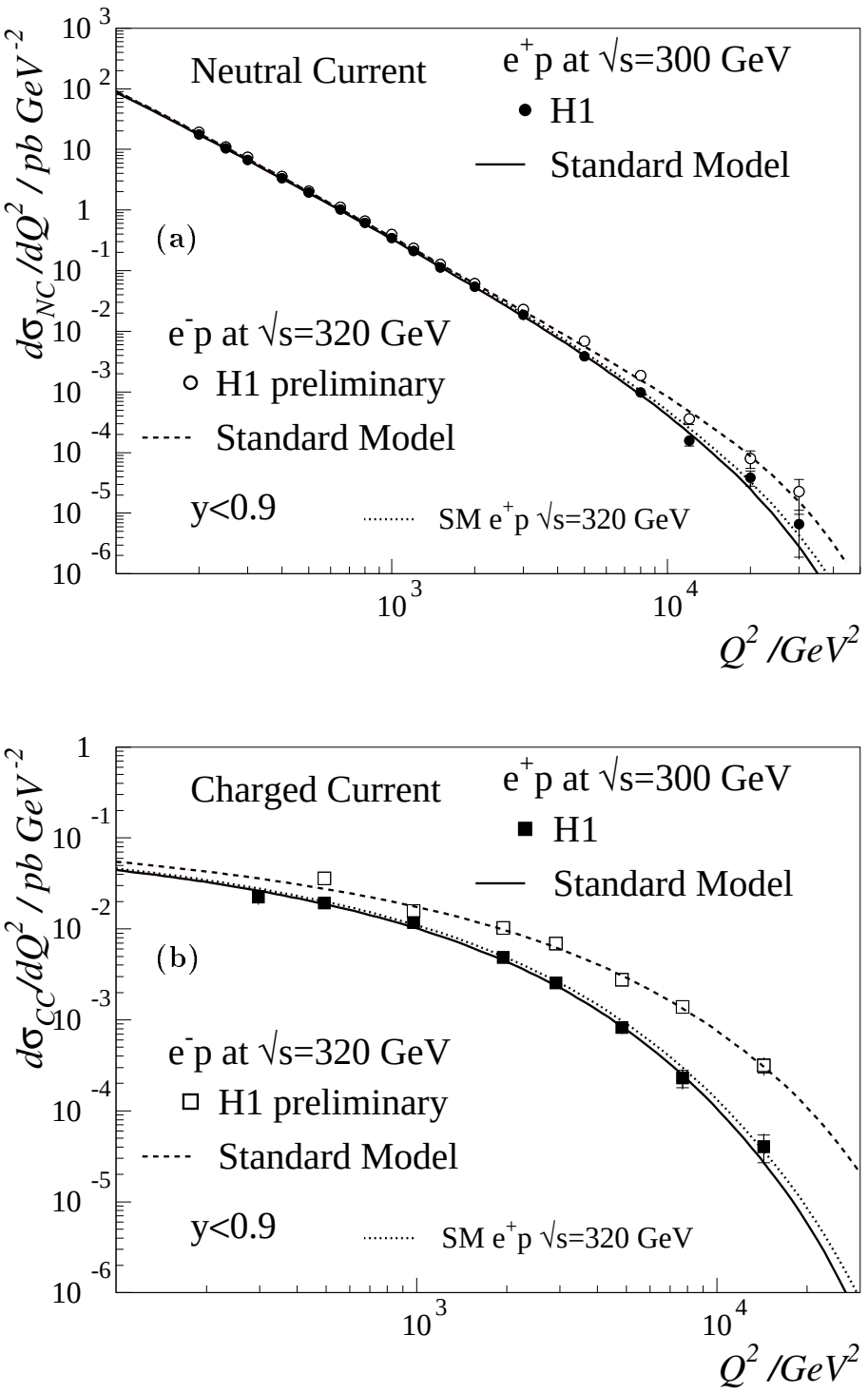

Figure 10.15: a) *NC cross section* $\mathrm{d}^2\sigma_{NC}/\mathrm{d}x\mathrm{d}Q^2$ *for* e^+p *and* e^-p *scattering. b) CC cross section* $\mathrm{d}^2\sigma_{CC}/\mathrm{d}x\mathrm{d}Q^2$ *for* e^+p *and* e^-p *scattering. The inner error bars represent the statistical errors, the outer ones correspond to the total error. The measurements are compared to the corresponding Standard Model predictions as given by the NLO QCD fit described in [25]. Also shown is the Standard Model prediction for* e^+p *scattering at* $\sqrt{s} = 320$ *GeV.*

interference of these two bosons. With increasing Q^2 the difference between e^-p and e^+p scattering becomes more pronounced in accordance with the Standard Model expectation. At $x = 0.4$ where there is a slight excess above the expectation seen in the e^+p data the e^-p data show no indication for such an excess.

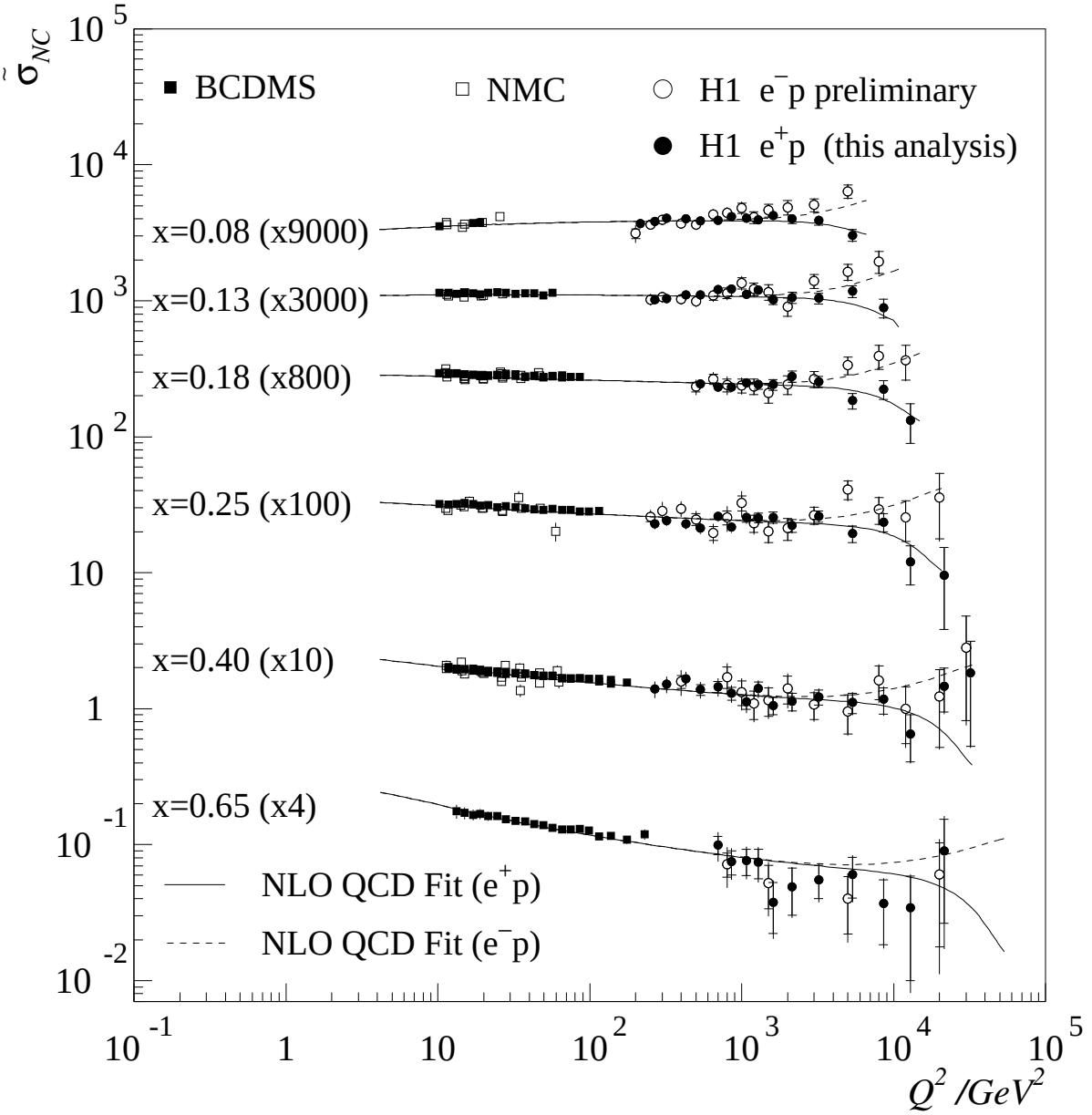

Figure 10.16: *NC reduced cross-section at high x for e^+p (closed circles) and e^-p (open circles) scattering. The data are compared with the corresponding Standard Model expectations as given by the NLO QCD fit. For display purposes the bin centres of the e^+p data are slightly moved from their true values. The inner error bars represent the statistical errors, the outer ones correspond to the total error. Also shown are the NMC data (open squares), and the BCDMS data (solid squares).*

Chapter 11

Summary and Outlook

In this thesis a measurement was presented of charged and neutral current cross sections in e^+p scattering using data taken between 1994 and 1997 in the H1 detector at HERA. Both cross sections are measured double differentially and single differentially in x and Q^2.

All studies necessary for the cross section measurements were presented. For certain studies novel analysis techniques were developed, in others existing techniques were adapted or refined for this analysis. The main emphasis was placed on studying the detector response in the data. Since a Monte Carlo simulation was used for the extraction of the cross section it was ensured that the simulation describes the data in every respect. A substantial reduction of the uncertainty on the electromagnetic and hadronic energy scales of the Liquid-Argon calorimeter was achieved.

The NC cross section is measured in the range $150 \leq Q^2 \leq 30000$ GeV^2 and $0.0032 \leq x \leq 0.65$. The double differential measurement comprises 130 data points with a precision of about 5% per data point at low Q^2 where the systematic error dominates. At higher Q^2 the precision is limited by the statistics of the data. The proton structure function F_2 was extracted from the measured cross section.

The CC cross section is measured in the kinematic range $300 \leq Q^2 \leq 15000$ GeV^2 and $0.013 \leq x \leq 0.4$. The double differential measurement comprises 25 points with a precision of about 30% per data point. The uncertainty on the cross section is dominated by the statistical error.

All measured cross section are in agreement with the Standard Model expectation:

- The Q^2 evolution of the NC cross section is well described by QCD fits based on the DGLAP evolution equations. The cross sections show the expected scaling violations at low x where the cross section rises with increasing Q^2 and at high x where it decreases with increasing Q^2. At high x the precision of the data is, however, limited.

- The CC cross section behaves as expected from the Standard Model. It was shown that the y-dependence of the CC cross section can be used to disentangle

the quark and anti-quark densities. At high x the CC cross section is mainly sensitive to the d-quark density.

- The Q^2 dependence of the NC cross section is much steeper than that of the CC cross section in the measured kinematic range. While the NC cross section is about 1000 times larger than the CC cross section at the lowest values of Q^2, the size of the two cross sections becomes similar at the electroweak unification scale $Q^2 \approx M_W^2 \approx M_Z^2$. The experimental uncertainty of the cross section is similar to the theoretical uncertainty on the Standard Model expectation which is evaluated in the QCD analysis.

- The NC cross section shows clear evidence for the destructive interference of the Z boson and the photon at high Q^2. This is seen in the double differential cross section and in the x-dependence of the cross section for $Q^2 > 10000$ GeV^2.

- The Fermi constant and the propagator mass were extracted from a fit to the CC cross sections. They are in agreement with the values of G_μ and M_W measured in other experiments.

- There is a slight excess of the NC cross section above the Standard Model expectation at the highest values of Q^2 and $x \simeq 0.4$. An analysis of the Q^2 dependence of the NC cross section in terms of contact interactions reveals limits on the compositeness scale of $\mathcal{O}(1 - 5$ TeV) depending on the exact structure of the new type of interaction.

There are several interesting issues remaining which can be investigated:

- The measurement of the NC cross section at lower Q^2 and x with the data of 1996 and 1997 will allow the gluon density to be determined with an accuracy of about 10% at low x. This analysis is presently in preparation for publication.

- The publication of the measurement of both the CC and NC cross section using the e^-p data collected in 1998 and 1999 will focus on the comparison of the e^-p and e^+p cross sections. The preliminary data show that the cross sections differ as expected in the Standard Model.

- A measurement of the structure function xF_3 can be made from the difference between the e^-p and e^+p NC cross sections. A direct measurement is possible from the comparison of the 1998/99 e^- data with the 1999/2000 e^+ data which are both taken at $\sqrt{s} = 320$ GeV. It remains to be seen whether the statistical precision is sufficient to extract xF_3 from these data.

- In general, the statistical error is still limiting the precision of the CC measurement and the NC measurement at high Q^2 and high x. Both measurements will therefore profit from the luminosity upgrade of the HERA machine which starts in May 2000. The CC data will then help to reduce the uncertainty on the d quark density in the proton. Both the NC and CC measurements will allow more precise tests of the electroweak sector of the Standard Model to be made.

- Polarised beams, which become available after the luminosity upgrade, will make possible a determination of the weak couplings of the light quarks.
- High statistics are necessary to establish whether the excess observed in the NC cross section at the highest Q^2 is only a statistical fluctuation or is due to contributions from physics beyond the Standard Model.

Appendix A

Tables of Results

Q^2 (GeV^2)	x	$\frac{d^2\sigma_{CC}}{dxdQ^2}$ $\frac{pb}{GeV^2}$	δ_{sta} (%)	δ_{tot} (%)	δ_{unc} (%)	δ_{V+} (%)	δ_{h+} (%)	δ_{N+} (%)	δ_{B+} (%)	ϕ_{CC}	δ^{QED} (%)
300	0.0130	0.637	27.4	31.8	9.9	11.9	−1.6	0.2	−3.8	1.075	−1.2
300	0.0320	0.124	28.1	30.0	7.9	6.2	−1.6	0.9	−0.7	0.514	−1.9
300	0.0800	0.053	23.8	25.5	7.0	2.2	−1.5	−0.6	−0.3	0.553	−2.5
500	0.0130	0.468	25.1	29.7	9.2	12.1	−1.5	1.0	−3.9	0.838	−0.3
500	0.0320	0.177	17.0	19.2	6.7	5.2	−1.2	0.4	−0.3	0.781	−0.4
500	0.0800	0.055	17.0	18.9	6.1	2.3	−0.5	0.2	−0.2	0.601	−1.5
500	0.1300	0.029	27.8	29.4	7.8	0.3	−1.3	−0.9	−0.1	0.518	−1.4
1000	0.0320	0.124	15.0	17.1	6.5	4.6	−1.3	0.2	−0.2	0.630	−0.2
1000	0.0800	0.049	13.3	14.8	5.7	2.1	−0.8	0.6	−0.1	0.616	−0.1
1000	0.1300	0.020	20.9	22.5	6.4	0.6	−0.7	−0.4	−0.1	0.410	0.0
1000	0.2500	0.010	31.7	34.1	10.4	0.0	3.1	−4.2	−0.1	0.415	−1.0
2000	0.0320	0.072	15.7	18.1	6.9	5.4	−1.5	1.7	−0.4	0.466	−2.9
2000	0.0800	0.026	13.5	14.8	5.6	1.6	0.3	0.3	−0.2	0.430	−2.5
2000	0.1300	0.009	20.6	21.4	5.7	0.4	0.3	0.4	−0.2	0.251	−0.1
2000	0.2500	0.006	23.0	24.6	7.0	0.1	−0.2	−2.2	−0.1	0.288	−0.6
3000	0.0800	0.016	15.2	16.8	6.2	2.1	1.5	0.7	−0.2	0.317	−2.6
3000	0.1300	0.009	17.0	18.1	5.8	0.6	0.8	0.6	−0.1	0.288	−4.1
3000	0.2500	0.003	23.6	25.1	7.8	0.1	2.5	−0.6	−0.1	0.180	−1.6
5000	0.1300	0.004	21.0	22.3	7.0	0.6	2.5	0.4	−0.1	0.195	−4.9
5000	0.2500	0.001	26.8	27.6	6.5	0.2	1.2	0.6	−0.1	0.103	−4.1
8000	0.1300	0.001	35.7	38.5	12.6	1.2	6.5	1.5	−0.3	0.097	−8.2
8000	0.2500	0.001	33.5	35.4	9.9	0.2	5.2	1.2	−0.1	0.079	−5.3
8000	0.4000	0.000	50.0	52.4	13.1	0.0	8.5	−0.8	0.0	0.056	−7.5
15000	0.2500	0.000	71.2	73.5	15.9	1.0	8.4	1.1	−0.2	0.025	−10.1
15000	0.4000	0.000	40.9	44.5	15.3	0.1	8.1	0.9	−0.1	0.059	−9.1

Table A.1: *CC double differential cross-section $d^2\sigma_{CC}/dxdQ^2$. The statistical error (δ_{sta}), the total error (δ_{tot}), the uncorrelated systematic error (δ_{unc}) are given. Also given are the contributions to the correlated systematic error from a positive variation of one standard deviation of the error coming from the cut on the V_{ap}/V_p ratio (δ^{V+}_{cor}), of the hadronic energy error (δ^{h+}_{cor}), of the error due to the noise subtraction (δ^{N+}_{cor}) and of the error due to the background subtraction (δ^{B+}_{cor}). The structure function term $\phi_{\rm CC}$ (computed assuming $M_W = 80.4$ GeV) and the δ^{QED} term defined in eq. 9.9 are also given. The normalization uncertainty, which is not included in the systematic error, is 1.5%.*

Q^2 (GeV^2)	x	$\tilde{\sigma}_{NC}$	δ_{sta} (%)	δ_{tot} (%)	δ_{unc} (%)	δ_{E+} (%)	$\delta_{[q]+}$ (%)	δ_{h+} (%)	δ_{N+} (%)	δ_{B+} (%)	F_2	Δ_{all} (%)
150	0.0032	1.284	1.7	5.1	4.7	−0.3	−0.6	0.3	−0.5	−0.7	1.338	−4.0
150	0.0050	1.114	1.8	3.7	3.1	0.0	−0.9	0.2	−0.3	−0.1	1.129	−1.3
150	0.0080	0.935	2.9	5.6	4.5	−1.4	−0.2	−0.5	0.9	0.0	0.939	−0.4
200	0.0050	1.103	1.8	3.8	3.2	−0.4	−0.2	0.8	−0.8	−0.2	1.131	−2.5
200	0.0080	0.945	1.8	4.0	3.3	0.6	−0.9	0.0	−0.3	0.0	0.952	−0.8
200	0.0130	0.745	2.2	3.8	3.0	−0.6	−0.2	0.0	−0.2	0.0	0.746	−0.2
200	0.0200	0.712	2.6	5.7	4.8	−1.2	−1.0	−0.6	0.1	0.0	0.713	−0.1
200	0.0320	0.592	3.2	5.9	4.6	−1.1	−1.2	−0.6	0.0	0.0	0.592	0.0
200	0.0500	0.515	3.8	8.2	6.4	−3.0	−1.0	0.0	−1.2	0.0	0.515	0.0
200	0.0800	0.412	4.4	7.4	5.5	−1.7	−1.1	−0.4	0.1	0.0	0.412	0.0
250	0.0050	1.105	2.2	5.2	4.7	−0.1	−0.5	0.2	−0.5	−0.6	1.152	−4.1
250	0.0080	0.989	2.0	3.8	3.1	0.4	−0.2	0.4	−0.6	−0.1	1.001	−1.2
250	0.0130	0.802	2.0	4.3	3.6	1.0	−0.6	0.3	−0.6	0.0	0.806	−0.4
250	0.0200	0.704	2.1	3.8	3.1	−0.2	−0.6	0.0	−0.5	0.0	0.704	−0.1
250	0.0320	0.610	2.2	3.9	3.1	0.4	0.0	0.1	−0.6	0.0	0.610	0.0
250	0.0500	0.528	2.5	4.3	3.3	−0.5	−0.6	0.0	−1.0	0.0	0.528	0.0
250	0.0800	0.426	2.7	4.5	3.1	−0.2	−0.4	−0.3	−1.6	0.0	0.426	0.0
250	0.1300	0.338	3.0	5.1	3.8	0.6	−0.9	−0.9	0.9	0.0	0.338	0.0
250	0.2500	0.229	4.2	8.9	5.6	1.9	−0.8	−1.5	4.8	0.0	0.229	0.1
250	0.4000	0.139	5.9	13.7	4.9	0.9	−0.5	−1.3	11.2	0.0	0.139	0.1
300	0.0050	1.170	3.3	6.1	4.8	0.9	−0.4	−0.2	0.0	−1.1	1.247	−6.2
300	0.0080	0.980	2.3	4.1	3.2	0.0	−0.6	0.7	−0.8	−0.2	0.999	−1.9
300	0.0130	0.842	2.3	3.8	3.0	0.0	−0.4	0.2	−0.3	0.0	0.847	−0.6
300	0.0200	0.712	2.3	4.0	3.2	0.6	−0.4	0.4	−0.6	0.0	0.713	−0.2
300	0.0320	0.594	2.5	4.3	3.4	0.7	−0.6	−0.2	−0.7	0.0	0.594	0.0
300	0.0500	0.507	2.7	4.7	3.6	0.9	−0.6	0.2	−0.8	0.0	0.507	0.0
300	0.0800	0.449	2.8	5.0	3.8	0.8	−1.0	−0.2	−1.3	0.0	0.449	0.0
300	0.1300	0.345	2.9	6.0	4.8	2.0	−0.5	−0.2	−0.6	0.0	0.344	0.1
300	0.2500	0.242	3.8	9.3	6.5	3.0	−1.0	−1.7	4.0	0.0	0.242	0.1
300	0.4000	0.151	5.7	13.9	8.0	3.9	−0.8	−1.8	8.8	0.0	0.151	0.1
400	0.0080	0.997	2.8	5.6	4.8	0.3	−0.5	0.4	−0.5	−0.3	1.034	−3.6
400	0.0130	0.834	2.7	4.4	3.3	0.6	−0.4	0.4	−0.5	0.0	0.843	−1.1
400	0.0200	0.717	2.7	4.3	3.2	0.4	−0.4	0.3	−0.5	0.0	0.720	−0.4
400	0.0320	0.609	2.8	4.3	3.0	0.5	−0.3	0.4	−0.6	0.0	0.609	−0.1
400	0.0500	0.506	3.1	5.0	3.6	1.5	−0.4	−0.1	−0.6	0.0	0.506	0.0
400	0.0800	0.444	3.1	4.9	3.4	0.6	−0.5	0.0	−1.4	0.0	0.444	0.0
400	0.1300	0.369	3.2	4.8	3.3	1.1	−0.2	−0.5	−0.5	0.0	0.369	0.1
400	0.2500	0.229	4.3	8.7	5.4	2.8	−0.4	−1.6	4.2	0.0	0.229	0.1
400	0.4000	0.166	6.3	12.6	6.3	3.7	−1.0	−1.4	7.9	0.0	0.166	0.1
500	0.0080	0.995	4.0	6.4	4.9	−0.9	−0.2	−0.2	0.0	−0.9	1.059	−6.0
500	0.0130	0.874	3.2	4.8	3.4	0.8	−0.3	0.7	−0.6	0.0	0.890	−1.8
500	0.0200	0.761	3.2	4.6	3.2	0.2	0.4	0.6	−0.6	0.0	0.765	−0.6
500	0.0320	0.630	3.1	4.6	3.2	0.0	−0.6	0.2	−0.8	0.0	0.631	−0.2
500	0.0500	0.515	3.4	4.7	3.1	0.7	−0.4	0.2	−0.3	0.0	0.515	0.0
500	0.0800	0.430	3.7	5.4	3.4	0.8	−0.4	0.5	−1.8	0.0	0.430	0.0
500	0.1300	0.368	4.2	6.5	4.2	2.3	−0.8	−0.8	0.0	0.0	0.368	0.1
500	0.1800	0.305	4.8	7.3	4.7	2.4	−0.4	−1.0	0.5	0.0	0.305	0.1
500	0.2500	0.212	6.2	9.2	4.9	2.3	−0.4	−1.2	4.0	0.0	0.212	0.1
500	0.4000	0.138	8.8	13.9	6.9	3.8	−0.4	−1.9	6.9	0.0	0.138	0.2
650	0.0130	0.910	3.6	6.1	4.8	−0.4	0.0	0.4	−0.5	−0.1	0.940	−3.2
650	0.0200	0.743	3.8	5.3	3.5	0.0	−0.6	0.8	−0.6	0.0	0.752	−1.2
650	0.0320	0.629	3.8	5.1	3.3	0.4	−0.1	0.6	−0.4	0.0	0.632	−0.4
650	0.0500	0.525	3.9	5.4	3.5	1.3	−0.6	−0.2	−0.3	0.0	0.525	−0.1
650	0.0800	0.432	4.1	5.5	3.3	0.9	−0.4	0.2	−1.2	0.0	0.432	0.0
650	0.1300	0.404	4.5	5.8	3.5	0.3	−0.3	0.2	−0.9	0.0	0.404	0.1
650	0.1800	0.291	5.4	7.4	4.4	2.1	−0.5	−0.9	0.0	0.0	0.290	0.1
650	0.2500	0.259	6.1	8.8	5.1	2.9	−0.3	−1.3	1.8	0.0	0.259	0.2
650	0.4000	0.145	9.2	15.1	8.0	4.8	−0.8	−2.2	7.1	0.0	0.145	0.2
650	0.6500	0.025	15.2	24.6	10.1	5.8	−1.2	−2.7	15.2	0.0	0.025	0.3

Table A.2: *NC reduced cross-section $\tilde{\sigma}_{NC}$ with statistical error (δ_{sta}), total error (δ_{tot}), uncorrelated error (δ_{unc}). Also given are the correlated systematic errors due to a positive variation of one standard deviation of the positron energy error (δ^{E+}_{cor}), of the polar positron angle error ($\delta^{\theta+}_{cor}$), of the hadronic energy error (δ^{h+}_{cor}), of the error due to the noise subtraction (δ^{N+}_{cor}) and of the error due to the background subtraction (δ^{B+}_{cor}). Also given are the corresponding values of F_2 when assuming the correction Δ_{all} (see eq. 9.8). The normalization uncertainty, which is not included in the systematic error, is 1.5%. The table continues on the next page.*

Q^2 (GeV^2)	x	$\tilde{\sigma}_{NC}$	δ_{sta} (%)	δ_{tot} (%)	δ_{unc} (%)	$\delta_{E}+$ (%)	$\delta_{[q]}+$ (%)	$\delta_{h}+$ (%)	$\delta_{N}+$ (%)	$\delta_{B}+$ (%)	F_2	Δ_{all} (%)
800	0.0130	0.942	4.7	7.0	5.0	0.5	−0.5	0.2	0.0	−0.6	0.993	−5.2
800	0.0200	0.753	4.3	5.8	3.7	0.3	0.1	0.7	−0.5	−0.2	0.768	−1.9
800	0.0320	0.689	4.2	5.6	3.4	0.9	−0.4	0.5	−0.3	0.0	0.694	−0.7
800	0.0500	0.521	4.5	6.0	3.7	1.4	−0.4	0.3	−0.4	0.0	0.522	−0.3
800	0.0800	0.462	4.6	6.0	3.5	1.1	0.4	0.4	−0.9	0.0	0.463	−0.1
800	0.1300	0.409	5.3	7.0	4.1	1.3	−0.6	0.0	−1.5	0.0	0.408	0.1
800	0.1800	0.291	6.2	8.3	4.9	2.5	0.3	−0.6	0.9	0.0	0.290	0.2
800	0.2500	0.216	7.4	9.4	4.9	2.3	−0.3	−1.3	1.4	0.0	0.215	0.2
800	0.4000	0.130	10.5	14.9	7.3	4.0	−0.6	−2.3	6.1	0.0	0.129	0.3
800	0.6500	0.019	20.0	26.4	9.1	4.2	−1.2	−2.8	13.8	0.0	0.019	0.3
1000	0.0200	0.788	4.9	7.1	5.1	0.0	−0.4	0.6	−0.4	−0.1	0.814	−3.2
1000	0.0320	0.610	5.2	6.5	3.5	−1.0	−0.3	0.8	−0.5	0.0	0.617	−1.2
1000	0.0500	0.510	5.1	6.3	3.5	0.8	0.0	0.6	−0.4	0.0	0.513	−0.5
1000	0.0800	0.449	5.2	6.3	3.4	0.7	−0.3	0.0	0.0	0.0	0.450	−0.2
1000	0.1300	0.372	6.1	7.2	3.6	−0.2	0.2	0.4	−1.2	0.0	0.372	0.0
1000	0.1800	0.313	6.7	8.4	4.4	2.1	−0.6	−0.3	−0.3	0.0	0.312	0.2
1000	0.2500	0.255	7.6	10.0	5.4	3.2	−0.8	−1.1	1.4	0.0	0.254	0.3
1000	0.4000	0.112	11.9	17.4	9.2	6.2	0.1	−3.6	5.0	0.0	0.112	0.4
1000	0.6500	0.019	21.8	26.8	9.8	4.7	0.6	−2.4	10.8	0.0	0.019	0.5
1200	0.0200	0.704	6.9	8.4	4.8	0.0	−0.4	0.3	−0.3	−0.3	0.739	−4.8
1200	0.0320	0.635	5.9	6.9	3.5	0.6	−0.3	0.8	−0.5	−0.1	0.648	−1.9
1200	0.0500	0.497	5.9	6.8	3.3	0.7	−0.3	0.3	−0.3	0.0	0.502	−0.9
1200	0.0800	0.439	5.9	6.7	3.1	0.0	−0.1	0.4	−0.6	0.0	0.440	−0.4
1200	0.1300	0.398	6.8	7.7	3.3	0.9	−0.2	0.4	−0.4	0.0	0.398	0.0
1200	0.1800	0.303	7.8	8.7	3.5	1.2	−0.2	−0.2	−1.0	0.0	0.303	0.1
1200	0.2500	0.254	8.4	10.0	4.5	2.2	−0.3	−1.3	1.4	0.0	0.253	0.3
1200	0.4000	0.141	11.6	14.7	6.7	3.9	0.6	−1.6	4.2	0.0	0.140	0.5
1200	0.6500	0.019	24.2	29.2	10.8	5.9	−0.8	−4.5	9.5	0.0	0.018	0.6
1500	0.0200	0.667	9.9	11.9	6.4	−1.2	−0.4	−0.6	0.4	−0.5	0.723	−7.7
1500	0.0320	0.527	7.9	9.5	5.2	0.2	−0.3	0.9	−0.5	−0.1	0.544	−3.2
1500	0.0500	0.483	6.9	7.8	3.4	−0.7	−0.2	0.8	−0.6	0.0	0.490	−1.6
1500	0.0800	0.469	6.6	7.4	3.2	0.5	0.0	0.3	0.0	0.0	0.472	−0.8
1500	0.1300	0.340	8.4	9.1	3.5	1.0	−0.2	0.2	−0.4	0.0	0.341	−0.2
1500	0.1800	0.302	9.2	10.1	3.8	1.3	−0.5	−0.6	−0.7	0.0	0.302	0.1
1500	0.2500	0.255	9.4	10.8	4.6	2.6	−0.2	−0.6	0.4	0.0	0.254	0.4
1500	0.4000	0.106	14.3	16.1	5.8	3.1	−0.2	−1.8	2.7	0.0	0.105	0.7
1500	0.6500	0.009	40.8	45.8	13.4	8.9	−1.2	−5.1	11.9	0.0	0.009	0.8
2000	0.0320	0.570	9.0	10.4	5.2	−0.6	0.0	0.6	−0.4	−0.1	0.607	−6.1
2000	0.0500	0.506	8.7	9.7	4.0	0.6	−0.4	0.9	−0.6	0.0	0.523	−3.2
2000	0.0800	0.446	7.9	8.8	3.7	0.7	−0.4	0.7	−0.3	0.0	0.453	−1.7
2000	0.1300	0.352	9.4	10.5	4.1	2.0	−0.2	−0.4	−0.3	0.0	0.354	−0.7
2000	0.1800	0.348	9.8	10.6	3.9	1.1	−0.2	0.3	−0.7	0.0	0.348	−0.1
2000	0.2500	0.222	11.0	12.3	4.8	2.6	−0.2	−1.0	−0.4	0.0	0.221	0.4
2000	0.4000	0.113	14.9	16.6	5.8	3.0	0.1	−1.6	2.5	0.0	0.112	0.9
2000	0.6500	0.012	37.8	40.9	11.9	6.6	0.6	−3.6	7.0	0.0	0.012	1.2
3000	0.0500	0.481	7.4	8.9	4.9	0.2	−0.4	0.6	−0.2	−0.2	0.523	−8.0
3000	0.0800	0.432	7.8	8.6	3.6	0.8	−0.2	0.9	−0.5	0.0	0.454	−4.8
3000	0.1300	0.347	8.9	9.7	3.6	0.8	0.5	0.8	−0.7	0.0	0.355	−2.3
3000	0.1800	0.317	9.4	10.3	4.0	1.5	−0.2	−0.2	−0.2	0.0	0.320	−1.0
3000	0.2500	0.260	9.4	10.2	3.6	1.4	0.1	−0.2	−0.3	0.0	0.259	0.1
3000	0.4000	0.122	12.8	15.6	7.1	4.8	−0.2	−1.5	1.7	0.0	0.120	1.3
3000	0.6500	0.014	27.7	31.7	11.2	7.0	0.9	−4.9	6.1	0.0	0.014	2.0
5000	0.0800	0.338	10.1	11.5	5.3	0.5	0.0	0.8	−0.3	−0.2	0.394	−14.3
5000	0.1300	0.391	10.0	10.9	4.4	0.0	−0.4	0.5	−0.4	0.0	0.428	−8.7
5000	0.1800	0.230	13.1	13.9	4.3	−0.2	−0.3	0.8	−0.2	0.0	0.243	−5.1
5000	0.2500	0.194	14.0	15.4	5.9	2.2	0.2	−0.5	−0.1	0.0	0.198	−2.1
5000	0.4000	0.111	17.4	19.2	7.6	2.5	0.7	−1.1	0.7	0.0	0.110	1.1
5000	0.6500	0.015	33.3	37.8	15.2	8.1	0.9	−3.7	3.1	0.0	0.015	3.0
8000	0.1300	0.296	15.8	17.1	6.4	1.0	−0.5	0.5	0.0	−0.3	0.384	−23.0
8000	0.1800	0.279	15.5	16.3	5.0	0.5	0.2	0.8	−0.3	−0.1	0.332	−16.0
8000	0.2500	0.236	15.6	17.9	8.3	2.3	−0.5	0.5	−0.3	0.0	0.259	−9.0
8000	0.4000	0.117	21.8	24.3	10.0	3.6	0.4	−0.8	0.5	0.0	0.119	−1.5
8000	0.6500	0.009	50.0	53.3	17.9	4.3	0.8	−2.2	1.4	0.0	0.009	3.1
12000	0.1800	0.166	32.3	32.8	5.4	1.2	−0.6	0.7	0.0	−0.7	0.252	−34.3
12000	0.2500	0.120	31.8	32.5	6.7	0.2	0.0	1.0	−0.2	−0.2	0.156	−23.5
12000	0.4000	0.065	37.9	39.6	11.5	2.3	0.4	−0.4	−0.2	−0.1	0.072	−8.8
12000	0.6500	0.009	70.8	76.4	27.9	6.2	1.2	−1.9	1.1	0.0	0.009	0.8
20000	0.2500	0.096	60.0	60.4	7.2	0.2	−0.6	−0.6	0.1	−1.2	0.200	−52.0
20000	0.4000	0.146	35.5	37.8	12.8	1.7	−0.1	1.0	−0.2	−0.1	0.212	−31.1
20000	0.6500	0.022	70.7	80.9	38.6	7.5	2.2	−0.6	0.0	0.0	0.025	−10.0
30000	0.4000	0.183	71.0	71.8	10.7	1.5	−1.0	−1.4	0.2	−0.1	0.440	−58.5

Q^2 (GeV^2)	$\mathrm{d}\sigma_{NC}/\mathrm{d}Q^2$ (pb/GeV^2)	C	δ_{sta} (%)	δ_{tot} (%)	δ_{unc} (%)	δ_{E+} (%)	$\delta_{\theta+}$ (%)	δ_{h+} (%)	δ_{N+} (%)	δ_{B+} (%)
200	$1.629 \cdot 10^{1}$	1.079	0.9	3.3	3.0	−0.8	−0.6	0.0	0.0	0.0
250	$9.646 \cdot 10^{0}$	1.076	0.8	3.2	3.0	0.4	−0.6	0.1	0.1	0.0
300	$6.253 \cdot 10^{0}$	1.071	0.9	3.4	3.2	0.9	−0.6	0.1	−0.2	−0.1
400	$3.130 \cdot 10^{0}$	1.060	1.1	3.2	2.9	0.9	−0.5	−0.1	−0.1	−0.1
500	$1.848 \cdot 10^{0}$	1.049	1.2	3.2	2.8	0.9	0.0	0.0	0.1	−0.1
650	$0.995 \cdot 10^{0}$	1.031	1.5	3.5	2.9	1.1	−0.4	0.1	0.0	−0.1
800	$0.608 \cdot 10^{0}$	1.013	1.7	3.6	2.9	1.1	−0.3	0.0	0.0	−0.1
1000	$0.347 \cdot 10^{0}$	1.000	2.0	3.6	2.8	0.8	0.3	0.0	0.0	−0.1
1200	$0.211 \cdot 10^{0}$	1.000	2.4	3.8	2.8	0.9	−0.1	0.0	0.0	−0.1
1500	$0.112 \cdot 10^{0}$	1.000	3.0	4.2	2.8	1.0	0.2	0.1	0.1	−0.1
2000	$0.541 \cdot 10^{-1}$	1.000	3.5	4.8	3.0	1.0	−0.3	0.0	0.0	−0.1
3000	$0.188 \cdot 10^{-1}$	1.000	3.4	4.5	2.8	0.9	−0.2	0.0	−0.1	−0.2
5000	$0.389 \cdot 10^{-2}$	1.000	5.0	6.2	3.5	−0.8	−0.1	−0.1	0.0	−0.3
8000	$0.987 \cdot 10^{-3}$	1.000	7.9	9.4	4.9	1.4	0.1	0.1	0.0	−0.5
12000	$0.158 \cdot 10^{-3}$	1.000	18.3	20.0	7.9	1.6	0.1	0.1	0.0	−0.6
20000	$0.386 \cdot 10^{-4}$	1.000	28.1	30.9	12.7	2.3	0.0	0.1	0.0	−0.4
30000	$0.656 \cdot 10^{-5}$	1.000	71.2	73.6	18.1	3.3	−0.1	−0.1	0.0	−0.2

Table A.3: *NC cross-section* $\mathrm{d}\sigma_{NC}/\mathrm{d}Q^2$ *measured for* $y < 0.9$ *and* $E'_e > 11$ GeV. *C gives the correction factor for the E'_e cut. The statistical error (δ_{sta}), the total error (δ_{tot}), the uncorrelated systematic error (δ_{unc}) and correlated error sources ($\delta_{E+}, \delta_{\theta+}, \delta_{h+}, \delta_{N+}, \delta_{B+}$) are also given (see caption of table A.2). The normalization uncertainty, which is not included in the systematic error, is* 1.5%.

Q^2 (GeV^2)	$\mathrm{d}\sigma_{CC}/\mathrm{d}Q^2$ (pb/GeV^2)	C	δ_{sta} (%)	δ_{tot} (%)	δ_{unc} (%)	δ_{V+} (%)	δ_{h+} (%)	δ_{N+} (%)	δ_{B+} (%)	δ^{QED} (%)
300	$0.164 \cdot 10^{-1}$	1.382	14.5	18.8	9.3	6.9	−1.6	0.2	−1.8	3.5
500	$0.165 \cdot 10^{-1}$	1.171	10.0	14.0	7.7	5.6	0.8	0.1	−1.1	−0.1
1000	$0.113 \cdot 10^{-1}$	1.041	8.2	11.4	6.6	3.7	−0.6	0.0	−0.3	−2.3
2000	$0.472 \cdot 10^{-2}$	1.027	8.4	10.9	6.2	2.3	0.0	0.2	−0.3	−3.4
3000	$0.247 \cdot 10^{-2}$	1.030	9.6	11.8	6.3	1.4	1.6	0.4	−0.2	−6.6
5000	$0.794 \cdot 10^{-3}$	1.037	13.1	15.3	7.3	0.9	2.3	0.5	−0.1	−9.0
8000	$0.220 \cdot 10^{-3}$	1.044	21.4	24.9	10.8	0.6	6.1	1.0	−0.2	−11.6
15000	$0.382 \cdot 10^{-4}$	1.061	33.4	37.7	15.3	0.6	7.8	0.9	−0.1	−17.9

Table A.4: *CC cross-section* $d\sigma_{CC}/dQ^2$ *measured for* $0.03 < y < 0.85$ *and* $P_{T,h} > 12$ *GeV. C gives the correction factor for the $P_{T,h}$ cut. The statistical error (δ_{sta}), the total error (δ_{tot}), the uncorrelated systematic error (δ_{unc}) and correlated error sources ($\delta_{V+}, \delta_{h+}, \delta_{N+}, \delta_{B+}$) are also given (see caption of table A.1). The δ^{QED} term gives the correction term which was applied due to QED radiation as defined in eq. 9.9. The normalization uncertainty, which is not included in the systematic error, is* 1.5%.

x	$\mathrm{d}\sigma_{NC}/\mathrm{d}x$ (pb)	δ_{sta} (%)	δ_{tot} (%)	δ_{unc} (%)	δ_{E+} (%)	$\delta_{\theta+}$ (%)	δ_{h+} (%)	δ_{N+} (%)	δ_{B+} (%)
0.020	$1.987 \cdot 10^3$	4.5	5.4	3.0	−0.4	−0.2	0.0	−0.3	−0.4
0.032	$1.909 \cdot 10^3$	3.6	4.7	2.9	0.2	−0.2	0.4	−0.2	−0.2
0.050	$1.343 \cdot 10^3$	3.2	4.4	3.0	0.6	−0.3	0.6	−0.4	−0.2
0.080	$9.092 \cdot 10^2$	3.0	4.2	2.8	0.6	−0.2	0.2	−0.4	−0.1
0.130	$5.403 \cdot 10^2$	3.4	4.6	2.9	0.9	−0.2	0.4	−0.4	0.0
0.180	$3.458 \cdot 10^2$	3.7	5.0	3.0	1.2	−0.2	−0.1	−0.6	0.0
0.250	$2.057 \cdot 10^2$	4.0	6.0	3.9	2.0	0.0	−0.7	0.3	0.0
0.400	$6.797 \cdot 10^1$	5.5	9.5	6.2	3.6	0.1	−1.8	2.5	0.0
0.650	$5.225 \cdot 10^0$	11.8	19.0	11.5	6.6	0.1	−3.2	6.2	0.0

Table A.5: *NC cross-section* $\mathrm{d}\sigma_{NC}/\mathrm{d}Q^2$ *measured for* $y < 0.9$ *and* $Q^2 > 1000$ GeV^2. *The statistical error* (δ_{sta}), *the total error* (δ_{tot}), *the uncorrelated systematic error* (δ_{unc}) *and correlated error sources* ($\delta_{E+}, \delta_{\theta+}, \delta_{h+}, \delta_{N+}, \delta_{B+}$) *are also given (see caption of table A.2). The normalization uncertainty, which is not included in the systematic error, is* 1.5%.

x	$\mathrm{d}\sigma_{NC}/\mathrm{d}x$ (pb)	δ_{sta} (%)	δ_{tot} (%)	δ_{unc} (%)	δ_{E+} (%)	$\delta_{\theta+}$ (%)	δ_{h+} (%)	δ_{N+} (%)	δ_{B+} (%)
0.130	$1.180 \cdot 10^0$	79.7	81.4	14.3	1.9	−3.7	−5.2	1.3	−3.8
0.180	$4.077 \cdot 10^0$	32.5	32.9	4.3	1.7	−0.2	0.0	0.0	−0.8
0.250	$3.447 \cdot 10^0$	28.1	28.9	6.2	1.4	−0.3	0.9	−0.4	−0.4
0.400	$2.859 \cdot 10^0$	24.3	27.1	11.7	1.8	0.4	0.2	0.0	−0.1
0.650	$0.265 \cdot 10^0$	50.0	59.2	30.8	6.3	1.8	−1.5	0.8	0.0

Table A.6: *NC cross-section* $\mathrm{d}\sigma_{NC}/\mathrm{d}Q^2$ *measured for* $y < 0.9$ *and* $Q^2 > 10000$ GeV^2. *The statistical error* (δ_{sta}), *the total error* (δ_{tot}), *the uncorrelated systematic error* (δ_{unc}) *and correlated error sources* ($\delta_{E+}, \delta_{\theta+}, \delta_{h+}, \delta_{N+}, \delta_{B+}$) *are also given (see caption of table A.2). The normalization uncertainty, which is not included in the systematic error, is* 1.5%.

x	$\mathrm{d}\sigma_{CC}/\mathrm{d}x$ (pb)	δ_{sta} (%)	δ_{tot} (%)	δ_{unc} (%)	δ_{V+} (%)	δ_{h+} (%)	δ_{N+} (%)	δ_{B+} (%)
0.032	$1.322 \cdot 10^2$	11.6	14.4	6.9	5.1	0.5	0.5	−0.3
0.080	$8.044 \cdot 10^1$	8.4	10.6	6.0	1.9	0.9	0.6	−0.2
0.130	$4.401 \cdot 10^1$	10.0	11.9	6.3	0.6	1.2	0.3	−0.2
0.250	$1.886 \cdot 10^1$	11.8	14.4	7.9	0.2	2.2	−0.3	−0.1
0.400	$5.556 \cdot 10^0$	25.9	30.7	14.6	0.0	7.4	−2.6	−0.1

Table A.7: *CC cross-section* $\mathrm{d}\sigma_{CC}/\mathrm{d}x$ *measured for* $y < 0.9$ *and* $Q^2 > 1000$ GeV^2. *The statistical error* (δ_{sta}), *the total error* (δ_{tot}), *the uncorrelated systematic error* (δ_{unc}) *and correlated error sources* ($\delta_{V+}, \delta_{h+}, \delta_{N+}, \delta_{B+}$) *are also given (see caption of table A.1). The normalization uncertainty, which is not included in the systematic error, is* 1.5%.

Bibliography

[1] E. D. Bloom et al., Phys. Rev. Lett. **23** (1969) 930;
M. Breitenbach et al., Phys. Rev. Lett. **23** (1969) 935.

[2] J. D. Bjorken, Phys. Rev. **179** (1969) 1547.

[3] R. P. Feynman, Phys. Rev. Lett. **23** (1969) 1415.

[4] M. Gell-Mann, Phys. Lett. **8** (1964) 214.

[5] Gargamelle Collab., F.J. Hasert et al., Phys. Lett. **B46** (1973) 138.

[6] S. L. Glashow, Nucl. Phys. **22** (1961) 579;
A. Salam, in: *Elementary Particle Physics*, Proc. 8th Nobel Symp., eds. Almquist and Wiksell, Stockholm 1968, 367;
S. Weinberg, Phys. Rev. Lett. **19** (1967) 1264.

[7] UA1 Collab., G. Arnison et al., Phys. Lett. **B 122** (1983) 103;
UA2 Collab., M. Banner et al., Phys. Lett. **B 122** (1983) 476.

[8] UA1 Collab., G. Arnison et al., Phys. Lett. **B 126** (1983) 398;
UA2 Collab., M. Banner et al., Phys. Lett. **B 129** (1983) 130.

[9] D.J. Fox et al., Phys. Rev. Lett. **33** (1974) 1504;
Y. Watanabe et al., Phys. Rev. Lett. **35** (1975) 898;
H.L. Anderson et al., Phys. Rev. Lett. **38** (1977) 1450;
B.A. Gordon et al., Phys. Rev. Lett. **41** (1978) 615;
EMC Collab., J.J. Aubert et al.,Nucl. Phys. **B213** (1983) 31;
E665 Collab., M.R. Adams et al., Z. Phys **C67** (1995) 403.

[10] BCDMS Collab., A.C. Benvenuti et al., Phys. Lett. **B223** (1989) 485.

[11] NMC Collab., M. Arneodo et al., Phys. Lett. **B364** (1995) 107.

[12] BEBC Collab., K. Varvell et al., Z. Phys. **C36** (1987) 1.

[13] CCFR Collab., P.Z. Quintas et al., Phys Rev. Lett. **71** (1993) 1307.

[14] CDHS Collab., H. Abramowicz et al., Z. Phys., **C25** (1984) 29;
CDHSW Collab., P. Berge et al., Z. Phys., **C49** (1991) 187.

[15] H1 Collab., I. Abt et al., Nucl. Phys. **B407** (1993) 515.

[16] H1 Collab., I. Ahmed et al., Nucl. Phys. **B439** (1995) 471.

[17] ZEUS Collab., M. Derrick et al., Phys. Lett. **B316** (1993) 412.

[18] ZEUS Collab., M. Derrick et al., Z. Phys. **C65** (1995) 379.

[19] H1 Collab., S. Aid et al., Nucl. Phys. **B470** (1996) 3.

[20] H1 Collab., T. Ahmed et al., Phys. Lett. **B324** (1994) 241.

[21] H1 Collab., S. Aid et al, Z. Phys. **C67** (1995) 565.;
H1 Collab., S. Aid et al, Phys. Lett. **B379** (1996) 319.

[22] ZEUS Collab., M. Derrick et al., Phys. Rev. Lett. **75** (1995) 1006.

[23] ZEUS Collab., M. Derrick et al., Z. Phys. **C72** (1996) 47.

[24] ZEUS Collab., M. Derrick et al., Z. Phys. **C72** (1996) 399.

[25] H1 Collab., C. Adloff et al., DESY-99-107, *submitted to Eur. Phys. J.*

[26] Yu.L. Dokshitzer, Sov. Phys. JETP **46** (1977) 641;
V.N. Gribov and L.N. Lipatov, Sov. J. Nucl. Phys. **15** (1972) 438 and 675;
G. Altarelli and G. Parisi, Nucl. Phys. **B126** (1977) 297;
G. Curci, W. Furmanski and R. Petronzio, Nucl. Phys. **B175** (1980) 27;
W. Furmanski and R. Petronzio, Phys. Lett. **B97** (1980) 437.

[27] E.A. Kuraev, L.N.Lipatov and V. Fadin, Sov. Phys. JETP45 (1978) 199;
Y.Y. Balitsky and L.N.Lipatov, Sov. Journ. Nucl. Phys. 28 (1978) 22.

[28] A.D. Martin et al., Eur. Phys. J **C4** (1998) 463.;
A. D. Martin et al., preprint hep-ph/9907231 (1999).

[29] CTEQ Collab., H. Lai et al., MSU-HEP-903100 (1999)

[30] H1 Collab., C. Adloff et al., Z. Phys. **C74** (1997) 191.

[31] ZEUS Collab., J. Breitweg et al., Z. Phys. **C74** (1997) 207.

[32] Y. Sirois, "Searches for New Bosons Coupling to $e-q$ Pairs at HERA and other Colliders", to be published in 'Proceedings of Conference WEIN 98' (1998), and references therein

[33] P. Haberl, F. Schrempp and H.-U. Martyn, Proc. of the Workshop 'Physics at HERA', vol.2,
eds. W.Buchmüller and G.Ingelman, DESY (1992), 1133.

[34] J. C. Pati and A. Salam, Phys. Rev. **D10** (1974) 275; P. Langacker, Phys. Rep. **72** (1981) 185; H. Georgi and S.L. Glashow, Phys. Rev. Lett. **32** (1974) 438.

[35] A. Dobado, M. J. Herrero and C. Munoz, Phys. Lett. **B191** (1987) 449; J. F. Gunion, E. Ma, Phys. Lett. **B195** (1987) 257; R.W:Robinett, Phys. Rev. **D37** (1988)1321; J. A. Grifols ans S.Peris, Phys. Lett. **B201** (1988) 287.

[36] B. Schrempp and F. Schrempp, Phys. Lett. **B153** (1985) 101, and references therein; J. Wudka, Phys. Lett. **B167** (1986) 337.

[37] S. Dimopoulos and L. Susskind, Nucl. Phys. **B155** (1979) 237; S. Dimopoulos, Nucl. Phys. **B168** (1980) 69; E. Fahri, L. Susskind, Phys. Rev. **D20** (1979) 3404; *idem* Phys. Rep. **74** (1981) 277.

[38] G. Altarelli et al., Nucl. Phys. **B 506** (1997) 3.;
H. Dreiner and P. Morawitz, Nucl. Phys. **B 503** (1997) 55.

[39] H1 Collab. , C. Adloff et al., Eur. Phys. J. **C5** (1998) 575.

[40] H1 Collab., I. Abt et al., Nucl. Instr. Meth. **A386** (1997) 310 and 348.

[41] H1 Calorimeter Group, B. Andrieu et al., Nucl. Instr. Meth. **A336** (1993) 499.

[42] H1 Calorimeter Group, B. Andrieu et al., Nucl. Instr. Meth. **A344** (1994) 492;
H1 Calorimeter Group, B. Andrieu et al., Nucl. Instr. Meth. **A350** (1994) 57.

[43] H.P. Wellisch et al., MPI-PhE/94-03 (1994).

[44] V. Shekelyan, H1 internal report, H1-01/93-288

[45] H1 Collab., "Performance of the H1 Liquid Argon Calorimeter", *in preparation.*

[46] H1 SPACAL Group, Nucl. Instr. Meth. **A382** (1996) 395.
H1 SPACAL Group, Nucl. Instr. Meth. **A374** (1996) 149.

[47] S. Levonian, A. Panitsch, H1 internal report, H1-09/95-454 (1995).

[48] T. Carli et al., H1 internal report, H1-07/95-445

[49] J. Riedlberger, H1 internal report, H1-01/95-419

[50] R. Bernet, Ph. D. Thesis, ETH Zürich (1995)

[51] M. Erdmann, DESY preprint 96-090, May 1996

[52] L. Lönnblad, Comp. Phys. Comm. **71** (1992) 15.

[53] G. Ingelman, Proc. of the Workshop 'Physics at HERA', vol. 3,
eds. W. Buchmüller and G. Ingelman, DESY (1992) 1366.

[54] T. Sjöstrand, M. Bengtsson, Comp. Phys. Comm. **43** (1987) 367.

[55] G. A. Schuler and H. Spiesberger, Proc. of the Workshop 'Physics at HERA', vol. 3, eds. W. Buchmüller and G. Ingelman, DESY (1992) 1419.

[56] H. Spiesberger, `DJANGOH` program manual, 1998, *unpublished*

[57] A.D Martin, W.J. Stirling and R.G. Roberts, Phys. Lett. **B306** (1993) 145;
A.D Martin, W.J. Stirling and R.G. Roberts, Phys. Lett. **B309** (1993) 492.

[58] A. Kwiatkowski, H. Spiesberger and H.-J. Möhring, Comp. Phys. Comm. **69** (1992) 155.

[59] T. Sjöstrand, Comput. Phys. Commun. **82** (1994) 74.

[60] M. Glück, E. Reya and A. Vogt, Phys. Rev. **D46** (1992) 1973.

[61] A. Courau and P. Kessler, Phys. Rev. **D46** (1992) 117.

[62] S. Baranov et al., Proc. of the Workshop 'Physics at HERA', vol. 3, eds. W. Buchmüller and G. Ingelman, DESY (1992) 478; J.A.M. Vermaseren, Nucl. Phys. **B229** (1983) 347.

[63] T.Sjöstrand, CERN-TH-6488/92 (1992), Comp. Phys. Comm. **82** (1994) 74.

[64] U. Bauer, J.A.M. Vermaseren and D. Zeppenfeld, Nucl. Phys. **B375** (1992) 3.

[65] R. Brun et al., GEANT3 User's Guide, CERN-DD/EE-84-1 (1987).

[66] M. Rudowicz, MPI-PhE/92-14, Ph.D. Thesis, Universität Hamburg (1992); S. Peters, MPI-PhE/92-13, Ph.D. Thesis, Universität Hamburg (1992)

[67] A.Blondel and F.Jacquet, Proc. of the 'Study of an *ep* Facility for Europe', ed. U. Amaldi, DESY 79/48 (1979) 391.

[68] U. Bassler and G. Bernardi, Nucl. Instr. Meth. **A361** (1995) 197.

[69] S. Bentvelsen et al., Proc. of the Workshop 'Physics at HERA', vol. 1, eds. W.Buchmüller and G.Ingelman, DESY (1992) 23; C. Hoeger, ibid., 43.

[70] U. Bassler and G. Bernardi, Nucl. Instr. Meth. **A426** (1998) 583.

[71] A. Glazov, Ph.D. Thesis, Berlin (1998).

[72] V. Shekelyan, personal communication

[73] C. Kleinwort, personal communication

[74] I. Abt et al., Nucl. Instr. and Meth. **A 386** (1997) 310 and **A 386** (1997) 348.

[75] U. Bassler and G. Bernardi, Z. Phys. **C76** (1997) 223.

[76] H1 Collab., C. Adloff et al., Z. Phys. **C74** (1997) 221.

[77] `H1PHAN` program manual, version 2.03/11, *available from the H1 Collaboration*

[78] A. Mehta, personal communication

[79] C. Wissing, Diploma thesis, Universität Dortmund (1998)

[80] P. Bruel, Ph.D. Thesis, Orsay (1998).

[81] U. Bassler and G. Bernardi, personal communication

[82] V. Effremenko, N. Tobien, H1 internal report, H1-0598-540 (1998)

[83] A. Schöning, Ph.D. Thesis, Hamburg (1996).

[84] F. Keil, Ph.D. Thesis, Heidelberg, *in preparation*

[85] J.-C. Bizot, H1 internal report, H1-07/99-574

[86] A. Babaev et al., H1 internal report, H1-07/96-470

[87] T. Carli et al., H1 internal report, H1-01/99-560

[88] A. Pieuchot, J. Marks, C.Vallee, H1 internal report, H1-IN-423 (01/95)

[89] E.Chabert et al., H1 internal report, H1-11/98-556 (1998)

[90] E. Chabert, Ph.D. Thesis, Marseille, *in preparation*

[91] I. Negri, Ph.D. Thesis, Marseille (1998).

[92] G. Martin, Ph.D. Thesis, Hamburg (1997).

[93] S. D. Ellis and D. E. Soper, Phys. Rev. **D48** 91993) 3160;
S. Catani, Yu. L. Dokshitzer, M. H. Seymour and B. R. Webber, Nucl. Phys. **B406** (1993) 187.

[94] H. Spiesberger et al., Proc. of the Workshop 'Physics at HERA', vol.2, eds. W.Buchmüller and G.Ingelman, DESY (1991), 798.

[95] D. Bardin, C. Burdik, C. Christova and T. Riemann, Z. Phys. **C44** (1989) 149

[96] B. Heinemann, S. Riess, H. Spiesberger, 'Radiative Corrections for Charged Current Scattering: A Comparison of Computer Codes', Proc. of the 1998/99 Workshop 'Monte Carlo Generators for HERA Physics', DESY, *to be published*

[97] J. Kripfganz and H. Perlt, Z. Phys. **C41** (1988) 319, H. Spiesberger, Phys. Rev. **D52** (1995) 4936.

[98] F. Jegerlehner, DESY 97-121, Proc. of the Workshop 'QCD and QED in Higher Orders', Rheinsberg (Germany) 1996, Nucl. Phys. B (Proc Suppl.);
H. Burkhardt et al., Z. Phys. **C43** (1989) 497.

[99] J. Blümlein, Proc. of the Workshop 'Physics at HERA' (1991), vol. 3, eds. W.Buchmüller and G.Ingelman, DESY (1992) 1270

[100] A. Arbuzov, D. Bardin, J. Blümlein, L. Kalnovskaya and T. Riemann, `HECTOR 1.00`, Comp. Phys. Comm. **94** (1996) 128.

[101] E. Rizvi and F. Zomer, personal communication

[102] A.M. Cooper-Sarkar, R.C.E. Devenish and A. De Roeck, Int. J. Mod. Phys. **A13** (1998) 3385.

[103] M. Klein, 'Structure Functions', invited talk to Lepton-Photon conference 1999 , Proceedings to appear

[104] A.M. Cooper-Sarkar et al., J. Phys. **G25** (1999) 1387-1409., and references therein

[105] H1 Collab., 'Measurement of the Charged and Neutral Current Cross Sections at HERA', paper #157 b submitted to HEP 99, Tampere

[106] R. Beyer et al., Proc. of the Workshop 'Future Physics at HERA', vol.1, eds. G. Ingelman, A. De Roeck and R. Klanner, DESY (1996) 140.

[107] PDG Tables 1998, Eur. Phys. J. **C3** (1998) 1.

[108] W. J. Marciano, preprint hep-ph/9903451 (1999)

[109] ALEPH Collab., R. Barate et al., Phys. Lett. **B453** (1999) 121-137;
DELPHI Collab., P. Abreu et al., CERN-EP/99-079 (1999), *submitted to Phys. Lett. B*;
L3 Collab., M. Acciarri et al., Phys. Lett. **B454** (1999) 386-398;
OPAL Collab., K. Ackerstaff et al., Phys. Lett. **B453** (1999) 138-152

[110] CDF Collab., F. Abe et al., Phys. Rev. Lett. **45** (1995) 11;
DØ Collab., B. Abbott et al., Phys. Rev. Lett. **80** (1998) 3008.

[111] LEP electroweak working group, see `http://www.cern.ch/LEPEWWG/`

[112] ZEUS Collab., J. Breitweg et al., DESY 99-59 (1999),
submitted to Eur. Phys. J.

[113] G. Köpp, D. Schaile, M. Spira and P. Zerwas, Z. Phys. **C65** (1965) 545.

[114] see e.g. rewies by T. Kinoshita and D.R. Yennie, H.-U. Martyn, and R.R. van Dyck Jr. in "Quantum Electrodynamics", ed. T. Kinoshita, World Scientific (1990).

[115] H1 Collab., 'Search for Contact Inteactions at HERA', paper #157 f submitted to HEP 99, Tampere

[116] J. Scheins, Ph.D. Thesis, Aachen University, *in preparation*

[117] H1 Collab.,C. Adloff et al., DESY-99-081, *to appear in Eur.Phys.J. C*

Acknowledgments

First of all I wish to thank Prof. Dr. F.-W. Büsser and Prof. Dr. J. Meyer for the great support and freedom they gave me during my time as a Ph.D. student.

I am indebted to A. Mehta and E. Rizvi who I have been working closely together with. This measurement would not have been possible without their readiness to help and to discuss many details of the analysis. I am also thankful to Julian Phillips for his help and judgement on important parts of the analyses. They together with other members of the "english Mafia" helped in making my time on H1 a fun and enjoyable experience.

Furthermore I would like to thank the convenors and the members of the ELAN, HIP, electroweak and ESCALE working group for providing a stimulating forum for the discussion of analysis topics. In particular I wish to thank U. Bassler and G. Bernardi for the great working relationship and J. Gayler, E. Elsen, J. B. Dainton and S. Riess for their guidance and their availability for discussions during the last three years.

I would also like to thank H. Spiesberger for the many discussions and his patience during those.

Last but not least I am thankful to my parents for the support, financial and moral, throughout my life. Also I would like to thank my two brothers; in particular Tobias for the sacrifice that he made in lending me his computer during the last few months.